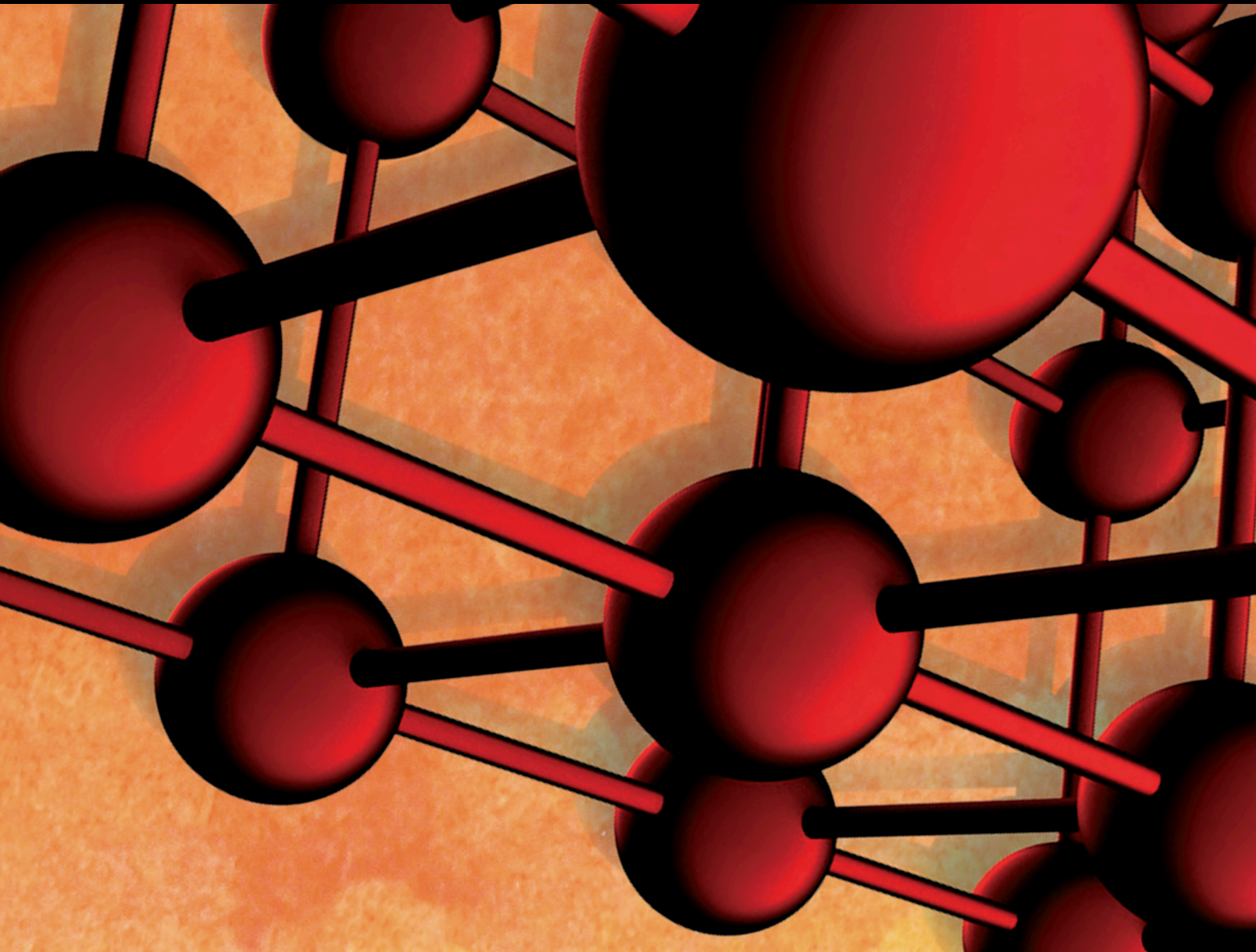# Aging of Concrete Structures and Infrastructures: Causes, Consequences, and Cures (C^3)

Lead Guest Editor: Mohammad A.Hariri-Ardebili
Guest Editors: Leandro Sanchez, Roozbeh Rezakhani, and Alain Giorla

Aging of Concrete Structures and Infrastructures: Causes, Consequences, and Cures (C3)

Aging of Concrete Structures and Infrastructures: Causes, Consequences, and Cures (C3)

Lead Guest Editor: Mohammad A.Hariri-Ardebili
Guest Editors: Leandro Sanchez, Roozbeh Rezakhani, and Alain Giorla

Antonio Gloria, Italy
Vincenzo Guarino, Italy
Daniel Guay, Canada
Gianluca Gubbiotti, Italy
Jenö Gubicza, Hungary
Xuchun Gui, China
Benoit Guiffard, France
Ivan Gutierrez-Urrutia, Japan
Hiroki Habazaki, Japan
Simo-Pekka Hannula, Finland
Akbar Heidarzadeh, Iran
David Holec, Austria
Satoshi Horikoshi, Japan
David Houivet, France
Rui Huang, USA
Yi Huang, United Kingdom
Michele Iafisco, Italy
Erdin Ibraim, United Kingdom
Saliha Ilican, Turkey
Md Mainul Islam, Australia
Ilia Ivanov, USA
Hom Kandel, USA
kenji Kaneko, Japan
Fuat Kara, Turkey
Katsuyuki Kida, Japan
Akihiko Kimura, Japan
Soshu Kirihara, Japan
Paweł Kłosowski, Poland
Jan Koci, Czech Republic
Ling B. Kong, Singapore
Lingxue Kong, Australia
Fantao Kong, China
Pramod Koshy, Australia
Hongchao Kou, China
Alexander Kromka, Czech Republic
Ravi Keshwar Kumar, India
Luciano Lamberti, Italy
Andrea Lamberti, Italy
Fulvio Lavecchia, Italy
Marino Lavorgna, Italy
Laurent Lebrun, France
Joon-Hyung Lee, Republic of Korea
Pavel Lejcek, Czech Republic
Cristina Leonelli, Italy
Ying Li, USA
Yuanshi Li, Canada
Yuning Li, Canada

Guang-xing Liang, China
Barbara Liguori, Italy
Shaomin Liu, Australia
Yunqi Liu, China
Jun Liu, China
Meilin Liu, Georgia
Zhiping Luo, USA
Fernando Lusquiños, Spain
Peter Majewski, Australia
Georgios Maliaris, Greece
Muhamamd A. Malik, United Kingdom
Dimitrios E. Manolakos, Greece
Necmettin Maraşlı, Turkey
Enzo Martinelli, Italy
Alessandro Martucci, Italy
Yoshitake Masuda, Japan
Bobby Kannan Mathan, Australia
Roshan Mayadunne, Australia
Mamoun Medraj, Canada
Shazim A. Memon, Kazakhstan
Philippe Miele, France
Andrey E. Miroshnichenko, Australia
Hossein Moayedi, Vietnam
Sakar Mohan, India
Jose M. Monzo, Spain
Michele Muccini, Italy
Alfonso Muñoz, Spain
Roger Narayan, USA
Rufino M. Navarro, Spain
Miguel Navarro-Cia, United Kingdom
Ali Nazari, Australia
Behzad Nematollahi, Australia
Luigi Nicolais, Italy
Peter Niemz, Switzerland
Hiroshi Noguchi, Japan
Chérif Nouar, France
Olanrewaju Ojo, Canada
Dariusz Oleszak, Poland
Laurent Orgéas, France
Togay Ozbakkaloglu, United Kingdom
Nezih Pala, USA
Marián Palcut, Slovakia
Davide Palumbo, Italy
Gianfranco Palumbo, Italy
Zbyšek Pavlík, Czech Republic
Matthew Peel, United Kingdom
Alessandro Pegoretti, Italy

Gianluca Percoco, Italy
Claudio Pettinari, Italy
Giorgio Pia, Italy
Silvia M. Pietralunga, Italy
Daniela Pilone, Italy
Teresa M. Piqué, Argentina
Candido Fabrizio Pirri, Italy
Marinos Pitsikalis, Greece
Alain Portavoce, France
Simon C. Potter, Canada
Ulrich Prahl, Germany
Viviana F. Rahhal, Argentina
Carlos R. Rambo, Brazil
Shahed Rasekh, Portugal
Manijeh Razeghi, USA
Paulo Reis, Portugal
Yuri Ribakov, Israel
Aniello Riccio, Italy
Anna Richelli, Italy
Antonio Riveiro, Spain
Marco Rossi, Italy
Sylvie Rossignol, France
Pascal Roussel, France
Fernando Rubio-Marcos, Spain
Francesco Ruffino, Italy
Mark H. Rümmeli, China
Pietro Russo, Italy
Antti Salminen, Finland
F.H. Samuel, Canada
MariaGabriella Santonicola, Italy
Hélder A. Santos, Finland
Carlo Santulli, Italy
Fabrizio Sarasini, Italy
Michael J. Schu#tze, Germany
Raffaele Sepe, Italy
Kenichi Shimizu, USA
Fridon Shubitidze, USA
Mercedes Solla, Spain
Donato Sorgente, Italy
Charles C. Sorrell, Australia
Andres Sotelo, Spain
Costas M. Soukoulis, USA
Damien Soulat, France
Adolfo Speghini, Italy
Antonino Squillace, Italy
Koichi Sugimoto, Japan
Baozhong Sun, China

Sam-Shajing Sun, USA
Youhong Tang, Australia
Shengwen Tang, China
Kohji Tashiro, Japan
Miguel Angel Torres, Spain
Laszlo Toth, France
Achim Trampert, Germany
Tomasz Trzepieciński, Poland
Matjaz Valant, Slovenia
Luca Valentini, Italy
Ashkan Vaziri, USA
Lijing Wang, Australia
Zhongchang Wang, Portugal
Rui Wang, China
Lu Wei, China
Jörg M. K. Wiezorek, USA
Jiang Wu, China
Guoqiang Xie, China
Jinyang Xu, China
Dongmin Yang, United Kingdom
Zhonghua Yao, China
Hemmige S. Yathirajan, India
Yee-wen Yen, Taiwan
Wenbin Yi, China
Ling Yin, Australia
Tetsu Yonezawa, Japan
Hiroshi Yoshihara, Japan
Belal F. Yousif, Australia
Lenka Zaji#c#kova#, Czech Republic
Zhigang Zang, China
Michele Zappalorto, Italy
Jinghuai Zhang, China
Li Zhang, China
Gang Zhang, Singapore
Mikhail Zheludkevich, Germany
Wei Zhou, China
You Zhou, Japan
Hongtao Zhu, Australia

Contents

Editorial

Aging of Concrete Structures and Infrastructures: Causes, Consequences, and Cures (C³)

Mohammad Amin Hariri-Ardebili [iD],[1,2] **Leandro Sanchez,**[3] **and Roozbeh Rezakhani**[4]

[1]*University of Colorado at Boulder, Boulder, CO, USA*
[2]*University of Maryland College Park, Park, MD, USA*
[3]*University of Ottawa, Ottawa, Canada*
[4]*EPFL, Lausanne, Switzerland*

Correspondence should be addressed to Mohammad Amin Hariri-Ardebili; mohammad.haririardebili@colorado.edu

Aging of any concrete structure is a natural process, but it has become an urgent and critical problem in recent years, during which long-operating dams and nuclear power plants have begun to lose reliable life. A large number of infrastructures all over the world are over 50 years old and suffer from extensive deterioration that affects their serviceability. The high costs associated with preserving the aging structures along with the limited funds allocated for their maintenance pose significant technical and financial challenges, which require the systematic approaches for risk-informed condition assessment. Only in the USA, the American Society of Civil Engineers (ASCE) estimates a required investment amount of about 3.6 trillion dollars by 2020 to improve the condition of infrastructures to an acceptable level. This is more than twice the anticipated available funding level. Aging usually begins to appear in individual elements of the structures, leading to nonuniform or heterogeneous behavior. The most well-known and widespread sign of structural aging is related to weakening of concrete mechanical properties.

Figure 1 schematically presents the performance assessment of concrete structures and infrastructures in their lifetime highlighting the aging effects. Besides typical uncertainties such as uncertainty in environmental loads, several other sources of uncertainty exist, including unknown initial and boundary conditions, unknown damage history to the structure, uncertainties in current laboratory test methods, and finally a big uncertainty in the available predictive models.

In order to develop a comprehensive performance assessment methodology, the past behavior (through diagnosis) should be combined by current observations and tests, and all should be used to predict the future life of the structure. Typically, the hybrid uncertainties are increased with lifetime of the system. Aging and deterioration is a factor which accelerates/intensifies the uncertain response of the structures to imposed environmental actions. Aging and deterioration of concrete structures and infrastructures can be incorporated in both design and analysis phases. In design of new structures, factors such as creep and shrinkage, temperature gradients, sustainability and life cycle cost, and resiliency of the system should be considered. In the analysis of existing structures, material uncertainty and current damage pattern are the key parameters.

The articles presented in this special issue are focused on the state-of-the-art techniques, methods, and applications employed in aging, deterioration, and damage analysis and assessment in concrete structures and infrastructures. Overall, 17 submissions were received by the editorial team, and 8 manuscripts have been accepted for publication.

Freeze-thaw cycling conditions are a primary cause of durability deterioration of concrete structures in the regions with extreme temperature variations. In the paper by Yang et al. "Equation for the Degradation of Uniaxial Compression Stress of Concrete due to Freeze-Thaw Damage," the authors conducted a series of experiments on concrete specimen and determined the freeze-thaw-based damage variable. Subsequently, they proposed an equation for the
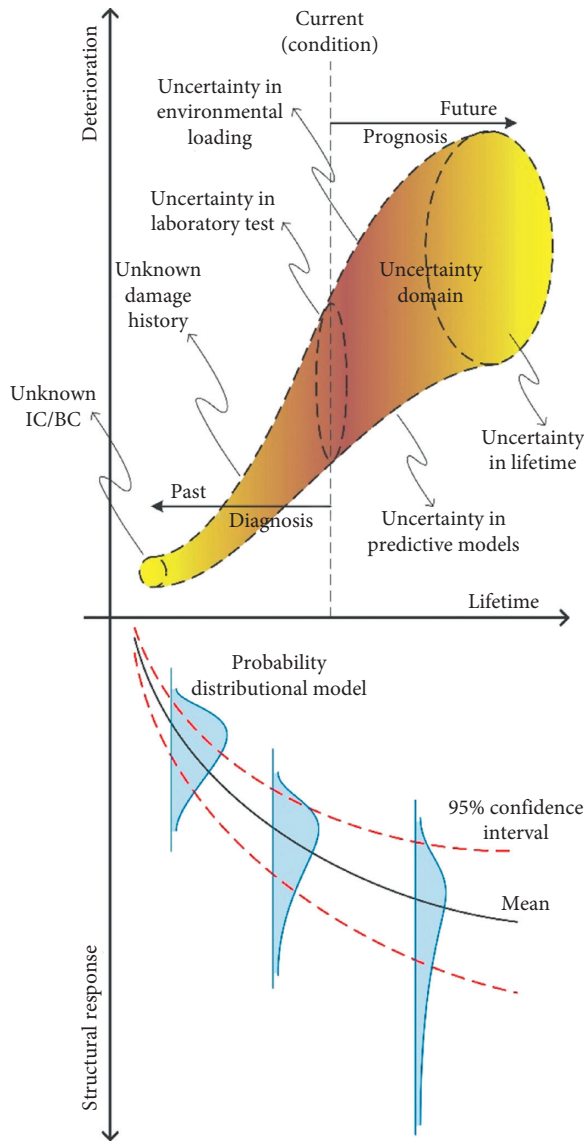
Figure 1: Diagnosis and prognosis of deteriorating concrete structures incorporating various uncertainties.

stress-strain constitutive relation including the freeze-thaw damage variable. They pointed out the observed changes in the elastic modulus with increase in the freeze-thaw cycle number.

Concrete paving stones are fabricated by mixing cement, aggregate, water, and additives in certain ratios. They are widely used in urban road, pavement, and recreation areas. Therefore, increasing their durability and strength is the key factor in sustainability design. In the paper by Bakis "Increasing the Durability and Freeze-Thaw Strength of Concrete Paving Stones Produced from Ahlat Stone Powder and Marble Powder by Special Curing Method," the author proposed a method to use construction waste materials, i.e., Ahlat stone powder and marble powder, in fabricating interlocked paving stones. Both the durability and freeze-thaw strength of the produced material increased by the special curing method.

Sulfate attack on cement is one of the reasons for degradation of concrete durability and subsequently reduces the service life of the concrete structures. In the paper by Liu et al. "Research on Sulfate Attack Mechanism of Cement Concrete Based on Chemical Thermodynamics," the authors characterized the relationship between temperature and the Gibbs free energy of erosion products generated during the sulfate attack on cement. The proposed model, which was based on principles of chemical thermodynamics, determined the phase composition, microstructure, crystal form, and morphology of erosion products before and after sulfate attack. They pointed out that the sulfate attack has double effects on mechanical properties of specimens.

Accurate performance evaluation of expressway pavement is a vital factor to determine the pavement design scheme and the future maintenance program. In the paper by Yang et al. "Highway Performance Evaluation Index in Semiarid Climate Region Based on Fuzzy Mathematics," the authors proposed a method based on fuzzy mathematics in order to evaluate the performance of a case study pavement. They incorporated multiple sources of fuzziness and randomness in their calculations. The performance grade is quantified by an iterative scheme and contrasted with traditional methods.

Although the long-span concrete girder bridges (including continuous rigid-frame bridges) have been widely used in construction, they suffer from excessive long term deflection. In the paper by Niu and Tang "Effect of Shear Creep on Long-Term Deformation Analysis of Long-Span Concrete Girder Bridge," the authors developed a systematic framework for long-term creep calculation of girder bridges using commercial finite element package. Based on linear creep and the superposition principle, the proposed method can consider both shear creep and segmental multiage concrete effect. For a case study bridge, they reported that shear creep causes 10%+ in long-term deformation. However, the impact of shear creep is close for a bridge with different degrees of prestressing.

The posttensioning by monostrands in substitute cable ducts is a highly efficient method for strengthening of existing bridges in order to increase their load-bearing capacities in terms of current traffic load and to extend their service life. In the paper by Svoboda et al. "Strengthening and Rehabilitation of U-Shaped RC Bridges Using Substitute Cable Ducts," the authors described strengthening and rehabilitation of 100+-year-old bridges. The proposed method minimizes the interventions into the constructions, unseen method of cable arrangement, and the absence of impact on appearance.

Adjacent precast concrete box-beam bridges have been a popular solution for small- and medium-span bridges worldwide. Although nonlinear FEA provides an accurate redundancy assessment of box-beam segments, its application is not always feasible for practitioners. In the paper by Leng et al. "Structural Redundancy Assessment of Adjacent Precast Concrete Box-Beam Bridges in Service," the authors proposed a simplified approach based on linear FEA coupled with field load testing to address the particular structural feature and topology of adjacent precast concrete box-beam

bridges. This method reduces the computation complexity and improves the reliability.

Multihazard resilience and sustainability of the structures decrease by aging of their components. In the paper by Hayashi et al. "Fundamental Investigation on Seismic Retrofitting Method of Aging Concrete Structural Wall using Carbon Fiber Sheet-Constitutive Law of Rectangular Section," the authors developed a method for seismic strengthening of aging RC buildings by wrapping the structural members with carbon fiber sheets. According to a series of monotonic uniaxial compression tests, they found that the compressive strength decreases and the ultimate strain increases as the ratio of long to short side of the rectangular cross section increases. They also proposed evaluation formulas for the constitutive law of concrete elements with rectangular cross sections.

We hope that this special issue would shed light on the recent advances and developments in the area of aging concrete structures and infrastructures and attract attention by the scientific community to pursue further research and studies on causes, consequences, and cures (C^3) of aging and deteriorating concrete components in various scales (micro, meso, and macro).

Conflicts of Interest

The editors declare that they have no conflicts of interest regarding the publication of this Special Issue.

Acknowledgments

Mohammad Amin Hariri-Ardebili
Leandro Sanchez
Roozbeh Rezakhani

Research Article

Fundamental Investigation on Seismic Retrofitting Method of Aging Concrete Structural Wall Using Carbon Fiber Sheet-Constitutive Law of Rectangular Section

Kazuhiro Hayashi [iD],[1] **Tomoya Matsui,**[1] **Taiki Saito,**[1] **and Roy Reyna**[2]

[1]*Department of Architecture and Civil Engineering, Toyohashi University of Technology, Toyohashi 441-8580, Japan*
[2]*Faculty of Civil Engineering, National University of Engineering, Lima 15333, Peru*

Correspondence should be addressed to Kazuhiro Hayashi; hayashi.kazuhiro@forest.ocn.ne.jp

Aging building structure has become a world problem. This problem is particularly serious in developing and underdeveloped countries. The multihazard resilience and sustainability (e.g., seismic performance) decrease at the aging building. A construction method for strengthening aging-reinforced concrete buildings by wrapping structural members with carbon fiber sheets has been proposed and implemented in recent years. Authors aim to develop a seismic retrofitting method of aging concrete structural wall with a rectangular cross section using carbon fiber sheets. In this paper, authors examined the stress-strain relationship of concrete elements with rectangular cross sections reinforced by wrapping with carbon fiber sheets. Monotonic uniaxial compression tests were performed on 21 specimens using the ratio of the long side to the short side and the ratio of the element height to the short side of the concrete cross section, the weight of the carbon fiber sheet, and the chamfer radius of section corners as variables. The tests revealed that (1) the compressive strength decreases and ultimate strain increases as the ratio of the long to short side (longitudinal ratio) of the cross section increases even in a range the ratio exceeds 2 and (2) the ratio of the element height to the short side does not significantly affect the stress-strain relationship. Furthermore, authors proposed evaluation formulas for the constitutive law of concrete elements with rectangular cross sections including the longitudinal ratio which exceeds 2 reinforced by carbon fiber sheets and confirmed that the formulas can reproduce the test results with good accuracy.

1. Introduction

A construction method for strengthening aging-reinforced concrete buildings against earthquakes by wrapping structural members with carbon fiber sheets (CF sheets) has been proposed and implemented in recent years [1–4]. It was conventionally believed that seismic reinforcement using CF sheet jackets (CF reinforcement) is applicable to beam and column members with circular [5, 6] or nearly square [7–9] cross sections and beam-column connections [10]. Lorenzis and Tepfers [5] proposed an evaluation formula for the axial strain at peak stress of FRP-confined concrete cylinders. Carey and Harries [6] presented the recommendations for modeling and designing of axially loaded circular confined concrete. Zhuang et al. [7] repaired the seriously damaged

RC beam specimens with CFRP and was verified the seismic performance experimentally. Lee et al. [8] presented the sectional renovation of RC beam members using CFRP composites. Ercan et al. [9] clarified experimentally that the reinforced concrete beam-column connections strengthened with carbon fiber-reinforced plastic (CFRP) sheets increase the bearing capacity and ductility. In recent years, new-type mixed structure connection consisting of the reinforced concrete column and steel beam (RCS) is developed [10]. Reinforcement with the CF sheet can be applied easily to mixed structures. So, the method had not been used on walls or other cross sections with extremely large aspect ratios. The authors have proposed seismic retrofitting using the wrapping method of structural members with CF sheets for the problem of flexural failure in aging columnless

multistory shear walls found in the 2010 Chile Earthquake and others and have verified the method's effectiveness using static loading tests [11, 12].

To design the CF reinforcement, the constitutive law of materials of the concrete element confined by the CF sheet (i.e., stress-strain relationship) has to be estimated. Most of the past studies [13–18] propose evaluation formulas for the constitutive law of CF-reinforced concrete elements with circular or square cross sections. Pessiki et al. [14] presented the experimental results of the axial loading behavior of circular and square concrete specimens confined with fiber-reinforced polymer (FRP) composite jackets. Nakatsuka et al. [13] and Lam and Teng [15] proposed a stress-strain model for carbon fiber sheet-confined concrete with a circular and square section based on the monotonic compression tests. Harries and Carey [16] investigated the effect of the gap between the concrete and confining FRP jacket and proposed a stress-strain relationship considering this effect. Lam and Teng [17] proposed a stress-strain model of FRP-confined concrete under cyclic compression loading. Mahdavi et al. [18] proposed the optimise design procedure (algorithm) of the seismically retrofitting reinforced concrete structures based on the stress-strain relationship of square column cross section with FRP. Some studies also consider rectangular cross sections [19–24]. Lam and Teng [19] and Ouyang and Liu [20] proposed a stress-strain model for the FRP-confined concrete of the rectangular columns. Wang et al. [22] presented the analysis models of the reinforced concrete frame (rectangular cross section) strengthened with carbon fiber-reinforced polymer (CFRP) sheets. However, the ratio of the long to short side (longitudinal ratio) on these studies is around 2, and wall members are beyond their scope of application. Triantafillou et al. [24] used compression test specimens of FRP-confined concrete elements with the longitudinal ratio exceeding 4. They proposed the evaluation method of a compressive strength but not a stress-strain relationship (especially postpeak behavior).

When concrete elements with circular cross sections are reinforced with CF, the confinement effect increases compressive strength and improves ductility capacity as discussed by Lam and Teng [15]. However, for rectangular cross sections, the confinement effect is not as large as in round sections. When the chamfer radius of section corners is small, ductility improves but the strength may not increase as discussed by Nakatsuka et al. [13]. Moreover, the confining effect of the CF sheet is further reduced when the longitudinal ratio is larger as discussed elsewhere [20, 23]. The maximum ratio of the long to short side on the previous studies is around 2. Thus, the constitutive law cannot be estimated based on previous studies of concrete elements when the CF reinforcement is applied to wall members.

In this paper, authors conducted uniaxial compression tests using the amount of fiber reinforcement, the ratios of the long side and height with respect to the short side of the cross section, and the chamfer radius of section corners as variables in order to shed light on the confinement effect of CF sheets on rectangular concrete sections and to empirically show their stress-strain relationships. Furthermore, in order to apply to rectangular cross sections designed as wall members as well, authors expanded the constitutive law suggested in a previous research [13] and derived evaluation formulas with explicit functions for effective confinement area and longitudinal ratio of the concrete element.

2. Evaluation Formulas for the Constitutive Law of CF-Reinforced Concrete

2.1. Monotonically Increasing Model of Stress-Strain Relationship. ACI Committee 440 [23] gives the stress-strain relationship shown in Figure 1 for the constitutive law of materials of concrete elements reinforced with CF. The linear quadratic slope E_2 and strain at ultimate state ε_{ccu} in Figure 1 are calculated from the cross-sectional quantities of the concrete element and CF sheet used for reinforcement. In addition to concrete elements with circular and square cross sections, the scope includes rectangular cross sections with longitudinal ratios not greater than 2. For the rectangular cross sections, the confinement effect of CF reinforcement is affected by the chamfer radius of section corners. In the ACI model, the effective confinement area ratio α_e of the concrete element confined by the CF sheet (see Figure 2) is estimated by the following equation, which reflects the evaluation based on the material constitutive law:

$$\alpha_e = \frac{A_e}{A_c} = \frac{1 - \left(\left[b/d\,(d - 2R)^2 + d/b\,(b - 2R)^2\right]/3A_g\right) - \rho_g}{1 - \rho_g},$$

(1)

where b is the shorter dimension of the cross section, d is the longer dimension, and R is the chamfer radius of section corners (see Figure 2). Also, A_c is the area of the cross section, A_e is the effective confinement area of the CF sheet, A_g is the total cross-sectional area of the concrete element (equal to A_c without steel rebars), and ρ_g is the ratio of reinforcement.

The ACI model has a monotonically increasing stress-strain relationship, in which the stress continues to increase until the concrete element reaches the ultimate state under compressive forces (see Figure 1). However, it has been noted that the stress-strain relationship does not necessarily increase monotonically when the CF sheet confinement is inadequate (such as when the chamfer radius is small with respect to cross-sectional dimensions) or when the longitudinal ratio of the element is large. This phenomenon is discussed elsewhere [13, 20].

2.2. Maxima Model of Stress-Strain Relationship. Nakatsuka et al. [13] proposed a method for evaluating the constitutive law of materials based on a maxima model, in which the slope of the stress-strain relationship becomes negative after reaching compressive strength (Nakatsuka model). The stress-strain relationship of the Nakatsuka model outlined in Figure 3 accommodates both a monotonically increasing model in which the strength uniformly rises until ultimate strain when the CF sheet ruptures and a maxima model in which the compressive strength is reached
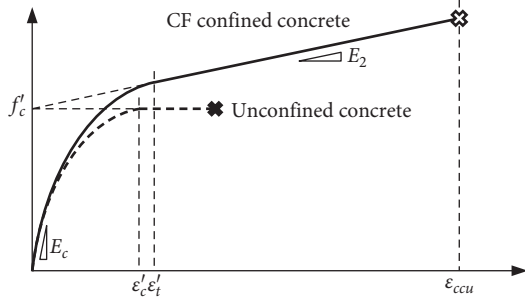
FIGURE 1: Stress-strain relationship of the ACI model.
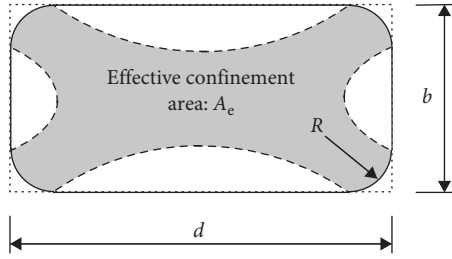
FIGURE 2: Effective confinement area according to the ACI model.

FIGURE 3: Stress-strain relationship of Nakatsuka model.

in the range of about 0.25 to 0.5% axial strain and the strength falls thereafter.

The Nakatsuka model calculates the six components that define the material constitutive law in Figure 3. σ_B is the compressive strength of concrete elements reinforced with CF calculated using the evaluation formula as follows:

$$\sigma_B = F_0 + 4p_f E_f \varepsilon_{fB} C_{\sigma B}, \tag{2}$$

where F_0 is the compressive strength of unreinforced plain concrete, p_f is the reinforcement ratio of the CF sheet, and E_f is Young's modulus of elasticity of the CF sheet. The unit of σ_B, F_0, and E_f are N/mm^2. Also, ε_{fB} is given by the following equation:

$$\varepsilon_{fB} = \begin{cases} 0.01\left(1 - \dfrac{1}{((F_0/140) + 1)}\right), & F_0 \leq 60, \\ \\ 0.003, & 60 < F_0 \leq 80. \end{cases} \tag{3}$$

ε_B is the strain when the stress reaches σ_B calculated using the evaluation formula as follows:

$$\varepsilon_B = \varepsilon_0 + 10\varepsilon_0 \frac{p_f E_f \varepsilon_{fB}}{F_0} C_{\varepsilon B}, \tag{4}$$

where ε_0 is the axial strain for the said compressive strength. E_{BT} is the stiffness of the 2nd region in Figure 3 calculated using the evaluation formula as follows:

$$E_{BT} = -0.4E_{0BT} + \frac{1.4E_{0BT}}{C_{EBT}\left(p_f E_f/0.06F_0^2\right) + 1}, \tag{5}$$

where E_{0BT} is given by the following equation:

$$E_{0BT} = 6000 - 430F_0. \tag{6}$$

ε_T is the strain of the boundary point between the 2nd region and the 3rd region in Figure 3 calculated using the evaluation formula as follows:

$$\varepsilon_T = \varepsilon_0(-0.016F_0 + 2.7) + \varepsilon_0(0.00001F_0 + 0.0016)C_{\varepsilon T} p_f E_f. \tag{7}$$

E_{TR} is the stiffness of the 3rd region in Figure 3 calculated using the evaluation formula as follows:

$$E_{TR} = -0.25E_{0BT} + \frac{0.55E_{0BT}}{C_{ETR}\left(p_f E_f/0.06F_0^2\right) + 1}. \tag{8}$$

ε_R is the ultimate strain of concrete elements reinforced with CF calculated using the evaluation formula as follows:

$$\varepsilon_R = \varepsilon_0(20\varepsilon_{fr} + 1.2) + \varepsilon_0(1000\varepsilon_{fr} - 3)C_{\varepsilon R}\frac{p_f E_f}{F_0^2}, \tag{9}$$

where ε_{fr} is the strain at rupture of the CF sheet. C in equations (2), (4), (5), (7), (8), and (9) is a cross-sectional shape factor based on the cross-sectional shape of the concrete element and is equal to 1.0 in all cases for circular sections. For square sections, $C_{\sigma B}$, $C_{\varepsilon B}$, and $C_{\varepsilon T}$ are equal to 0.6, C_{EBT} and C_{ETR} are equal to 0.4, and $C_{\varepsilon R}$ is equal to 1.0.

Nakatsuka et al. [13] performed a number of uniaxial compression tests on concrete elements with CF reinforcement to verify the accuracy of this model. However, the study only considered concrete elements with circular and square cross sections, and the chamfer radius R of square-sectioned specimens was not considered as an experimental variable.

2.3. Expansion of Evaluation Formulas for the Constitutive Law in This Paper.

For evaluation formulas of the constitutive law for concrete elements reinforced with CF, the Nakatsuka model is advantageous because it can accommodate both a monotonically increasing model and a maxima model. But, it does not take into account the variation in confinement effect due to changes in chamfer radius of section corners (i.e., the impact of effective confinement area A_e) in rectangular sections. Moreover, it does

not consider rectangular cross sections. Authors aim to expand the scope of the Nakatsuka model in this paper.

First, authors set the cross-sectional shape factors C in equations (2), (4), (5), (7), (8), and (9) as functions of the effective confinement area ratio α_e instead of fixed values. The previous Nakatsuka's work [13] used $\phi 150 \times 300$ mm round specimens and $150 \times 150 \times 300$ mm square specimens (with chamfer radius R equal to 30 mm for all). For round sections, the CF sheet exerts a confinement effect on the entire cross section (i.e., the effective confinement area ratio α_e based on equation (1) is equal to 1.00), and the cross-sectional shape factors C in the study are all equal to 1.0 (i.e., without correction). For square-sectioned specimens, since the value of the effective confinement area ratio α_e fell to 0.75, the cross-sectional shape factors C take the values given in Section 2.2. Furthermore, since the effect of CF reinforcement is lost in the case when the effective confinement area ratio α_e becomes zero, the cross-sectional shape factors C should also be zero. Accordingly, the cross-sectional shape factors C of the Nakatsuka model are extended and defined as follows in this paper:

$$C_{\sigma B} = C_{\varepsilon B} = C_{\varepsilon T} = \max \begin{cases} 1.6\alpha_e - 0.6, \\ 0.8\alpha_e, \end{cases} \tag{10}$$

$$C_{EBT} = C_{ETR} = \max \begin{cases} 2.4\alpha_e - 1.4, \\ 0.53\alpha_e, \end{cases} \tag{11}$$

$$C_{\varepsilon R} = 1.33\alpha_e \leq 1.00. \tag{12}$$

In order to apply to rectangular cross sections, new correction factors are defined as functions of the longitudinal ratio (d/b). These correction factors are defined and derived in the latter part of this paper, and their accuracy is verified against the test results in order to conform with the experimental results given in Section 3.

3. Uniaxial Compression Tests of the CF-Reinforced Concrete Element

3.1. Specimen Setup. The test specimens are shown in Table 1, while the material properties of the CF sheet are shown in Table 2. There are five C-series test specimens with circular cross sections, seven S-series test specimens with square cross sections, and nine R-series test specimens with rectangular cross sections for a total of 21 specimens. Figure 4 shows the configuration of rectangular-sectioned specimens.

The C series uses the weight of the CF sheet (five types weighing from 0–600 g/m²; the 400 g/m² and 600 g/m² weights are double wrapped 200 g/m² and 300 g/m² CF sheets) as the variable, with the aim of re-examining the validity of the Nakatsuka model proposed in a previous Nakatsuka's study [13]. The S series uses the weight of the CF sheet (five types weighing from 0–600 g/m², as in the C series), the chamfer radius R of section corners (two types at 15 mm and 30 mm; the 30 mm radius test specimen S12-3R has the same cross-sectional shape as a test specimen in the Nakatsuka's previous study), and the height ratio (i.e., ratio

TABLE 1: Test specimens.

Specimen	Dimension of concrete				CF sheet	
	b (mm)	d (mm)	h (mm)	R (mm)	ρ_f (g/m²)	p_f (%)
C12-0	$\phi 150$		300		—	—
C12-2	$\phi 150$		300		200	0.148
C12-3	$\phi 150$		300	—	300	0.223
C12-4	$\phi 150$		300		400	0.296
C12-6	$\phi 150$		300		600	0.446
S12-0	150	150	300		—	—
S12-2	150	150	300		200	0.148
S12-3	150	150	300	15	300	0.223
S12-4	150	150	300		400	0.296
S12-6	150	150	300		600	0.446
S13-3	150	150	450		300	0.223
S12-3R	150	150	300	30	300	0.223
R22-2	150	300	300		200	0.148
R22-3	150	300	300		300	0.223
R23-3	150	300	450		300	0.223
R32-2	100	300	200		200	0.222
R32-3	100	300	200	15	300	0.334
R33-3	100	300	300		300	0.334
R42-2	100	400	200		200	0.222
R42-3	100	400	200		300	0.334
R43-3	100	400	300		300	0.334

of height h to the short side b; two types at 2 and 3 in this paper) as variables, with the aim of verifying the validity of cross-sectional shape factors C that depend on the effective confinement area ratio α_e (equations (10)–(12)). The R series uses the longitudinal ratio d/b (four types from 1–4), the weight of the CF sheet (two types at 200 g/m² and 300 g/m²), and the height ratio (two types at 2 and 3) as variables, with the aim of studying applicability to rectangular cross sections. The maximum longitudinal ratio is set to 4 based on the fact that the distance between the neutral axis of the wall base cross section subjected to flexural compression and the wall end on the compression side is 3 to 4 times the wall thickness in static loading tests of columnless walls reinforced with CF in a previous study.

For the names of test specimens, the second character indicates the value of the longitudinal ratio d/b, the third character indicates the value of the height ratio h/b, and the fourth character indicates the CF sheet weight ρ_f (0: no reinforcement, 2: 200 g/m², 3: 300 g/m², 4: 400 g/m², and 6: 600 g/m²). Note that, in Table 1, p_f is the reinforcement ratio of the CF sheet, which is the ratio of the sheet thickness t over the short side b of the concrete cross section. The fifth character indicates the chamfer radius (no letter: $R = 15$ mm, R: 30 mm).

3.2. Loading and Measuring System. The loading used is the monotonic uniaxial compression system. The displacement of the axial direction is measured from four displacement transducers. These are placed at every 90° circumferential direction of the specimen cross section. The axial strain of the specimen is defined as the average of four displacement transducers.

TABLE 2: Properties of the carbon fiber sheet.

ρ_f (g/m^2)	E_f (N/mm^2)	f_f (N/mm^2)	ε_{fr} (%)	Specific weight ($\times 10^6$ g/m^2)	t (mm)
200	251,000	4,445	1.72	1.80	0.111
300	251,000	4,728	1.88	1.80	0.167

f_f: tensile strength of the carbon fiber sheet.
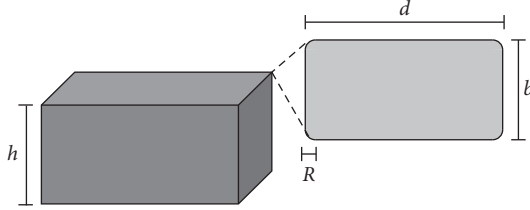
FIGURE 4: Dimensions of the test specimen with rectangular cross section.

3.3. Test Results of C-Series Test Specimens.

Figure 5 shows the results of the monotonic uniaxial compression tests on the C series. In the figure, the vertical axis is the stress σ and the horizontal axis is the strain ε. The graph in Figure 5(a) shows the comparison of test results for the five C-series test specimens, while graphs 5(b)–5(e) show the comparison of test results for each of the four test specimens with CF reinforcement and the Nakatsuka model [13]. For round specimens with effective confinement area ratio α_e of 1.0, all of the stress-strain relationships are described by the monotonically increasing model (see Figure 3).

The failure mode (ultimate strain ε_R) of specimens was determined by the rupture behavior of CF sheets. Comparing on the basis of the weight of the CF sheet, the maximum bearing strength and ultimate strain ε_R of the concrete element significantly improved with higher CF sheet weight. Comparing the test results of the CF-reinforced test specimens and the Nakatsuka model shown in Figures 5(b)–5(e), the test values and the evaluation model are generally in good agreement. Based on these results, it can be said that the Nakatsuka model can accurately estimate the stress-strain relationship of CF-reinforced concrete elements on the condition that the effective confinement area ratio α_e is 1.0.

3.4. Test Results of S-Series Test Specimens.

Figure 6 shows the results of the monotonic uniaxial compression tests on the S series. Figure 6(a) shows the comparison of different CF sheet weights, while Figure 6(b) compares different chamfer radii R and Figure 6(c) compares different height ratios h/b. Note that, for test specimen S13-3 with a height ratio of $h/b = 3$, the test results are based on the gauge length of the specific section. For the rectangular specimens in this paper, all of the stress-strain relationships are described by the maxima model (see Figure 3).

The failure mode of specimens was determined by the rupture behavior of CF sheets as well as the C series. Comparing on the basis of the weight of the CF sheet, the plastic deformation capacity of the concrete element rose with higher weight of the CF sheet, with a particularly

pronounced change in the ultimate strain ε_R. For the compressive strength σ_B, a tendency for the strength to increase with higher CF sheet weight can also be seen, although the change is not as extreme as in the ultimate strain ε_R. Comparing on the basis of chamfer radius shown in Figure 6(b), the strength reduction after reaching compressive strength σ_B of test specimen S12-3R (provided with an equivalent effective confinement area ratio $\alpha_e = 0.75$ as a test specimen in a previous Nakatsuka's study [13]) is comparatively more gradual than that of test specimen S12-3 ($\alpha_e = 0.57$). Comparing on the basis of height ratio h/b in Figure 6(c), test specimens S12-3 and S13-3 show nearly the same stress-strain relationship. In this paper, authors argue that the effect of the height ratio h/b on the stress-strain relationship of CF-reinforced concrete elements is small.

Table 3 presents the six components that define the constitutive law of the Nakatsuka model: σ_B, ε_B, EBT, ε_T, ETR, and εR, for the 15 rectangular specimens reinforced with CF. The experimental values (Exp.) in the table are the values that identify the six components above, taken from the stress-strain relationships obtained by experiments according to the previous study. The estimation values (Est.) in the table are the values obtained by evaluating the CF-reinforced test specimens in this paper based on equations (1) through (12) (i.e., considering the effect of effective confinement area ratio α_e). For F_0, the compressive strength of test specimen S12-0 which equals 38.46 MPa is used, while for ε_0, the strain for the same compressive strength which equals 0.0024 is used.

Figure 7 shows the comparison of the test results for the six S-series test specimens with CF reinforcement and the evaluation results based on the constitutive law. The solid lines in the figure show the experimental results, the short dashed lines show the Nakatsuka model (i.e., without considering the effect of effective confinement area ratio α_e), and the dashed-dotted lines show the constitutive law proposed in this paper (equations (1)–(12)). The Nakatsuka model tends to overestimate the experimental values in the second region and thereafter. This may be attributed to the fact that the Nakatsuka model does not consider the effect of the effective confinement area ratio α_e, which is linked to the chamfer radius R. In general, the constitutive law proposed in this paper may be considered as capable of reproducing the experimental results well. Note that, for test specimen S12-6, in which the weight of the CF sheet is extremely large, although the estimation of the stiffness in the third region E_{TR} is too large, the ultimate strain ε_R is almost the same as the experimental value.

The aforementioned results suggest that the constitutive law proposed in this paper (i.e., expanded formulas of the Nakatsuka model), which can take into account the effect of the effective confinement area ratio α_e, can generally
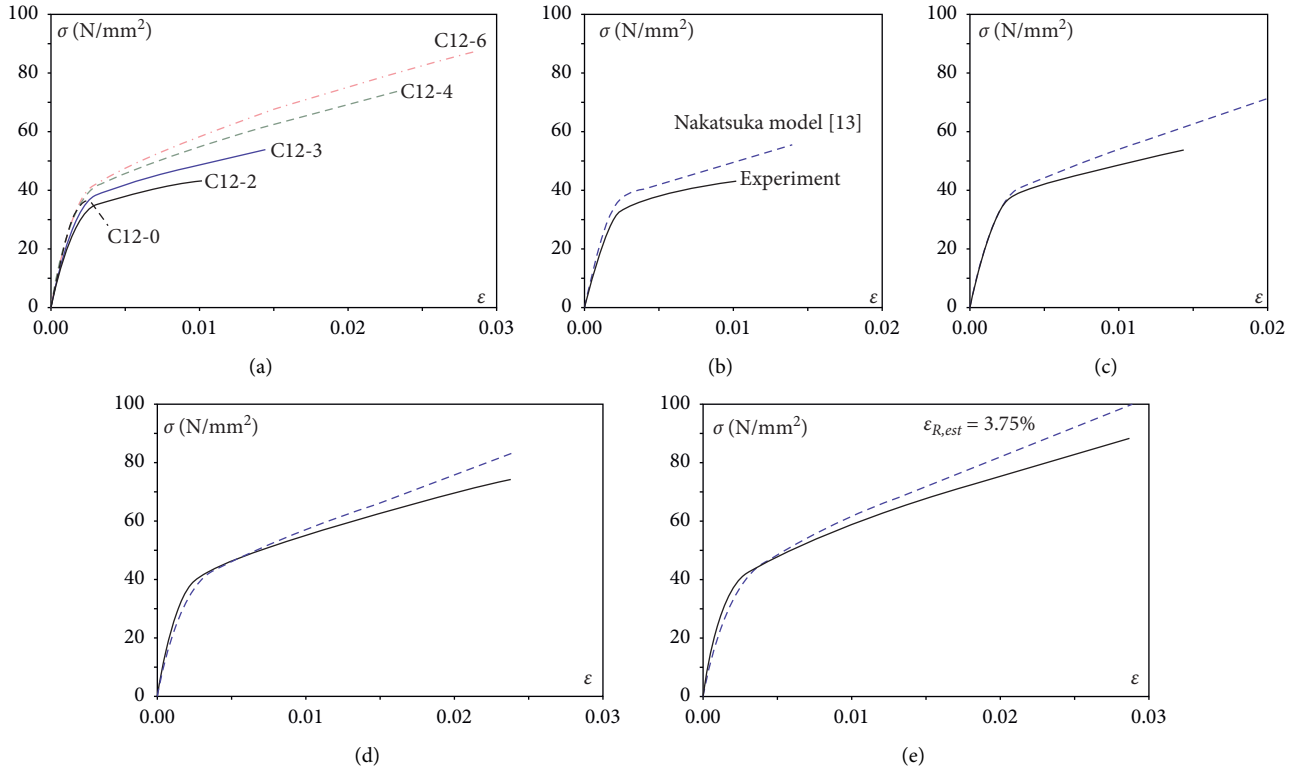
FIGURE 5: Test results for the C-series test specimens and the Nakatsuka model. (a) Comparing on the basis of CF sheet weight. (b) Comparing test results and Nakatsuka model of specimen C12-2. (c) C12-3. (d) C12-4. (e) C12-6.
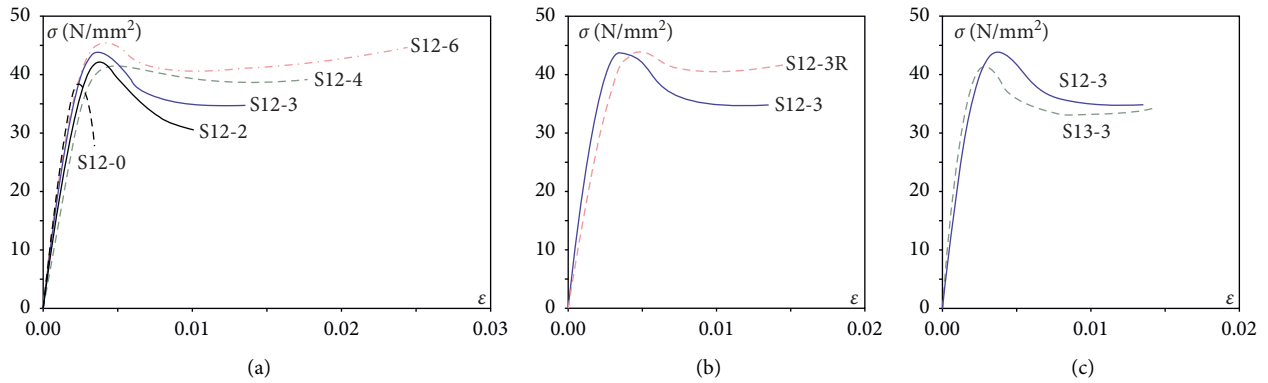
FIGURE 6: Comparing the test results for the C-series specimens. (a) CF sheet weight. (b) Different chamfer radii R. (c) Different height ratios h/b.

estimate the behavior of square concrete elements reinforced with CF well. The accuracy of the estimation is particularly good when the weight of the CF sheet is $300\,\mathrm{g/m^2}$ or less.

3.5. Test Results of R-Series Test Specimens.

For the R-series test specimens, the comparison of the six component values of the constitutive law identified from experimental results and the estimation values based on equations (1)–(12) (without considering the effect of longitudinal ratio d/b) is shown in Table 3. *First, for the compressive strength σ_B, the estimation values overestimate the experimental values for* all test specimens in which the longitudinal ratio d/b is 2 or more. On the contrary, the strain at point of constant sloping ε_T and ultimate strain ε_R tend to be underestimated. The ultimate strain ε_R relative to the failure mode is defined as the point when rupture occurs in the CF sheet. Figure 8 shows examples of the ultimate state of the test specimens due to CF sheet rupture. All of the test specimens with a longitudinal ratio d/b of 2 or more had concrete on the long side bulging out of plane at the final stage. This behavior is quite pronounced in the R42-3 test specimen shown in Figure 8(d). Figure 9 shows the failure mode of rectangle specimen R42-3. The rupture of the CF sheet occurred at the

TABLE 3: Comparison of the test results and the constitutive law using the Nakatsuka model with six components.

Specimen	σ_B (Mpa)			$\varepsilon_B \times 10^{-2}$			E_{BT} (Mpa)			$\varepsilon_T \times 10^{-2}$			E_{TR} (MPa)			$\varepsilon_R \times 10^{-2}$		
	Exp.	Est.	$\frac{Est.}{Exp.}$	Exp.	Est.	$\frac{Est.}{Exp.}$	Exp.	Est.	$\frac{Est.}{Exp.}$	Exp.	Est.	$\frac{Est.}{Exp.}$	Exp.	Est.	$\frac{Est.}{Exp.}$	Exp.	Est.	$\frac{Est.}{Exp.}$
S12-2	42.21	39.92	0.95	0.38	0.26	0.69	−2760	−2302	0.83	0.65	0.54	0.83	−1304	74	−0.06	1.06	1.01	0.95
S12-3	43.83	40.66	0.93	0.37	0.27	0.73	−2084	−870	0.42	0.73	0.57	0.78	−247	637	−2.58	1.35	1.45	1.07
S12-4	41.89	41.38	0.99	0.50	0.28	0.57	−591	33	−0.06	0.78	0.60	0.76	−92	991	−10.7	1.79	1.66	0.93
S12-6	45.55	42.85	0.94	0.42	0.31	0.73	−1005	1143	−1.14	0.91	0.64	0.71	261	1428	5.47	2.45	2.53	1.03
S13-3	41.46	40.66	0.98	0.30	0.27	0.92	−2836	−870	0.31	0.48	0.57	1.19	−235	637	−2.71	1.44	1.45	1.01
S12-3R	43.93	41.36	0.94	0.49	0.28	0.58	−985	10	−0.01	0.80	0.59	0.74	120	982	8.21	1.44	1.79	1.24
R22-2	36.61	39.80	1.09	0.37	0.24	0.70	−2669	−2674	1.00	1.14	0.54	0.47	−860	-72	0.08	1.22	0.96	0.79
R22-3	36.85	40.44	1.10	0.42	0.27	0.64	−2630	−1214	0.46	1.07	0.56	0.53	−198	502	−2.53	1.91	1.35	0.71
R23-3	36.71	40.44	1.10	0.40	0.27	0.67	−3349	−1214	0.36	0.82	0.56	0.68	−453	502	−1.11	1.09	1.35	1.23
R32-2	39.80	40.63	1.02	0.34	0.27	0.79	−2259	−914	0.40	1.01	0.57	0.56	−1094	619	−0.57	2.35	1.33	0.56
R32-3	39.01	41.72	1.07	0.54	0.29	0.54	−2376	356	−0.15	1.12	0.61	0.54	−582	1118	−1.92	2.16	1.97	0.91
R33-3	39.87	41.72	1.05	0.32	0.29	0.90	−2866	356	−0.12	1.01	0.61	0.60	−134	1118	−8.38	2.15	1.97	0.92
R42-2	40.05	40.57	1.01	0.37	0.27	0.73	−3172	−1002	0.32	1.01	0.57	0.56	−750	584	−0.78	1.94	1.30	0.67
R42-3	38.59	41.64	1.08	0.50	0.29	0.58	−1391	281	−0.20	2.00	0.60	0.30	−127	1089	−8.58	3.07	1.93	0.63
R43-3	32.60	41.64	1.28	0.39	0.29	0.74	−2249	281	−0.12	1.02	0.60	0.59	−370	1089	−2.94	1.87	1.93	1.04

corner of the specimen. In the ultimate state, both surfaces of the long side swelled to the out of plane. Along with this behavior, large tension was acting on the long side CF sheets. This implies that the link between the longitudinal ratio d/b and magnitude of ultimate strain is related to this failure behavior.

The aforementioned results suggest that, for CF-reinforced concrete elements with rectangular sections, although compressive strength σ_B fell compared to square sections, plastic deformation capacity tends to improve.

4. Constitutive Law for Rectangular Cross Sections

4.1. Discussion of Test Results. With regard to the tendency for compressive strength σ_B to fall with increasing longitudinal ratio d/b, a similar behavior has been observed for plain concrete without CF reinforcement. Yamamoto and Koike [25] carried out a number of uniaxial compression tests on rectangular concrete element specimens with longitudinal ratios d/b less than 6 and gave the following equation for the reduction factor $\alpha_{\sigma B}$ of compressive strength σ_B estimation according to longitudinal ratio d/b:

$$\alpha_{\sigma B} = \left(\frac{d}{b}\right)^{-0.1}. \tag{13}$$

Based on this, authors applied the following equation in lieu of equation (2) as the evaluation formula for compressive strength σ_B of CF-reinforced concrete elements in this paper:

$$\sigma_B = \alpha_{\sigma B}\left[F_0 + 4p_f E_f \varepsilon_{fB} C_{\sigma B}\right]. \tag{14}$$

Moreover, authors evaluated the strain at compressive strength σ_B using the following equation, considering that, to a certain extent, a proportional relationship with compressive strength σ_B exists:

$$\varepsilon_B = \alpha_{\sigma B}\left[\varepsilon_0 + 10\varepsilon_0 \frac{p_f E_f \varepsilon_{fB}}{F_0} C_{\varepsilon B}\right]. \tag{15}$$

It has also been observed that, with respect to the strain at point of constant sloping ε_T, which defines the boundary between the second and third regions and was shown to deteriorate in the test specimens and the ultimate strain ε_R of the specimens determined by the CF sheet ruptures, the magnitude of strain tends to increase as the longitudinal ratio d/b becomes larger. In the test results of this study, the experimental values of test specimens with longitudinal ratio $d/b = 4$ generally reached about twice the estimation values of equations (1)–(12). In contrast, the estimation values for stiffness in the second region E_{BT} and stiffness in the third region E_{TR} tend to overestimate the experimental values.

Figure 10 shows the ratios of cross-sectional shape factors C_{EBT}, $C_{\varepsilon T}$, C_{ETR}, and $C_{\varepsilon R}$ inversely estimated from experimental values over estimation values from equations (10)–(12) for the four components E_{BT}, ε_T, E_{TR}, and ε_R of the R-series test specimens. In the figure, the vertical axis is the ratio of experimental over estimation values C_{exp}/C_{est} and the horizontal axis is the longitudinal ratio d/b. Similar to the previous discussion, the ratio C_{exp}/C_{est} tends to fall with increasing longitudinal ratio d/b with respect to E_{BT} in Figure 10(a) and E_{TR} in Figure 10(c). Conversely, the ratio C_{exp}/C_{est} also becomes large as the longitudinal ratio d/b increases for ε_T in Figure 10(b) and ε_R in Figure 10(d). In this paper, authors modified the evaluation formulas for four components: E_{BT}, ε_T, E_{TR}, and ε_R from equations (5), (7), (8), and (9) to the following in order to take the longitudinal ratio d/b into account:

$$E_{BT} = -0.4E_{0BT} + \frac{1.4E_{0BT}}{\alpha_{EBT}C_{EBT}\left(p_f E_f/0.06F_0^2\right) + 1}, \tag{16}$$

$$\alpha_{EBT} = -0.2\left(\frac{d}{b}\right) + 1.2, \tag{17}$$
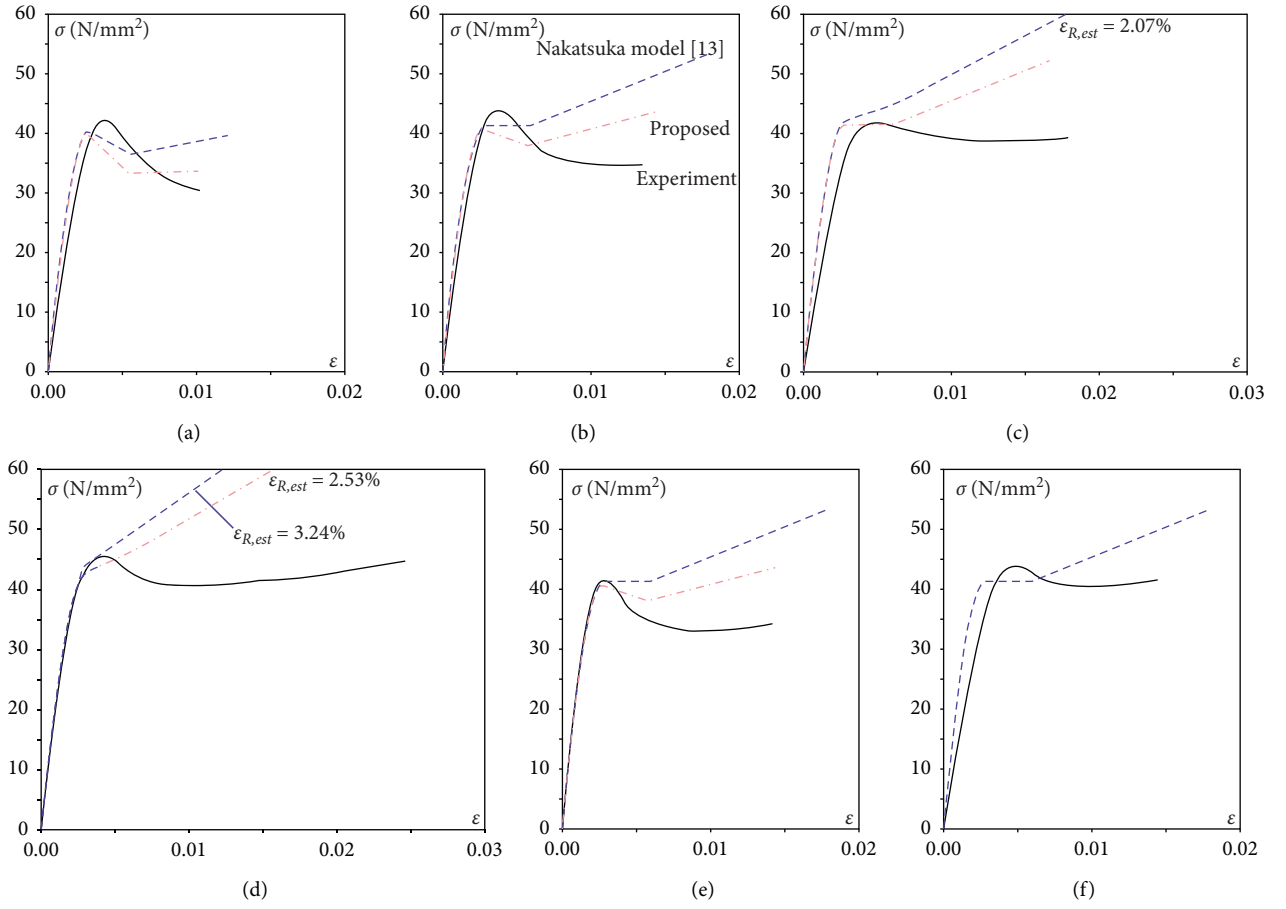
FIGURE 7: Test results for the S-series test specimens, the Nakatsuka model, and the proposed constitutive law in this paper. (a) S12-2. (b) S12-3. (c) S12-4. (d) S12-6. (e) S13-3. (f) S12-3R.
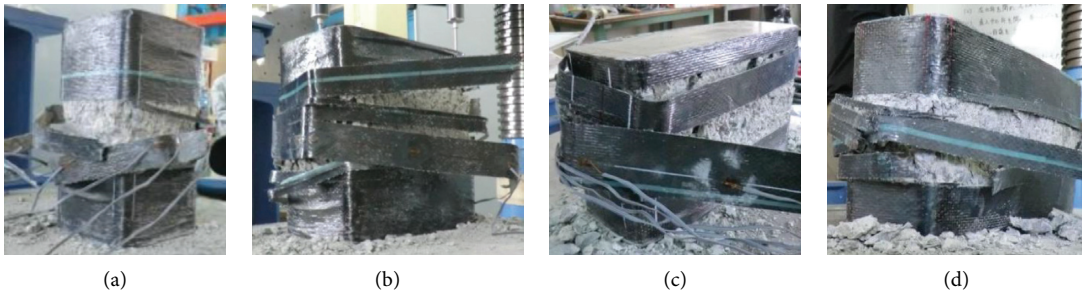
FIGURE 8: Ultimate state of test specimens. (a) S12-3. (b) R22-3. (c) R32-3. (d) R42-3.
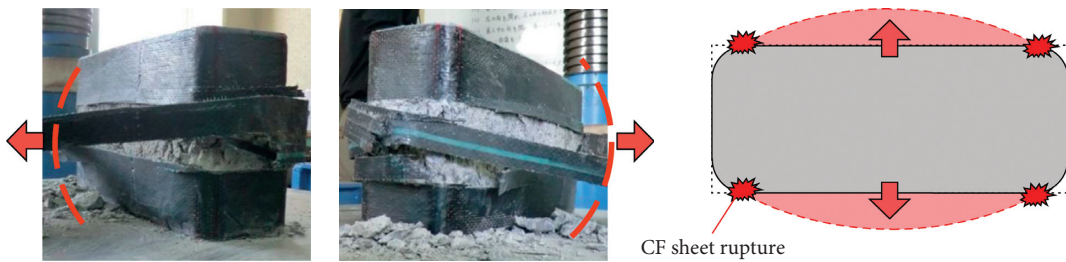
FIGURE 9: Failure mode of rectangle specimen R42-3.
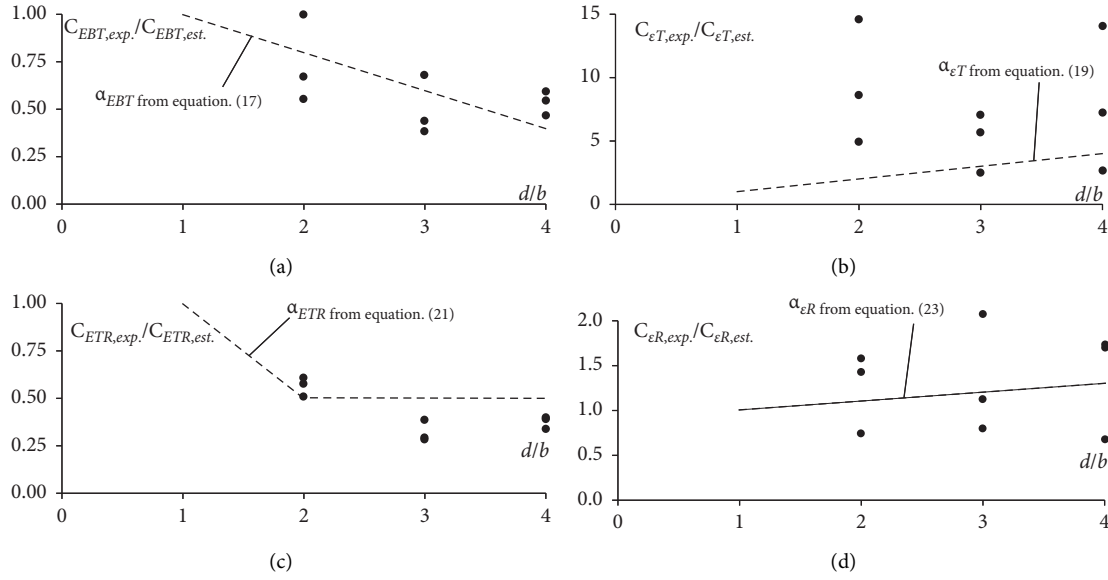
FIGURE 10: Correction factor for longitudinal ratio of nine R-series test specimens. (a) E_{BT} and α_{EBT}. (b) ε_T and $\alpha_{\varepsilon T}$. (c) E_{TR} and α_{ETR}. (d) ε_R and $\alpha_{\varepsilon R}$.

$$\varepsilon_T = \varepsilon_0\left(-0.016F_0 + 2.7\right) \\ + \varepsilon_0\left(0.00001F_0 + 0.0016\right)\alpha_{\varepsilon T}C_{\varepsilon T}p_f E_f, \tag{18}$$

$$\alpha_{\varepsilon T} = \frac{d}{b}, \tag{19}$$

$$E_{TR} = -0.25E_{0BT} + \frac{0.55E_{0BT}}{\alpha_{ETR}C_{ETR}\left(p_f E_f/0.06F_0^2\right) + 1}, \tag{20}$$

$$\alpha_{ETR} = -0.5\left(\frac{d}{b}\right) + 1.5 \geq 0.5, \tag{21}$$

$$\varepsilon_R = \varepsilon_0\left(20\varepsilon_{fr} + 1.2\right) + \varepsilon_0\left(1000\varepsilon_{fr} - 3\right)\alpha_{\varepsilon R}C_{\varepsilon R}\frac{p_f E_f}{F_0^2}, \tag{22}$$

$$\alpha_{\varepsilon R} = 0.1\left(\frac{d}{b}\right) + 0.9. \tag{23}$$

The dashed lines in Figure 10 indicate the correction factor α, which represents the effect of longitudinal ratio d/b based on equations (17), (19), (21), and (23) above. Table 4 presents the error of the proposed equation to the experimental results. For α_{EBT}, α_{ETR}, and $\alpha_{\varepsilon R}$, the correction factors given above generally capture the characteristics of the experimental results. For $\alpha_{\varepsilon T}$, the correspondence with the experimental results was not reasonable. The evaluation value from (19) mostly corresponds to the lower limit of the experimental results. At the Nakatsuka model, the strain at the point of constant sloping ε_T is specified as the point at which the tangential slope of an infinitesimal area in the stress-strain relationship becomes nearly constant. However, if the stress-strain relationship is such that the tangential stiffness after reaching compressive strength σ_B keeps on changing continuously, as in the case of the S12-3R test specimen, then ε_T is overestimated when obtained from experimental results. Therefore, the estimation of $\alpha_{\varepsilon T}$ is set at around the lower limit of experimental results in this paper. When using the lower limit value for $\alpha_{\varepsilon T}$, the stress-strain relationship is underestimated (safe side).

4.2. Comparison of Test Results and the Proposed Constitutive Law.

Figure 11 shows the comparison of the test results for the nine R-series test specimens and the proposed constitutive law estimated from equations (1), (3), (6), and (10) through (23). In the figure, the vertical axis is the stress σ, and the horizontal axis is the strain ε. The solid lines in the figure show the experimental results, the short dashed lines show the Nakatsuka model (i.e., without considering the effects of both effective confinement area ratio α_e and longitudinal ratio d/b), and the dashed-dotted lines show the constitutive law proposed in this paper (i.e., considering the effects of both effective confinement area ratio α_e and longitudinal ratio d/b). Similar to the S-series test specimens, the Nakatsuka model greatly overestimates the experimental values in the second region and thereafter. On the contrary, the evaluation formulas for the constitutive law proposed in this paper are generally able to trace the progress of experimental results regardless of the longitudinal ratio d/b. However, for some specimens, the initial stiffness of the proposed model is stiffer than the experimental results as shown in Figure 11. The evaluation of initial stiffness that measures infinitesimal displacement is very sensitive and is always associated with errors and uncertainties. In the future, the parametric study and/or the evaluation of dispersion about initial stiffness range is essential.

For the 15 test specimens of square and rectangular cross sections with CF reinforcement in this study, the

TABLE 4: Properties of the carbon fiber sheet.

|	α_{EBT}	$\alpha_{\varepsilon T}$	α_{ETR}	$\alpha_{\varepsilon R}$
Average (exp. result/proposed method)	1.03	2.79	0.84	1.10
Standard deviation of error	0.28	1.83	0.21	0.37
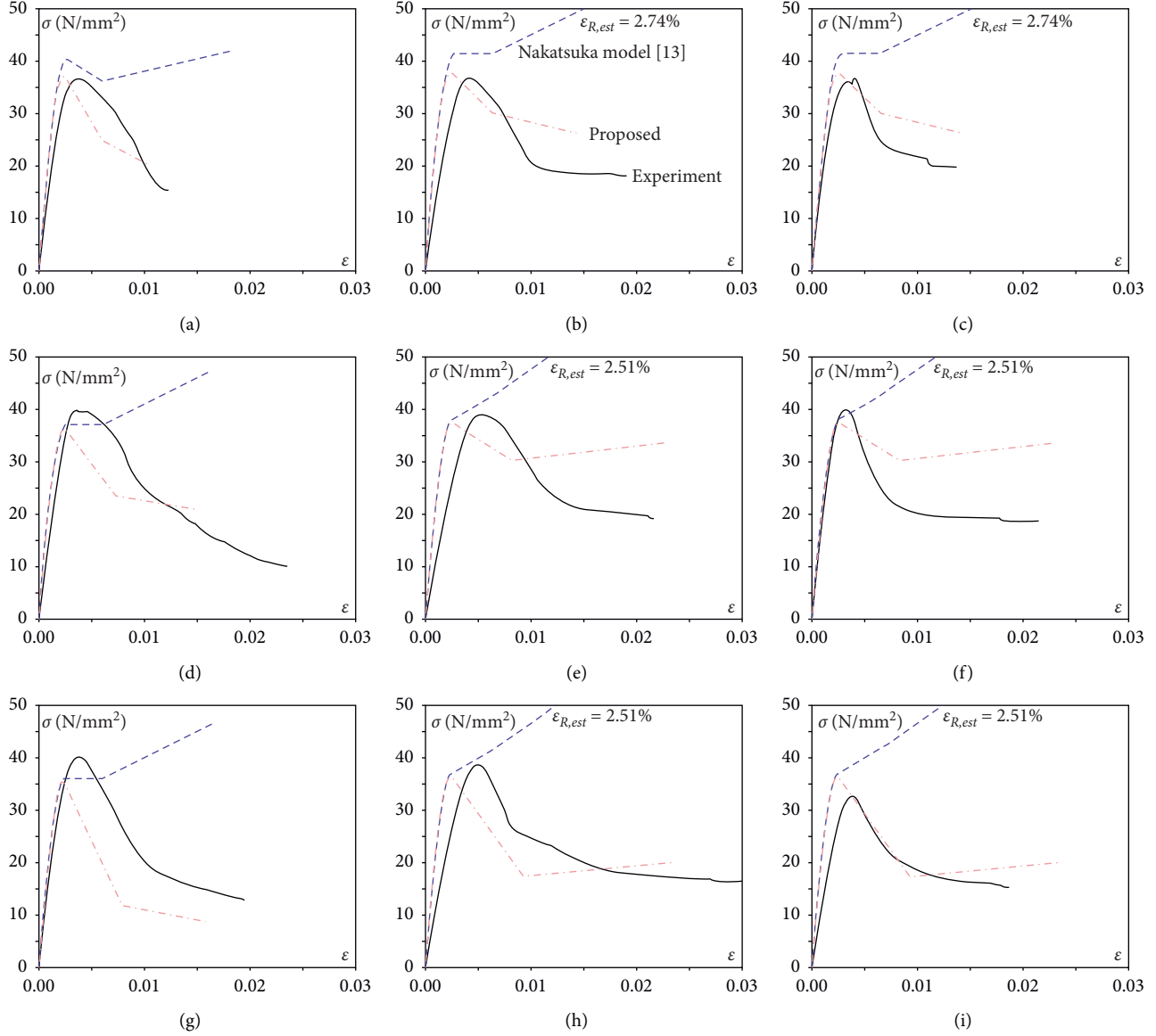
FIGURE 11: Test results for the R-series test specimens, the Nakatsuka model, and the proposed constitutive law in this paper. (a) R22-2. (b) R22-3. (c) R23-3. (d) R32-2. (e) R32-3. (f) R33-3. (g) R42-2. (h) R42-3. (i) R43-3.

energy consumed by the test specimens until reaching the ultimate state was in the range of 60% to 148% of the proposed evaluation formulas in this paper, with an average of 111% and standard deviation of 27.2%. If this is limited to the R-series test specimens with rectangular cross sections, the average is 104% and standard deviation is 30.8%. All of the above results show that the evaluation formulas for the constitutive law of CF-reinforced concrete elements proposed in this paper can generally estimate the stress-strain relationship, even for rectangular

cross sections with widely different lengths on the long and short sides.

5. Conclusions

Monotonic uniaxial compression tests were performed on 21 specimens of concrete elements reinforced by wrapping with carbon fiber sheets. The following are our findings within the scope of the specifications of specimens used in the tests (specimen dimensions and CF sheet weight):

(1) As the aspect ratio of the concrete section increases, the compressive strength decreases, while on the contrary, the ultimate strain determined by the rupture of the carbon fiber sheet increases and ductility capacity improves.

(2) For the experiments in this study, there were no changes observed in the stress-strain relationships of concrete elements reinforced with the carbon fiber sheet as the ratio of height in the direction of axial compression of the element over the short side of the cross section changes.

(3) For rectangular cross sections, the effective confinement area of the CF sheet changes depending on the chamfer radius of section corners. In this paper, authors expanded a previously suggested constitutive law by Nakatsuka et al. [13] and derived evaluation formulas as functions of the effective confinement area ratio for the concrete elements under study. The proposed formulas are generally able to estimate the behavior of concrete elements reinforced with carbon fiber with good accuracy, and the accuracy of the estimation is particularly high when the weight of the sheet is $300 \, \text{g/m}^2$ or less.

(4) In order to apply to rectangular cross sections with widely different lengths on the long and short sides, authors proposed correction factors for the constitutive law evaluation formulas as functions of the cross-sectional aspect ratio. Taking these correction factors into account, the formulas proposed in this paper are able to trace the experimental results well, while the energy consumed by the concrete element until the carbon fiber sheet ruptures is generally reproduced.

As described above, the CF sheet has the ability to improve the seismic performance of rectangular cross-section concrete such as a structural wall member, and it is possible to evaluate the effect of retrofitting. These research results can contribute to the improvement of resilience and sustainability of the building structure through retrofit of aging concrete.

The experimental test results about the concrete material are associated with errors and uncertainties. In the future, the evaluation of dispersion (e.g., errors and uncertainties) is essential. Authors will apply a parametric study using the FEM model in the next step.

Data Availability

The experimental data (stress-strain relationship) used to support the findings of this study are available from the corresponding author upon request.

Conflicts of Interest

The authors declare that they have no conflicts of interest.

References

[1] A. Nanni, "Concrete repair with externally bonded FRP reinforcement," *Concrete International*, vol. 17, no. 6, pp. 22–26, 1995.

[2] H. Toutanji, "Stress-strain characteristics of concrete columns externally confined with advanced fiber composite sheets," *ACI Materials Journal*, vol. 96, no. 3, pp. 397–404, 1999.

[3] A. M. Vasumathi, K. Rajkumar, and G. G. Prabhu, "Compressive behaviour of RC column with fibre reinforced concrete confined by CFRP strips," *Advances in Materials Science and Engineering*, vol. 2014, Article ID 601915, 10 pages, 2014.

[4] J. R. Murugadoss, B. J. Lee, J. W. Bang, G. G. Prabhu, and Y. Y. Kim, "Performance analysis of CFRP composite strips confined RC columns under axial compression," *Advances in Materials Science and Engineering*, vol. 2015, Article ID 170295, 18 pages, 2015.

[5] L. D. Lorenzis and R. Tepfers, "Comparative study of models on confinement of concrete cylinders with fiber-reinforced polymer composites," *Journal of Composites for Construction, ASCE*, vol. 7, no. 3, pp. 219–237, 2003.

[6] S. A. Carey and K. A. Harries, "Axial behavior and modeling of small-, medium-, and large-scale circular sections confined with CFRP jackets," *ACI Structural Journal*, vol. 102, no. 4, pp. 596–604, 2005.

[7] N. Zhuang, H. Dong, D. Chen, and Y. Ma, "Experimental study of aged and seriously damaged RC beams strengthened using CFRP composites," *Advances in Materials Science and Engineering*, vol. 2018, Article ID 6260724, 9 pages, 2018.

[8] J. Y. Lee, H. O. Shin, K. H. Min, and Y. S. Yoon, "Flexural assessment of blast-damaged RC beams retrofitted with CFRP sheet and steel fiber," *International Journal of Polymer Science*, vol. 2018, Article ID 2036436, 9 pages, 2018.

[9] E. Ercan, B. Arisoy, and O. B. Ertem, "Experimental assessment of RC beam-column connections with internal and external strengthening techniques," *Advances in Civil Engineering*, vol. 2019, Article ID 2828353, 12 pages, 2019.

[10] S. Ghods, A. Kheyroddin, M. Nazeryan, S. M. Mirtaheri, and M. Gholhaki, "Nonlinear behavior of connections in RCS frames with bracing and steel plate shear wall," *Steel and Composite Structures*, vol. 22, no. 4, pp. 915–935, 2016.

[11] T. Matsui, T. Saito, and R. Reyna, "Basic study on reinforced concrete shear walls without boundary columns retrofitted by carbon fiber sheets," *Journal of Disaster Research*, vol. 9, no. 6, pp. 1008–1014, 2014.

[12] K. Suzuki, K. Hayashi, and T. Saito, "Study on the material properties of rectangular concrete reinforcing carbon fiber sheet and evaluation of deformation performance of RC reinforced wall," *Proceedings of the Japan Concrete Institute*, vol. 38, pp. 433–438, 2016, in Japanese.

[13] T. Nakatsuka, K. Komure, and K. Tagaki, "Stress-strain characteristics of confined concrete with carbon fiber sheet,"

Concrete Research and Technology, vol. 9, no. 2, pp. 65–78, 1998, in Japanese.

[14] S. Pessiki, K. A. Harries, J. Kestner, R. Sause, and J. M. Ricles, "The axial behavior of concrete confined with fiber reinforced composite jackets," *Journal of Composites in Construction, ASCE*, vol. 5, no. 4, pp. 237–245, 2001.

[15] L. Lam and J. G. Teng, "Design-oriented stress strain model for FRP-confined concrete," *Construction and Building Materials*, vol. 17, no. 6, pp. 471–489, 2003.

[16] K. A. Harries and S. A. Carey, "Shape and "gap" effects on the behavior of variably confined concrete," *Cement and Concrete Research*, vol. 33, no. 6, pp. 881–890, 2003.

[17] L. Lam and J. G. Teng, "Stress-strain model for FRP-confined concrete under cyclic axial compression," *Engineering Structures*, vol. 31, no. 2, pp. 308–321, 2009.

[18] G. Mahdavi, K. Nasrollahzadeh, and M. A. Hariri-Ardebili, "Optimal FRP jacket placement in RC frame structures towards a resilient seismic design," *Sustainability*, vol. 11, no. 24, p. 6985, 2019.

[19] L. Lam and J. G. Teng, "Design-oriented stress strain model for FRP-confined concrete in rectangular columns," *Journal of Reinforced Plastics and Composites*, vol. 22, no. 13, pp. 1149–1186, 2003.

[20] Y. Ouyang and N. K. Liu, "Stress strain model for FRP-confined concrete rectangular columns," in *Proceedings of the Asia-Pacific Conference on FRP in Structures*, pp. 149–154, Hong Kong, December 2007.

[21] S. Rocca, N. Galati, and A. Nanni, "Review of design guidelines for FRP confinement of reinforced concrete columns of noncircular cross sections," *Journal of Composites for Construction*, vol. 12, no. 1, pp. 80–92, 2008.

[22] L. Wang, W. Xuan, Y. Zhang et al., "Experimental and numerical research on seismic performance of earthquake-damaged RC frame strengthened with CFRP sheets," *Advances in Materials Science and Engineering*, vol. 2016, Article ID 6716329, 11 pages, 2016.

[23] ACI Committee 440, *Guide for the Design and Construction of Externally Bonded FRP Systems for Strengthening Concrete Structures*, ACI, Michigan, USA, 440.2R-08, 2008.

[24] T. C. Triantafillou, E. Choutopoulou, E. Fotaki, M. Skorda, M. Stathopoulou, and K. Karlos, "FRP confinement of wall-like reinforced concrete columns," *Materials and Structures*, vol. 49, no. 1-2, pp. 651–664, 2016.

[25] T. Yamamoto and K. Koike, "Study on the influence of cross section size on the compressive strength of concrete circular and square specimens," *Proceedings of the Japan Concrete Institute*, vol. 34, no. 1, pp. 322–327, 2012, in Japanese.

Research Article

Research on Sulfate Attack Mechanism of Cement Concrete Based on Chemical Thermodynamics

Peng Liu [ID],[1,2] **Ying Chen** [ID],[1,2,3] **Zhiwu Yu**,[1,2] **Lingkun Chen**,[4] and **Yongfeng Zheng** [ID][5]

[1]*School of Civil Engineering, Central South University, 22 Shaoshan Road, Changsha 410075, China*
[2]*National Engineering Laboratory for High Speed Railway Construction, 22 Shaoshan Road, Changsha 410075, China*
[3]*School of Civil Engineering, Central South University of Forestry and Technology, 498 Shaoshan Road, Changsha 410004, China*
[4]*School of Civil Engineering, Southwest Jiaotong University, 6 Jingqu Road, Chengdu 610031, China*
[5]*Key Laboratory of Building Structural Retrofitting and Underground Space Engineering, Shandong Jianzhu University,*
 Ministry of Education, Jinan, Shandong 250101, China

Correspondence should be addressed to Ying Chen; cheny83@csu.edu.cn and Yongfeng Zheng; zhyf-fb@163.com

Received 18 September 2019; Revised 16 December 2019; Accepted 28 January 2020; Published 9 March 2020

Academic Editor: Mohammad A. Hariri-Ardebili

Based on principles of chemical thermodynamics, the relationship between temperature and the Gibbs free energy of erosion products generated during the sulfate attack on cement concrete was deduced. The orientation of chemical reactions of sulfate attack on cement concrete was theoretically determined as well as the critical sulfate ion concentration and the formation conditions of erosion products. The phase composition, microstructure, crystal form, and morphology of erosion products before and after sulfate attack were investigated by environmental scanning electron microscope and energy spectrum analysis (ESEM-EDS) and X-ray diffraction (XRD). The results show that the effects of sulfate ion concentration and temperature on cement concrete sulfate attack are significant, and different influencing factors correlate with each other. The crystal transition temperature between the anhydrite and dihydrate gypsum is 42°C, and the corresponding concentration of sulfate ion is about 2.3×10^{-3} mol/L. Simultaneously, the crystal transition temperature between the thenardite and mirabilite is 32.4°C. Moreover, the theoretical upper limit temperature and sulfate ion lower limit concentration of thaumasite are 44°C and 0.0023 mol/L, respectively. The ESEM-EDS and XRD results imply that the chemical thermodynamics can be used to reveal the erosion mechanism of sulfate attack on cement concrete. The major erosion products of sulfate attack on cement concrete are rod-like ettringite with a larger slenderness ratio, plate-like gypsum, granular sulfate salt, incompletely corroded calcium hydroxide, and residual skeleton of calcium silicate hydrate. The sulfate attack has double effects on mechanical properties of specimens, which can affect the microstructure, phase composition, type, and morphology of erosion products.

1. Introduction

Sulfate attack on cement concrete can degrade the durability and reduce the service life of concrete building structures [1, 2]. There are plenty of influence factors of sulfate attack on concrete, which are mainly focused on the kind and concentration of sulfate solution, temperature, pH value, cement composition, admixtures, and erosion form [3–7]. Among them, the temperature, concentration, and type of the sulfate solution are considered as the most important factors of sulfate attack [1, 8, 9]. For example, Valencia et al.

[10] indicated that the $MgSO_4$ had more influence on the deterioration of concrete than that of Na_2SO_4; the results showed that after attacked for 360 days in 5% $MgSO_4$ solution, the concrete expanded by 0.04%, and its mechanical resistance decreased by 33%. Axel et al. [11] regarded the erosion product as monosulfate when the concentration of sulfate ion was less than 1 g/L. Lawrence [12] proposed that the highest stable temperature of the ettringite (AFt) was about 65°C~70°C, and the AFt was decomposed when the temperature was higher than 70°C [13]. Hekal et al. [14] investigated the variation of the strength of the concrete

under different circumstances, and they declared that the high temperature of 60°C played a significant effect on mechanical properties of concrete. Dehwah [15] investigated the effect of sodium sulfate concentrations (to yield 1%, 2.5%, and 4% [SO_4^{2-}]) on concrete deterioration and morphological changes in cement hydrates; their results indicated that the deterioration was noted in the plain and fly ash cement concrete specimens exposed to sodium chloride admixed with magnesium sulfate. In general, the sulfate solution concentration and temperature have remarkable influence on sulfate erosion mechanism, crystal form and type, erosion rate, spontaneity of reaction, and stable existence condition [16]. Therefore, it is very important to investigate the effects of sulfate solution concentration and temperature on sulfate attack of concrete.

Although a lot of achievements of sulfate attack on cement concrete have been made [17], some divergences of sulfate solution concentration and temperature on sulfate attack also exist. For example, Biczok [18] considered that the erosion products of sulfate attack on concrete were AFt and gypsum when [SO_4^{2-}] was less than 1 g/L and more than 8 g/L, respectively, and gypsum and AFt could be observed when [SO_4^{2-}] ranged from 1 g/L to 8 g/L. Bellmann et al. [19] pointed out that the portlandite reacted to gypsum at a minimal sulfate concentration of approximately 1400 mg/L (pH = 12.45). Zhang et al. [20] conducted the accelerated laboratory tests on resistance of concrete exposed to sulfate attack with high concentration sulfate solutions or under drastic drying-wetting cycle conditions; their results showed that the exposure regime of full immersion in 2.1% sulfate sodium solutions subjected to natural drying-wetting cycles can well reproduce the field exposure condition of concrete under certain sulfate-rich environments. Both concentration and exposure type affect the nature of sulfate attack mechanism on concrete, along with the evolution of physical and mechanical properties. Yu et al. [21] investigated the evolution properties of the cement mortar fully immersed in sodium sulfate solutions of different concentrations (0%, 5%, and 15%); their results showed that the properties deterioration at the late stage was accelerated with increase of the concentration of the sodium sulfate solution. Santhanam [22] carried out an experimental investigation to understand the influence of the solution concentration of seawater on performance of the cement mortars, and the results indicated that higher concentrations of seawater did not cause the same level of damage as higher concentrations of groundwater relative to the typical seawater/groundwater solutions. The temperature not only affects the reaction rate and diffusion of ions, but also changes the erosion mechanism and products in cement concrete. Xie et al. [23] proposed a novel theory concerning sulfate expansion phenomena in cement concrete systems based on the principles of chemical thermodynamics, and their results showed that temperature had a significant effect on the concrete expansion. Blanco-Varela et al. [24] regarded that the low temperature of less than 15°C as one of the essential conditions for the formation of thaumasite (CS$\overline{C}$SH). Hartshorn et al. [25] demonstrated that plenty of thaumasite could be generated at 5°C, and a little of thaumasite could also be formed at 20°C, which caused a

deterioration of concrete. However, Santhanam [5] proposed that the forming condition of thaumasite was temperature less than 20°C, and the carbonation was another essential condition. Moreover, Brown et al. [26] employed the scanning electron microscope (SEM) to investigate the thaumasite generated in concrete attacked by sulfate, and their results indicated that the formation of thaumasite was related to concrete carbonation.

Although many achievements regarding the effects of sulfate solution concentration and temperature on the erosion mechanism of sulfate attack have been made, the researches of sulfate attack on cement concrete based on principles of chemical thermodynamics have no breakthrough progress as yet. Furthermore, there exists a deviation between the theoretical analysis and the in-site test results. The objective of this study is to investigate the relationship between temperature and the Gibbs free energy of the erosion products generated during the sulfate attack based on the principle of chemical thermodynamics. The orientation of chemical reactions of sulfate attack on concrete was theoretically determined as well as the critical sulfate ion concentration and forming conditions of erosion products. Moreover, the phase composition, microstructure, crystal form, and morphology of erosion products of cement before and after sulfate attack were studied by ESEM-EDS and XRD. The research results in this study can provide a support for the erosion mechanism of sulfate attack, crystal form, and forming conditions of erosion products in cement concrete.

2. Theoretical Analysis

The sulfate attack on cement concrete is a complex physical and chemical process [4, 5]. The temperature and sulfate solution concentration have remarkable effects on the thermodynamic equilibrium state of the reaction, so it is very important to establish their international relationship. In order to simplify the theoretical analysis, we assume that the temperature and concentration of various ions are uniform and unchangeable, and the theoretical analysis of thermodynamic equilibrium state of the sulfate attack on cement concrete is conducted as in the following section.

2.1. Qualitative Analysis of the Erosion Products of Sulfate Attack on Cement Concrete. The relationship between thermodynamic equilibrium constant and the Gibbs free energy of the reaction can be used to characterize the spontaneity of the generation of erosion products [27], written as equation (1). Based on Gibbs–Helmholtz equation [27], the relationship between Gibbs energy and temperature can be obtained, written as equation (2).

$$\Delta G^\Theta = -RT \ln K^\Theta, \tag{1}$$

$$\mathrm{d}\frac{\ln K^\Theta}{\mathrm{d}T} = \frac{\Delta H^\Theta}{RT^2}, \tag{2}$$

where ΔG^Θ is standard Gibbs free energy, ΔH^Θ is the standard enthalpy change of reaction, T is temperature, K^Θ

stands for thermodynamic equilibrium constant, and R is ideal gas constant with a recommended value of 8.314 J/(mol·K).

Kirchhoff equation is usually used to describe the relationship between ΔH_T^Θ and T, formulated as equation (3).

$$d\left(\Delta H_T^\Theta\right) = \Delta C_p dT, \tag{3}$$

$$\Delta C_p = \sum \Delta C_{p-\text{products}} - \sum \Delta C_{p-\text{reactants}} = \Delta a + \Delta b T + \Delta c T^{-2}, \tag{4}$$

where $\Delta C_{p-\text{products}}$ and $\Delta C_{p-\text{reactants}}$ are the differences in the specific heat at constant pressure between the products and reactants, respectively. ΔC_p is the difference in the heat capacity of the reaction, i.e., the difference between the sum of molar heat capacity under constant pressure of products and the sum of molar heat capacity under constant pressure of reactants. Δa, Δb, and Δc are fitted constants, respectively.

The change of the molar heat capacity C_p under constant pressure of products with temperature T can be approximately described by equation (5). Hence, equation (4) can be represented as equation (6).

$$C_p = A_1 + A_2 \times 10^{-3}T + A_3 \times 10^5 T^{-2} + A_4 \times 10^{-6}T^2 + A_5 \times 10^8 T^{-3}, \tag{5}$$

$$\Delta C_p = \Delta A_1 + \Delta A_2 \times 10^{-3}T + \Delta A_3 \times 10^5 T^{-2} + \Delta A_4 \times 10^{-6}T^2 + \Delta A_5 \times 10^8 T^{-3}, \tag{6}$$

where A_1, A_2, A_3, A_4, and A_5 are the fitted data, respectively. ΔA_1, ΔA_2, ΔA_3, ΔA_4, and ΔA_5 are the differences in the corresponding fitted data, respectively.

Integrating equations (3) and (5), the expression of the heat function of the reaction can be determined by [28]

$$\Delta H_T^\Theta = \Delta A_1 T + \frac{1}{2}\Delta A_2 \times 10^{-3}T^2 - \Delta A_3 \times 10^5 T^{-1} + \frac{1}{3}\Delta A_4 \times 10^{-6}T^3 - \frac{1}{2}\Delta A_5 \times 10^8 T^{-2}. \tag{7}$$

If the standard molar formation heats of various substances at room temperature $\Delta H_{i,f,298}^\Theta$ are known, the corresponding reaction heat of the system at $T = 298$ K can be determined as

$$\Delta H_T^\Theta = \sum\left(n_i \Delta H_{i,f,298}^\Theta\right)_{\text{reactants}} - \sum\left(n_i \Delta H_{i,f,298}^\Theta\right)_{\text{products}}. \tag{8}$$

Substituting the ΔH_{298}^Θ calculated by equation (8) and $T = 298$ K into equation (7), the corresponding integration constant A_6 can be determined.

$$A_6 = \Delta H_{298}^\Theta - \Delta A_1 T - \frac{1}{2}\Delta A_2 \times 10^{-3}T^2 + \Delta A_3 \times 10^5 T^{-1} - \frac{1}{3}\Delta A_4 \times 10^{-6}T^3 + \frac{1}{2}\Delta A_5 \times 10^8 T^{-2}. \tag{9}$$

Using a numerical integrating of equation (2), the corresponding equation can be obtained as equation (10). Integrating equations (7) and (9), the standard Gibbs free energy of the reaction at T can be expressed as equation (11).

$$\frac{\Delta G_T^\Theta}{T} = -\int \frac{\Delta H_T^\Theta}{T^2}dT, \tag{10}$$

$$\Delta G_T^\Theta = -\Delta A_1 T \ln T - \frac{1}{2}\Delta A_2 \times 10^{-3}T^2 - \frac{1}{2}\Delta A_3 \times 10^5 T^{-1} - \frac{1}{6}\Delta A_4 \times 10^{-6}T^3 - \frac{1}{6}\Delta A_5 \times 10^8 T^{-2} + A_6'T + A_6, \tag{11}$$

where A_6' is the integration constant of the Gibbs–Helmholtz equation.

If the change of the standard enthalpy ΔH_{298}^Θ and the thermal entropy ΔS_{298}^Θ of the reaction at room temperature (298 K) are known, the corresponding standard Gibbs free energy of the reaction at 298 K can be determined by equation (12). Substituting the ΔG_{298}^Θ calculated by equation (12) and $T = 298$ K into equation (11), the corresponding integration constant A_6' can be determined by equation (13).

$$\Delta G_{298}^\Theta = \Delta H_{298}^\Theta - 298\Delta S_{298}^\Theta, \tag{12}$$

$$A_6' = \frac{\Delta G_{298}^\Theta}{T} + \Delta A_1 \ln T + \frac{1}{2}\Delta A_2 \times 10^{-3}T + \frac{1}{2}\Delta A_3 \times 10^5 T^{-2} + \frac{1}{6}\Delta A_4 \times 10^{-6}T^2 + \frac{1}{6}\Delta A_5 \times 10^8 T^{-3} - A_6 T^{-1}. \tag{13}$$

A conclusion can be drawn from equation (1) that the sulfate attack on cement concrete can be spontaneous when the Gibbs free energy is less than zero. Conversely, the reaction cannot progress spontaneously. Equation (11) shows the relationship between temperature and the Gibbs free energy of the erosion products generated during the sulfate attack on cement concrete, which can be used to reveal the direction of chemical reaction, existing condition and chemical stability of erosion products, and spontaneity of the erosion reaction.

2.2. Critical Ion Concentration of Erosion Products of the Sulfate Attack on Cement Concrete. Some researchers [27] proposed the expression of the thermodynamic equilibrium constant, written as

$$\lg K_{\text{eq}}^\Theta = A + BT + \frac{C}{T} + D\lg(T) + \frac{E}{T^2}, \tag{14}$$

where K_{eq}^{Θ} stands for the thermodynamic equilibrium constant at standard conditions. A, B, C, D, and E are constant, respectively.

The main erosion products of sulfate attack on cement concrete may be gypsum, ettringite, and sulfate salt, [29, 30] and [31], and the corresponding reactions can be written as [19, 32]

$$Ca_{(aq)}^{2+} + SO_{4(aq)}^{2-} \underset{\text{Dissolve}}{\overset{\text{Crystallize}}{\rightleftharpoons}} CaSO_{4(s)} \tag{15}$$

$$Ca_{(aq)}^{2+} + SO_{4(aq)}^{2-} + 2H_2O_{(l)} \underset{\text{Dissolve}}{\overset{\text{Crystallize}}{\rightleftharpoons}} CaSO_4 \cdot 2H_2O_{(s)} \tag{16}$$

$$2Na_{(aq)}^{+} + SO_{4(aq)}^{2-} \underset{\text{Dissolve}}{\overset{\text{Crystallize}}{\rightleftharpoons}} Na_2SO_{4(s)} \tag{17}$$

$$2Na_{(aq)}^{+} + SO_{4(aq)}^{2-} + 10H_2O_{(l)} \underset{\text{Dissolve}}{\overset{\text{Crystallize}}{\rightleftharpoons}} Na_2SO_4 \cdot 10H_2O_{(s)} \tag{18}$$

$$6Ca^{2+} + 2Al^{3+} + 3SO_4^{2-} + 32H_2O_{(l)} \underset{\text{Dissolve}}{\overset{\text{Crystallize}}{\rightleftharpoons}} 3CaO \cdot Al_2O_3$$
$$\cdot 3CaSO_4 \cdot 32H_2O_{(s)} \tag{19}$$

$$CaSiO_3 \cdot CaSO_4 \cdot CaCO_3 \cdot 15H_2O_{(s)} + 3H^+ \underset{\text{Dissolve}}{\overset{\text{Crystallize}}{\rightleftharpoons}} 3Ca^{2+}$$
$$+ SO_4^{2-} + HCO_3^- + H_4SiO_4 + 14H_2O_{(l)} \tag{20}$$

where subscripts s, aq, and l stand for solid state, ionic state in solution, and liquid, respectively.

Correspondingly, the decomposition reactions of the cement hydration products can be expressed as follows [19, 33, 34]:

$$Ca(OH)_{2(s)} + 2H^+ \rightleftharpoons Ca^{2+} + 2H_2O \tag{21}$$

$$C_3AH_{6(s)} + 12H^+ \rightleftharpoons 2Al^{3+} + 3Ca^{2+} + 12H_2O \tag{22}$$

$$C_4AH_{13(s)} + 14H^+ \rightleftharpoons 2Al^{3+} + 4Ca^{2+} + 20H_2O \tag{23}$$

$$C\text{-}S\text{-}H(0.8)_{(s)} + 1.6H^+ \rightleftharpoons 0.34H_2O + 0.8Ca^{2+} + H_4SiO_4 \tag{24}$$

$$C\text{-}S\text{-}H(1.2)_{(s)} + 2.4H^+ \rightleftharpoons 1.26H_2O + 1.2Ca^{2+} + H_4SiO_4 \tag{25}$$

$$Ca_2SiO_{4(s)} + 4H^+ \rightleftharpoons 2Ca^{2+} + H_4SiO_4 \tag{26}$$

$$Al(OH)_{3(s)} + 3H^+ \rightleftharpoons Al^{3+} + 3H_2O \tag{27}$$

$$Ca_6Al_2(SO_4)_3(OH)_{12} \cdot 26H_2O_{(s)} + 12H^+ \rightleftharpoons 2Al^{3+} + 6Ca^{2+}$$
$$+ 3SO_4^{2-} + 38H_2O \tag{28}$$
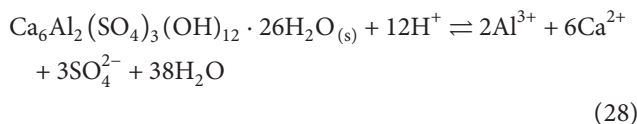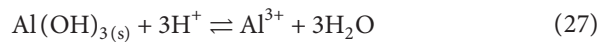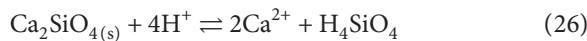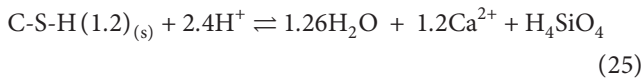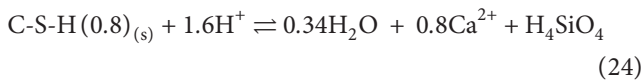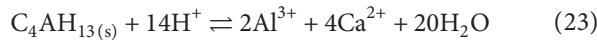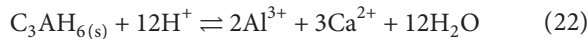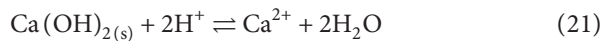
The reference values recommended by researchers [35, 36] are listed in Table 1.

The above reaction equations can be formulated as equation (29), and the relationship between the thermodynamic equilibrium constant and concentration of different substances can be expressed as equation (30).

$$dD + eE \rightleftharpoons gG + hH, \tag{29}$$

$$K_{eq}^{\Theta} = \frac{[G]^g [H]^h}{[D]^d [E]^e}, \tag{30}$$

where $[D]$, $[E]$, $[G]$, and $[H]$ mean the concentration of different substances, respectively. d, e, g, and h are the stoichiometric numbers, respectively.

Combining equations (14) and (30), the formation conditions and the critical ion concentration of sulfate ion for the formation of erosion products can be determined based on the thermodynamic parameter of different substances in Table 1.

3. Experimental Procedure

3.1. Raw Materials. Portland cement of P O. 32.5 class was produced by Pingtang Cement Plant of Hunan, and the polycarboxylic acid series of superplasticizer with solid content of 30% provided by Changsha Huangteng Chemical Technology Co., Ltd was used as a water reducer. ISO standard sand with a fineness modulus of 3.0 was produced by Xiamen Aisiou Standard Sand Co., Ltd. Local river sand with a fineness modulus of 2.9, continuous grading limestone gravel with grains sizes of 5 mm~20 mm, and tap water were used to prepare the specimens. Moreover, the industrial grade sodium sulfate with purity of 99% was purchased from market. The chemical composition and physical properties of cement are listed in Tables 2 and 3.

3.2. Specimen Preparation, Experimental Process, and Test Devices. According to *Common Portland Cement* and *Test Methods for Water Requirement of Normal Consistency, Setting Time and Soundness of the Portland Cement* [37, 38], the paste specimens of 40 mm × 40 mm × 160 mm were cast with a water to cement ratio of 0.28 and were used for XRD analysis. According to *Method of Testing Cements–Determination of Strength*, the mortar specimens of 40 mm × 40 mm × 160 mm were cast with a water: cement: sand ratio of 0.5 : 1 : 3 by weight [39]. According to *Standard for Test Method of Mechanical Properties on Ordinary Concrete* [40], the concrete specimens of 100 mm × 100 mm × 300 mm were cast, and there are three specimens for each group. The C20 grade concrete was prepared with a weight ratio of cement : sand : limestone : water: water reducer of 305 : 831 : 1102 : 158 : 3.5. All specimens were cured in standard curing pool at a temperature of $(20 \pm 1)^{\circ}$C and a relative humidity of (95 ± 3)%. The specimens were demolded after 24 h and cured in water for 28 d at a temperature of $(20 \pm 1)^{\circ}$C. Subsequently, the specimens were taken out from water to carry out sulfate attack test.

TABLE 1: Thermodynamic parameters of different substances.

Items	A	B	C	D	E
$CaSO_4 \cdot 2H_2O_{(s)}$	$1.62021439e+3$	$2.57234846e-1$	$-8.91506186e+4$	$-5.87385148e+2$	$5.34735206e+6$
$CaSO_{4(s)}$	$1.61807826e+3$	$2.62044313e-1$	$-8.95853477e+4$	$-5.86632877e+2$	$5.35893242e+6$
$CaSO_{4(aq)}$	$1.72034184e+3$	$2.65734992e-1$	$-9.42553556e+4$	$-6.23563883e+2$	$5.49729959e+6$
$Na_2SO_4 \cdot 10H_2O_{(s)}$	$1.58837182e+3$	$2.31777424e-1$	$-8.43055786e+4$	$-5.78226172e+2$	$5.09260164e+6$
$Na_2SO_{4(S)}$	$1.61633032e+3$	$2.53239679e-1$	$-8.98032147e+4$	$-5.86414685e+2$	$5.40049408e+6$
$AFt_{(s)}$ $Ca_6Al_2(SO_4)_3(OH)_{12}\cdot26H_2O$	$-6.67460197e+3$	-1.04743390	$3.78708023e+5$	$2.42662966e+3$	$-2.05189885e+7$
$Ca(OH)_{2(s)}$	$-2.84930557e+2$	$-4.47108160e-2$	$2.13801821e+4$	$1.04205027e+2$	$-7.54252617e+5$
$Al(OH)_{3(s)}$	$-4.93752625e+2$	$-8.09001544e-2$	$2.97138788e+4$	$1.77903516e+2$	$-1.26765911e+6$
$NaAlO_{2(aq)}$	$7.04197406e+2$	$1.11341739e-1$	$-4.74872291e+4$	$-2.53129969e+2$	$2.18693139e+6$
$AlO_2^-{}_{(aq)}$	$-1.78049448e+2$	$-2.68902416e-2$	$1.86721225e+3$	$6.68330936e+1$	$-7.50442968e+5$
$H_2O_{(aq)}$	-701.957319	-0.112739992	36168.254	253.60128	-2423273.06
C-S-H $(0.8)_{(s)}$ $Ca_{0.8}SiO_{2.8}\cdot1.54H_2O$	$-2.51027448e+2$	$-3.65449659e-2$	$1.55601183e+4$	$9.21931312e+1$	$-6.52576525e+5$
C-S-$H(1.2)_{(s)}$ $Ca_{1.2}SiO_{3.2}\cdot2.06H_2O$	$-3.72034132e+2$	$-5.41579845e-2$	$2.39845213e+4$	$1.36559314e+2$	$-9.66181083e+5$
C-S-$H(1.6)_{(s)}$ $Ca_{1.6}SiO_{3.6}\cdot2.58H_2O$	$-4.91723254e+2$	$-7.17628896e-2$	$3.25370146e+4$	$1.80399649e+2$	$-1.27964571e+6$
$C_2AH_{8(s)}$ $Ca_2Al_2O_5\cdot8H_2O$	$-1.73467190e+3$	$-2.38046203e-1$	$1.10411145e+5$	$6.23227246e+2$	$-4.18576035e+6$
$C_3AH_{6(s)}$ $Ca_3Al_2(OH)_{12}$	$-1.78581145e+3$	$-2.88036362e-1$	$1.19706499e+5$	$6.47583573e+2$	$-4.61172146e+6$
$CaSiO_3CaSO_4CaCO_3\cdot15H_2O_{(s)}$	$-2.76283310e+3$	$-4.32736383e-1$	$1.49848596e+5$	$1.00850740e+3$	$-8.52601737e+6$
α-$Ca_2SiO_{4(s)}$	$-5.26934036e+2$	$-8.67703839e-2$	$3.89768377e+4$	$1.92577860e+2$	$-1.36961546e+6$
$CaSiO_{3(s)}$	$-2.65453934e+2$	$-4.41966587e-2$	$1.77395216e+4$	$9.72523635e+1$	$-6.65653039e+5$

TABLE 2: Chemical composition of cement (%).

CaO	SiO_2	Al_2O_3	P_2O_5	Fe_2O_3	MgO	K_2O	Na_2O	Loss
65.61	19.89	4.73	2.88	1.45	2.01	1.14	0.21	1.98

TABLE 3: Physical properties of cement.

Average diameter (μm)	Specific surface area (m^2/kg)	Bulk density (g/cm^3)	Initial setting time (min)	Final setting time (min)	Water requirement for standard consistency (%)
34.6	345.2	1.35	172	251	28

The experimental process of the concrete attacked by sulfate was carried out as follows. Firstly, the sulfate solutions of different concentrations (i.e., 1%, 5%, 10%, and saturated solution) were prepared, and various specimens were immersed into sulfate solution. In order to ensure the uniformity of sulfate solution, the distance of specimens was set as no less than 2 cm. Then, the sealed solution box was covered with plastic film to prevent the water from evaporation. Moreover, the sulfate solution was changed once a week. Finally, the specimens were taken out from sulfate solution and dried at room temperature of 25°C and a relative humidity of 70% for 3 days when the erosion ages reached the setting time of 2 and 4 months. The flexural strength of the mortar and paste specimens was first tested, and then the corresponding compressive strength.

The preparation process of the samples for micro-properties test was as follows. Firstly, the specimens reaching the sulfate attack age were cleaned with distilled water and broken into particles of 2 mm~5 mm. Secondly, the particles were immersed into alcohol for 24 h to terminate reaction. Then, the particles were dried at 60°C for 48 h. Finally, the processed particles were placed and stored in a dryer. The proceeded particles containing surface were selected, and their cross-sections were sprayed with gold for ESEM-EDS analysis. The observed localization of the proceeded particle for ESEM-EDS analysis was near the outer surface of the cross-sections. In order to conduct the XRD analysis, the superficial region within 2 mm from cement sample surface was obtained and treated as mentioned above. Subsequently, the proceeded cement paste particles were ground to powder through 200 mesh, and the scanning step of XRD analysis was 0.02°. All samples were prepared and tested according to the equipment guide.

The main test devices were as follows. The Quanta-200 Environment Scanning Electronic Microscope (ESEM-EDS) produced by FTI Company of Czech Republic with an amplification of 600,000 times was used to measure the microstructure. The D/max-2550 X-ray diffraction (XRD) with the angular range of 5°~120° and a minimum scanning step size of 0.01° was used to carry out the phase analysis. The YAW-300D produced by Jinan Kesheng Test Equipment Co. Ltd. of China was used to measure the flexural and compressive strength of the specimens. The maximum compressive and flexural loads were 300 kN and 10 kN, respectively. The corresponding loading rates of compressive and flexural strength were (2.4 ± 0.2) kN/s and (50 ± 10) N/s, respectively. Moreover, the WAW-1000 electrohydraulic servo universal testing machine made by Shanghai Sansi Co. Ltd. of China was used to measure the compressive strength of the concrete. According to *Standard for Test Method of*

Mechanical Properties on Ordinary Concrete [40], the corresponding loading rate was in the range of 0.3 MPa/s~0.55 MPa/s.

4. Results and Discussions

4.1. Assessment of Erosion Products of Sulfate Attack on Cement Concrete. The main erosion products of sulfate attack on cement concrete may be gypsum, ettringite, sulfate salt, and so on. Therefore, the formation spontaneity of the above erosion products was deduced firstly based on the principles of chemical thermodynamics. Because the thermodynamics parameters of different erosion products were affected by environmental conditions remarkably, the thermodynamics parameters of different reactions for erosion products at different conditions including dry, humid, and water environment were calculated theoretically. The reactions of dihydrate gypsum and anhydrite, and mirabilite and thenardite can be written as follows (subscript (g) stands for the gaseous state) [19, 32, 36].

$$CaSO_{4(s)} + 2H_2O_{(g)} \rightleftharpoons CaSO_4 \cdot 2H_2O_{(s)} \tag{31}$$

$$CaSO_{4(s)} + 2H_2O_{(l)} \rightleftharpoons CaSO_4 \cdot 2H_2O_{(s)} \tag{32}$$

$$Na_2SO_{4(s)} + 10H_2O_{(g)} \rightleftharpoons Na_2SO_4 \cdot 10H_2O_{(s)} \tag{33}$$

$$Na_2SO_{4(s)} + 10H_2O_{(l)} \rightleftharpoons Na_2SO_4 \cdot 10H_2O_{(s)} \tag{34}$$
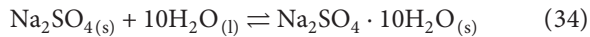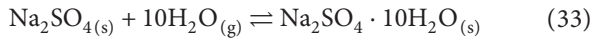
The corresponding thermodynamic parameters of different reactions can be determined based on equations (4)~(13) and Table 4, as listed in Table 5. Moreover, the Gibbs free energy curves of various erosion products under different conditions as a function of temperature are plotted in Figure 1.

Figure 1(a) shows that the theoretical transformation temperature between dihydrate gypsum and anhydrite under humid and water conditions is about 91°C; that is, the dihydrate gypsum can be spontaneously formed when the temperature is lower than 91°C. However, the corresponding temperature under dry condition is about 56°C; i.e., the dihydrate gypsum can be translated into anhydrite when the temperature exceeds 56°C. Figure 1(b) indicates that the theoretical transformation temperature between mirabilite and thenardite under dry condition is about 45°C; however, it is about 88°C under humid and water conditions. From the above discussions, a conclusion can be drawn that the environment conditions have significant effects on the transformation of the crystals with combined water. Therefore, the environmental condition should be considered as an important factor of sulfate attack on cement concrete during the test process of sulfate attack and specimens' preparation. It is the theoretical transformation temperature curve based upon which the substances with or without crystal water would be converted. In Figure 1, the Gibbs free energy curves are calculated based on the theoretical transformation temperature of the substances without crystal water converted into the substances with crystal water. Because the theoretical calculated data do not consider the activity of substances, there exists a difference between the theoretical calculated results and the in-site measured data. The research [41] showed that the solubility of calcium sulfate at normal temperatures and pressures was about 0.2%, and the temperature corresponding to the intersection of solubility curves of dihydrate gypsum and anhydrite was 42°C [42]. The above achievements accord well with the theoretical calculated data in Figure 1, which implies that equation (11) proposed by this study can be used to determine the mechanism of sulfate attack. Because all the sulfate attacks took place in the concrete pore solution, the deterioration mechanism and erosion products of sulfate attack reacting in solution were further investigated.

4.2. Numerical Analysis of Critical Concentration of Sulfate Ion of Different Erosion Products with Temperature. Calcium hydroxide (CH) in cement and concrete has a significant effect on the thermodynamic equilibrium of various products, so the variation of critical concentration of $[OH^-]$ and $[Ca^{2+}]$ with temperature is investigated firstly. Assuming the content of hydroxyl ion is generated by CH and dominated by CH saturated solution, the corresponding chemical equilibrium based on Hess's law can be expressed as follows [36]:

$$\left. \begin{array}{ll} Ca(OH)_{2(s)} + 2H^+ = Ca^{2+} + 2H_2O & (1) \\ H_2O = H^+ + OH^- & (2) \end{array} \right\} \Longrightarrow (1) + 2 \times (2) \Longrightarrow$$
$$Ca(OH)_{2(s)} = Ca^{2+} + 2OH^- \tag{35}$$
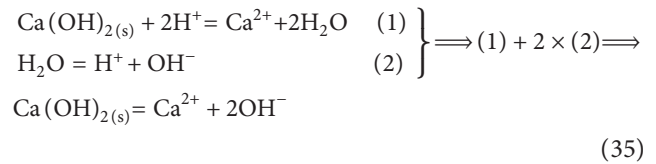
The corresponding thermodynamic equilibrium constant at standard conditions of the above reaction can be determined based on equation (1), written as

$$\ln K^\Theta = \ln K_1^\Theta + 2\ln K_2^\Theta. \tag{36}$$

Assuming the $[OH^-]$ in the system is generated by $Ca(OH)_2$, the concentration of calcium ion is half of the hydroxyl ion. The concentration of hydroxyl ion with temperature can be determined based on equation (36), as shown in Figure 2. If the activity of condensed matters is set as 1, the critical concentration of sulfate ion for the formation of dihydrate gypsum and anhydrite in equations (15) and (16) can be deduced on the basis of the calcium ion concentration and thermodynamic equilibrium constant, written as equations (37) and (38). The corresponding critical concentration curves of sulfate ions for the formation of dihydrate gypsum and anhydrite as a function of temperature are plotted in Figure 2.

$$\left[SO_4^{2-} \right] = \frac{K_{CaSO_4 \cdot 2H_2O}^\Theta \cdot c^\Theta}{a_{\left[Ca^{2+} \right]}} \tag{37}$$

$$\left[SO_4^{2-} \right] = \frac{K_{CaSO_4}^\Theta \cdot c^\Theta}{a_{\left[Ca^{2+} \right]}} \tag{38}$$

As seen from Figure 2(a), the theoretical concentrations of $[Ca^{2+}]$ and $[OH^-]$ corresponding to the thermodynamic

TABLE 4: Thermodynamic parameters for different products.

Items	$\Delta_f H^{\ominus}_{298}$ (J/mol)	$S^{\ominus}_{298}$ (J/mol·K^{-1})	C_P (J/K·mol^{-1})				
			A_1	A_2	A_3	A_4	A_5
$CaSO_{4(s)}$	−1434108	105.228	70.208	98.742	0	0	0
$CaSO_4 \cdot 2H_2O_{(s)}$	−2022629	194.138	91.379	317.984	0	0	0
$H_2O_{(g)}$	−241814	188.724	29.999	10.711	0.335	0	0
$H_2O_{(l)}$	−285840	69.94	33.1799	70.9205	11.1715	0	0
$Na_2SO_{4(s)}$	−1387205	149.62	82.299	154.348	0	0	0
$Na_2SO_4 \cdot 10H_2O_{(s)}$	−4327791	591.9	574.46	0	0	0	0
$Ca(OH)_{4(s)}$	−982611	83.387	105.269	11.294	−18.954	0	0
$NaOH_{(s)}$	−428023	64.434	71.756	−110.876	0	235.768	0

TABLE 5: Thermodynamic parameters of different reactions.

Items	$\Delta H^{\ominus}_{298}$ (J/mol)	$\Delta S^{\ominus}_{298}$ (J/mol·K^{-1})	$\Delta G^{\ominus}_{298}$ (kJ/mol)	ΔA_1	ΔA_2	ΔA_3	ΔA_4	ΔA_5	$\Delta C_{p,298}$ (J/K mol^{-1})	ΔA_6	$\Delta A'_6$	$\Delta A''_6$
Equation (31)	−104893	288.538	−18908.676	−38.827	197.82	−0.67	0	0	19.369	−102330.99	87.8375	−126.665
Equation (32)	−16841	−50.97	−1651.94	−45.1888	77.401	−22.343	0	0	−47.283	−14309.1	−216.018	170.829
Equation (33)	−522446	−1444.96	−91847.9	192.171	−261.458	−3.35	0	0	110.484	−569227.9	2655.92	−2463.75
Equation (34)	−82168	−257.12	−5564.24	160.362	863.553	−111.715	0	0	−222.776	−129118.7	1136.64	−976.278
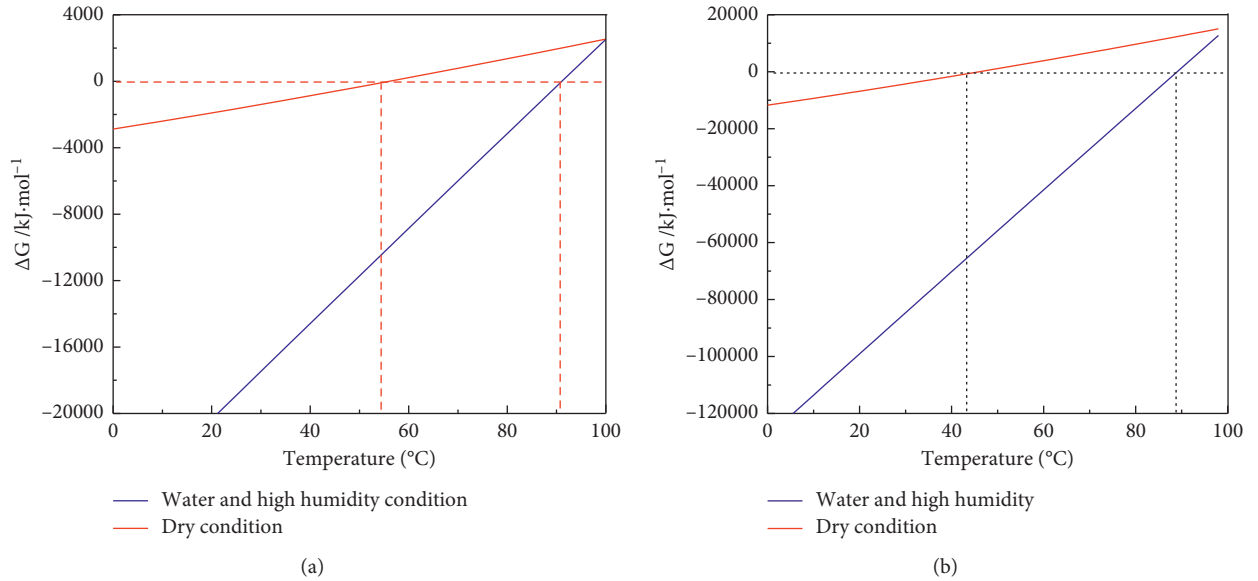
FIGURE 1: Gibbs free energy of various erosion products under different conditions versus temperature. (a) Dihydrate gypsum and anhydrite. (b) Mirabilite and thenardite.

equilibrium state of the system decrease with increase of the temperature, which accords well with the variation rule of actual solubility of CH with temperature. Figure 2(b) shows that there exists an intersection of the critical sulfate ion concentration curves of $CaSO_4$ and $CaSO_4 \cdot 2H_2O$ at about 42°C. This indicates that $CaSO_4 \cdot 2H_2O$ can be preferentially generated when the reaction temperature is less than 42°C.

Conversely, it will be $CaSO_4$. Figure 2 also reveals that the critical concentration of sulfate ion for the formation of $CaSO_4 \cdot 2H_2O$ is more than 2.3×10^{-3} mol/L, which is in accordance with the solubility of calcium sulfate (about 0.2 wt.%) [41] under normal temperature and pressure. The change law of sulfate ion concentration with temperature also accords well with the actual solubility of gypsum, which

(a)

(b)
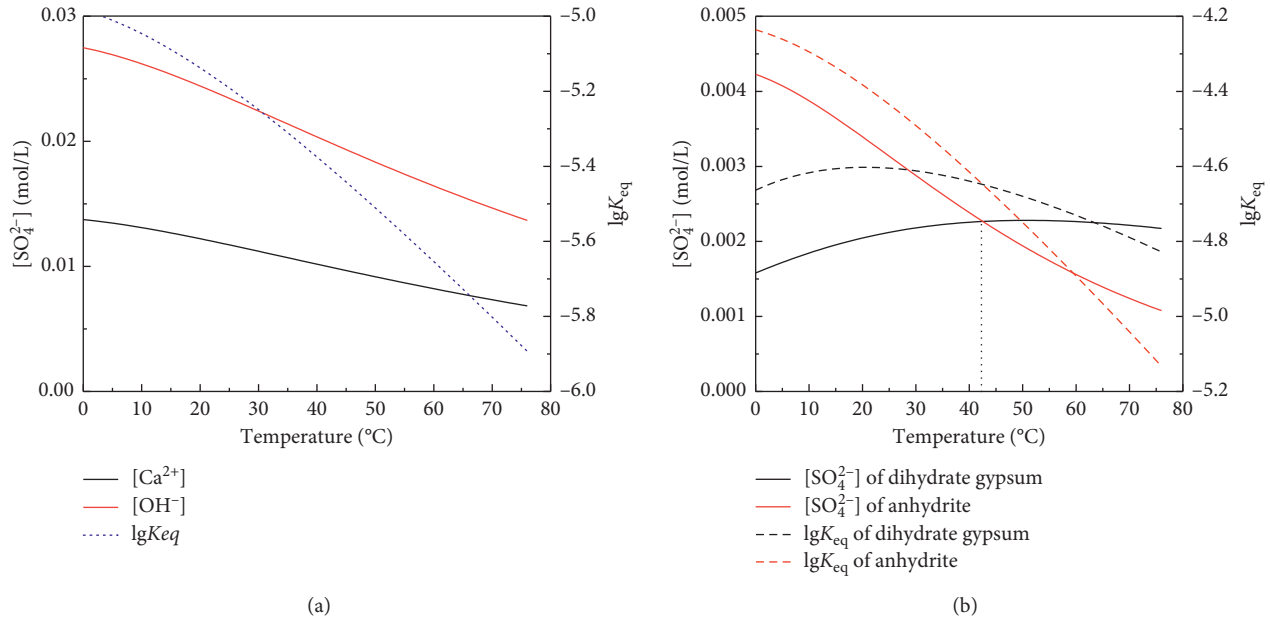
FIGURE 2: Curves of critical sulfate ion concentration and thermodynamic equilibrium constant with temperature. (a) $Ca(OH)_2$. (b) $CaSO_4$ and $CaSO_4 \cdot 2H_2O$.

indicates that the principles of chemical thermodynamics can be used to determine the formation condition and critical concentration of various ions. Moreover, the logarithm values of the thermodynamic equilibrium constant in Figure 2 are all negative numbers, which implies that the Gibbs free energy of the reactions is less than zero. Therefore, the corresponding erosion reaction is spontaneous.

The variations of critical concentration of sulfate ion for the formation of AFt, AFm, and thaumasite ($CS\overline{C}SH$) as a function of temperature were also investigated. Assuming the $[Al^{3+}]$ generated by the decomposition of C_3AH_6 and C_4AH_{13} can react with $[Ca^{2+}]$ and $[SO_4^{2-}]$, and the concentration of $[Ca^{2+}]$ and $[OH^-]$ is also dominated by $Ca(OH)_2$ solution, the chemical equations of AFt, AFm, and $CS\overline{C}SH$ can be expressed as follows [36].

$$
\left.
\begin{aligned}
&CS\overline{C}SH_{(s)} + 3H^+ = HCO_3^- + 3Ca^{2+} + SO_4^{2-} + H_4SiO_4 + 14H_2O \quad (1)\\
&CaCO_{3(s)} + H^+ = HCO_3^- + Ca^{2+} \quad (2)\\
&CaSO_4 \cdot 2H_2O_{(s)} + H^+ = Ca^{2+} + SO_4^{2-} \quad (3)\\
&CaSiO_{3(s)} + 2H^+ + H_2O_{(l)} = Ca^{2+} + H_4SiO_{4(s)} \quad (4)
\end{aligned}
\right\} \Longrightarrow \quad (39)
$$

$$(1) - (2) - (3) - (4) \Longrightarrow CS\overline{C}SH_{(s)} = CaCO_{3(s)} + CaSO_4 \cdot 2H_2O_{(s)} + CaSiO_{3(s)} + 13H_2O_{(l)}$$

$$
\left.
\begin{aligned}
&C_3AH_{6(s)} + 12H^+ = 2Al^{3+} + 3Ca^{2+} + 12H_2O \quad (1)\\
&H_2O = H^+ + OH^- \quad (2)
\end{aligned}
\right\} \Longrightarrow \quad (40)
$$

$$(1) + 12 \times (2) \Longrightarrow C_3AH_{6(s)} = 2Al^{3+} + 3Ca^{2+} + 12OH^-$$

$$
\left.
\begin{aligned}
&AFt + 12H^+ = 2Al_{(aq)}^{3+} + 6Ca_{(aq)}^{2+} + 3SO_{4(aq)}^{2-} + 38H_2O \quad (1)\\
&H_2O = H^+ + OH^- \quad (2)
\end{aligned}
\right\} \Longrightarrow \quad (41)
$$

$$(1) + 12 \times (2) \Longrightarrow AFt_{(s)} = 2Al^{3+} + 6Ca^{2+} + 3SO_4^{2-} + 12OH^- + 26H_2O$$
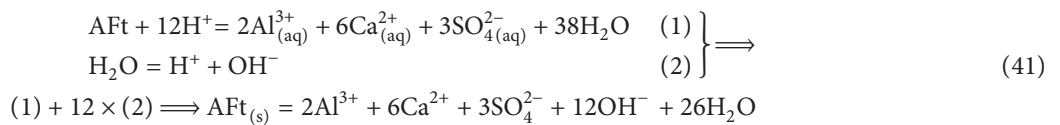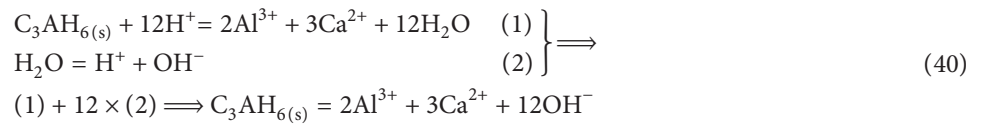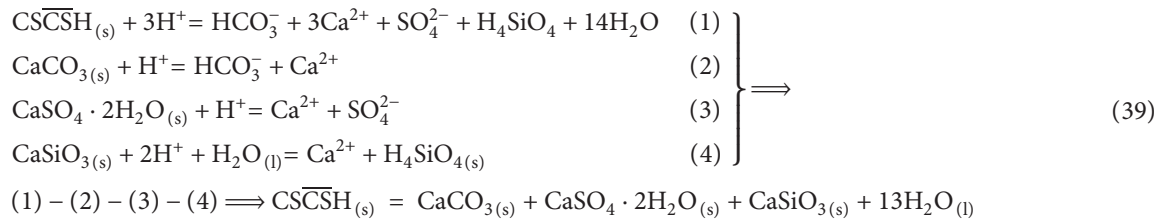
The corresponding thermodynamic equilibrium constant at standard conditions of the reaction can be determined based on equation (1), written as follows:

$$K^{\ominus}_{CS\overline{C}\overline{S}H} = \frac{a_{[HCO_3^-]} \cdot a^3_{[Ca^{2+}]} \cdot a^{12}_{[SO_4^{2-}]} \cdot a_{[H_4SiO_4]} \cdot a^{14}_{[H_2O]}}{a_{[CS\overline{C}\overline{S}H]} \cdot a^3_{[H^+]}}$$

(42)

$$K^{\ominus}_{C_3AH_6} \cdot \left(K^{\ominus}_{H_2O}\right)^{12} = \frac{a^2_{[Al^{3+}]} \cdot a^3_{[Ca^{2+}]} \cdot a^{12}_{[OH^-]}}{a_{[C_3AH_6]}}$$

(43)

$$K^{\ominus}_{AFt} \cdot \left(K^{\ominus}_{H_2O}\right)^{12} = \frac{a^2_{[Al^{3+}]} \cdot a^6_{[Ca^{2+}]} \cdot a^{26}_{[H_2O]} \cdot a^3_{[SO_4^{2-}]} \cdot a^{12}_{[OH^-]}}{a_{[AFt]}}$$

(44)

Assuming the activity of condensed matter equals 1, the corresponding activity of the sulfate ion for different erosion products can be written as follows:

$$a_{[SO_4^{2-}]} = \frac{K^{\ominus}_{CS\overline{C}\overline{S}H}}{a_{[Ca^{2+}]}}$$

(45)

$$a_{[SO_4^{2-}]} = \frac{1}{a_{[Ca^{2+}]}} \sqrt[3]{\frac{K^{\ominus}_{AFt}}{K^{\ominus}_{C_3AH_6}}}$$

(46)

Simultaneously, the corresponding activity of the critical sulfate ion for AFt generated by C_4AH_{13} can be represented as follows:

$$a_{[SO_4^{2-}]} = \sqrt[3]{\frac{K^{\ominus}_{AFt} \cdot a^2_{[OH^-]}}{K^{\ominus}_{C_4AH_{13}} \cdot \left(K^{\ominus}_{H_2O}\right)^2 \cdot a^2_{[Ca^{2+}]}}}$$

(47)

If the erosion product of sulfate attack on cement and concrete is AFm which was generated by $[Al^{3+}]$ decomposed by C_3AH_6 and C_4AH_{13}, the corresponding activity of the sulfate ion can be written as follows:

$$a_{[SO_4^{2-}]} = \frac{K^{\ominus}_{AFm}}{K^{\ominus}_{C_3AH_6} \cdot a_{[Ca^{2+}]}}$$

(48)

$$a_{[SO_4^{2-}]} = \frac{K^{\ominus}_{AFm} \cdot a^2_{[OH^-]}}{K^{\ominus}_{C_4AH_{13}} \cdot \left(K^{\ominus}_{H_2O}\right)^2}$$

(49)

The critical concentrations of sulfate ion for different erosion products calculated by equations (45)~(49) as a function of temperature are plotted in Figure 3.

As seen from Figure 3(a), the upper limit temperature for CS$\overline{C}\overline{S}$H to exist steadily is 44°C. Once the system temperature is larger than this temperature, the CS$\overline{C}\overline{S}$H may be decomposed. Simultaneously, the critical concentration of sulfate ion for the formation of CS$\overline{C}\overline{S}$H is about 0.0023 mol/L. The above results change the traditional viewpoint that CS$\overline{C}\overline{S}$H can only exist in low temperature [24] and provide theoretical support for the formation of CS$\overline{C}\overline{S}$H under room temperature. Figure 3(b)

shows that temperature and types of calcium aluminate hydrate have significant effects on the critical concentration of sulfate ion for the formation of AFt and AFm. Compared with C_4AH_{13}, the C_3AH_6 reacts more easily with sulfate ion at room temperature, and the corresponding critical concentration of sulfate ion is also lower. Figure 3 also reveals that the critical concentration of sulfate ion for the formation of AFt and AFm is lower than that of the gypsum, which implies that the AFt and AFm can be generated preferentially with better thermostability [43]. It is also the reason that the early strength of Portland cement can be enhanced by adding gypsum as well as the improvement in the finial and initial setting time.

Integrating equations (46) and (48), the critical concentration of sulfate ion for the transformation between AFt and AFm generated by C_3AH_6 can be expressed as equation (50). The theoretical thermodynamic equilibrium constant and sulfate ion concentration as a function of temperature are plotted in Figure 4.

$$a_{[SO_4^{2-}]} = \frac{1}{a_{[Ca^{2+}]}} \sqrt{\frac{K^{\ominus}_{AFt}}{K^{\ominus}_{AFm}}}$$

(50)

Figure 4(a) shows that the thermodynamic equilibrium constant of the AFt and AFm increases with temperature, and that of the AFm is larger. The critical concentration of sulfate ion corresponding to the transformation between them at room temperature is very low, but its variation becomes more significant when the temperature is higher than 40°C. In general, the thermodynamic equilibrium constant of the AFt is less than that of the AFm. However, their thermodynamic equilibrium constants show the cubic and linear function relationship with the concentration of sulfate ion, respectively. Hence, the AFm can be preferentially generated under a low concentration of sulfate ion. The subsequent results are the decrease of sulfate ion concentration and the destruction of the thermodynamic equilibrium state, which may result in the decomposition of the AFt. Therefore, the AFt and AFm can transform each other and reach a new thermodynamic equilibrium state under a certain sulfate ion concentration. It may be related to the thermodynamic stability of the AFt, as shown in Figure 4(b). It can be seen from Figure 4(b) that the thermodynamic stability of the AFt is about 97°C; that is, the AFt may be decomposed when the system temperature is higher than the critical temperature. However, Lawrence [12] pointed out that the measured decomposition temperature of the AFt was about 60°C~70°C. The difference may be due to the fact that theoretical results do not consider the effect of activity of various products.

Some researches [44, 45] revealed the relationship of thenardite, mirabilite, and solution, expressed as follows:

$$y = 1 - 2.304x - 14.618x^2,$$

(51)

$$x = a_{tr} \cdot \exp(b \cdot T),$$

(52)

(a)

(b)
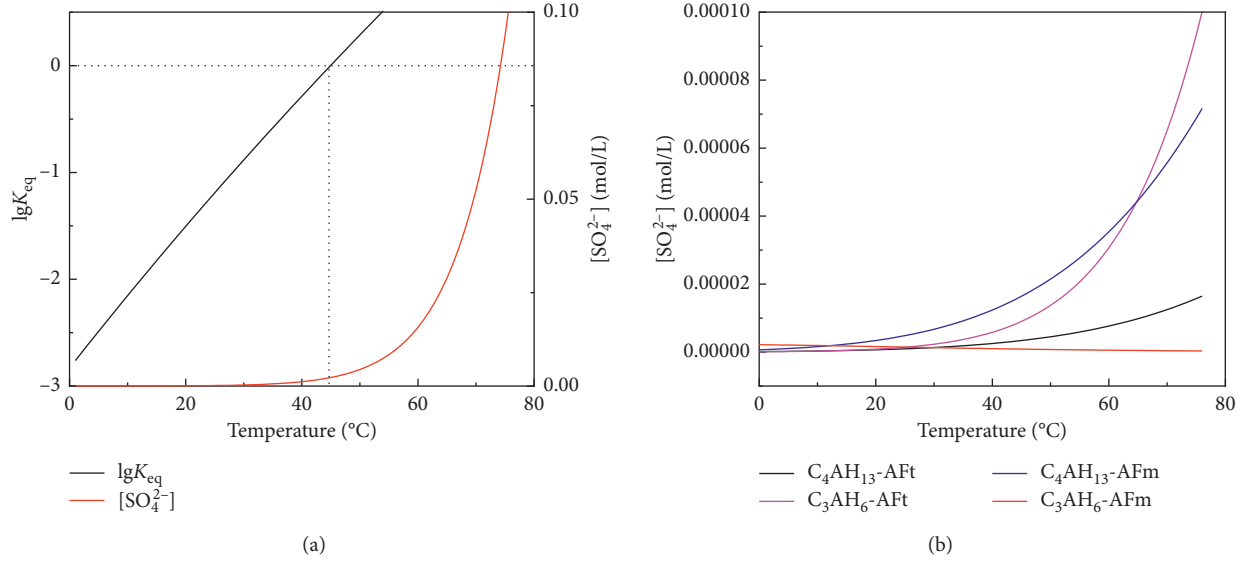
FIGURE 3: Variation curves of critical ions for different erosion products in system versus temperature. (a)$C\overline{S}\overline{C}SH$. (b) AFt and AFm.

(a)

(b)
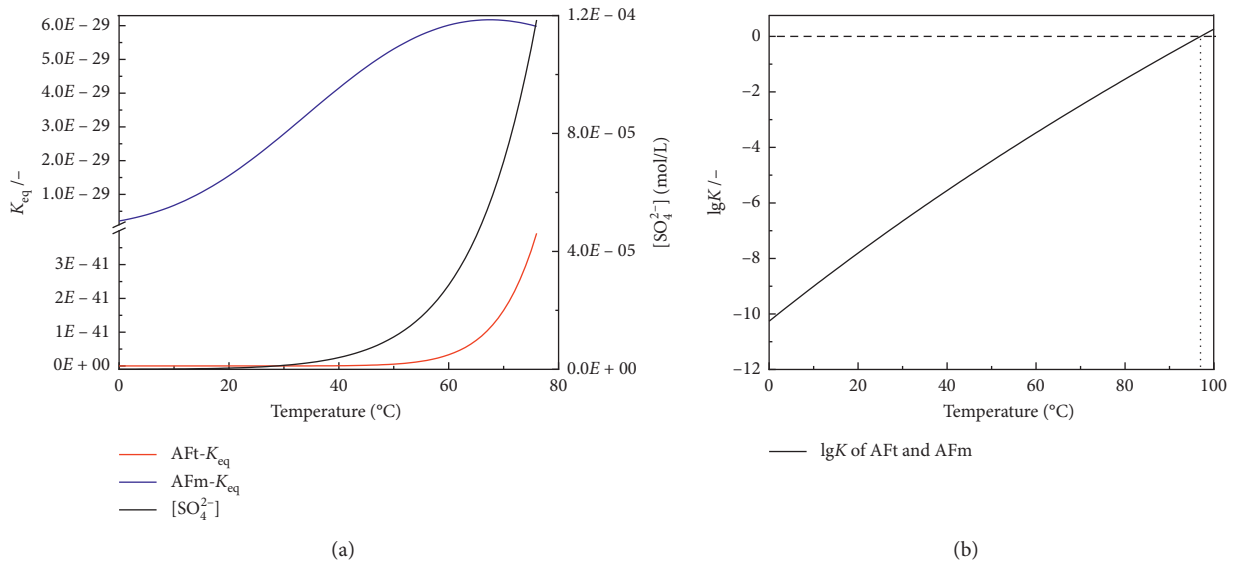
FIGURE 4: Curves of thermodynamic equilibrium constant and critical concentration of sulfate ion versus temperature. (a) Thermodynamic equilibrium constant and sulfate ion concentration. (b) Thermostability of the AFt and AFm.

where T is the temperature, y is the activity of liquid water, and x stands for the mole fraction of sodium sulfate solution. a_{tr} and b are the fitted constants, respectively, and the recommended values are listed in Table 6.

The crystal transition point of $Na_2SO_4 \cdot 10H_2O$ and Na_2SO_4 can be determined based on equations (51) and (52), and the corresponding phase spectrum and solubility of sodium sulfate are plotted in Figure 5.

As seen from Figure 5, the crystal transition temperature between Na_2SO_4 and $Na_2SO_4 \cdot 10H_2O$ is about 32.4°C; that is, the Na_2SO_4 may be crystallized from saturated solution when the temperature is higher than 32.4°C. Correspondingly, the $Na_2SO_4 \cdot 10H_2O$ is the thermodynamical stable phase under high humidity and temperature lower than

32.4°C. Conversely, the Na_2SO_4 salt may be crystallized under a lower temperature and humidity conditions. Although the solubility of sodium sulfate increases with the increase of the temperature, it gradually decreases when the temperature exceeds 32.4°C, as shown in Figure 5. A conclusion can be drawn from the above discussion that the types and solubility of sodium sulfate are closely related to the temperature and relative humidity. Therefore, the types of erosion products in cement and concrete attacked by sulfate, i.e., Na_2SO_4 and $Na_2SO_4 \cdot 10H_2O$, are related to the reaction conditions; that is, they can transform each other and even coexist at a certain condition. The above theoretical deduction changes the traditional perception of the existence of single salt crystals of Na_2SO_4 and $Na_2SO_4 \cdot 10H_2O$.

TABLE 6: Value of the fitted data.

Items	a_{tr}	b
Na_2SO_4	0.11322	-0.0024978
$Na_2SO_4 \cdot 10H_2O$	$4.3751e - 11$	0.068435
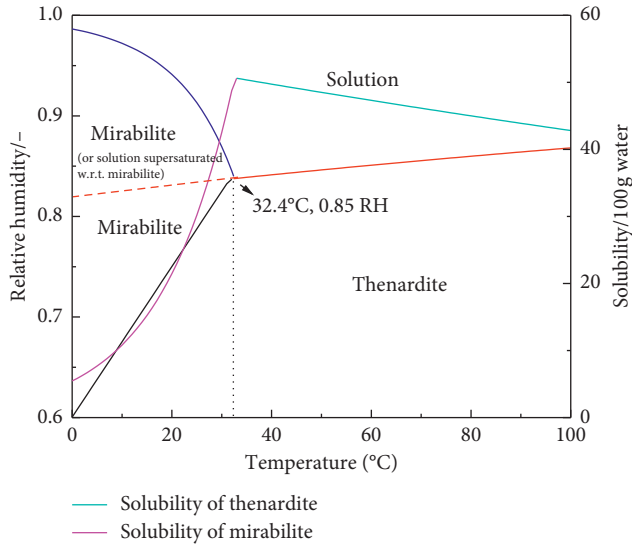
FIGURE 5: Phase spectrum and solubility of sodium sulfate.

Moreover, the critical concentration of sulfate ion for the formation of different erosion products can be determined based on the solubility curve in Figure 5, which provides theoretical support for the types and existence conditions of erosion products in cement.

To sum up, the generation of erosion products in cement is related to temperature, relative humidity, and sulfate ion concentration, and these factors affect each other. Among them, the $[SO_4^{2-}]$ is one of the most important factors. The dihydrate gypsum is preferentially generated when the temperature is less than 42°C and $[SO_4^{2-}]$ concentration is more than 2.3×10^{-3} mol/L. However, the corresponding formation concentration of anhydrite is more than 4.2×10^{-3} mol/L, and the temperature is larger than 42°C. The theoretical thermodynamic stable temperature of AFt is about 97°C, and the critical concentration of sulfate ion for the AFt is no less than 2.8×10^{-3} mol/L. The mirabilite and thenardite may be generated when the concentration of sulfate ion is more than 1.5×10^{-3} mol/L. The mirabilite can be spontaneously crystallized when the temperature is less than 32.4°C. Moreover, the thaumasite can be formed when the temperature is less than 44°C and $[SO_4^{2-}]$ concentration is more than 0.0023 mol/L. The above theoretical results accord well with the recommended value proposed by some researchers [46–48]; however, because the theoretical results do not consider the effect of activity of various products and the coupled effects of ions in system, it is a little bit different from that (less than 20°C) reported by Blanco et al. [24]. The above results imply that the erosion products in cement attacked by different sulfate conditions can be determined by the principles of chemical thermodynamics, which provides

theoretical support for the determination of erosion products in cement concrete.

4.3. ESEM-EDS and XRD Analysis of Sulfate Attack on Cement Concrete. In order to verify the rationality of the above theoretical calculation, the sulfate attack on cement and concrete was studied. The theoretical formation conditions including temperature and critical concentration of sulfate ion were all based on ideal solution; the activity of various ions and erosion products was not considered. Therefore, there would be a difference between theoretical calculation results and actual values. In order to determine the concentration range of sulfate concentration of different erosion products, the sulfate solution of different concentrations was prepared to conduct sulfate attack, i.e., 1%, 5%, 10%, 20%, and saturated solution. Figure 6 shows the ESEM-EDS spectra of microstructure, types, and morphology of erosion products of cement concrete attacked by sulfate solution of different concentrations for 4 months.

Figure 6 shows that the microstructure, types, and morphology of substances of the specimens before and after sulfate attack are different. As seen from Figure 6(a), the major hydration products of the unattacked specimen are hexagonal plate-like calcium hydroxide (CH), needle-like ettringite (AFt), flocculent and gelatinous calcium silicate hydrate (C-S-H), and calcium aluminate hydrate (C-A-H). Moreover, some micro pores and cracks can also be observed. With the increase of sulfate solution concentration (i.e., 1% and 5%), plenty of rod-like AFt with a larger diameter-length ratio is generated in system, and the amount of hexagonal plate-like CH decreases, as shown in Figures 6(b) and 6(c). Some plate-like erosion products can be observed from the specimen attacked by 10% sulfate solution, which may be dihydrate gypsum or the partially corroded CH, as shown in Figure 6(d). Moreover, plenty of dendritic and fibriform erosion products are observed in specific region of the specimen, as shown in Figure 6(e). The EDS analysis indicates that the major elements are Ca, Si, O, and S, which may be considered as the residual skeleton of C-S-H based on its morphology and characteristic, as shown in Figure 6(f). The higher the sulfate solution concentration, the more excellent the crystallinity of granular sulfate salt and plate-like erosion products, as shown in Figures 6(g) and 6(h). The EDS analysis indicates that the major elements are Ca, O, and S, which may be dihydrate gypsum based on the characteristic of morphology, as shown in Figure 6(i). The concentration range of sulfate ion for the formation of erosion products in Figure 6 accords well with the theoretical calculated value in Section 4.2, which implies that the mechanism of sulfate attack on cement concrete can be represented by the principles of chemical thermodynamics. Moreover, the amount of hydration products including CH, C-S-H, and C-A-H in the specimens attacked by sulfate is reduced, which may be due to the fact that the sulfate attack reduces pH value, destroys thermodynamic equilibrium state, and accordingly results in the decomposition of hydration products. It can be seen that, compared with the microstructure of specimens attacked by sulfate solution of

(a)

(b)

(c)

(d)

(e)

(f)

(g)

(h)

(i)
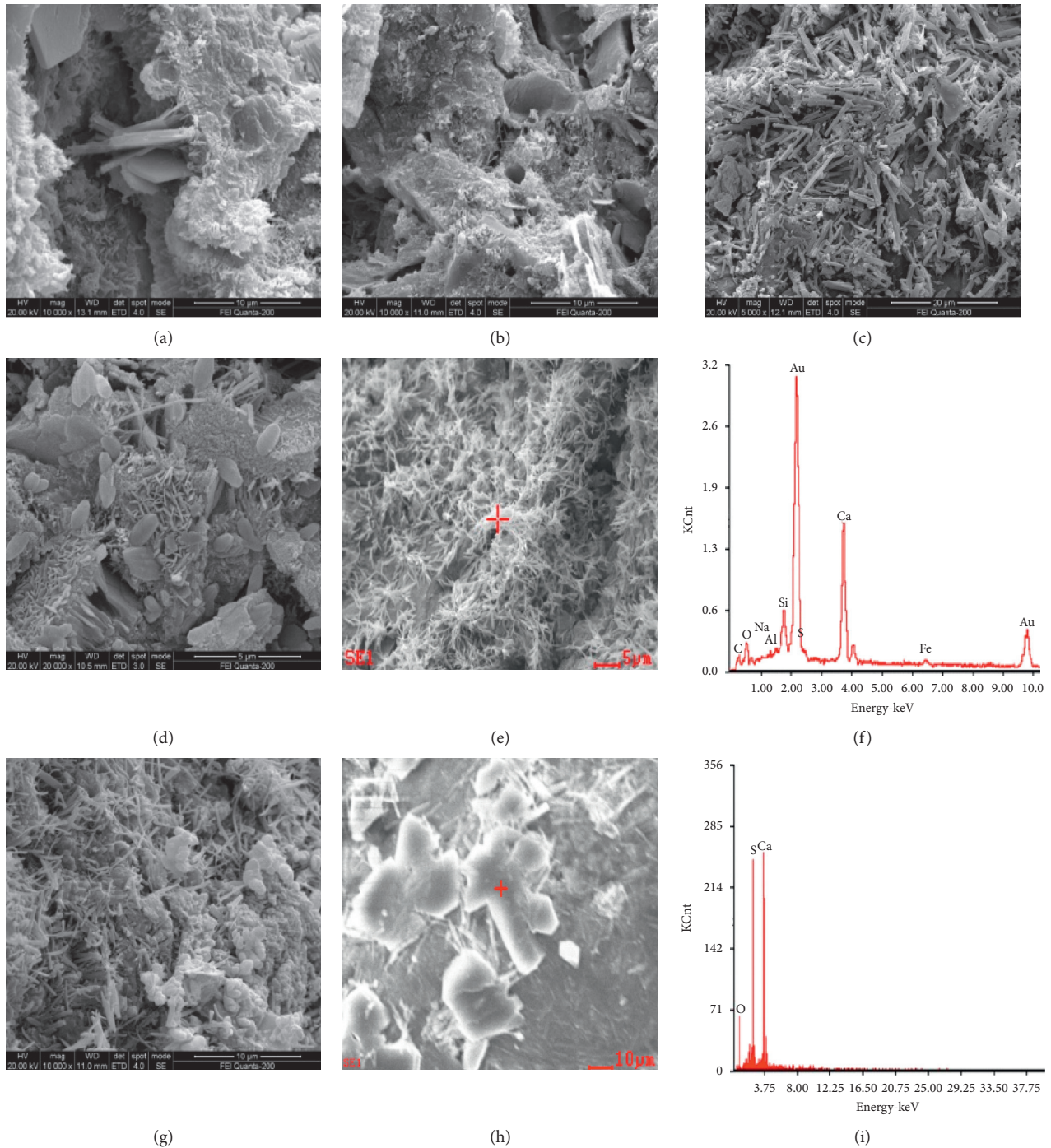
Figure 6: ESEM-EDS spectra of cement and concrete attacked by sulfate solution of different concentrations. (a) Non attacked. (b) 1%. (c) 5%. (d) 10%. (e) 10%. (f) EDS analysis. (g) 20%. (h) Saturated solution. (i) EDS analysis.

different concentrations, the microstructure of the specimen attacked by 1% sulfate solution becomes denser, which is caused by the generation of expansive substances of the AFt and AFm which fill in pores and reduce part of the porosity. Therefore, it has a positive effect on the performances of the specimens attacked by low sulfate solution concentration. However, if the sulfate attack reduces pH value of the system and causes the decomposition of hydration products and

deterioration of microstructure, it will have a negative effect on the performance of the specimens.

In order to investigate the effect of sulfate solution concentration on the phase composition of cement concrete, the XRD spectra of the cement attacked by sulfate for 4 months were tested, as shown in Figure 7.

As seen from Figure 7, there exist some significant differences in the erosion products' spectra before and after
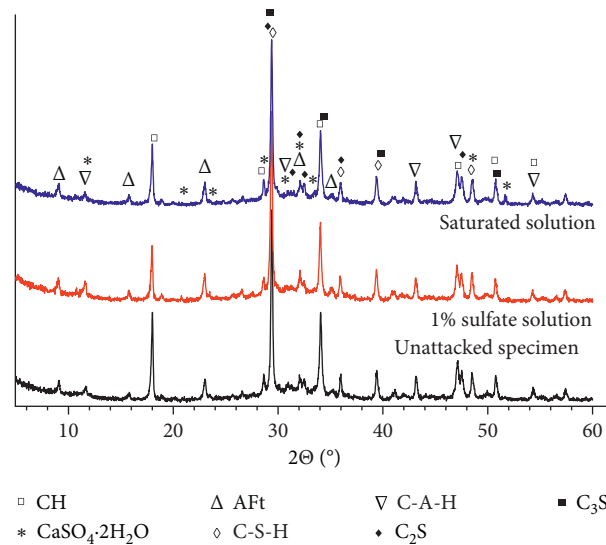
FIGURE 7: XRD spectra of phase composition of specimens attacked by sulfate solution.

sulfate attack, shown as the appearance and disappearance of some diffraction peaks, and variations of intensity and width of diffraction peaks. Based on the characteristic diffraction peak of the substances, it can be seen that the major hydration products of the specimens without sulfate attacked are calcium hydroxide (CH), calcium aluminate hydrate (C-A-H), calcium silicate hydrate (C-S-H), unhydrated tricalcium silicate (C_3S), and dicalcium silicate (C_2S). Their diffraction peaks' intensity is stronger and the width is narrower. After being attacked by sulfate solution of different concentrations, i.e., 1% and saturated sulfate solution, some diffraction peaks' intensity of the hydration products including CH, C-A-H, and C-S-H decreases, and the characteristic diffraction peaks' intensity belonging to the AFt enhances. Moreover, some new diffraction peaks corresponding to the gypsum appear. This is due to the fact that the sulfate ion reacts with hydration products of CH and C-A-H and is generated into AFt and gypsum. Furthermore, some characteristic diffraction peaks' intensity weakens, which may be caused by the decrease of pH value due to reaction of the sulfate ion with CH. Therefore, the thermodynamic equilibrium state of system is destroyed and results in the decomposition of cementitious hydration products. The variation of diffraction peaks of the specimens before and after sulfate attack accords well with the results in Figure 6. No diffraction speaks of mirabilite and thenardite are observed in Figure 7, which may be due to the fact that the sulfate ion intruding into specimen is reacted, and the dehydration of mirabilite resulted from the preparation method of XRD analysis.

4.4. Variation of Mechanical Properties of the Specimens Attacked by Sulfate.
The microstructure, types, and morphology of erosion products and phase compositions of the specimens can be affected by sulfate attack. In order to investigate the effects of sulfate attack on macro properties of the specimens, the mechanical properties of the specimens attacked by sulfate solution of different concentrations and erosion ages (i.e., 2 and 4 months) were investigated, as shown in Figure 8.

As seen from Figure 8, the mechanical properties of the specimens attacked by sulfate for 2 months first increase and then decrease with the increase of sulfate solution concentration, and the corresponding strength is larger than that of the unattacked specimens. Compared with mortar and concrete, the variation of the paste strength is more significant. There may be two primary reasons for the confusion. First, the water to cement ratio is lower, so the porosity of cement paste specimen is less. Some sulfate ion intruding into specimens could be reacted and generated into expansive substances, which can fill and refine the micro pores. Second, the formed erosion products could enhance the compactness of system and reduce the amount of CH in cement specimen [21, 49, 50], so the microstructure and the performance of the specimens are improved. The higher the concentration of sulfate solution, the greater the concentration gradient between the solution and specimen surface. Therefore, more sulfate ion intrudes into specimen, and plenty of expansive substances are generated. If the expansive substances generated by sulfate attack can be accommodated by pores in system, the sulfate attack has a positive effect on performance of the specimens. Conversely, the sulfate attack destroys the thermodynamic equilibrium state of the system and results in micro damage, so it has a negative effect. Macroscopically, it is manifested as the decrease of the mechanical properties of the specimens. Although the compressive strength of paste and mortar attacked by sulfate for 4 months decreases with the increase of sulfate solution concentration, the corresponding compressive strength of the concrete first increases and then decreases. The maximum decreasing amount of the compressive strength of the specimens can reach up to 30%. The flexural strength of the paste first increases and then decreases with increase of the sulfate solution concentration. However, the corresponding flexural strength of the mortar decreases, and the maximum decreasing amount can reach up to 50%. The paste has a better resistance to sulfate attack, which is due to generation of plenty of

(a)

(b)

(c)
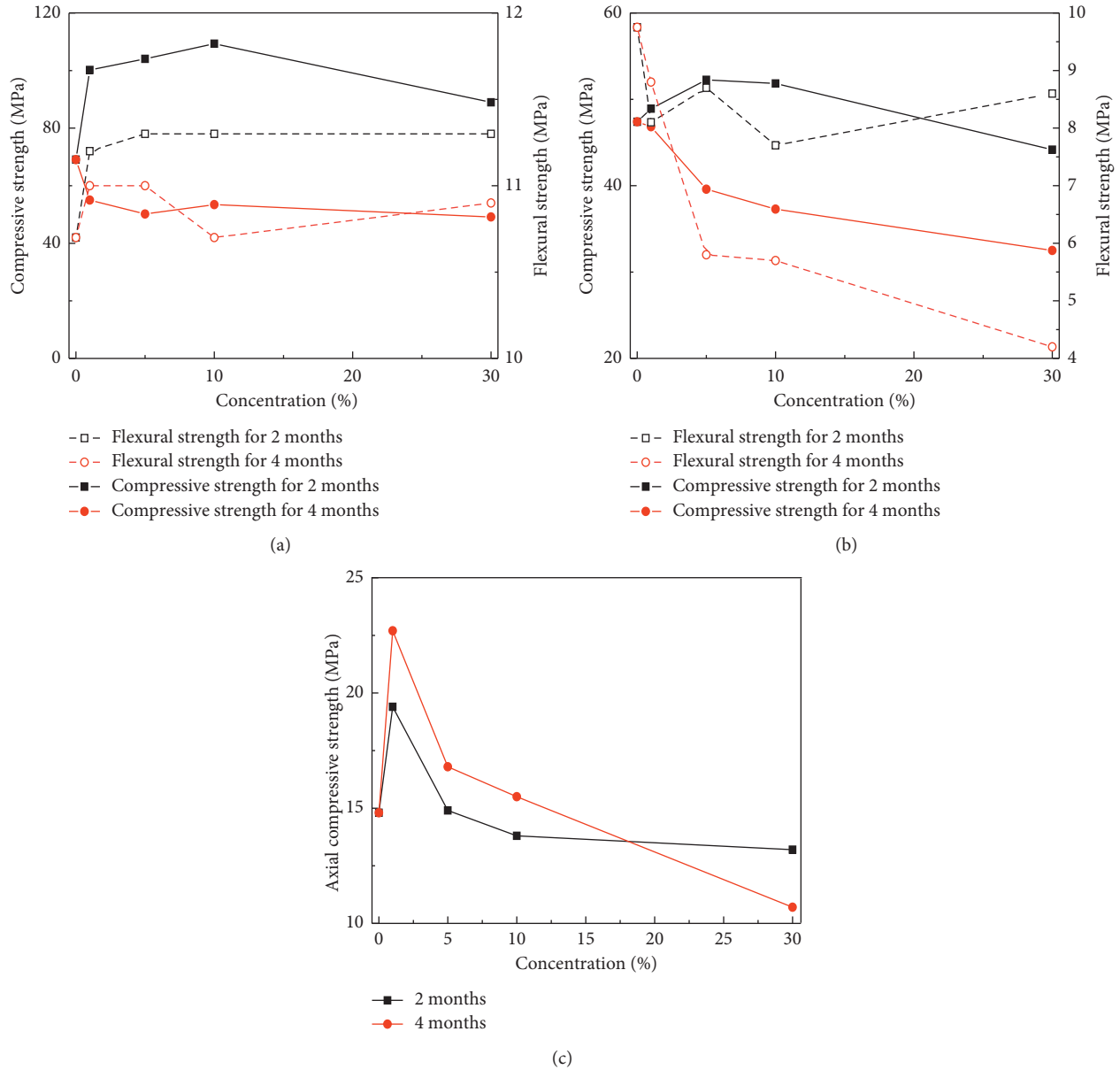
FIGURE 8: Mechanical properties of different specimens attacked by sulfate solution. (a) Paste. (b) Mortar. (c) Concrete.

hydration products resulting from the more usage of cementitious minerals per unit volume. The longer the erosion age, the more the sulfate ion intruding into specimens. More expansive substances are formed and reacted with CH, which results in the micro damage and decrease of pH value of the system. With increasing erosion time, more and more hydration products are decomposed. Therefore, the sulfate attack has a negative effect on performance of the specimens. Macroscopically, it is manifested as the decrease of strength of various specimens.

5. Conclusions

(1) The relationship between the temperature and the Gibbs free energy of the erosion products generated during the sulfate attack was deduced. Theoretical

orientation of sulfate attack on concrete was determined, and the critical sulfate ion concentration and forming conditions of erosion products were determined. The results show that the generation of the erosion products in cement concrete is related to temperature, relative humidity, and sulfate ion concentration, which affect each other. The dihydrate gypsum is preferentially generated when the temperature is less than 42°C and $[SO_4^{2-}]$ concentration is more than 2.3×10^{-3} mol/L. However, the corresponding formation $[SO_4^{2-}]$ concentration and temperature of anhydrite are more than 4.2×10^{-3} mol/L and 42°C, respectively. The theoretical thermodynamic stable temperature of AFt is about 97°C, and the critical $[SO_4^{2-}]$ concentration of AFt dominated significantly by temperature is no less

than 2.8×10^{-3} mol/L. The mirabilite and thenardite may be generated when the concentration of sulfate ion is more than 1.5×10^{-3} mol/L. The mirabilite can be spontaneously crystallized when the temperature is less than 32.4°C. Moreover, the theoretical thermodynamic stable temperature for thaumasite is less than 44°C, and the corresponding critical $[SO_4^{2-}]$ concentration is more than 0.0023 mol/L. Therefore, there is a significant difference in the theoretical temperature from that reported by existing documents.

(2) The phase composition, microstructure, crystal form, and morphology of erosion products of cement before and after sulfate attack were investigated by ESEM-EDS and XRD. The mechanism of sulfate attack on cement and concrete was investigated based on principles of chemical thermodynamics. The major erosion product of cement attacked by low concentration sulfate solution is rod-like AFt with a larger diameter-length ratio generated in the system, but plate-like dihydrate gypsum and granular sulfate salt are the major products when the concentration of sulfate solution is more than 10%. Moreover, there exist the residual skeletons of C-S-H or CH. The XRD spectra show that the phase composition, intensity, and width of diffraction peaks of erosion products in cement are changed before and after sulfate attack. The diffraction peaks' intensity of the AFt and dehydrate gypsum increases, but the corresponding diffraction peaks' intensity of the CH, C-S-H, and C-A-H decreases and even disappears. The sulfate solution concentration and erosion age have significant effects on the mechanical properties of the specimens. Although the compressive strength of the paste and mortar attacked by sulfate for 4 months decreases with the increase of sulfate solution concentration, the corresponding compressive strength of the concrete first increases and then decreases. This is due to the double effects, i.e., positive and negative effects, of the sulfate attack on performance of the specimens.

Data Availability

The data used to support the findings of this study are available from the corresponding author upon request.

Conflicts of Interest

The authors declare that they have no conflicts of interest.

Acknowledgments

References

[1] A. Neville, "The confused world of sulfate attack on concrete," *Cement and Concrete Research*, vol. 34, no. 8, pp. 1275–1296, 2004.

[2] M. Yao and J. Li, "Effect of the degradation of concrete friction piles exposed to external sulfate attack on the pile bearing capacity," *Ocean Engineering*, vol. 173, pp. 599–607, 2019.

[3] S. F. Etris, Y. R. Fiorni, and K. C. Lieb, "A new test for sulfate resistance of cements," *Journal of Testing and Evaluation*, vol. 2, no. 6, pp. 510–515, 1974.

[4] R. Dhole, M. D. A. Thomas, K. J. Folliard, and T. Drimalas, "Chemical and physical sulfate attack on fly ash concrete mixtures," *ACI Materials Journal*, vol. 116, no. 4, pp. 31–42, 2019.

[5] M. Santhanam, M. D. Cohen, and J. Olek, "Mechanism of sulfate attack: a fresh look: part 2. proposed mechanisms," *Cement and Concrete Research*, vol. 32, no. 6, pp. 915–921, 2003.

[6] O. S. B. Al–Amoudi, "Attack on plain and blended cements exposed to aggressive sulfate environments," *Cement and Concrete Composites*, vol. 24, no. 3, pp. 305–316, 2002.

[7] L. Pel, H. Huinink, K. Kopinga, R. P. J. van Hees, and O. C. G. Adan, "Efflorescence pathway diagram: understanding salt weathering," *Construction and Building Materials*, vol. 18, no. 5, pp. 309–313, 2004.

[8] E. Álvarez-Ayuso and H. W. Nugteren, "Synthesis of ettringite: a way to deal with the acid wastewaters of aluminium anodising industry," *Water Research*, vol. 39, no. 1, pp. 65–72, 2005.

[9] L. Jiang, D. Niu, L. Yuan, and Q. Fei, "Durability of concrete under sulfate attack exposed to freeze-thaw cycles," *Cold Regions Science and Technology*, vol. 112, pp. 112–117, 2015.

[10] S. Valencia, G. William, A. D. Eugenia, and G. R. Mejia de, "Fly ash slag geopolymer concrete: resistance to sodium and magnesium sulfate attack," *Journal of Materials in Civil Engineering*, vol. 28, no. 12, Article ID 04016148, 2016.

[11] N. C. Axel, R. J. Torben, and C. Jonathan, "Formation of ettringite, $Ca_6Al_2(SO_4)_3$ $(OH)_{12} \cdot 26H_2O$, AFt and mono-sulfate, $Ca_4Al_2O_6(SO_4) \cdot 14H_2O$, AFm–14, in hydrothermal hydration of Portland cement and of calcium aluminum oxide–calcium sulfate dihydrate mixtures studied by in situ synchrotron X–ray powder diffraction," *Journal of Solid State Chemistry*, vol. 177, pp. 1944–1951, 2004.

[12] C. D. Lawrence, "Mortar expansions due to delayed ettringite formation. Effects of curing period and temperature," *Cement and Concrete Research*, vol. 25, no. 4, pp. 903–914, 1995.

[13] R. H. Michael, K. B. Steven, and B. Ronald, "The evolution of structural changes in ettringite during thermal decomposition," *Journal of Solid State Chemistry*, vol. 179, no. 4, pp. 1259–1272, 2006.

[14] E. E. Hekal, E. Kishar, and H. Mostafa, "Magnesium sulfate attack on hardened blended cement pastes under different circumstances," *Cement and Concrete Research*, vol. 32, no. 9, pp. 1421–1427, 2002.

[15] H. A. F. Dehwah, "Effect of sulfate concentration and associated cation type on concrete deterioration and

morphological changes in cement hydrates," *Construction and Building Materials*, vol. 21, no. 1, pp. 29–39, 2007.

[16] P. W. Brown, "Thaumasite formation and other forms of sulfate attack," *Cement and Concrete Composites*, vol. 24, no. 3-4, pp. 301–303, 2002.

[17] T. Liu, S. Qin, D. Zou, and W. Song, "Experimental investigation on the durability performances of concrete using cathode ray tube glass as fine aggregate under chloride ion penetration or sulfate attack," *Construction and Building Materials*, vol. 163, pp. 634–642, 2018.

[18] I. Biczok, *Concrete Corrosion and Concrete Protection*, Chemical Publishing, Palm Springs, CA, USA, 1967.

[19] F. Bellmann, B. Möser, and J. Stark, "Influence of sulfate solution concentration on the formation of gypsum in sulfate resistance test specimen," *Cement and Concrete Research*, vol. 36, no. 2, pp. 358–363, 2006.

[20] Z. Zhang, X. Jin, and W. Luo, "Long-term behaviors of concrete under low-concentration sulfate attack subjected to natural variation of environmental climate conditions," *Cement and Concrete Research*, vol. 116, pp. 217–230, 2019.

[21] X. Yu, Y. Zhu, Y. Liao, and D. Chen, "Study of the evolution of properties of mortar under sulfate attack at different concentrations," *Advances in Cement Research*, vol. 28, no. 10, pp. 617–629, 2016.

[22] M. Santhanam, "Effect of solution concentration on the attack of concrete by combined sulphate and chloride solutions," *European Journal of Environmental and Civil Engineering*, vol. 15, no. 7, pp. 1003–1015, 2011.

[23] P. B. Xie, "Mechanism of sulfate expansion II: vali DTA ion of thermodynamie theory," *Cement and Concrete Research*, vol. 22, no. 5, pp. 845–854, 1992.

[24] M. T. Blanco-Varela, J. Aguilera, and S. Martínez-Ramírez, "Effect of cement C3A content, temperature and storage medium on thaumasite formation in carbonated mortars," *Cement and Concrete Research*, vol. 36, no. 4, pp. 707–715, 2006.

[25] S. A. Hartshorn, J. H. Sharp, and R. N. Swamy, "The thaumasite form of sulfate attack in Portland-limestone cement mortars stored in magnesium sulfate solution," *Cement and Concrete Composites*, vol. 24, no. 3-4, pp. 351–359, 2002.

[26] P. Brown, R. D. Hooton, and B. Clark, "Microstructural changes in concretes with sulfate exposure," *Cement and Concrete Composites*, vol. 26, no. 8, pp. 993–999, 2004.

[27] X. C. Fu, W. X. Shenm, T. Y. Yao, and W. H. Hou, *Physical Chemistry*, Higher Education Press, Beijing, China, 2009.

[28] D. L. Ye, *Shi Yong Wu Ji Wu Re Li Xu Shu Ju Shou Ce*, Metallurgical Industry Press, Beijing, China, 2002.

[29] D. Freyer, S. Fischer, K. Kohnke, and W. Voigt, "Formation of double salt hydrates I. Hydration of quenched $Na_2SO_4\_CaSO_4$ phases," *Solid State Ionics*, vol. 96, no. 1-2, pp. 29–33, 1997.

[30] G. W. Scherer, "Crystallization in pores," *Cement and Concrete Research*, vol. 29, no. 8, pp. 1347–1358, 1999.

[31] G. W. Scherer, "Stress from crystallization of salt," *Cement and Concrete Research*, vol. 34, no. 9, pp. 1613–1624, 2004.

[32] S. Jan, M. Jacques, and O. Ivan, *Sulfate Attack on Concrete*, Spon press, London, UK, 2002.

[33] J. Skalny, J. Marchand, and I. Odler, *Sulfate Attack on Concrete*, Spon Press, London, UK, 2002.

[34] J. R. Clifton and J. M. Pommersheim, *Sulfate Attack of Cementitious Materials: Volumetric Relations and Expansions (NISTIR 5390)*, NIST, Gaithersburg, MA, USA, 1994.

[35] Z. D. Niu, F. Q. Cheng, C. B. Li, and X. Chen, *Shui Yan Ti Xi Xiang Tu Ji Qi Ying Yong*, Tianjin University Press, Tianjin, China, 2002.

[36] Thermoddem, http://thermoddem.brgm.fr/2019.

[37] GB175–2007, *Common Portland Cement*, China Standards Press, Beijing, China, 2008, in Chinese.

[38] GB/T 1346–2011, *Test Methods for Water Requirement of Normal Consistency, Setting Time and Soundness of the Portland Cement*, China Standards Press, Beijing, China, 2012, in Chinese.

[39] GB/T 17671–1999, *Method of Testing Cements–Determination of Strength*, China Standards Press, Beijing, China, 1999, in Chinese.

[40] GB/T 50081–2002, *Standard for Test Method of Mechanical Properties on Ordinary Concrete*, China Architecture & Building Press, Beijing, China, 2014, in Chinese.

[41] S. B. Wang, S. X. Ji, Y. J. Liu, and K. Y. Hu, "Effect of alkali on expansion of sulfoaluminate cement," *Journal of the Chinese Ceramic Society*, vol. 14, no. 3, pp. 31–38, 1986.

[42] Y. H. Li, S. Y. Gao, P. S. Song, and S. P. Xia, "Effect of Pitzer mixing parameters on the solubility prediction of the phae system $HCl–NaCl–H_2O$," *Acta Physico-Chimica Sinica*, vol. 17, no. 1, pp. 91–94, 2001.

[43] J. G. Xue, "On the expansion associated with etringite formation," *Journal of the Chinese Ceramic Society*, vol. 2, pp. 252–256, 1984.

[44] J. F. Robert, "Salt damage in porous materials: how high supersaturations are generated," *Journal of Crystal Growth*, vol. 242, no. 3, pp. 435–454, 2002.

[45] N. Tsui, R. J. Flatt, and G. W. Scherer, "Crystallization damage by sodium sulfate," *Journal of Cultural Heritage*, vol. 4, no. 2, pp. 109–115, 2003.

[46] CCES 01–2004, *Guide to Durability Design and Construction of Concrete Structures*, China Architecture & Building Press, Beijing, China, 2005, in Chinese.

[47] GB 50212–1991, *Specification for Construction and Acceptance of Anticorrosive Engineering of Buildings*, China plan publishing house, Beijing, China, 2002, in Chinese.

[48] K. P. Mehta, P. K. Mehta, and P. J. M. Monteiro, *Concrete Structure, Properties and Materials*, Tongji Press, Shanghai, China, 1991.

[49] Y. Gu, R.-P. Martin, O. Omikrine Metalssi, T. Fen-Chong, and P. Dangla, "Pore size analyses of cement paste exposed to external sulfate attack and delayed ettringite formation," *Cement and Concrete Research*, vol. 123, p. 105766, 2019.

[50] I. Tai, H. P. C. Sergio, and S. Ignacio, "The role of porosity in external sulphate attack," *Cement and Concrete Composites*, vol. 97, pp. 1–12, 2019.

Research Article

Structural Redundancy Assessment of Adjacent Precast Concrete Box-Beam Bridges in Service

Yanling Leng [ID],[1] **Jinquan Zhang,**[2] **Ruinian Jiang** [ID],[3] **and Yangjian Xiao**[2]

[1]*Senior Bridge Engineer, Clark Engineering Corp., Huron, USA*
[2]*Chongqing Jiaotong University, Chongqing, China*
[3]*New Mexico State University, Las Cruces, USA*

Correspondence should be addressed to Ruinian Jiang; rjiang@nmsu.edu

Present approaches for assessing bridge redundancy are mainly based on nonlinear finite element (FE) analysis. Unfortunately, the real behavior of bridges in the nonlinear range is difficult to evaluate and a sound basis for the nonlinear FE analysis is not available. In addition, a nonlinear FE analysis is not feasible for practitioners to use. To tackle this problem, a new simplified approach based on linear FE analysis and field load testing is introduced in this paper to address the particular structural feature and topology of adjacent precast concrete box-beam bridges for the assessment of structural redundancy. The approach was first experimentally analyzed on a model bridge and then validated by a case study. The approach agrees well with the existing recognized method while reducing the computation complexity and improving the reliability. The analysis reveals that the level of redundancy of the bridge in the case study does not meet the recommended standard, indicating that the system factor recommended by the current bridge evaluation code for this bridge is inappropriate if considering the field condition. Further research on the redundancy level of this type of bridges is consequently recommended.

1. Introduction

Adjacent precast concrete box-beam bridges have been a popular solution for small and medium span bridges worldwide. The bridges are built by placing precast concrete box-beams side-by-side in parallel, which are then connected laterally by shear keys (hinge joints) longitudinally grouted in between the beams and covered with a concrete deck. The shear keys and the concrete deck provide the transverse connection between the concrete box beams. Tie rods or transverse posttensioning strands are sometimes used to further strengthen the transverse connection.

The system performance of adjacent precast concrete box-beam bridges is presently reflected by the design lateral load distribution factors (LLDFs), which are determined based on the assumption that the points of contact in two adjacent beams deform equally [1]. This assumption does not reflect the actual joint condition between adjacent beams when there are cracks in the joints. In the present design

practice, shear keys are relatively weaker compared to the beams and cracking and deterioration of shear keys are prevalent [2]. The prior experimental investigations conducted by the authors revealed that the cracking of shear keys significantly change their functional capability, which causes the load redistribution among beams [3, 4]. Analyses on catastrophic collapse of some adjacent precast concrete box-beam bridges also indicated the fact that the shear keys between the adjacent beams were insufficiently designed [5]. Thus, the redundancy level of adjacent precast concrete box-beam bridges in service should be evaluated according to the actual conditions of the shear keys and box beams, and the current safety evaluation procedure for this type of bridges should be revisited.

Redundancy is defined as the ability of a bridge to continue to safely carry some level of load in a damaged state [6]. Some bridge codes have considered structural redundancy of bridges in the design and evaluation procedures. For example, redundancy factors have been adopted in the

LRFD Highway Bridge Design Specification by the American Association of State Highway and Transportation Officials [6], and system factors have been defined in the AASHTO Manual of Bridge Evaluation [7]. However, the determination of redundancy factors or system factors mainly relies on engineering judgment due to lack of practical guidance. The main difficulty in the computation of bridge redundancy lies in the estimation of the ultimate loading capacity of the bridge, which is presently evaluated through a nonlinear finite element (FE) analysis. Normally, pushdown analysis is used to facilitate a complete analysis of collapse sequences in structures. The loading will be increased in a stepwise iterative manner with successive elements reaching their mean capacities till the structure fails or collapses.

On the basis of this principle, Ghosn and his colleagues [8, 9] developed a framework to quantify redundancy and robustness for highway bridges. The redundancy ratios R_u, R_f, and R_d are defined, respectively, as the ratios of (1) the force causing the failure of the system (LF_u), (2) the force causing a considerable deflection of a main member, and (3) the force causing the failure of a damaged bridge system, to the force causing the failure of any member (LF_1). A bridge system is considered redundant if the redundancy ratios, computed according to equations (1) through (3), satisfy the following conditions: $R_u \geq 1.30$; $R_f \geq 1.10$; and $R_d \geq 0.50$.

$$R_u = \frac{LF_u}{LF_1}, \tag{1}$$

$$R_f = \frac{LF_f}{LF_1}, \tag{2}$$

$$R_d = \frac{LF_d}{LF_1}. \tag{3}$$

This methodology has been generally recognized; however, it is impractical for practitioners to conduct a nonlinear FE analysis; in addition, the nonlinear FE analysis results cannot be verified without the knowledge of the bridge behavior in the nonlinear range. Field load testing, including diagnostic load testing and proof load testing, can only capture the linear response of in-service bridges at specific load levels. As shown in Figure 1, the diagnostic test load defined in a diagnostic test and the target proof load specified in a proof load test are both smaller than the elastic load limit of the bridge; nonlinear behavior is not tested because of the safety considerations.

This paper summarizes the test results on a model adjacent precast concrete box-beam bridge. A parameter sensitivity study was performed to identify factors that have most influence on the loading capacity of the bridge system. It was found that the three most sensitive parameters are all associated with the properties of shear keys, indicating that the behavior of shear keys plays a dominant role in the performance of adjacent precast concrete box-beam bridges. A method is proposed accordingly based on a linear FE analysis and field deflection measurement, which is able to address the particular structural feature and topology of adjacent precast concrete box-beam bridges. The method
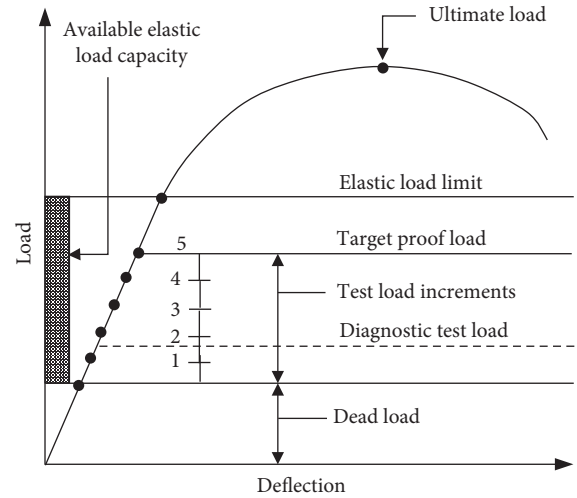
FIGURE 1: Hypothetical load-deflection response of a bridge [10].

was analyzed theoretically based on the experiment results and validated by a case study on a bridge in service. The results obtained with the new approach agree well with those obtained by using the recognized method proposed by Ghosn and his colleagues. The computing complexity is reduced in the proposed method, which makes it suitable for the practitioners to use. It is verified that the level of redundancy of the bridge in the case study does not meet the recommended code standard.

2. Experimental Investigation on Lateral Load Distribution among Beams

A model adjacent precast reinforced concrete box-beam bridge was tested in the full load range.

The model bridge used China's standard drawing of a 10-meter prefabricated prestressed concrete hollow core slab beam as a prototype [11], which consists of eight slab beams, each 1-meter wide. The scale of the model bridge is 1 : 2, that is, the span was reduced to five meters. The shape and sizes of the cross section of the test beams and joints were determined so that the moment and shear stresses remained unchanged from the original beams. A comparison of the cross sections of the original and model beams is presented in Figure 2. As principal transverse connectors, shear keys play a critical role in the integrity of the bridge. The pavement is composed of a concrete deck and a wearing course on top of it. The deck also helps distribute loads transversely. Both the prototype and model bridges used shallow shear keys without transverse prestressing rods, which were the prevalent precast adjacent box-beam bridges built in or before the 1990s. These bridges were built according to the old design standards and construction techniques, which are lower than their counterparts employed nowadays; as a result, these bridges are more vulnerable and have a higher demand for safety evaluation. In addition, visual inspection of grouted shallow shear keys is difficult while the bridges are in service because of the compact shallow shear key configuration; the poor
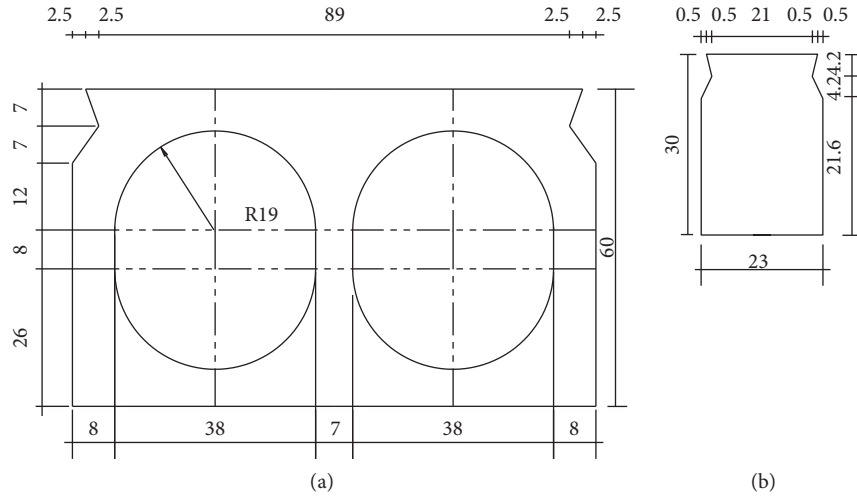
FIGURE 2: Cross sections of the adjacent beams: (a) the prototype; (b) test model (unit: cm).

inspection accessibility increases the risk of not discovering severe damages in time.

Loading at the midspan on the edge beam was found to be the most critical, and two loading cases at this location were studied to evaluate the change of the lateral load distribution among the beams of the model bridge that consisted of eight identical beams.

2.1. Loading Case 1. The load was limited in the elastic range, and the load distribution among beams with various shear key crack lengths was investigated. A concentrated load was applied at the midspan of the edge beam (#1) with different crack lengths of the edge shear key (#1, i.e., between beams 1 and 2), as shown in Figure 3. The corresponding lateral load distribution factors (LLDFs) of beam #1 of the bridge were calculated and are illustrated in Figure 4. The LLDF was calculated using the deflection of the beams because the load is proportional to the deflection if it is in the elastic range and the beams are identical. The results show that beam #1 received 29% of the total load with a joint crack length of $0.1L$ (L is the span length of the beam); the load share increased to 87% when the crack length reached $0.8L$. This finding reveals that the cracking of the edge shear key significantly changes the lateral load distribution among beams and thus changes the system behavior of the bridge.

2.2. Loading Case 2. A stepwise concentrated load was applied at the middle span of beam #1. The load was increased until beam #1 yielded (when the loading cell unloaded automatically as triggered by a sudden increase of deflection, hereinafter referred to as load case 2-1). Beam #1 was again loaded until the bridge failed with large deflection (referred to as load case 2-2). The deflection distribution factor of beam #1 in loading case 2 was calculated and is shown in Figure 5. Note that the deflection gages were set to zero before each loading case.

Because load is not proportional to deflection beyond the elastic range, LLDF becomes unstable and the deflection
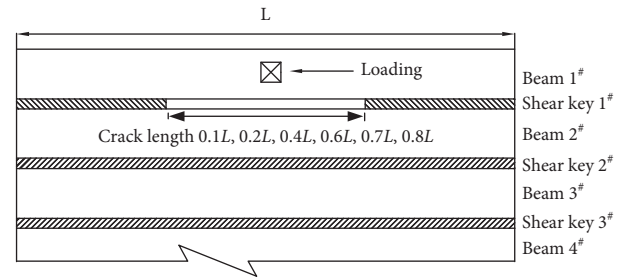
FIGURE 3: Loading scheme of the model bridge with edge shear key (#1) cracks.
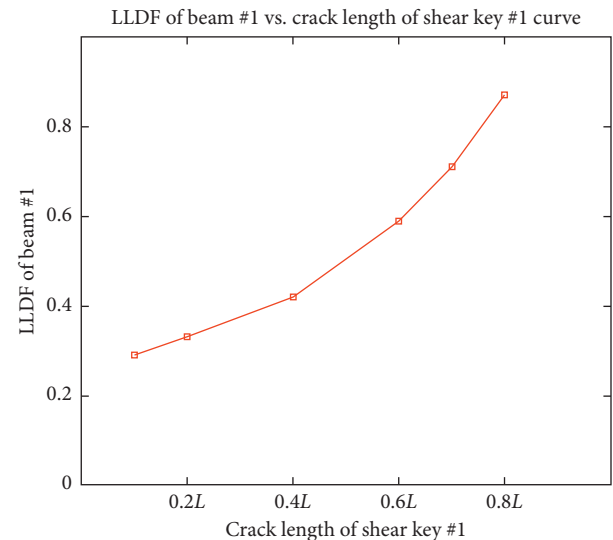
FIGURE 4: The LLDF of beam #1 corresponding to different crack lengths of shear key #1.

distribution factor is used instead of LLDF for the system behavior analysis of the bridge. The deflection distribution factor (DDF) of the ith beam is calculated according to the following equation:
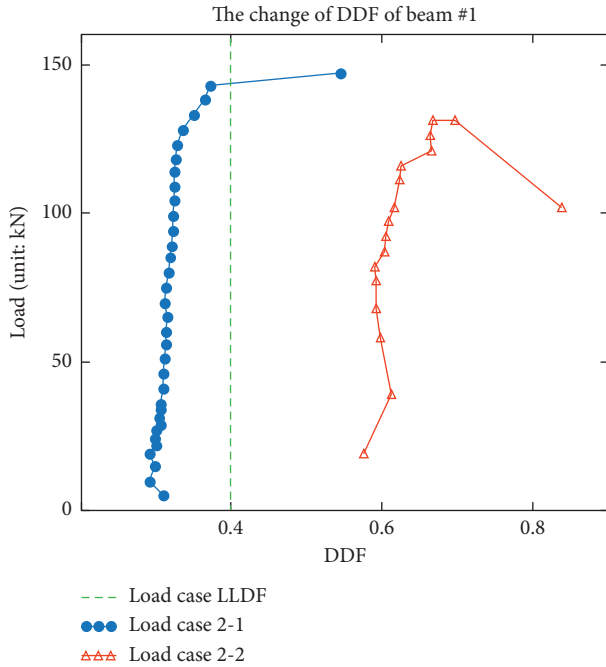
Figure 5: Change of the deflection distribution factor of beam #1 with load.

$$\mathrm{DDF}_i = \frac{\omega_i}{\sum_1^n \omega_i}, \tag{4}$$

where ω_i = deflection of the ith beam under a vertical load obtained through a load test or simulation.

The change of DDF among beams is closely related to the redundancy of adjacent precast concrete box-beam bridges. As shown in Figure 5, beam #1 was first in the linear range with a DDF of about 0.30 in load case 2-1. The DDF increased slowly to about 0.37 when the load on beam #1 reached 143 kN and then jumped to 0.54 when the edge shear key severely cracked and beam #1 yielded. When the beam was reloaded in load case 2-2, the DDF of beam #1 was about 0.57. It soon increased to and stayed at about 0.6 until the load reached 92 kN, increased to 0.7 at 131 kN, then increased quickly to 0.84 when the beam collapsed, and then the load dropped to 102 kN. A linear response was observed over the major portion of the load range. The change of DDF also reflects the condition deterioration of the shear keys. The design LLDF of beam #1 is 0.40 (displayed as the reference line in Figure 5). The DDF (equal to LLDF in the elastic range) of beam #1 was under 0.4 before shear key #1 lost its function, which verifies that the design LLDF of 0.4 is reasonable. When evaluating bridges in service, however, the change of DDF must be considered according to the condition of the shear keys.

3. Parameter Sensitivity Study on the Ultimate Loading Capacity of Adjacent Precast Concrete Box-Beam Bridges

A parameter sensitivity study was conducted to identify which structural parameters have significant effects on the loading capacity of the adjacent precast concrete beam

model bridge. As observed in the field investigation and laboratory tests, the failure mode of the shear keys is the delamination and slip at the interaction surfaces of adjoining shear keys and beams [5]. Delamination cracking is an out-of-plane damage model (normally involving both opening and sliding delamination crack displacement), and the evolution is indicated by the interlaminar stresses. The shear bond strength at the interface between the beam concrete and shear key concrete highly depends on the roughness of the contact interface, the bonding material applied, and the contour of the contact surface. Thus, a surface-based cohesive behavior is employed in this study. And the cohesive strength, cohesive stiffness, and plastic displacement of shear keys were considered selected in the sensitivity study. In addition, the yield strength of main reinforcement and the total area of main reinforcement usually dominate the load capacity of concrete beams. For the above consideration, the following five independent variables were considered in the sensitivity study: the cohesive strength of shear keys (C_s), the cohesive stiffness (K) of shear keys, the plastic displacement (d_p) of shear keys, the yield strength of main reinforcement (f_y), and the total area of main reinforcement bars (A_s).

The statistical parameters of variables C_s, K, and d_p were considered to follow a normal distribution, and the coefficient of variance (COV) was taken as 0.15 according to previous studies, comparable to the COV used for the variables for load distribution because all the three variables contribute to the load distribution of the beams [12]. When no reinforcement crossing the interface is provided, the cohesive strength of shear key, C_s, is approximatively equal to the product of the design strength of the shear key concrete and design coefficient of cohesion, where in the absence of detailed information and for nonuniform interface surfaces, design coefficient of cohesion is 0.5 [13]. The design tensile strength of the shear key concrete (C20) is 1.54 MPa. Thus, $C_s = 0.77$ MPa. The cohesive stiffness of shear key, K, was estimated by dividing the maximum cohesive stress by corresponding separation, which was obtained in the laboratory load tests. d_p is the depth of shear key concrete. The statistical parameters of f_y and A_s were taken from the values recommended by Chinese bridge design standards [14]. The statistical parameters are summarized in Table 1.

The marginal effect of each variable on the loading capacity of the bridge was investigated using a 3D nonlinear finite element analysis with the Abaqus/CAE 6.14 software package, which was calibrated using the experiment results of the model bridge. A concrete damaged plasticity (CPD) model was employed to define the plastic properties of concrete. The stress-strain curve of the reinforcement bar was assumed to be perfectly elastic-plastic. The loading capacity of the bridge was determined when the tensile strain of the reinforcement reached 0.002. A total of 9 points were considered for each variable, including μ, $\mu \pm \sigma$, $\mu \pm 1.5\sigma$, $\mu \pm 2\sigma$, and $\mu \pm 3\sigma$, where μ and σ are the mean value and standard deviation of the variable, respectively. All other variables were held constant when one variable was evaluated. The marginal effect of the variables is graphed in Figure 6. It is shown that in the range of three sigma, the

TABLE 1: Statistical parameters of each variable.

Variable	Distribution type	Mean value, μ	COV
C_s	Normal	0.77 MPa	0.15
K	Normal	3 MPa/mm	0.15
d_p	Normal	0.0008 m	0.15
A_s	Normal	201.1 mm^2	0.035
f_y	Normal	380 MPa	0.068
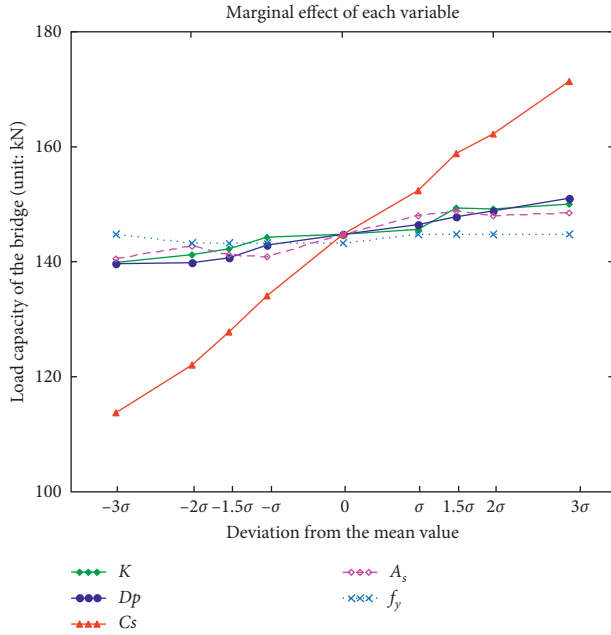
FIGURE 6: Marginal effect of the variables on the load-carrying capacity of the bridge.

slope coefficients (equivalent to the overall marginal effects) of C_s, d_p, and K_c were slightly greater than the other two. Thus, the sensitivity follows the order $C_s > d_p > K_c > A_s > f_y$. The three most sensitive parameters on the loading capacity of the bridge are all associated with the properties of the shear keys. This verifies the observation that cracking and deterioration of shear keys significantly affect the system capacity of the bridge. Compared to the property change of shear keys, the residual strength (embodied in A_s and f_y) of the beam has less influence on the loading capacity of the bridge. Besides, the failure of a shear key (shear failure) is brittle. Based on the above analysis, it is concluded that the nonlinear behavior is less significant for the redundancy assessment for adjacent precast concrete box-beam bridges, which agrees with the test results shown in Figure 5.

4. Proposed System Performance Evaluation Method

The load-carrying capacity of an adjacent precast concrete box-beam bridge is presently evaluated by calculating the ultimate section capacity of an individual beam and the load distribution factors among the beams of the bridge. The system capacity of a bridge is evaluated according to

redundancy at two levels: the system and component level, as demonstrated in Figure 7. The load redistribution capacity among beams is considered the system-level redundancy. The reserve strength over the design capacity of a component is considered the component-level redundancy, which permits local yielding and redistribution of component internal forces (especially in most heavily loaded members). Studying both the system-level and component-level redundancy provides a full understanding of the system mechanism in a multibeam bridge system.

The redundancy factors are calculated as

$$RF = RF_{comp} \times RF_{sys}, \tag{5}$$

$$RF_{comp} = \frac{R_{real}}{R_{design}}, \tag{6}$$

$$RF_{sys} = \frac{LLDF_{design}}{DDF_{real}}, \tag{7}$$

where R_{real} is the actual resistance of an individual beam obtained from simulation or load testing, R_{design} is the unfactored design resistance of the beam, DDF_{real} is the measured DDF, which can be obtained by linear simulation or diagnostic load test, and $LLDF_{design}$ is determined according to bridge codes, which is equal to the design DDF in the elastic range.

For concrete beams, RF_{comp} is normally higher than 1.0 and can be neglected. The system-level redundancy can be evaluated by the ratio of the design LLDF (or DDF) to measured DDF. The LLDF and DDF are equal for bridges in service, which are generally in the elastic range. The design load distribution factor can be calculated with the method provided in a design code or through a linear analysis. The measured DDF is computed using equation (1), and the data used in equation (1) can be obtained through a field load testing or an FE simulation. The approach is demonstrated in the following case study.

5. Case Study

Beida Bridge was built in 1999 that crosses the Tuman river in Kashi city, Xinjiang Uygur Autonomous Region, China. The bridge has three simply supported prestressed concrete spans, as shown in Figure 8. For each half of the bridge, six adjacent precast prestressed concrete box beams are used for the sidewalk and bike lane and nine adjacent prestressed concrete box beams are used for the driving lane. No as-built drawings were available; thus, efforts were made to determine the geometric information of the bridge. Dimensions of the bridge were measured in the field, and the drawings of bridges of the same structural type on the same route or nearby were checked. It was decided that the standard drawing JT/GQB001-91 was the right one for this bridge. Noted that this bridge used shallow shear keys without any transverse post-tensioning, and concrete pavement on the top was not composite with the beams,
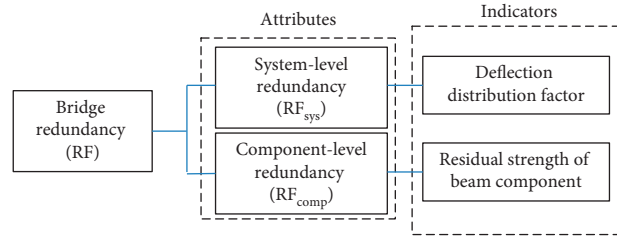
FIGURE 7: Structural redundancy of a multibeam bridge.

(a)

(b)
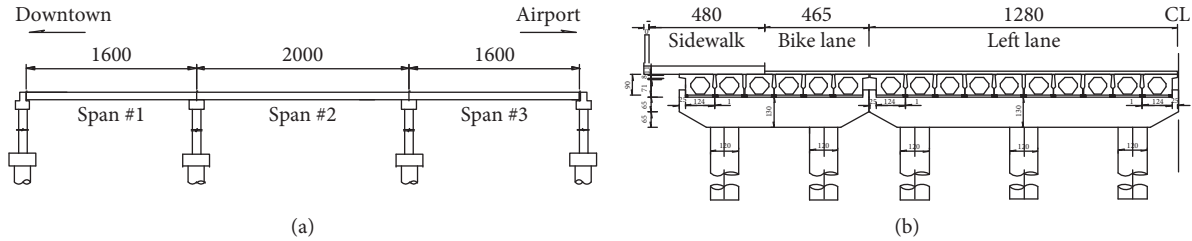
FIGURE 8: Schematic of Beida Bridge (unit: cm). (a) Elevation. (b) Half cross section (left) of the bridge.

which was the prevalent precast adjacent box beam bridges built in or before the 1990s in China.

Field inspection and material examinations were conducted on the bridge. The field inspection revealed that the shear keys of the bridge were in a severe condition, especially on span #3, as shown in Figure 9.

Diagnostic loading tests were conducted on the left lanes of spans #2 and #3, respectively. Since the left lanes of span #3 were in a worse condition, it was the focus of this research. Two load cases were tested: in load case I, the bridge was subjected to a symmetrical loading, and in load case II, the bridge was subjected to an asymmetrical loading. The loading layout is shown in Figure 10. Trucks were moved one meter towards beam #10 (B10 in Figure 10) in load case II based on the basis of load case I. Each load case consisted of four loading steps or subload cases, as summarized in Table 2. For example, LC I-1 denotes placing truck SYC1 at the designated position in the symmetrical load case; LC II-3 denotes placing 3 trucks, SYC1, SYC2, and SYC3, at the designated positions in the asymmetrical load case.

A grillage model was constructed following the approach proposed by Hambly [15] using the structural analysis program Midas Civil 2016, where the bridge system was discretized as longitudinal and transverse beam elements, as shown in Figure 11. Beam elements were used for the box beams, and pavement on the top of the beams were simulated as plates attached to the same nodes as beam elements, but with different offsets. The shear keys (hinge joints) were simulated as virtual transverse beams. A total of 10 longitudinal grillage beams were placed along the centerline of each beam. 16 virtual beams were used to simulate each shear key, and the length of each virtual beam was $L/16$ (L denotes the length of the shear key). The properties of the virtual transverse beams that were deemed to transfer loads between longitudinal beams were determined based on the shear capacity of the shear keys. For instance, the cross

FIGURE 9: Water leakage and corrosion of the shear keys in span #3.

section of the virtual beam was 0.125 m (width) × 0.05 m (depth). The length and location of the virtual beam were adjusted in response to the cracking of the shear key. For instance, if a crack length of $L/16$ was assumed at the midspan, the corresponding portion of the virtual beam would be deleted in the finite element model. The failure of the bridge was defined in terms of the load that leads to the formation of a plastic mechanism in one longitudinal beam. The plastic hinge depth was assumed to be ½ of the depth of the cross section [9]. The maximum plastic hinge rotation determines the critical point at which the prestressed beam fails. For the bridge members, the critical plastic hinge rotation was equal to 0.0402 rad [8]. The convergence criterion was that the tensile strain of rebar reaches 0.002.

The simulation results agree well with the actual deflection obtained from the diagnostic load test, as shown in Figure 12. Load case II-2 was used in the calculation where two trucks were placed side-by-side at the designated positions, which causes the biggest deflection differences between beams and is the most critical load configuration. The load transverse distribution factor of the exterior beam in
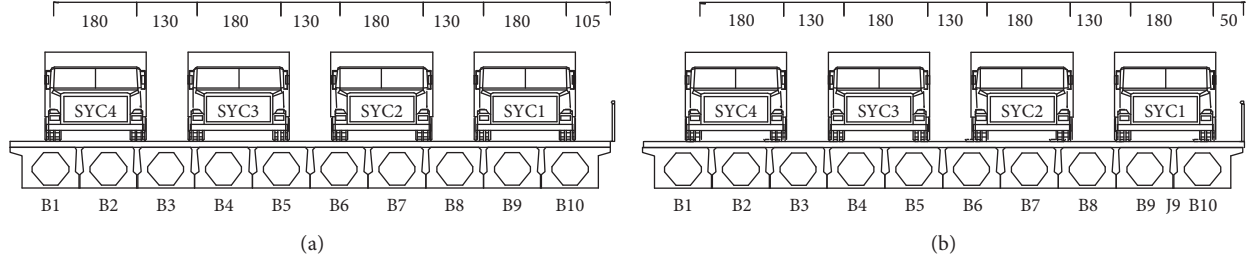
FIGURE 10: Loading layout (unit: cm). (a) Load case I: symmetrical loading. (b) Load case II: asymmetrical loading.

TABLE 2: Loading cases.

Load case	Truck(s) in position (a)	Load case	Truck(s) in position (b)
LC I-1	SYC1	LC II-1	SYC1
LC I-2	SYC1 + SYC2	LC II-2	SYC1 + SYC2
LC I-3	SYC1 + SYC2 + SYC3	LC II-3	SYC1 + SYC2 + SYC3
LC I-4	SYC1 + SYC2 + SYC3 + SYC4	LC II-4	SYC1 + SYC2 + SYC3 + SYC4
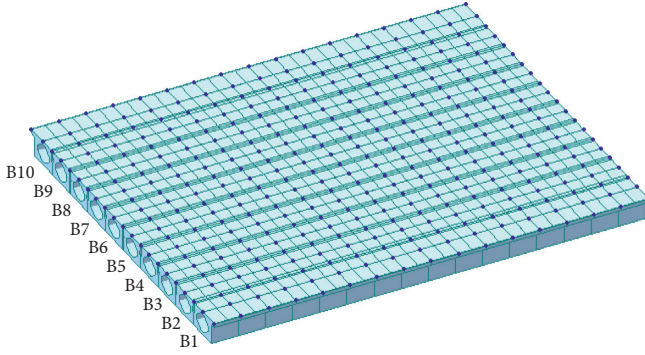
FIGURE 11: Midas Civil grillage model of Beida bridge.

load case II-2 (beam B10) is 0.34, which was used as a reference for assessing the crack length of the exterior shear key that is between beams #9 and #10 (B9 and B10 in Figure 11).

V-20 trucks were used that is a single unit truck with one 60 kN front axle and two 120 kN back axles, as shown in Figure 13.

According to the bridge loading capacity evaluation code [7], the loading capacity of the bridge in terms of the number of V-20 truck pairs (load factor 1) in load case II-2 that would lead to the first beam failure is [8]

$$\mathrm{LF}_1 = \frac{R - D}{\mathrm{DF}_1 \times \mathrm{LL}_{V-20}}, \qquad (8)$$

where R is the beam's unfactored moment capacity, D is the beam's unfactored dead load moment, DF_1 is the elastic lateral distribution load factor of the beam, and LL_{V-20} is the total live load moment effect caused by the two V-20 vehicles. Since the cracking of shear key would considerably affect the lateral distribution of the vehicle load among the beams, the load share $\mathrm{DF}_1 \mathrm{LL}_{V-20}$ (or LF_1) can reflect the condition deterioration of the shear key. Thus, the approximate crack length of the shear key can be deduced if the corresponding LF_1 for specified crack lengths (e.g. tenth

points) was available; this methodology was employed in this study to estimate the cracking length of the exterior shear key of Beida bridge.

For better accuracy, the load share of the beam $\mathrm{DF}_1 \mathrm{LL}_{V-20}$ was obtained from a Midas Civil simulation, rather than using a theoretical load share obtained using a distribution factor. Note that the load and resistance factors were ignored in equation (8) because the intention is to evaluate the load-carrying capacity rather than to provide safety envelops for design and load rating purposes.

The moment capacity of the exterior beam, denoted by R, is equal to 3891 kN-m calculated from the beam cross section configuration. The dead load moment at the midspan of the exterior beam is $D = 605.4$ kN-m from a linear elastic analysis. The share of the moment by the exterior beam from the two side-by-side design trucks is 362.9 kN-m, which is $\mathrm{DF}_1 \mathrm{LL}_{V-20}$ in equation (5). The load factor that leads to first member failure in bending (LF_1) is 9.1, as calculated using equation (8), assuming the bridge is in a good condition and the traditional linear elastic analysis method applies. This result reveals that if one is to follow the traditional bridge analysis method, the first member of the bridge will reach its ultimate capacity at a load equal to 9.1 times the effect of two V-20 trucks placed at the designated locations in load case II-2.

The system performance of the bridge in terms of redundancy was first evaluated using an existing recognized method [8]. A nonlinear pushdown analysis was performed on the bridge assuming that the bridge will behave nonlinearly after damages occur. The analysis was applied with load case II-2 for the intact condition and for different crack lengths of the edge shear key (hinge joint J9). LF_u is designated as the ultimate load capacity of the bridge in terms of the number of V-20 truck pairs in the designated location. According to the nonlinear pushdown analysis, $\mathrm{LF}_u \approx 10$ when the bridge is intact, $\mathrm{LF}_u \approx 9$ when the crack length of the edge shear key is in the range of $L/16$ to $9L/16$, and $\mathrm{LF}_u \approx 8$ when the crack length of the shear key exceeds $11L/16$.

(a)

(b)
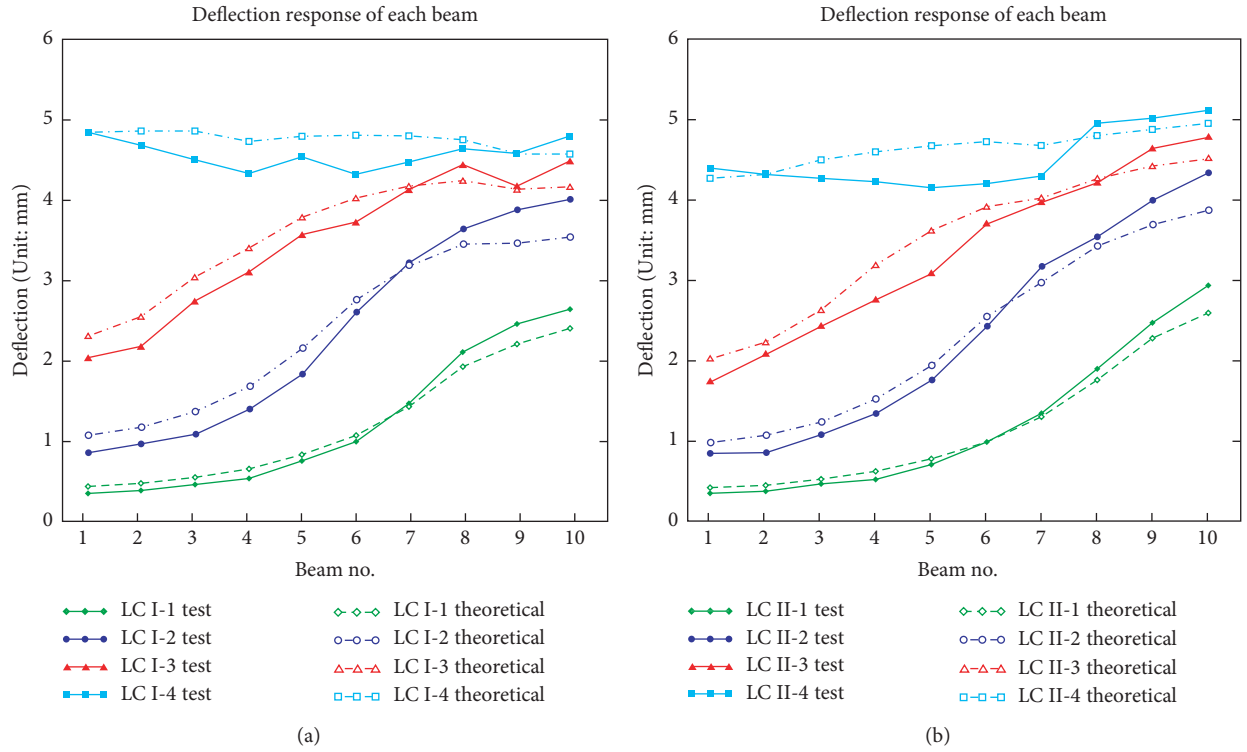
FIGURE 12: Vertical displacement response of beams for each load case. (a) Load case I: symmetrical loading. (b) Load case II: asymmetrical loading.
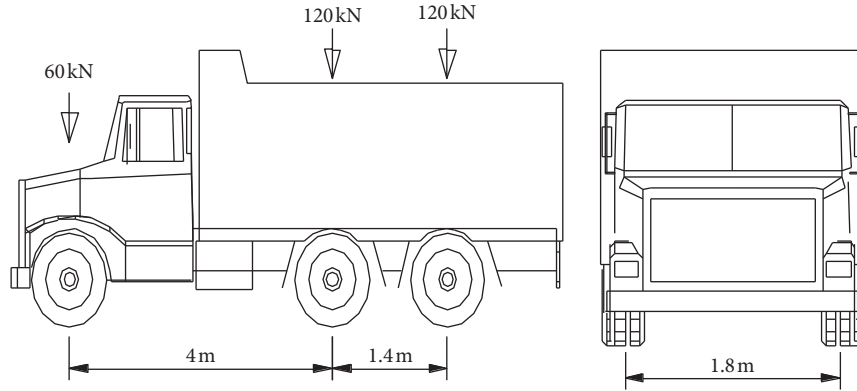
FIGURE 13: V-20 truck load.

The system resistance reserve ratio, R_u, of the bridge with different exterior shear key crack lengths was computed by using the data obtained through simulation and is summarized in Table 3. As an example, $LF_u = 9.01$ when the crack length is $9L/16$, and $R_u = LF_u/LF_1 = 9.01/9.1 = 0.99$ according to Ghosn's approach.

The design load distribution factor for the exterior beam is $1/2\,(0.099 + 0.145 + 0.192 + 0.259) = 0.3475$, according to the design code method, as shown in Figure 14. The field LLDF based on the deflection measurement is 0.345. Because the simulation results show that the LLDF of the exterior beam is 0.345 when the crack length of the exterior shear key is about $9L/16$, the crack length of the exterior shear key was estimated as $9L/16$.

TABLE 3: System reserve ratio, R_u, of the superstructure with different crack lengths of the shear key #9.

Crack length of shear key #9	Ghosn's approach	Proposed approach
0 (intact)	1.10	1.04
$1L/16$	1.01	1.04
$3L/16$	1.01	1.03
$5L/16$	1.00	1.02
$7L/16$	1.00	1.01
$9L/16$	0.99	1.01
$11L/16$	0.90	0.93
$13L/16$	0.87	0.87
$15L/16$	0.79	0.81
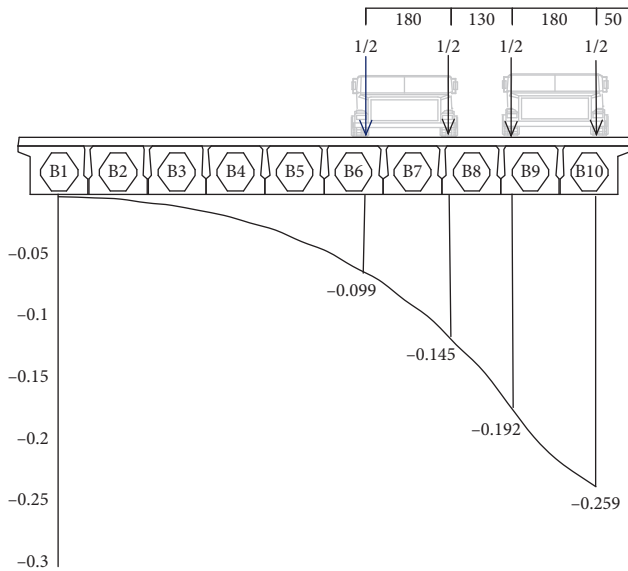
FIGURE 14: The influence line of beam #10 and the layout for computing the LLDF of beam #10 with two trucks at critical positions.

The system reserve factor was then calculated according to the method proposed in this research. For instance, the deflection distribution factor for the exterior beam is 0.345 based on the field deflection measurement when the crack length is $9L/16$; thus, the system-level redundancy $RF_{sys} = 0.3475/0.345 = 1.01$ according to equation (4). According to the field inspection, the beam was observed in good condition, as shown in Figure 9; the longitudinal cracks were basically in the shear keys between the beams. Therefore, the beam was considered having sufficient strength reserve and the component-level redundancy factor can be conservatively assumed as 1.0, that is, $RF_{comp} = 1.0$. Consequently, the system reserve ratio $R = RF_{sys} = 1.01$ according to equation (5).

The system reserve ratios for various joint crack lengths were calculated using the two approaches and are compared in Table 3. It is found that the two approaches agree well with each other. However, the proposed approach can greatly reduce the computation complexity. Also, as mentioned before, the crack length of the edge shear key (J9) of this bridge is $9L/16$, and the system reserve ratio is about 0.99 based on Ghosn's approach and 1.01 based on the proposed method. The recommended minimum system reserve ratios for system ultimate limit state and functionality limit state are 1.30 and 1.10, respectively, according to NCHRP reports 406 and 776. Thus, the redundancy of this bridge is not satisfactory.

6. Summary and Conclusion

A new approach is developed in this research based on a linear finite element analysis and the field deflection measurement to evaluate the system performance of adjacent precast concrete box-beam bridges. The results obtained using the approach agree well with those from a recognized method in the case study. The proposed approach can reduce the computation complexity and is suitable for the practitioners to use. Another advantage of the proposed method over the existing method is that it can be verified through field load testing. The analysis revealed that the level of redundancy of the bridge in the case study does not meet the recommended standard, indicating that the system factor recommended by the bridge evaluation code for this bridge is not appropriate. Further research on the redundancy level of this type of bridges is recommended.

Data Availability

The data used to support the findings of this study are available upon request. Dr. Leng should be contacted to request the data; she can be reached at yllengnmsu@gmail.com.

Conflicts of Interest

The authors declare that they have no conflicts of interest.

References

[1] C. L. Hulsbos, "Lateral distribution of load in multibeam bridges," Highway Research Board Bulletin 339 Transportation Research Board, Washington, DC, USA, 1962.

[2] H. G. Russell, "Adjacent precast concrete box beam bridges: connection details," NCHRP Report Synthesis 393, Transportation Research Board, Washington, DC, USA, 2009.

[3] Y. Leng, J. Zhang, R. Jiang, and H. He, "Experimental research on transverse load distribution of prefabricated hollow slab concrete bridges with shear key cracks," IABSE Symposium Report vol. 99, International Association for Bridge and Structural Engineering, Zürich, Switzerland, 2013.

[4] Y. Leng, J. Zhang, R. Jiang, H. He, and J. Zhou, "Experimental research on strengthening transverse connections of prefabricated concrete hollow core slab beam bridges," in Proceedings of Transportation Research Board 94th Annual Meeting, Washington DC, January 2015.

[5] Y. Leng, "System safety and reliability assessment for adjacent precast concrete box beam bridges," Doctorate dissertation New Mexico State University, Las Cruces, NM, USA, 2017.

[6] AASHTO, AASHTO LRFD Bridge Design Specifications, AASHTO, Washington, DC, USA, 7th edition, 2017.

[7] AASHTO, AASHTO Manual for Bridge Evaluation, AASHTO, Washington, DC, USA, 3rd edition, 2018.

[8] M. Ghosn and F. Moses, "Redundancy in highway bridge superstructures," NCHRP Report No. 406, Transportation Research Board, Washington, DC, USA, 1998.

[9] M. Ghosn and J. Yang, Bridge System Safety and Redundancy, NCHRP Report No. 776, Washington, DC, USA, 2014.

[10] S. G. Pinjarkar, "An overview of current worldwide practices for nondestructive load testing for bridge rating and evaluation," in Proceedings of the 5th Annual International Bridge Conference, Pittsburgh, PA, USA, 1988.

[11] GB/J50283-1999, Unified Standard for Reliability Design of Highway Engineering Structures, China Plan Press, Beijing, China, 1999, in Chinese.

[12] F. Moses and V. Dhirendra, "Load Capacity Evaluation of Existing bridges," NCHRP Report No. 301, Transportation Research Board, Washington, DC, USA, 1987.

[13] M. Pedro and N. Eduardo, "Assessment of the Shear Strength between Concrete layers," in *Proceedings of the 8th Fib Ph.D. Symposium in KGS*, Lyngby, Denmark, June 2010.

[14] GB50010-2010, *Code for Design of Concrete Structures*, China Plan Press, Beijing, China, 2010, in Chinese.

[15] E. C. Hambly, *Bridge Deck Behaviour*, CRC Press, New York, NY, USA, 1991.

Research Article

Equation for the Degradation of Uniaxial Compression Stress of Concrete due to Freeze-Thaw Damage

Xiaolin Yang (ID),[1,2] Genhui Wang (ID),[1] Shiwu Gao (ID),[2] Min Song,[3] and Anqi Wang [2]

[1]*School of Civil Engineering, Lanzhou Jiaotong University, Lanzhou, Gansu 730070, China*
[2]*School of Civil Engineering, Qinghai University, Xining, Qinghai 810016, China*
[3]*Institute of Applied Mechanics, Taiyuan University of Technology, Taiyuan, Shanxi 030024, China*

Correspondence should be addressed to Genhui Wang; 13609341991@139.com

To study the freeze-thaw damage characteristics of concrete, the uniaxial compressive tests of concrete under different number of freeze-thaw cycles were conducted, and the damage variable of freeze-thaw was obtained. The test results showed that the stress was a function of strain and freeze-thaw damage variable, and it can describe the degradation of concrete strength. Meanwhile, the equation for the stress-strain curved surface about strain and freeze-thaw damage variable was also proposed in this paper. The derivative function of the stress-strain curved surface equation with respect to strain presented the change of elastic modulus with the increase of freeze-thaw cycle number. Equation proposed in this paper can be used for predicting the concrete lifetime effectively in cold and large temperature difference regions.

1. Introduction

Due to the cold weather and large temperature difference between day and night in the Qinghai-Tibet Plateau, concrete and prestressed concrete structures are likely to freeze at night and thaw due to solar radiation during the day, operating under frequent freeze-thaw cycles. Freeze-thaw cycling conditions are a primary cause of durability deterioration of concrete structures in the areas with large temperature differences in the Qinghai-Tibet Plateau.

In recent years, many scholars have studied the macroscopic characterization and microscopic mechanism of the mechanical properties of concrete after freeze-thaw cycles. The typical research methods include macroscopic mechanical property and microscopic characterization. Guo [1] summarized and studied the principle of reinforced concrete. He suggested that the compressive stress-strain curve of concrete was a comprehensive and macroscopic response of its mechanical properties and that this relationship was the most basic constitutive relationship in the nonlinear analysis of reinforced concrete structures. Huda and Shahria Alam [2] studied freeze-thaw durability

performance of recycled coarse aggregate concrete in accordance with a national standard, and their experimental results showed that the performance of recycled aggregate concrete (RAC) slightly decreased with increasing RCA replacement levels. However, the overall performance was comparable to natural aggregate concrete. Liu and Wang [3] investigated the stress-strain relationship of fly ash concrete after 0, 5, 15, 30, 50, 75, 100, and 125 freeze-thaw cycles by testing 24 prism-shaped specimens. A damage constitutive model based on the damage mechanics and a multiple sharp degradation point model were presented. The proposed model was proven to be effective for evaluating the stress-strain relationship of fly ash concrete under freeze-thaw cycles. Guo and Weng [4] used relative dynamic elastic modulus tests and scanning electron microscopy (SEM) images to study the durability of airport pavement concrete, and their experimental results indicated that the freeze-thaw durability of the concrete coated with surface treatments improved compared with noncoated concrete, and the modified polyurea exhibited good freeze-thaw resistance. Tian et al. [5] used computed tomography (CT) scans and SEM technology to study the erosion degradation behavior

of concrete due to the combined influence of freeze-thaw cycles and sulfate solutions from a microscopic perspective. It was found that the mass loss of the concrete samples increased initially and then decreased slightly. The uniaxial compressive strength increased first and subsequently decreased. Based on the characteristics of the whole stress-strain curve of concrete undergoing different numbers of freeze-thaw cycles, Guan et al. [6] studied the variables that cause damage and established a damage evolution equation for concrete after freeze-thaw cycling. Wang et al. [7] studied the stress-strain relationship of concrete using an ultralow temperature freeze-thaw environment. The experimental results showed that the peak stress during concrete uniaxial compression decreased with the increase in the number of freeze-thaw cycles for ultralow temperature freeze-thaw cycling, whereas the peak strain increased and the stress-strain curve decreased.

In this paper, the microscopic pore structure characteristics of concrete were measured using SEM during the freeze-thaw cycling of air-freezing and water-thawing, and the variation of the microcracks and void ratio were analyzed quantitatively. The stress-strain curve of concrete with different numbers of freeze-thaw cycles was measured. A freeze-thaw damage variable related to modified Loland damage model was proposed in this paper. Based on the four stress-stain curves, the equation for the stress-strain curved surface about strain and freeze-thaw damage variable were determined, and the evolution of the elastic modulus during freeze-thaw cycles was discussed.

2. Materials and Methods

The superstructures of concrete bridges in Qinghai-Tibet Plateau are mainly composed of C40 concrete. Based on the mixture ratio recommended in the literature [8] (Table 1), eight groups of cubic specimens with dimensions of $100 \, \text{mm} \times 100 \, \text{mm} \times 100 \, \text{mm}$ were poured with Shuoshan PO.42.5 ordinary Portland cement from Datong County, Qinghai Province, China. After 28 d in the standard curing room, the samples were used for quasi-static compression and splitting tension tests.

The freeze-thaw test of the concrete followed the slow freezing method stipulated in the "Standard for Testing Method of Long-term Performance and Durability of Ordinary Concrete" [9]. Before freezing and thawing, the specimens were immersed in water for 4 d, after which they were placed in a freezer at $-18°C$ for no less than 4 h. After freezing, the melting time should be no less than 4 h after water at $20°C$ was added. During the freeze-thaw process, a thermocouple was used to measure the center temperature of the test block to ensure that the center temperature of the test block reached the freeze-thaw temperature. The numbers of freeze-thaw cycles of the concrete blocks were 0, 25, 50, and 75. The microstructure of the concrete included aggregate, hydrated cement paste, and an interface transition zone between the cement paste and aggregate [10]. In this study, the micromorphology of the concrete after freeze-thaw cycling was observed by means of high-resolution SEM (JSM-6610LV).

TABLE 1: Mix proportions of concrete.

Elements	Cement	Water	Sand	Gravel
Material content (kg/m³)	388	190	601	1221
Ratio of weight	1	0.49	1.55	3.15

The compression of the concrete cubes was based on a test method standard for determining the mechanical properties of ordinary concrete [11]. The full stress-strain curves of concrete subjected to different numbers of freeze-thaw cycles were measured using a HUT1000k computer-controlled hydraulic universal testing machine manufactured by Shenzhen Wance Experimental Equipment Co. Ltd. Displacement loading mode was adopted in the experiment, and the loading rate was 1 mm/min. Data processing was conducted based on the requirements of the standard test method for the mechanical properties of ordinary concrete. According to this standard, the measured strength values of the $100 \, \text{mm} \times 100 \, \text{mm} \times 100 \, \text{mm}$ specimens must be multiplied by a dimension conversion coefficient of 0.95 [11].

3. Results

3.1. Micropore Structure under Freeze-Thaw Cycles. Figures 1(a), 1(c), 1(e), and 1(g) show the microstructures of the hydrated cement pastes observed using SEM with 500x magnification. With the increase in the number of freeze-thaw cycles, the micropore structure developed gradually, and microcracks formed after 75 freeze-thaw cycles. Figures 1(b), 1(d), 1(f), and 1(h) show binary diagrams of the micropore structures of the concrete analyzed by the pore and crack image identification and analysis system (PCAS) [12, 13]. With the increase in the number of freeze-thaw cycles, the percentage of microcracks and micropores in the concrete gradually increased from 2.74% to 10.83% after 75 freeze-thaw cycles. Generally, the number of cracks and micropores increased during the freeze-thaw cycling.

3.2. Compressive Properties of Concrete. During the quasi-static compression tests, the stress-strain curves of the concrete blocks subjected to 0, 25, 50, and 75 freeze-thaw cycles were measured (Figure 2). During the displacement loading tests, the peak stress corresponding to the stress-strain curve decreased gradually, whereas the peak strain increased gradually, and the compressive stress-strain full curve had a tendency to shift downward and to the right. The peak stress and peak strain values of the typical stress-strain curves of each group are shown in Table 2. The peak stress of the unfrozen-thawed concrete was 44.93 MPa, and the value of the peak strain was 2150.3 $\mu\varepsilon$, which was close to the value given by the FIP Model Code (2010) specification [14]. When the graded concrete had a strain of 2%, the average compressive strength was 48 MPa. The variation of the quasi-static stress-strain curve with the number of freeze-thaw cycles was consistent with that reported previously [7]. As the number of freeze-thaw cycles increased, the peak stress of the concrete decreased, the peak strain increased, the number of internal microcracks and pores increased, and
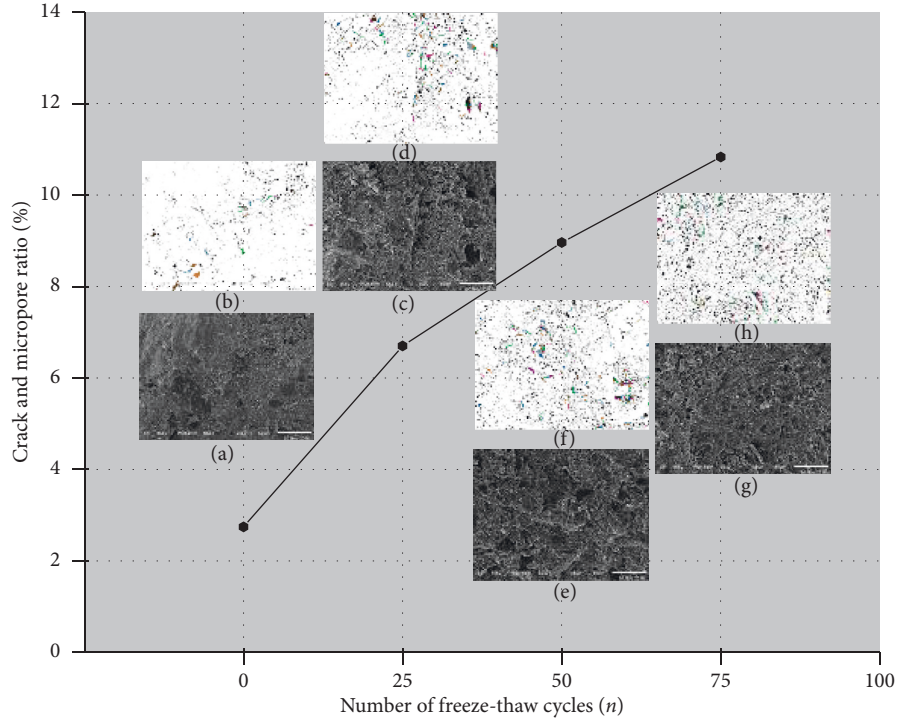
FIGURE 1: Micropore structure growth behavior for specimen (SEM 500x). (a) FTC00. (b) Binary diagram for FTC00. (c) FTC25. (d) Binary diagram for FTC25. (e) FTC50. (f) Binary diagram for FTC50. (g) FTC75. (h) Binary diagram for FTC75.
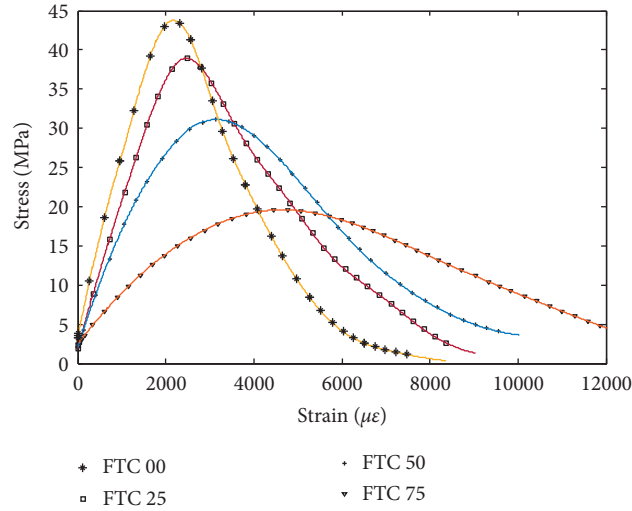
FIGURE 2: Full uniaxial compression stress-strain curves of concrete after different freeze-thaw cycling.

TABLE 2: Quasi-static compression test results of concrete after different numbers of freezing-thaw cycles.

Number of freeze-thaw cycles	f_{cm} (MPa)	ε_{cm} (10^{-6})	ε_{cm} (10^{-6}) (model code 2010)
0	44.93	2150.3	2400
25	40.10	2482.0	—
50	31.57	3095.0	—
75	19.67	4696.7	—

Note. f_{cm} is the peak stress and ε_{cm} is the strain at peak stress.

the pore size increased; these results agreed with those reported previously [8]. The peak stress of the concrete under uniaxial compression decreased, and the peak strain increased.

4. Discussion

4.1. Freeze-Thaw Damage Variable. Many studies had been conducted and some damage models were proposed by

researchers [15, 16]. Among these models, Loland damage model was considered as an effective method to study the damage in concrete [17]. Based on the macroscopic phenomenological theory, the Loland damage model mainly considered the influence of damage on the macroscopic mechanical properties of materials. In order to study the damage evolution in freeze-thaw cycles, a modified Loland damage model was proposed by Cai [18]. In this paper, the model from [18] was used to describe the damage law of concrete peak compressive strength about the number of freeze-thaw cycles. The relative dynamic elasticity modulus was used to evaluate the damage situation. And, the ratio of the peak compressive strength for different freeze-thaw numbers to the concrete strength without freeze-thaw was also used to describe damage circumstance [19].

Generally, an isotropic scalar D can be used to indicate the damage degree of concrete after freeze-thaw cycles, and the value was in the interval of [0, 1]. When $D = 0$, the material was not damaged, and when $D = 1$, the material was damaged completely. The damage variable can be expressed as follows:

$$D = D_0 + C_1\left(\frac{n}{N}\right)^{\beta}, \qquad (1)$$

where n is the number of freeze-thaw cycles and N is the freeze-thaw lifetime, which was assumed to be 100 in this study ($N = 100$). D_0 is the initial damage, and its value is set to be zero ($D_0 = 0$). C_1 and β are parameters related to peak compressive strength for concrete under different freeze-thaw cycles. And, the values of C_1 and β were 1.03 and 1.258, respectively. Then, the freeze-thaw damage variable is illustrated as follows:

$$D = 1.03 \times \left(\frac{n}{100}\right)^{1.258}. \qquad (2)$$

The increase in trend of damage variable versus different number of freeze-thaw cycles is shown in Figure 3(a). In order to verify the effectiveness of equation (2), the damage variable was calculated by two ways. The number of freeze-thaw cycles, elastic modulus, and peak compressive strength were obtained from [20], and then the corresponding values of C_1 and β were acquired. Meanwhile, the ratio of the error between initial elastic modulus and the elastic modulus for

different freeze-thaw number to initial elastic modulus was obtained to evaluate the damage variable values. And, the values of damage variable are shown in Figure 3(b). The well agreement between the values from two methods was found. Thus, the correctness for the method proposed in this paper was verified.

The four uniaxial compressive stress-strain curves of concrete subjected to different freeze-thaw cycles can be plotted in a three-dimensional coordinate system (Figure 4) with the freeze-thaw damage variable as one of the independent variables.

The stress-strain relationship of concrete subjected to 0, 25, 50, and 75 freeze-thaw cycles can be clearly expressed in the stress space with the freeze-thaw damage factor as the Y-axis. The ascending and descending sections were steeper for the undamaged specimen curve than those of the damaged specimen curves. As shown in Figure 1, the microscopic pore structure grew, which caused the concrete to become looser and spalled. At the macroscopic level, the microstructures, which included micropores and microcracks, tended to close under compression, resulting in a decrease in the slope of the ascending section of the stress-strain curve and a flattening of the overall curve [21].

4.2. Stress-Strain Curved Surface Equation of Concrete after Freezing and Thawing.

To account for the influence of the freeze-thaw cycling and evaluate the stress-strain constitutive relation associated with the freeze-thaw damage variable, a 2D rational function (equation (3)) and Levenberg–Marquardt optimization algorithm [22] were employed. Defining the vector $\mathbf{A} = [a_1, a_2, a_3, a_4]$ as the coefficient matrix of the strain and vector $\mathbf{B} = [b_1, b_2, b_3, b_4, b_5]$ as the coefficient matrix of the freeze-thaw damage variable, the rational function was defined as follows:

$$\sigma_{(\varepsilon, D)} = \frac{a_1\varepsilon + b_1 D + b_2 D^2 + b_3 D^3}{1 + a_2\varepsilon + a_3\varepsilon^2 + a_4\varepsilon^3 + b_4 D + b_5 D^2}, \qquad (3)$$

where D is the freeze-thaw damage variable in a freeze-thaw cycle, ε is the strain, and σ is the stress.

Using the experimental data, the damage evolution equation due to concrete freeze-thaw cycling can be expressed as follows:

$$\begin{cases} \sigma_{(\varepsilon, D)} = \dfrac{0.019\varepsilon - 1.89 D + 124.36 D^2 - 106.3 D^3}{1 - 0.00024\varepsilon + 1.79 \times 10^{-8}\varepsilon^2 + 4.08 \times 10^{-11}\varepsilon^3 + 0.417 D + 4 D^2}, \\ \\ R^2 = 0.85, \end{cases} \qquad (4)$$

where R^2 is the coefficient for the fitted function.

The influence of the strain and freeze-thaw damage variable on the concrete stress strength was captured by equation (4). Combining equation (2) and equation (4), the concrete stress about strain and the number of freeze-thaw cycles were obtained under uniaxial compression. The stress surfaces are plotted in Figure 5. Figure 5(a)

shows the curved surface drawn by fitting the data, and Figure 5(b) shows a curved surface drawn using the Wolfram Mathematica software based on equation (4). The unit of strain in the figures was microstrain (10^{-6}), the freeze-thaw damage variable was a dimensionless quantity with values between 0 and 1, and the unit of stress was MPa.

(a)

(b)
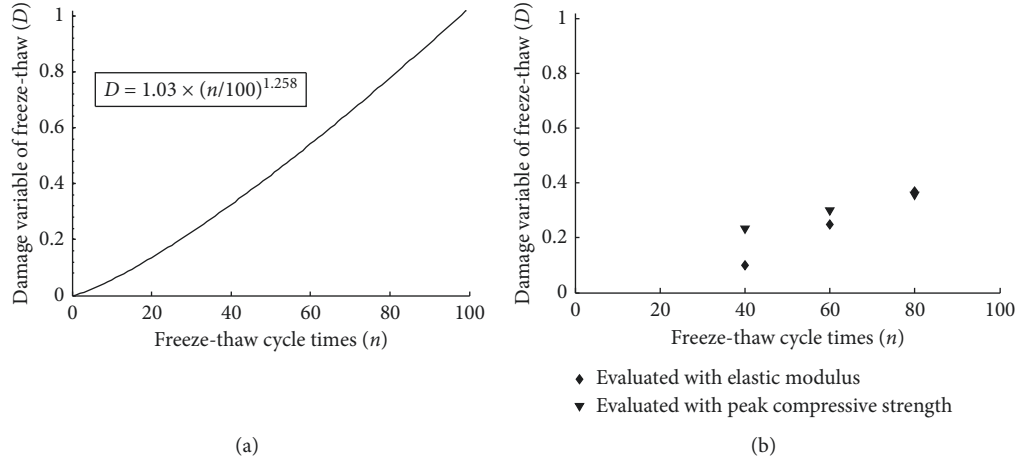
Figure 3: Damage variable versus freeze-thaw cyclic times: (a) experiment results; (b) comparison between two methods based on [20].
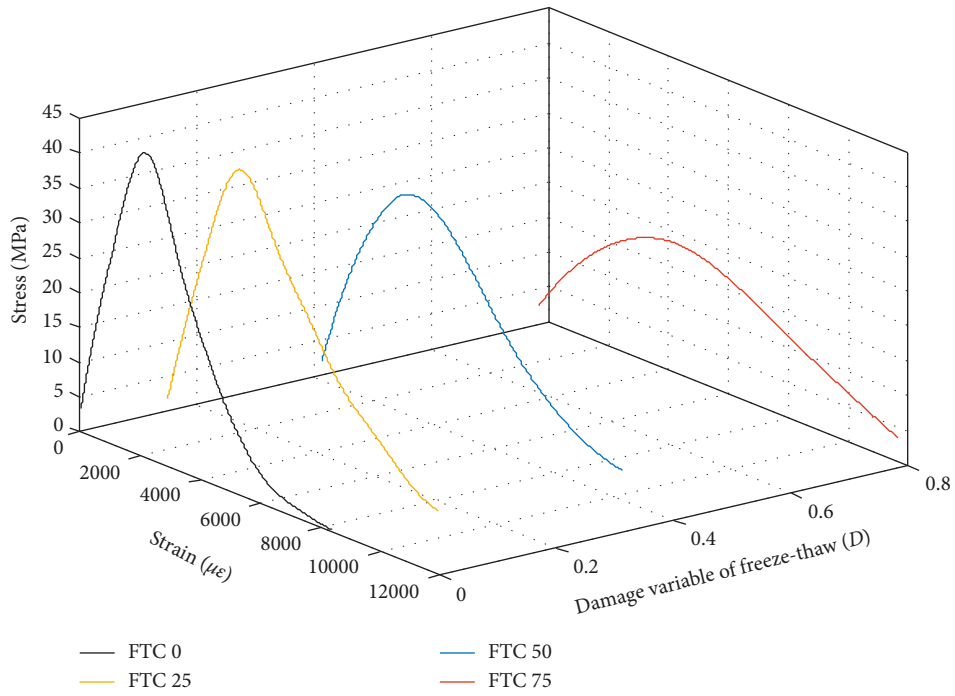
Figure 4: Uniaxial compression stress-strain curves in a three-dimensional coordinate system.

(a)

(b)
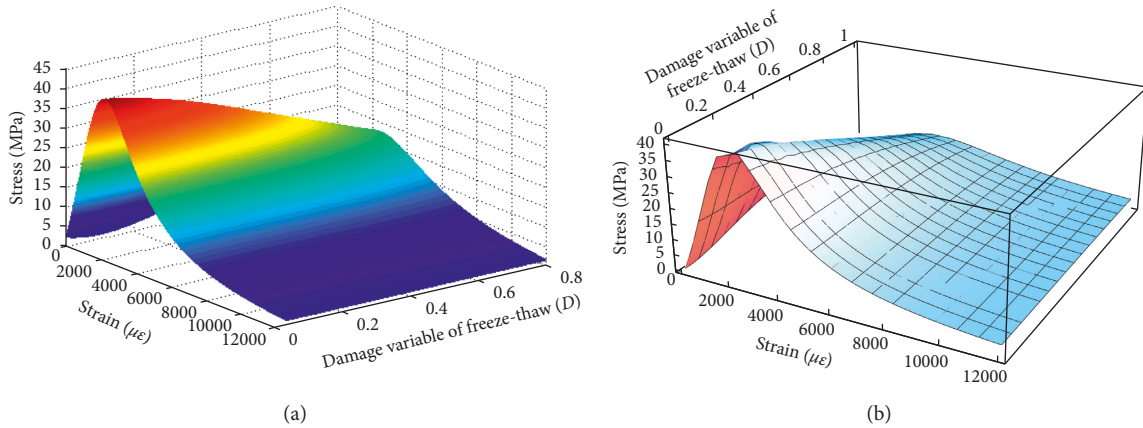
Figure 5: Full stress-strain surface with freeze-thaw damage variable. (a) Drawn by fitting the data. (b) Drawn using equation (4).
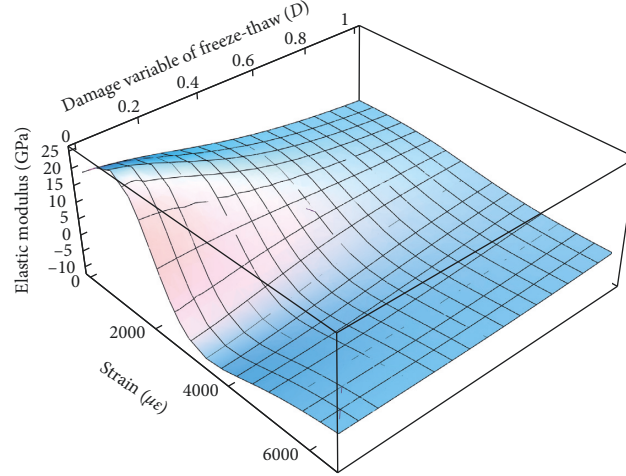
FIGURE 6: Stress-strain surface with varying freeze-thaw damage variable and elastic modulus surface.

TABLE 3: Quasi-static compression test data and elastic modulus after different numbers of freeze-thaw cycles.

Number of freeze-thaw cycles	f_{cm} (MPa)	ε_{cm} (10^{-6})	D	E_0 (GPa)	E_{max} (GPa)	E_c (GPa)
0	44.93	2150.3	0.003	13.6	23.5	35.5
25	40.10	2482.0	0.115	12.8	21.9	34.2
50	31.57	3095.0	0.267	9.7	12.4	31.5
75	19.67	4696.7	0.502	4.4	4.6	26.9

Note. f_{cm} is the peak stress, ε_{cm} is the strain at peak stress, E_0 is the initial tangential elastic modulus, E_{max} is the maximum tangential elastic modulus, and E_c is the elastic modulus estimated by the FIP Model Code (2010) in dry state.

4.3. Application for Stress-Strain Curved Surface Equation. The mass loss rate, dynamic elastic modulus, peak stress, and peak strain were commonly used to indicate the stress-strain relationship of concrete after freezing and thawing. Studies have shown that the dynamic elastic modulus was significantly reduced with the expansion of the microscopic pore structure inside the concrete during freeze-thaw cycles [23]. Meanwhile, the peak stress decreased and the peak strain increased [24]. By finding the partial derivative of the stress corresponding to the change in equation (4), the distribution of elastic modulus for each point in the stress-strain space was obtained as follows:

$$E_{(\varepsilon, D)} = \frac{\partial \sigma}{\partial \varepsilon} = \frac{190}{1 - 0.00024\varepsilon + 1.79 \times 10^{-8}\varepsilon^2 + 4.08 \times 10^{-11}\varepsilon^3 + 0.417 D + 4D^2}$$
$$- \frac{\left(-0.24 + 3.58 \times 10^{-5}\varepsilon + 1.223 \times 10^{-7}\varepsilon^2\right)\left(0.019\varepsilon - 1.89 D + 124.36D^2 - 106.3D^3\right)}{\left(1 - 0.00024\varepsilon + 1.79 \times 10^{-8}\varepsilon^2 + 4.08 \times 10^{-11}\varepsilon^3 + 0.417 D + 4D^2\right)^2}. \tag{5}$$

The dimensions and units of the quantities in the above formula were the same as those in equation (4).

Equation (5) was used to calculate the change in the tangential elastic modulus. And, Figure 6 shows the surfaces plotted with equations (5) in the 0–6500 microstrain range, 0–1.0 freeze-thaw damage range. The tangential elastic modulus of concrete can be divided into the following stages as the strain changes: (a) during the ascending section of the stress-strain curve, the tangential elastic modulus first increased and subsequently decreased, and the elastic modulus reached the peak value within the first 1/2–2/3 of the ascending section of the curve; (b) at the peak stress, the value of the elastic modulus was close to 0; and (c) in the descending section of the stress-strain curve, the elastic modulus was negative.

The values of elastic modulus computed from equation (4) and the FIP Model Code (2010) for 0, 25, 50, and 75 freeze-thaw cycles are shown in Table 3.

The formula for the elastic modulus of ordinary concrete specified by the FIP Model Code (2010) is as follows:

$$E_c = 2.15 \times 10^4 \left(\frac{f_{cm}}{10}\right)^{1/3}, \tag{6}$$

where E_c is the elasticity modulus of concrete (MPa) and f_{cm} is the average value of the compressive strength (MPa).

The three elastic moduli (initial tangential, maximum tangential, and estimated elastic moduli) shown in Table 3 are in the same order of magnitude, and E_{max} and E_0 were

small than the value of E_c, which resulted that the elastic modulus of concrete in the saturated state was lower than the value in the dry state [20].

5. Conclusions

SEM images and macromechanical properties were used to study the damage of concrete due to freeze-thaw cycling. The stress-strain curves under uniaxial compression were discussed in detail. The main conclusions were summarized as follows.

The microcracks and pores in the concrete increased with the increase of freeze-thaw cycles. During the freeze-thaw process, the periodic reciprocating stress around the internal microporosity structure made the internal damage accumulate gradually. With the increase in the number of freeze-thaw cycles, the peak stress of the concrete under uniaxial compression decreased gradually, while the strain corresponding to the peak stress increased.

The modified Loland damage model was used to evaluate the mechanical behavior of the freeze-thaw damage. The damage evolution variable could express the damage evolution behavior of the concrete. Based on the stress-strain full curve of concrete under the different number of freeze-thaw cycles, the stress-strain curved surface equation was proposed.

The value of elastic modulus predicted from the equation in this paper agrees well with the value in FIP Model Code (2010). And, the equation can help predict the mechanical properties for major engineering structure in the cold region.

Data Availability

All experimental data, models, and code generated or used during the study are available from the corresponding author upon request.

Conflicts of Interest

The authors declare that there are no conflicts of interest regarding the publication of this paper.

Acknowledgments

References

[1] Z. Guo, *Principles of Reinforced Concrete*, Elsevier, Amsterdam, Netherlands, 2014.

[2] S. B. Huda and M. Shahria Alam, "Mechanical and freeze-thaw durability properties of recycled aggregate concrete made with recycled coarse aggregate," *Journal of Materials in Civil Engineering*, vol. 27, no. 10, Article ID 04015003, 2015.

[3] M.-H. Liu and Y.-F. Wang, "Damage constitutive model of fly ash concrete under freeze-thaw cycles," *Journal of Materials in Civil Engineering*, vol. 24, no. 9, pp. 1165–1174, 2012.

[4] T. Guo and X. Weng, "Evaluation of the freeze-thaw durability of surface-treated airport pavement concrete under adverse conditions," *Construction and Building Materials*, vol. 206, pp. 519–530, 2019.

[5] W. Tian, X. Li, and F. Wang, "Experimental study on deterioration mechanism of concrete under freeze-thaw cycles coupled with sulfate solution," *Bulletin of the Chinese Ceramic Society*, vol. 38, no. 3, pp. 119–127, 2019.

[6] X. Guan, D. Niu, J. Wang, and L. Jiang, "Study on freeze-thaw damage constitutive model of concrete considering plastic strain and damage threshold," *Journal of Disaster Prevention and Mitigation Engineering*, vol. 35, no. 6, pp. 777–784, 2015.

[7] X. Wang, J. Xie, P. Li, and X. Li, "Experimental study on complete stress-strain curve of concrete after freeze-thaw cycles under extra-low temperatures," *Water Resources and Hydropower Engineering*, vol. 45, no. 8, pp. 159–164, 2014.

[8] B. Zhang, *Concrete and Mortar Mixing Ratio Manual*, Tianjin University Press, Tiasnjin, China, 2012.

[9] China Academy of Building Research, *Standard Test Method for Long-Term Performance and Durability of Ordinary Concrete GB/T50082-2009*, China Architecture & Building Press, Beijing, China, 2010.

[10] P. K. Mehta and P. J. M. Monteiro, *Concrete: Microstructure, Properties, and Materials*, McGraw Hill Professional, New York, NY, USA, 2013.

[11] China Academy of Building Research, *Standard Test Method for Mechanical Properties of Ordinary Concrete GB/T 50081-2002*, China Architecture & Building Press, Beijing, China, 2004.

[12] C. Liu, C.-S. Tang, B. Shi, and W.-B. Suo, "Automatic quantification of crack patterns by image processing," *Computers & Geosciences*, vol. 57, pp. 77–80, 2013.

[13] C. Liu, B. Shi, J. Zhou, and C. Tang, "Quantification and characterization of microporosity by image processing, geometric measurement and statistical methods: application on SEM images of clay materials," *Applied Clay Science*, vol. 54, no. 1, pp. 97–106, 2011.

[14] Fib, *Fib Model Code for Concrete Structures 2010*, International Federation for Structural Concrete (Fib), Lausanne, Switzerland, 2010.

[15] A. Duan, Y. Tian, J.-G. Dai, and W.-L. Jin, "A stochastic damage model for evaluating the internal deterioration of concrete due to freeze–thaw action," *Materials and Structures*, vol. 47, no. 6, pp. 1025–1039, 2014.

[16] Y.-L. Chen, J. Ni, L.-H. Jiang, M.-L. Liu, P. Wang, and R. Azzam, "Experimental study on mechanical properties of granite after freeze–thaw cycling," *Environmental Earth Sciences*, vol. 71, no. 8, pp. 3349–3354, 2014.

[17] N. Gong and X. Liu, "Concrete failure criterion under freeze-thaw condition in structural engineering," *Sichuan Building Science*, vol. 31, no. 6, pp. 144–147, 2005.

[18] H. Cai, *Prediction Model of Concrete Freeze-Thaw Durability*, Tsinghua University, Beijing, China, 1998.

[19] A. Chen, Q. Zhang, J. Wang, and Z. Gai, "Freeze-thaw cycle test and a damage mechanics model for recycled concrete," *Engineering Mechanics*, vol. 26, no. 11, pp. 102–107, 2009.

[20] W. Tian, K. Xing, and Y. Xie, "Experimental study of concrete of damage degradation mechanism in freeze-thaw environment," *Journal of Experimental Mechanics*, vol. 30, no. 3, pp. 299–304, 2015.

[21] J. Wu, X. Jing, and Z. Wang, "Uni-axial compressive stress-strain relation of recycled coarse aggregate concrete after freezing and thawing cycles," *Construction and Building Materials*, vol. 134, pp. 210–219, 2017.

[22] P. L. Gould and Y. Feng, *Introduction to Linear Elasticity*, Springer, Basel, Switzerland, 2018.

[23] J. Zhang, X. Weng, L. Jiang, B. Yang, and J. Liu, "Frost resistance of concrete reinforced using surface-strengthening materials in airport pavements," *Journal of Materials in Civil Engineering*, vol. 30, no. 3, Article ID 04018006, 2018.

[24] X. Guan, J. Qiu, H. Song, Q. Qin, and C. Zhang, "Stress–strain behaviour and acoustic emission characteristic of gangue concrete under axial compression in frost environment," *Construction and Building Materials*, vol. 220, pp. 476–488, 2019.

Research Article

Effect of Shear Creep on Long-Term Deformation Analysis of Long-Span Concrete Girder Bridge

Yanwei Niu [1] and **Yingying Tang**[2]

[1]*College of Highway, Chang'an University, Xi'an 710064, China*
[2]*College of Science, Chang'an University, Xi'an 710064, China*

Correspondence should be addressed to Yanwei Niu; niuyanwei@chd.edu.cn

The purpose of this paper is to report on the development of a three-dimensional (3D) creep calculation method suited for use in analyzing long-term deformation of long-span concrete girder bridges. Based on linear creep and the superposition principle, the proposed method can consider both shear creep and segmental multiage concrete effect, and a related program is developed. The effects of shear creep are introduced by applying this method to a continuous girder bridge with a main span of 100 m. Comparisons obtained with the nonshear case show that shear creep causes long-term deformation to increase by 12.5%. Furthermore, the effect of shear creep is proportional to the shear creep coefficient; for a bridge with different degrees of prestress, the influence of shear creep is close. Combined with the analysis of a continuous rigid bridge with a main span of 270 m, the results based on the general frame program suggest that shear creep amplification is multiplied by a factor of 1.13–1.15 in terms of long-term deformation. Moreover, the vertical prestress has little effect on shear creep and long-term deformation. The 3D creep analysis shows a larger long-term prestress loss for vertical prestress at a region near the pier cross section. The relevant computation method and result can be referenced for the design and long-term deformation analysis of similar bridges.

1. Introduction

Long-span concrete girder bridges (including continuous rigid-frame bridges) were first constructed in the 1950s. By utilizing the cantilever construction method, the difficulty of construction was greatly reduced, which caused this bridge type to develop rapidly. It gradually became the dominant bridge type in the medium- to large-span bridges. However, the problem of the excessive long-term deflection of long-span concrete bridges has frequently appeared in recent years [1–5] and has become a bottleneck restricting their development. Currently, the testing and computational effort involved in the problem of excessive long-term deformation is quite substantial and can mainly be divided into the following aspects: (1) long-term deflection observation and regular analysis of actual bridges [1–4]; (2) parameter analysis and suggestions for the control of long-term deflection [6–8]; and (3) improvement in long-term deflection

calculation methods [9–15]. With regard to calculation methods, the current mainstream structure analysis software ignores the influence of shear creep. It is noted that an analysis of the long-span concrete girder bridge that ignores the effect of shear creep will cause error in the predicted value due to its large section and thin web [16]. In this regard, some scholars have proposed a more refined calculation method: Bažant et al. used a specialized material program based on ABAQUS to calculate the creep with a solid element model [11]. In addition, Cao et al. studied the effect of the law of cracks on the creep deformation of prestressed beams using experiments and proposed a relevant formula for analysis [12]. Moreover, Guo and Chen proposed a deflection control strategy for long-span concrete box-girder bridges based on field monitoring and probabilistic finite element (FE) analysis [13]. Niu et al. used ANSYS to develop a three-dimensional concrete creep calculation program [14]; Huang et al. developed a creep

program based on ADINA to analyze the effect of shear lag [15]. Zhang et al. calculated the creep effect of reinforced concrete frames by fitting the axial creep curve [17]. However, the existing studies have not separated out the effects of shear creep. In this paper, for the long-span concrete girder bridge, a three-dimensional creep calculation method including segmental multiage concrete structures was considered and programmed by using MATLAB and ANSYS to realize a shear-creep-independent analysis. A continuous-girder bridge with a span of $65 + 100 + 65$ m was taken as an example of the analysis of the influence of shear creep on long-term deformation. The study examined the range of influence of shear creep on different prestressed bridges and the effect of vertical prestress on long-term deformation. The method of calculation of standard long-term deformation was discussed, and corresponding calculation suggestions were put forward.

2. Analysis Method

2.1. Consideration of Shear Creep. The long-term deformation analysis of concrete bridges can be divided into differential equations, algebraic equations, and a step-by-step approach [18]. It is generally accepted that the first two methods remain feasible for the analysis of simple structures. However, for complicated structures such as segmental multiage concrete bridges, the adoption of the step-by-step accumulation method based on the superposition principle is necessary, which is suitable for programming calculations. In this study, the step-by-step accumulation method is used to calculate the creep effect by changing the initial strain of each integration point of each concrete element. The formula for calculating the long-term strain of the integration point at time t is as follows:

$$
\varepsilon(t) = \frac{\sigma(t_0)}{E(t_0)} \left[1 + \phi(t, t_0) \right] + \sum_{i=1}^{n} \frac{\Delta\sigma(t_i)}{E(t_i)} \left[1 + \phi(t, t_i) \right] \\
+ \varepsilon_{cs}(t, t_0),
\tag{1}
$$

where t is the calculation time (days), t_0 is the initial loading age of the concrete, $\sigma(t_0)$ is the initial stress, E is the elastic modulus, and $\phi(t, t_0)$ is the creep coefficient. The first term of the formula represents the total strain generated by the initial stress, including elastic strain and creep strain. The age of concrete varies continuously from time t_0 to t, so the creep coefficient also varies. It must be divided into n time steps to approximate this process. The creep coefficient of each time step is $\phi(t, t_i)$, and $\Delta\sigma(t_i)$ is the change in stress between the two adjacent times t_i and t_{i-1}. $\varepsilon_{cs}(t, t_0)$ is the shrinkage strain, which can be calculated according to the standard formula [19]. Generally, in the planar frame FE creep computation, only three normal stresses (strains) are considered for each integration point. For three-dimensional (3D) solid or shell elements, the stress $\overline{\sigma}$ (and strain $\overline{\varepsilon}$) of the integration point is composed of six components as shown in the following equation:

$$
\overline{\sigma} = \left\{ \sigma_x, \sigma_y, \sigma_z, \tau_{xy}, \tau_{yz}, \tau_{xz} \right\},
\tag{2}
$$

where $\sigma_x, \sigma_y, \sigma_z$ constitute the normal stress and $\tau_{xy}, \tau_{yz}, \tau_{xz}$ constitute the shear stress. The calculation of the influence on the shear deformation is achieved by using a 3D element and accounting for the creep effect of the shear stress. The creep correction coefficient is introduced to correct the creep coefficient of the six strain components $m\_\phi = [m_x, m_y, m_z, m_{xy}, m_{yz}, m_{xz}]$, where m_x (and m_y, m_z) = 1, and the axial creep is the same as the norm creep coefficient. On the contrary, if m_{xy} (and m_{yz}, m_{xz}) = 1, the shear creep coefficient is the same as that in the axial direction, and the modified shear value is calculated by a different shear creep coefficient. Specifically, if m_{xy} (and m_{yz}, m_{xz})) is set to zero, the long-term deformation subjected to axial creep alone is calculated.

The creep deformation at any time t_i is obtained by multiplying the elastic strain increment $\overline{\varepsilon}_0$, $(\overline{\varepsilon}_1 - \overline{\varepsilon}_0)$, $(\overline{\varepsilon}_2 - \overline{\varepsilon}_1), \ldots, (\overline{\varepsilon}_{i-1} - \overline{\varepsilon}_{i-2})$ of the previously calculated time point $t_0, t_1, \ldots, t_{i-1}$ by the creep coefficient $\phi(t_i, t_\tau)$ of the corresponding time, wherein t_τ is the age of loading. Under the action of a dead load, the stress of the statically determinate structure no longer changes. Therefore, except for the initial elastic strain $\overline{\varepsilon}_0$, which has an influence on the creep at the calculation point t_i, the other effects are all zero. For a long-span concrete continuous-girder bridge constructed by segmentation, the creep will generate secondary internal forces that will cause changes in the elastic stress and strain at each calculation time point. The creep effect is cumulative; therefore, it is necessary to consider the effect of the elastic strain increment of each calculation point on the subsequent calculation point. The batch mode of ANSYS can be revoked by the programming languages, e.g., C++ and MATLAB [20]. In this study, the FE results are read by MATLAB, and the initial strain input data of the subsequent calculation time points are calculated and generated. The FE calculation and the stress redistribution are completed by ANSYS in the batch mode. The flow chart is shown in Figure 1. In the computation of a time point, i.e., time t_i, we first read the increase in strain of the preceding steps and recall the relevant creep coefficient. We then obtain the initial data of the current step: $\overline{\varepsilon}_0 \cdot \phi(t_i, t_0) + (\overline{\varepsilon}_1 - \overline{\varepsilon}_0) \cdot \phi(t_i, t_1) + \cdots + (\overline{\varepsilon}_{i-1} - \overline{\varepsilon}_{i-2}) \cdot \phi(t_i, t_{i-1})$. ANSYS is then revoked to complete the FE analysis and to output the result of the current step. This loop will be controlled by MATLAB and will continue till attaining the objective computation time point and completing the analysis.

2.2. Shear Creep Coefficient. Specifications and research institutions have different creep functions, but they can basically be expressed as the product of the creeping ultimate value and the development function. For example, according to JTG 3362-2018 [19], the creep function formula is as follows:

$$
\phi(t, t_0) = \phi_0 \cdot \beta_c(t - t_0),
\tag{3}
$$

where ϕ_0 is the final value (nominal creep coefficient), related to the concrete grade, loading age, component thickness, and environmental humidity. $\beta_c(t - t_0)$ is a creep development function, used to calculate the creep deformation at a certain time t, divided into exponential
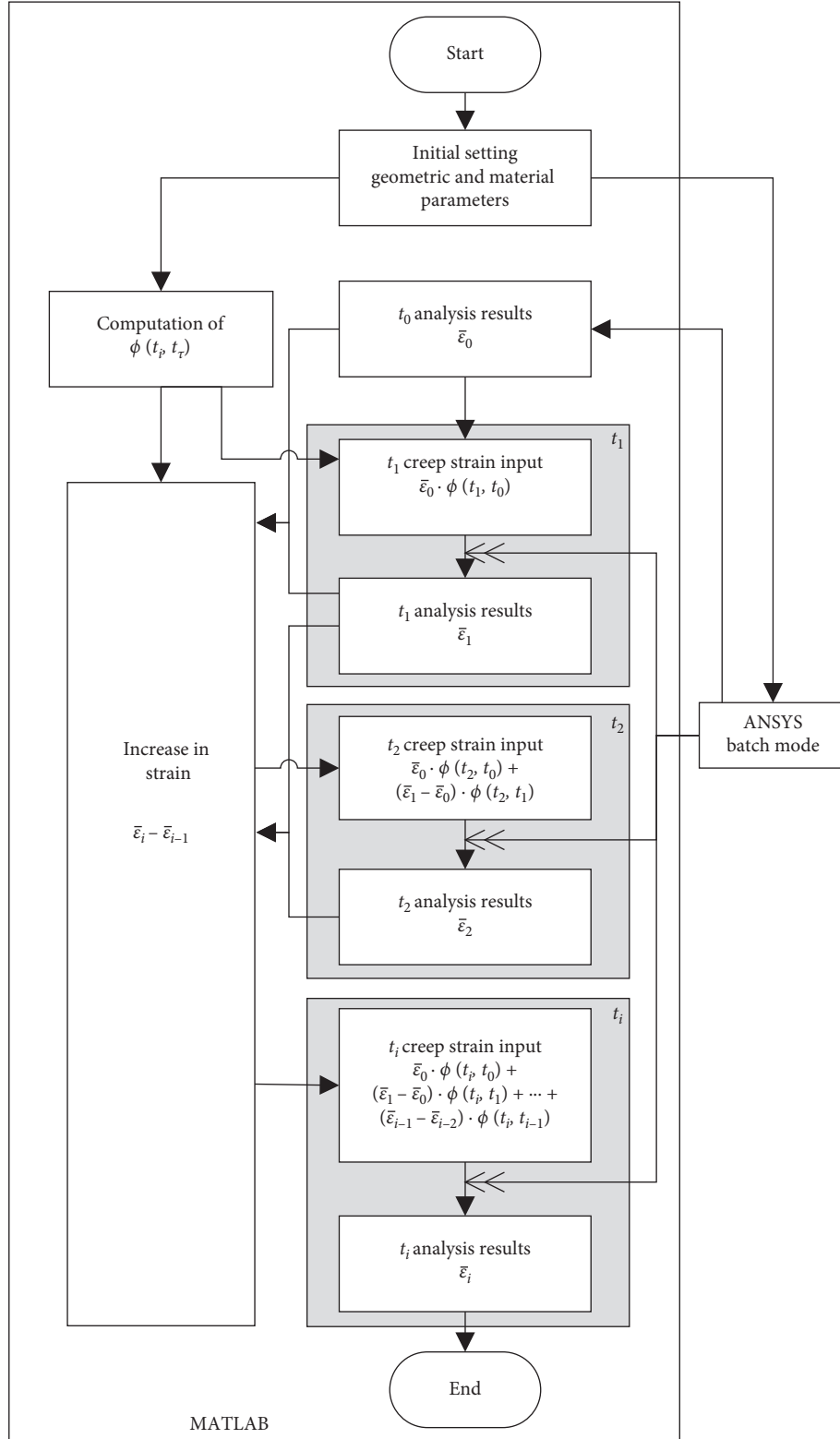
Figure 1: Flow chart of creep calculation.

functions, as well as the form of the score and the sum. In this study, $\beta_c(t - t_0) = [((t - t_0)/t_1)/(\beta_H + (t - t_0)/t_1)]^{0.3}$, where t is the targeted computation time, t_0 is the concrete age when loading is applied, $\beta_H = 150[1 + (1.2\,(\mathrm{RH}/\mathrm{RH}_0))^{18}]\,(h/h_0) + 250 \leq 1500$, RH is the yearly average humidity, h is the nominal depth in units of mm and equal to $2A/u$, A is the area of the girder section, and u is the length of the edge exposed to the atmosphere. The current creep coefficient of concrete is tested by axial loading. The creep coefficient in the shear direction has rarely been reported. A

recent experimental study showed that the one-year shear creep of three torsion columns made of C30 concrete may attain twice the creep of the axial member [21]. However, further long-term laboratory and field tests of high-grade concrete are needed for general application purposes. In this study, based on the normative formula as shown in Equation (3) and considering the concrete grade of the prototype bridge, the creep correction coefficient m_ϕ for shear creep consideration is used within a fluctuation range of 50% (0.5, 1.0, and 1.5) to analyze the influence of the shear creep coefficient on the long-term deflection of the bridge.

Another ingredient of time-dependent deformation in equation (1) is shrinkage that is independent of the stress state so that the expression of the shrinkage strain can be written directly [19]: $\varepsilon_{cs}(t, t_s) = \varepsilon_{cso} \cdot \beta_s(t - t_s)$, where ε_{cso} is the ultimate shrinkage value and t_s is the age of the concrete at the beginning of shrinkage related to the curing date and is different from the value of t_0 used in developing the creep function. In addition, the function β_s is developed in a like manner to that of creep: $\beta_s(t - t_s) = [((t - t_s)/t_1)/ 350(h/h_0)^2 + (t - t_s)/t_1]^{0.5}$.

2.3. Consideration of Segmental Construction.

For bridges using the falsework construction method, the age of each part of the structure is the same. Taking the calculation time t_0 as an example (assuming the concrete age is t_0), the creep function of all the concrete for the subsequent calculation moments t_0 is the same, namely, $\phi(t_i, t_0)$. In contrast, for bridges with the segmental construction method, the concrete age of each section is different. Correspondingly, the creep function is different for the subsequent calculation time t_i. For example, if the age of section A is t_0 and section B is poured Δt days later than A, the age of section B should be $t_0 + \Delta t$. Therefore, the creep coefficients of the two segments at the calculation moment t_i are $\phi(t_i, t_0)$ and $\phi(t_i, t_0 + \Delta t)$ for sections A and B, respectively. Additionally, concrete of multiple ages is commonly seen in long-span concrete girder bridges constructed using the cantilever construction method. In such cases, the age difference between the first and the last pouring sections can reach hundreds of days; subsequently, the creep coefficient varies greatly. Therefore, the difference in age should be considered. In the ANSYS modeling process, the elements are grouped according to the construction section. When MATLAB recalls the creep coefficient module, the element group is first identified and the corresponding loading age is then given. Finally, the initial strain input data of the subsequent calculation time can be generated.

3. Calculation of the Prototype Bridge

3.1. Structural Parameters.

To illustrate the effect of shear creep on long-term deflection, a prestressed concrete continuous girder bridge with a main span of 100 m is used as background. This bridge is located on a highway in Guangdong, China. It is a prestressed concrete continuous girder bridge with a span combination of $65 + 100 + 65$ m (Figure 2(a)). The traffic lanes are dual direction and are separated on two independent bridges with a gap of 1.274 m. The single-room box section was used in the superstructure layout. The depth of the girder section over the pier is 5.6 m, decreasing to 2.2 m at the midspan section. The bottom of the box girder varies from the midspan to the top of the pier according to the formula for a parabola. The width of the box girder is 11.898 m, with a 1.5 m pedestrian way connected to the flange, as shown in Figure 2(b).

The main beam used C50 concrete. The girder section over the pier is arranged with prestress tendons in the flange and the web, each consisting of 26 tendons. The prestressed midsection contains 20 tendons in the bottom slab. Each tendon consists of twelve 15.2 mm diameter high-strength and low-relaxation steel strands. The vertical prestressing consists of a 25 mm diameter fine-rolled rebar, and the spacing is 60 cm around the sections over the piers and 65 cm at other locations. We use a simplified manner to consider initial prestress loss of the tendons, in which the "effective prestress" of 1350 MPa on longitudinal tendons and 675 MPa on vertical tendons are used. The long-term prestress loss caused by creep and shrinkage deformation will be automatically considered by the program.

The cantilever segmental casting process is divided into 16 segments (blocks #0~#15), of which block #15 is the closure segment. The side spanning cast-in segment consists of blocks #16~#18. The lengths of the segments are 2 m~4 m. Each segmental construction step lasts approximately 7 days. The concrete ages of the closure segment and the pier #0 block are different by 105 days. When calculating the creep during the operation of the bridge, the creep coefficient of the corresponding age is adopted for each segment. Material parameters are listed in Table 1.

The prototype bridge was completed and opened to traffic in the 1990s. A significant downward deflection in the midspan was observed in 2001. A full-bridge deformation observation system was then established. The observation points were placed along the central reservation and the safety barriers at both sides. In all, 34 measuring points were distributed over each side of the bridge. Their locations are shown in Figure 3(a). During the following 10-year period, the midspan of the bridge continued to deflect. As shown in Figure 3(b), the maximum relative deformation of the left span is 16 cm and that of the right bridge is 21 cm, which are close to or larger than the specification deformation limit 1/600 of the span length. This made a difference in the appearance of the bridge (Figure 3(b)) and affected driving comfort. The side span had a certain camber, with a maximum value of approximately 10 cm.

3.2. FE Model Parameters.

The background bridge model is established by ANSYS. To consider the shear deformation, the concrete box beam adopts the element SHELL181, including in-plane and out-of-plane bending stiffness (KEYOPT (1) = 0). The exact integral calculation (KEYOPT (3) = 2) is adopted. The prestressed tendons are simulated by the element LINK180, and the prestress forces are applied by

(a)

(b)

(c)
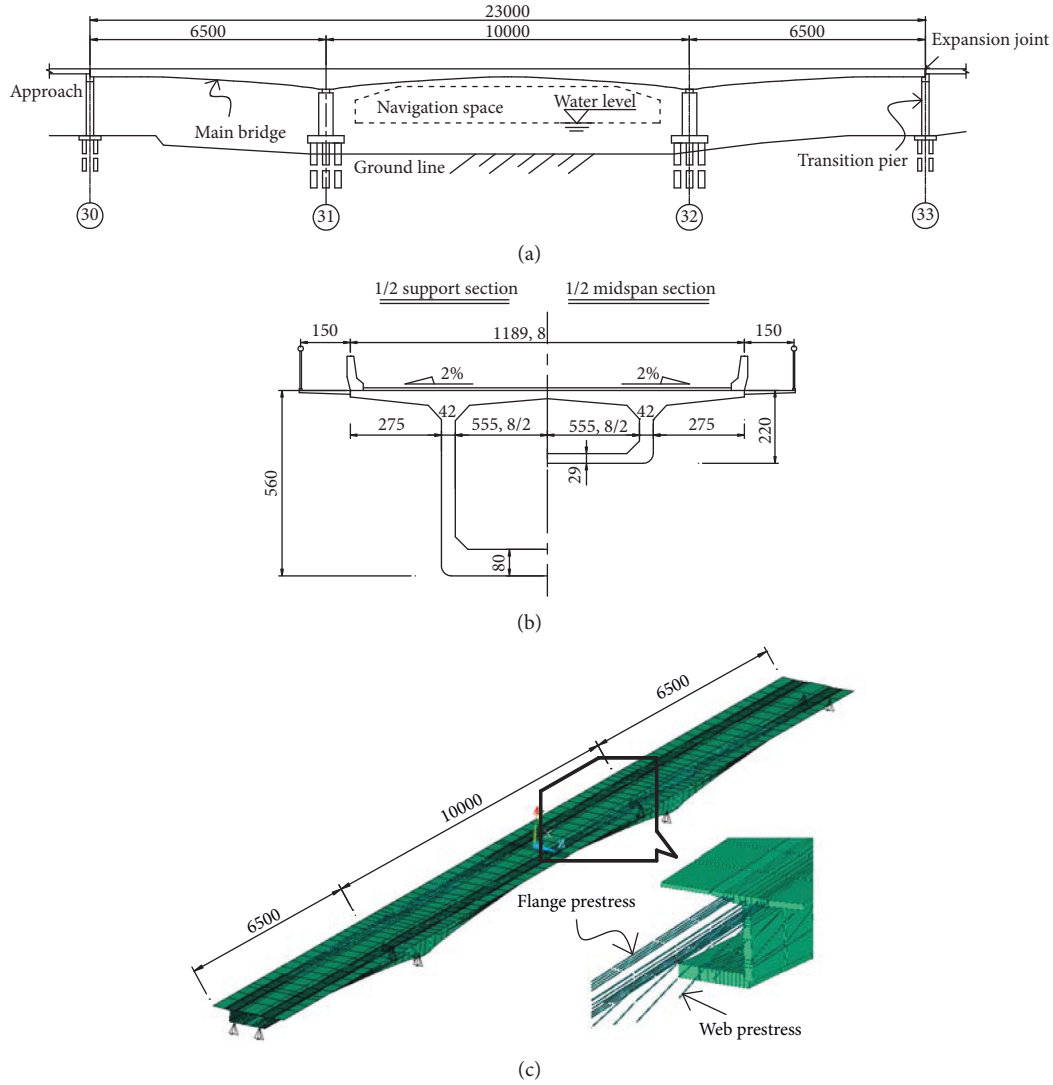
FIGURE 2: Model of the prototype bridge (unit: cm). (a) Elevation. (b) Cross section of box girder. (c) ANSYS model and prestress.

TABLE 1: Parameters of modeling.

Term	Value
Grade of concrete	C50
Average humidity (RH)	70%
t_0 (d)	5
t_s (d)	3
Time interval between adjacent segments (d)	7
Initial prestress of longitudinal tendon (MPa)	1350
Initial prestress of vertical tendon (MPa)	675

decreasing the equivalent temperature. The FE model is shown in Figure 2(c), and the materials used are shown in Table 1.

The long-term deformation of concrete girder bridges is caused by the long-term effect of dead load and the camber by prestress. As the creep of concrete under dead load affects the prestress loss, they are therefore interrelated and can be automatically included in the spatial model. In addition, live load also has a certain impact on bridge deflection, but the proportion is usually low. After vehicles leave the bridge, the bridge deck alignment is restored. While the cumulative effect of residual deformation under live load and its impact on concrete fatigue does need to be studied, in this paper the effect of live load is ignored, and only the long-term deformation under dead load is considered.

4. Results and Discussion

4.1. Effect of Shear Creep. The deformation of girder bridges is mainly due to the bending moment of the dead load, which grows significantly with increasing design span length. It becomes difficult to set the prestressing steel tendons in the limited section space of long-span girder bridges to completely compensate for the dead-load moment. As shown in Table 2, the prestress bending moment is less than dead load bending moment at the section over pier of the 100 m span bridge, which results in the overall deflection of the bridge. At the same time, the bending moment distribution of a 270 m main span bridge [1] is calculated.
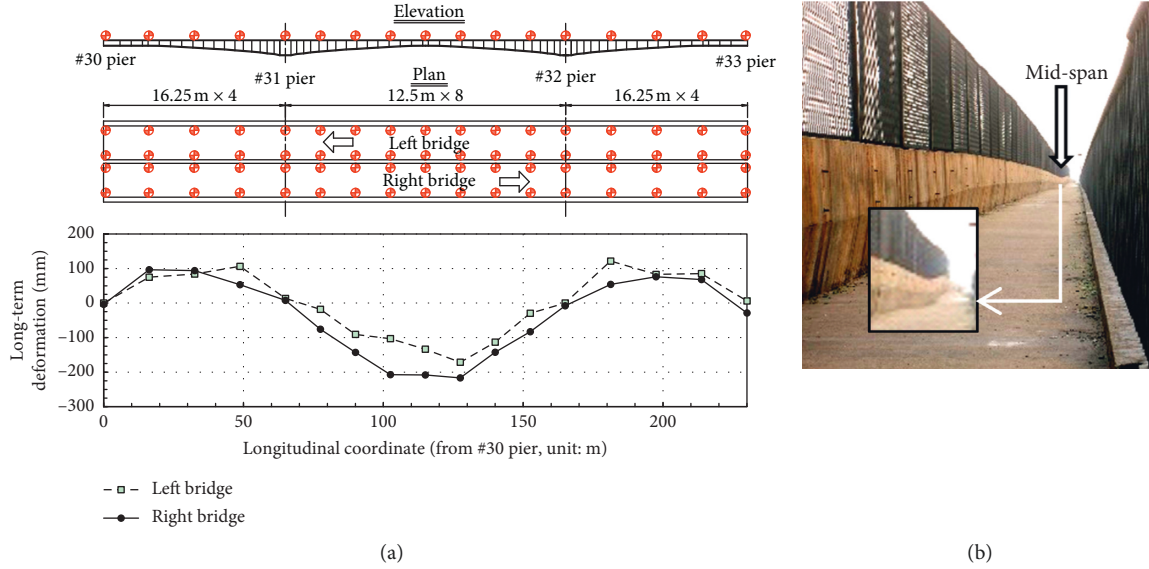
FIGURE 3: Deformation investigation of the prototype bridge. (a) Investigation points of the deck and long-term deformation over 10 years. (b) Deflection of midspan (pedestrian parapet view).

TABLE 2: Comparison of bending moments of the critical section (unit: kN·m).

Bridge span length	Section over pier			Midspan section		
	Dead load (1)	Prestress (2)	(2)/(1)	Dead load (1)	Prestress (2)	(2)/(1)
100 m	$-2.75E+05$	$2.54E+05$	-0.92	$5.68E+04$	$-6.80E+04$	-1.20
270 m	$-2.30E+06$	$1.99E+06$	-0.86	$2.78E+05$	$-2.02E+05$	-0.73

The ratios of the prestress bending moment to the dead-load bending moment at pier top and midspan are 0.86 and 0.73, respectively. The trend of bridge deflection becomes obvious with increasing span.

As shown in Figure 4(a), the main span of the prototype bridge deflected, and the side span cambered under dead load. The deflection will be further developed according to the elastic deformation of dead load due to the inherent creep characteristics of concrete. Ten years after the completion of the bridge, the total deformation of the main span will reach 2.57 times of the elastic deflection. As shown in Figures 4(b) and 4(c), for elastic deformation and long-term deformation, the calculated values considering shear deformation are larger than those without considering shear deformation. When the bridge is completed, the midspan deflection considering shear deformation is 6.9 cm, and the midspan deflection excluding shear deformation is 6.1 cm. Without considering shear deformation, the elastic deformation will be reduced by 12.5%. After 10 years of operation, the calculated value considering shear deformation is 17.7 cm and the calculated value excluding shear deformation is 15.8 cm.

In the practical construction of bridges, the elastic deformation can be eliminated by setting the precamber and adjusting the elevation of the vertical formwork of each segment in the construction process so that the alignment of the completed bridge can meet the design requirements. Therefore, the long-term relative deformation that affects the performance of bridges is based on the alignment of

completed bridges. For the research prototype bridge, as shown in Figure 4(d), the calculated value of relative deformation considering shear is 12.4% larger than that of nonshear relative deformation. The error of the shear effect in calculating long-term deformation should not be ignored.

4.2. Effect of Creep Coefficient. As a mixed material, concrete is highly discrete and stochastic, in which the mechanical properties are different in different locations of bridges even in the same batch of concrete. The creep coefficient is the main parameter used to characterize the creep characteristics of concrete. Gilbert points out that the creep deviation of concrete can reach more than 50% [18]. There are few studies at present on the shear creep coefficient. Bažant et al. took the 3D creep into account using the method of creep rate, assuming that the shear creep coefficient is the same as that in the axial direction [11]. In this paper, the influence of shear creep and axial creep on the overall linear deformation of bridges is calculated using the creep correction coefficients m_{xy}, m_{yz}, m_{xz}. In this study, we consider shear creep by using three series of coefficients: 0.5, 1.0, and 1.5 times the standard axial creep coefficient. The factor of 1.0 times the standard axial creep coefficient means the shear creep coefficient is identical to the standard axial creep coefficient. Likewise, the factors of 0.5 and 1.5 indicate that the shear creep coefficient the computation used is 50% smaller or larger compared with the standard axial creep coefficient. The analysis is divided into three cases based on
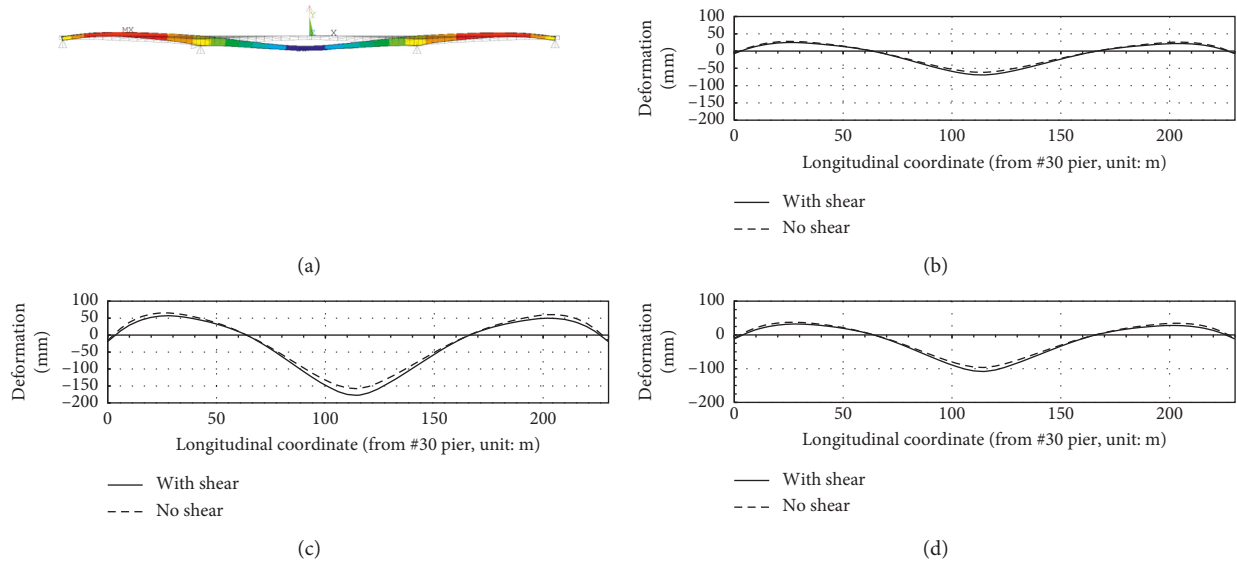
(a)

(b)

(c)

(d)

Figure 4: Long-term deformation of the prototype bridge. (b) Age: 0 days. (c) Age: 3650 days, absolute value. (d) Age: 3650 days, relative value c–b.

the value setting of the creep correction coefficients m_{xy}, m_{yz}, m_{xz}: (1) 0.5; (2) 1.0, and (3) 1.5.

As shown in Figure 5, the midspan deflection develops rapidly within 5 years (1825 days) after completion of the bridge and more than 90% of the ultimate creep deformation takes place. For example, in the case of 1.0 shear, the midspan displacement is 104.4 mm at 5 years and sags only slightly more to 110.6 mm at 20 years. When the shear creep coefficient increases, the trend of the bridge deformation remains the same, but the deflection value increases. The long-term deflection has a linear relationship with the shear creep coefficient (Figure 5(a)). For example, in the analysis of the midspan long-term deformation of 20 years, the mid-span deflection increases from 110.5 mm to 116.4 mm (by approximately 5%) with the shear creep coefficient increasing from 1.0 to 1.5.

4.3. Effect of Different Degrees of Prestress.

The long-term deflection of the bridge consists of two parts: the prestressing camber and the dead load deflection, both of which contain shear creep components. To analyze the shear and creep effects on bridges with different degrees of prestress, the stress of the prestress tendon is taken as a parameter for analysis.

As shown in Figure 6, the change in the degree of prestress has an obvious influence on the elastic deflection and long-term deflection of the middle span. For every 10% reduction in the degree of prestress, the initial elastic deflection and long-term deflection increase by approximately 10%. The results show that the effect of shear creep remains stable even when the degree of prestress is different. In the calculation of long-term deformation of the bridge, the displacement accounted for by the shear creep is 10.5–12.5% larger than that without considering the shear effect. It can be seen that, for the same bridge, a unified amplification factor can be used to consider the effect of shear creep when the degree of prestress is different.

To further illustrate the influence range of shear deformation, a continuous rigid-frame bridge model with a 270 m main span is established. The height of the section over a pier is 14.17 m, and the midspan section is 3.2 m high. The detailed structural parameters of the bridge can be found in the relevant literature [1]. The long-term deformation at 20 years is calculated as shown in Figure 7. The long-term deformation value increases by approximately 14.6% considering shear creep. In conclusion, combined with the analysis of 100 m and 270 m main span concrete continuous girder bridges, the long-term deformation deflection calculated by the planar frame system program can be multiplied by the magnification factor of 1.13–1.15 to consider the effect of shear creep.

There are corresponding specifications and suggestions for the calculation of long-term deformation of concrete structures in specification and codes, including the limit value and calculation method. In terms of the limit value, CEB-FIP [22] ensures stiffness by limiting span-to-height ratio, while Chinese codes adopt the method of limiting the final value of long-term deformation, which is consistent with AASHTO [23]. The creep formula of the JTG 3362-2018 code [19] is similar as CEB-FIP. In addition, a simplified method for calculating the final value of long-term deformation is provided, in which the short-term elastic deflection is multiplied by the long-term growth factor η_θ, and the obtained value is related to the strength of concrete. According to the above analysis, if the elastic deflection is calculated by the planar frame system program, the long-term deflection magnification factor affected by shear creep should be considered.

4.4. Effect of Vertical Prestress.

Because a box section is often used in long-span concrete girder bridges, the spatial stress characteristics are remarkable. In addition to longitudinal prestressing tendons, transverse prestress of the flange and
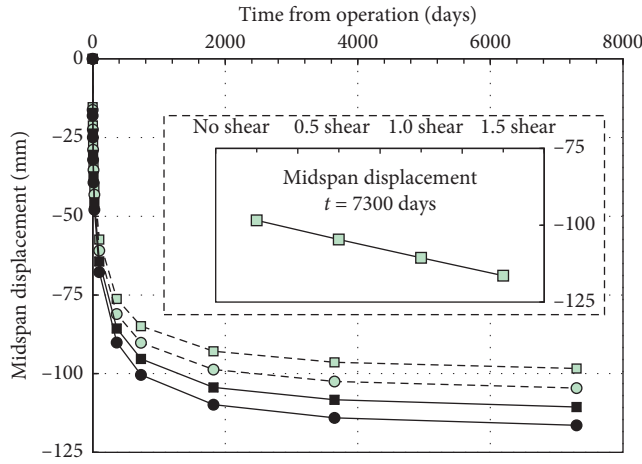
(a)
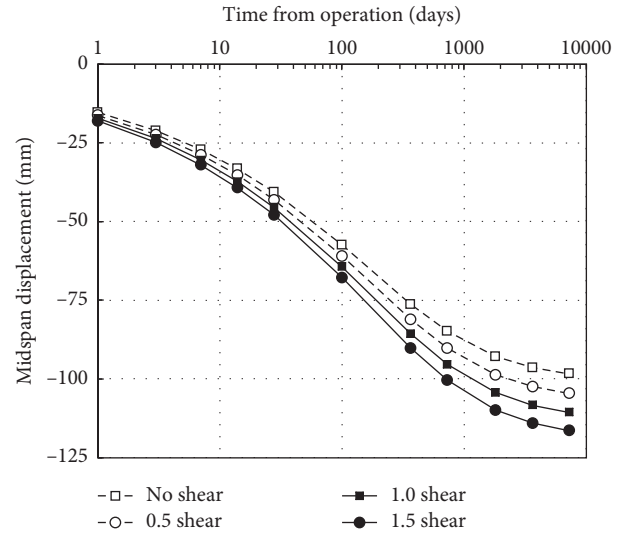
(b)

FIGURE 5: Deflection of midspan with different shear creep coefficients. (a) Linear coordinates. (b) Logarithmic coordinates.
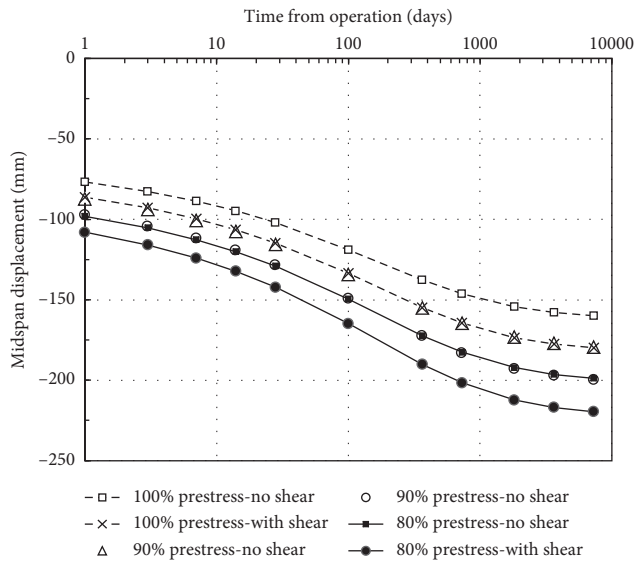
FIGURE 6: Deflection of midspan with different degrees of prestress.

FIGURE 7: Long-term midspan deflection of a continuous rigid bridge with a main span of 270 m.

vertical prestress of webs are also set up to form a three-dimensional prestressing system. Vertical prestressing can improve the shear capacity of the cross section. In some bridge designs, the downward bending of webs is cancelled for the convenience of construction so that the shear capacity is completely provided by the concrete and vertical prestressing. For service performance, the role the vertical prestressing can play in long-term deformation is studied. We compare two cases: (1) setting up vertical prestressing tendons using tensioning and (2) setting up vertical prestressing tendons without tensioning. The results show that, even considering shear creep, the application of vertical prestressing has no effect on the long-term deflection (the calculation results are consistent with the

previous results, so they are not listed). The reason is that according to the equivalent load method, the vertical prestressing force is equivalent to two vertical concentrating forces on the top along the box girder section, which has no effect on the shear force on the structure and has little effect on the stiffness of the structure, so it cannot reduce the long-term deformation of the structure. It can be seen that the increase in vertical prestressing force can only increase the shear capacity of the superstructure but cannot reduce the long-term deformation. In addition, the long-term loss of prestressing near the top of the middle pier is relatively large, the loss at which in 20 years is approximately 3.7%, whereas at other locations, it is less than 1%, as shown in Figure 8.
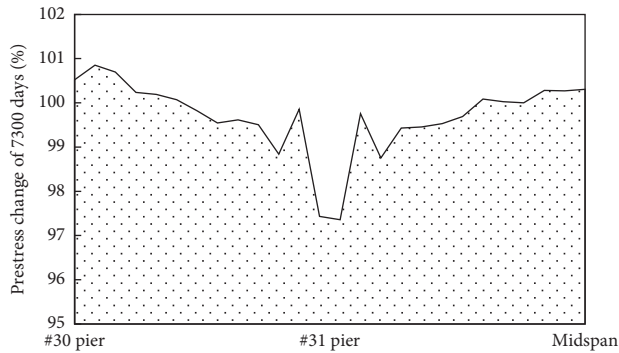
FIGURE 8: Prestress loss distribution of vertical prestress (half structure).

5. Conclusions

How to accurately predict the long-term deformation and mechanical characteristics of long-span concrete girder bridges is of great importance. In this paper, the conclusions on the influence of the studied shear creep are as follows:

(1) A three-dimensional creep calculation program based on the superposition principle is developed by MATLAB and ANSYS, which provides a separate interface for the shear creep coefficient. The analysis of the prototype bridge shows that the long-term deformation increases by 12.5% after shear creep is considered. It is suggested that the long-term deformation be calculated by multiplying the magnification factor of shear creep of 1.13–1.15 based on the analysis results of the general planar frame program.

(2) The parameter analysis of the shear creep coefficient shows that the long-term deformation of long-span concrete girder bridges is proportional to the shear creep coefficient. The shear creep effects of bridges with different degrees of prestress are close, so a unified amplification factor can be adopted.

(3) Vertical prestressing has no effect on the shear creep and long-term deformation of bridges. The long-term loss of vertical prestressing with time is relatively large at the pier top section.

(4) The three-dimensional creep calculation method in this paper considers the age variation in concrete and the influence of the shear creep coefficient, which can provide a reference for the fine analysis of creep of concrete bridges.

The long-term deflection of long-span concrete girder bridges is a complicated engineering problem involving materials, design, construction, maintenance, and management. Attention is confined herein to the calculation error with the limitation of the linear elastic stage of materials. It has been found that the deflection of concrete bridges is accompanied by cracks, which indicates that the stress of concrete is approaching or exceeding the ultimate strength. In such case, it will be unsafe to use the assumption of linear creep. There is an urgent need for accurate consideration of the effect of nonlinear creep on the behavior of long-term deformation in subsequent research.

Data Availability

The measured data included in the article are freely available.

Conflicts of Interest

The authors declare no conflicts of interest.

Acknowledgments

References

[1] Z. P. Yang, G. X. Zhu, and W. Li, "Long-term deflection investigation of prestress concrete rigid bridge," *Highway*, vol. 49, no. 8, pp. 285–289, 2004.

[2] Z. H. Lou, "Main faults in large span beam bridges," *Journal of Highway and Transportation Research and Development*, vol. 23, no. 4, pp. 84–87, 2006.

[3] Y. W. Niu, X. F. Shi, and X. Ruan, "Measured sustained deflection analysis of long-span prestressed concrete beam bridges," *Engineering Mechanics*, vol. 25, no. S1, pp. 116–119, 2008.

[4] I. N. Robertson, "Prediction of vertical deflections for a long-span prestressed concrete bridge structure," *Engineering Structures*, vol. 27, no. 12, pp. 1820–1827, 2005.

[5] J. Xie, G. L. Wang, and X. H. Zheng, "Review of study of long-term deflection for long span prestressed concrete box-girder bridge," *Journal of Highway and Transportation Research and Development (English Edition)*, vol. 2, no. 2, pp. 47–51, 2007.

[6] X. Q. Meng, L. F. Wei, J. C. Zhang et al., "Study of down warping in the midspan of long-span rigid frame bridge," *World Bridges*, vol. 41, no. 2, pp. 76–79, 2013.

[7] F. W. Wang and X. F. Shi, "Study on long-term deflection control of large span prestressed concrete girder bridge," *Shanghai Highways*, vol. 25, no. 1, pp. 29–32, 2006.

[8] H. J. Li, J. Liu, R. X. Wang et al., "Effect of segmental joints on structural deformation in long-span prestressed concrete box girders," *Journal of Basic Science and Engineering*, vol. 21, no. 3, pp. 562–568, 2013.

[9] J. Wang, J. C. Zhao, and L. X. Liu, "Numerical relationship between creep coefficient and creep deflection coefficient of prestressed concrete beams effected by partial pre-stressing ratios," *Journal of Zhengzhou University (Engineering Science)*, vol. 34, no. 5, pp. 26–30, 2013.

[10] J. Q. Bu and J. C. Cui, "Impacts of prestress loss on the deflection for large-span prestressed concrete continuous girder bridges," *Journal of Railway Engineering Society*, vol. 31, no. 7, pp. 57–61, 2014.

[11] Z. P. Bažant, Q. Yu, and G.-H. Li, "Excessive long-time deflections of prestressed box girders. II: numerical analysis and lessons learned," *Journal of Structural Engineering*, vol. 138, no. 6, pp. 687–696, 2012.

[12] G. H. Cao, S. Zhang, W. Zhang, and X. R. Peng, "Long-term deflection test and theoretical analysis on cracked prestressed

concrete box beams," *KSCE Journal of Civil Engineering*, vol. 22, no. 2, pp. 688–695, 2018.

[13] T. Guo and Z. Chen, "Deflection control of long-span PSC box-girder bridge based on field monitoring and probabilistic FEA," *Journal of Performance of Constructed Facilities*, vol. 30, no. 6, pp. 4016053–4016110, 2016.

[14] Y. W. Niu, X. F. Shi, and X. Ruan, "A Finite element analysis method of concrete structure with three dimensional creep," *Journal of Tongji University (Natural Science)*, vol. 37, no. 4, pp. 475–480, 2009.

[15] H. D. Huang, Z. F. Xiang, and J. L. Zheng, "Refined analysis of three-dimensional creep effect for PC box-girder bridges," *Journal of China Highway*, vol. 26, no. 5, pp. 108–114, 2013.

[16] Z. T. Lv and Z. F. Pan, "Issues in design of long-span prestressed concrete box girder bridges," *China Civil Engineering Journal*, vol. 43, no. 1, pp. 70–96, 2010.

[17] W. X. Zhang, Z. T. Tan, and K. Xue, "Analysis of shrinkage and creep of reinforced concrete based on ABAQUS," *Journal of Xi'an University of Architecture & Technology (Natural Science Edition)*, vol. 47, no. 3, pp. 347–353, 2015.

[18] R. I. Gilbert, *Time Effects in Concrete Structures*, Spon Press, Newyork, NY, USA, 2011.

[19] CCCC Highway Consultants Co., Ltd, *Code of Design of Highway Reinforced Concrete and Prestressed Concrete Bridges and Culverts JTG 3362-2018*, China Communications Press, Beijing, China, 2018.

[20] M. Pouraminia and M. Ghaemian, "Shape optimization of concrete open spandrel arch bridges," *Građevinar*, vol. 67, no. 12, pp. 1177–1185, 2015.

[21] Y. W. Niu, H. E. Cao, Y. Y. Tang, and T. Wang, "Concrete torsion shear creep experimental method and application," *Journal of Tongji University (Natural Science)*, vol. 47, no. 7, pp. 475–480, 2019.

[22] CEB-FIP, *Model Code 1990 (Design Code)*, Thomas Telford Press, Lausanne, Switzerland, 1993.

[23] American Association of State Highway and Transportation Officials, *LFRD Bridge Design Specifications*, American Association of State Highway and Transportation Officials, Washington, DC, USA, 8th edition, 2017.

Research Article

Strengthening and Rehabilitation of U-Shaped RC Bridges Using Substitute Cable Ducts

Adam Svoboda [ID]**, Ladislav Klusáček, and Martin Olšák**

Institute of Concrete and Masonry Structures, Brno University of Technology, Veveří 331/95, 602 00 Brno, Czech Republic

Correspondence should be addressed to Adam Svoboda; svoboda.a@fce.vutbr.cz

The presented paper deals with strengthening and rehabilitation of U-shaped reinforced concrete bridges from the period of 1905–1930 using post-tensioning, which is a suitable, reliable, and durable method. These bridges have two main beams pulled over the bridge deck, which is supported by cross girders. The cross girders connect the two main beams forming a half-frame in the transverse direction, which provides spatial rigidity to the structure. The spans of these bridges are usually between 15 and 25 m. The high efficiency of post-tensioning can be seen on many implemented applications for bridge reconstructions worldwide. However, in this paper, the post-tensioning method is extended by a unique structural system of substitute cable ducts that allows for significantly expanding applicability of this method on existing concrete bridges. This method is highly recommended due to minimization of interventions into the constructions, unseen method of cable arrangement, and hence the absence of impact on appearance, which is appreciated not only in case of valuable historical structures but in general as well. In conclusion, the post-tensioning by monostrands in substitute cable ducts is a highly efficient method for strengthening of existing bridges in order to increase their load-bearing capacities in terms of current traffic load and to extend their service life. This method was also verified by monitoring the behavior of rehabilitated bridges before and after strengthening.

1. Introduction

Reinforced concrete beam bridges have been built since the very beginnings of reinforced concrete. Both simple and continuous parapet bridges represent a suitable structural option of beam bridges because of their small construction height (U-shaped bridges, camelback bridges, and trough girder bridges). These structures have been developed near Michigan, USA, and soon they have spread in Europe as well [1]. There is still a couple of hundred of these structures around the roadways in the Czech Republic [2].

The oldest U-shaped bridges were built between 1905 and 1915, and they were designed in accordance with the Austrian Ministry of Railways Bridge Standard of August 1904 [3]. At that time, the largest load the road bridges had to endure on the primary roads was an $18\,t$ $(180\,kN)$ steamroller or a uniformly distributed load of $460\,kg/m^2$ $(4.6\,kN/m^2)$ over the surface of the bridge [4]. This bridge type was very popular up until 1930, but from the standpoint

of current traffic demands upon bridge structures, it usually does not comply because of its load-bearing capability and an efficient strengthening and total reconstruction has to be performed upon bridge structure [5]. These concrete bridges are also valuable from the historical standpoint because they represent a legacy of the first generation of reinforced concrete bridge engineers.

1.1. Reinforced Concrete Bridge Strengthening Using the Substitute Cable Duct Method. Post-tensioning is a suitable, reliable, and durable method for reinforced concrete bridge strengthening. A strengthening system using post-tensioning effects has also been discussed in previous studies and applications; for example, Recupero et al. [6, 7] presented an application of external prestressing technique for strengthening a single-span concrete railway bridge in Italy. The effect of strengthening was also researched with the help of numerical simulations. Nilimaa et al. [8] focused on

strengthening of concrete railway bridges (in Sweden) in the transverse direction using prestressed bars installed in additionally drilled holes in the existing concrete. Petrangeli et al. [9] published a paper focused on strengthening of the continuous reinforced concrete bridge in 1976 in Ethiopia across the Gibe river using external prestressing tendons. Daly and Witarnawan in articles [10, 11] presented two applications of strengthening composite (steel-concrete) bridges in Indonesia using external prestressing and also discussed key parameters for designing such a system. Woodward and Daly [12] examined the effect of external prestressed tendons within an experiment on a bridge model of a 1 : 4 scale. The experimental load tests have shown that the post-tensioning method provides a safe and stable method of strengthening. Dai et al. [13] examined the strengthening technique with double-layer prestressed steel wire ropes (PSWRs) to enhance the serviceability of an existing concrete box girder. Miyamoto et al. [14] studied the behavior of prestressed beams strengthened with external tendons. In the presented paper, simply supported prestressed composite girders with alternating prestressing levels, eccentricity of tendons, and tendon properties are examined. Mimoto et al. [15] developed a strengthening system using post-tensioned tendons with internal anchorages in the existing concrete. The internal anchorage hole is made using a special drilling machine, and the system provides joints between the existing and additionally cast concrete parts. Other researchers focused on post-tensioning of concrete using FRP elements; for example, Lee et al. [16] and Jung et al. [17] presented a post-tensioned FRP near-surface mounted system for strengthening of existing structures without changing its dimensions. The strengthening effect was investigated both experimentally and numerically. Aravinthan and Heidt [18] studied innovative methods for strengthening of bridge headstocks using post-tensioned fibre composite wraps as an alternative to steel prestressing tendons. Some scientists deal with the comparison of prestressing methods using steel tendons or FRP elements; for example, Choi [19] examined effective stresses of concrete beams strengthened using CFRP and external prestressing tendons. The strengthening effect of external tendons was found to be significantly greater in comparison with CFRP. Also, RC beams strengthened with external tendons showed small difference between the analysis and experimental results compared to beams strengthened by the CFRP method.

However, none of the cited authors applied the post-tensioning method for strengthening the described U-shaped RC bridges. Researchers at the Brno University of Technology (Czech Republic) have developed the substitute cable duct method, whose structural design pushes the limitations of historical structure prestressing.

Basic structural arrangement of prestressing cables in beam bridge strengthening using the method of substitute cable ducts is shown in Figure 1. After a previous detailed diagnostics, usable spaces between reinforcement are determined and substitute cable ducts are drilled through the beams. The direction and distribution of ducts is intentionally selected so that the anchorage area could be created above or behind the bearing axis, and the

distribution of saddles was selected at 1/5 to 1/4 from the theoretical support in compliance with the static calculation. Preparatory works for cables are finished by creating the saddles in such a manner that the radial forces of the cables are directed straight into the concrete of the retrofitted structure, and the complex and unclear transformation of forces is not performed. After prestressing, the anchoring areas are filled with concrete and the cables (monostrands) on the bottom side of the beams are covered with an additional concrete covering layer, or they are hidden in the reconstructed original covering layer. The suitability of the method was confirmed for both simple and continuous U-shaped bridges with span lengths from 8 to 25 m [20].

1.2. Cables in Substitute Ducts in Original Beams.

Using the substitute cable duct method leads to a placement of post-tensioning cables and monostrands directly into the concrete of the original beams. The essential requirement of this method is a favourable distribution of the original main load-bearing reinforcement, which provides abundant space for suitable drilling of substitute ducts in the available spaces between the original reinforcements without its interruption, or with just a small decrease in strength, which can be included in the strengthening design calculations and which can be compensated by the post-tensioning effects. This requirement is met relatively often (in most cases resolved by post-tensioning, suitable spaces could be found between the original reinforcements), which is given by the design customs from the time of construction. Use of the substitute cable duct method then provides significant advantages:

(1) Through saddles, the cables lean directly on the concrete of the beams, and therefore, the radial effects of cables directly affect the original structure (practically in the vertical axis of the beams). Therefore, they do not have to be rather intricately transformed by weldments placed on beam sides, or with separately cast blocks with duct saddles.

(2) The saddles can be created very simply as steel sheets (strap steel) bent into the prescribed radius of 1.2 m to 1.5 m, which are mounted into high-strength microconcrete with a full-area anchored saddle.

(3) The prestressing reinforcement (cables composed of monostrands) is completely protected against mechanical damage after subsequent filling of ducts with injection. If this protection is further complemented with additionally anchored cable sheathing in a straight section between saddles on the bottom surface of beams, then the entire prestressing set is hidden in the original concrete and in the newly constructed cover. Therefore, the requirements for perfect mechanical protection of the plastic sheaths of individual monostrands are met. If the stable conditions for primary and secondary protection of prestressing reinforcement are observed, long lifetime (long-term reliability) of this type of strengthening is guaranteed.
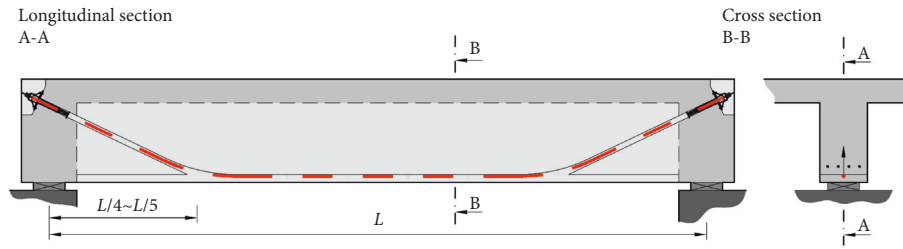
FIGURE 1: The basic scheme of cable arrangement in the case of strengthening a simple span bridge by post-tensioning using the substitute cable duct method.

Substitute cable ducts require drilling of holes into concrete and masonry in lengths multiple times longer than the commonly manufactured machines and tools allow. A special positioning drilling device—a drilling support—was designed and manufactured for this purpose. The main parts of the device are guiding bars and a drilling cart.

The cart allows defined clamping of drilling machines and a transfer of force for provision of the necessary drilling thrust. Together with the cart, the guiding bar allows prolongation of drilling shafts. This device (Figure 2) composed of the cart and the guiding bars provides machine guidance for the drilling machine and decreases strain of the operators of the drilling machine to an acceptable level. Secondly, it also increases the accuracy of drilled cable duct trajectory to the highest degree possible. Thirdly, it allows the operators to set a completely arbitrary trajectory because they can set any angle in both the horizontal plane and the vertical plane (usually an angle towards the longitudinal axis of the load-bearing structure). The drilling support can be axially equipped with both diamond and impact drilling technology, and these can be swapped even during the drilling of a single cable duct. Another advantage of the drilling support is that it can be attached to the retrofitted structure itself. Figure 3 shows a deployment of the drilling support with diamond drilling technique.

Both simple and continuous reinforced concrete beam structures can be strengthened using cables in substitute ducts. In the case of simple structures (usually simply supported beams), the ducts and prestressing reinforcements are arranged in accordance with Figure 1; in the case of continuous structures, they are arranged in accordance with Figure 4. Continuous structures can be efficiently tensioned with continuous raised cables, tensioned from both sides. In accordance with static requirements, these cables can be complemented with noncontinuous cables, anchored in a composite slab or in anchoring blocks (extensions), which will be placed between the original beams.

In monostrand prestressing, the coefficient of friction μ, which is used only in saddles in this distribution, has the value of 0.06 to 0.10, which was repeatedly verified during prestressing of structures strengthened in this manner by comparing the calculated and the achieved monostrand extension sizes. The friction does not apply in direct sections of cable trajectories (in such case, monostrands mostly lead almost linearly from saddle to saddle, through air and without friction).

Substitute cable ducts can be drilled into the structure very accurately and with very little damage to the original
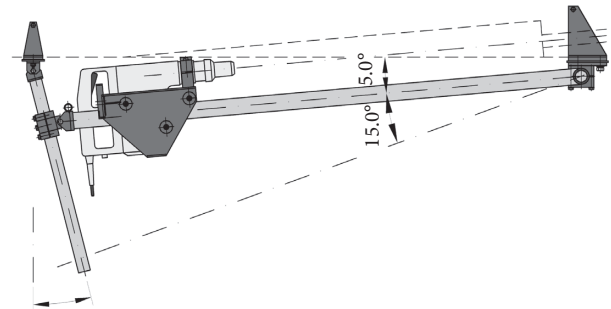
FIGURE 2: Scheme of the drilling support for drilling substitute cable ducts of relatively small diameters ($\phi = 35 \sim 52$ mm) into the concrete of the existing bridge structure. It allows adjustment of both vertical and horizontal drilling angles. The picture shows a support fitted with a drill using the impact technology.

FIGURE 3: A realization of drilling substitute cable ducts on the bottom side of a U-shaped bridge using a drilling support [21]. The photo shows the use of invented drilling support equipped with a drilling machine with the diamond drilling technology. The drilling machine, clamped into a cart, is led by guiding bars in the required angle (both vertical and horizontal) relative to the bottom face of the structure while drilling a duct.

beam reinforcement. Site diagnostic of beam reinforcement, which provides information on the most suitable space for duct drilling, is necessary for drilling the cable duct. The designer defines the position of theoretical points (TP) only in the longitudinal direction, and they let the exact outlets of ducts in the transverse direction of the beams up to the construction process. In many cases, the concrete of the strengthened structure is more damaged by corrosion in the area of the bottom face of the beams that the concrete cover layer has already fallen off and the distribution of reinforcements is
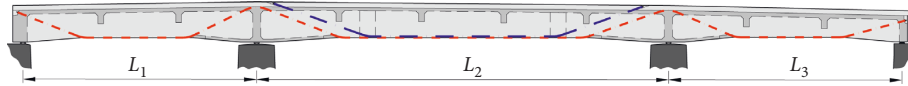
FIGURE 4: The basic scheme of cable arrangement in the case of strengthening a continuous span bridge by post-tensioning using the substitute cable duct method. Also, it is an example of the usage of multiple phases of post-tensioning. The first phase (on the picture described by red dashed lines) creates a possibility for casting an additional concrete composite slab for slab strengthening. The second phase (on the picture described by blue dashed lines) increases the overall load-bearing capacity of the critical middle span.

clearly visible. In other cases, in the area of future saddles, the original cover can be removed because after prestressing, the cables will be protected by the anchored cover and the surfaces of the entire structure are usually retrofitted with a special layer. Figure 5 shows an example of a duct outlet between beam reinforcements of a strengthened continuous beam structure in accordance with project documentation. It shows that suitable space could always have been found and that the substitute ducts could have been prepared without or with minimum damage to the original profiles of the main load-bearing reinforcement.

2. Strengthening of U-Shaped Bridges

U-shaped bridges have two main girders extending above the roadway, and the bridge deck is supported by cross girders. The cross girders connect both main girders, and together with them, they form a half-frame in the transverse direction; the half-frame provides spatial rigidity to the structure. These bridges can also be efficiently strengthened using the substitute cable duct method both in the longitudinal and transverse directions [22]. The spans of these structures are between 15 and 25 mm, and the described strengthening was used in the realized designs, e.g., [21, 23].

The main girders are usually reinforced with the original reinforcement in the amount of 8 to 12 pieces with ϕ of 35 to 50 mm in two or three rows. This provides enough space for substitute ducts. The main girders of U-shaped bridges are regularly strengthened with two to four cables with three to four monostrands in every cable. Similarly to main beams, the transverse girders can be strengthened with cables in substitute ducts anchored on side areas of main girders. Basic distribution of post-tensioning cables is shown in Figures 6 and 7.

U-shaped bridges, built between 1905 and 1930, are suitable structures for strengthening using the substitute cable duct method, which is given by the following structural particularities:

(1) Girder front sides are available for cable anchoring in the main girders (U-shaped). Cable lines can be designed with zero end eccentricity above the supports. The tensioning set can be best anchored in the center of gravity of girders, which contributes to high efficiency of post-tensioning and to a good distribution of forces in anchors into the concrete of the original girders.

(2) Completely free side areas of main girders are available for anchoring of transverse cables (cables strengthening the transverse beams). On the free side areas, the anchoring areas can be created either with

FIGURE 5: An example of a substitute cable duct (ϕ 52 mm) outlet at the bottom side of the beam in a suitable position in a gap between the existing reinforcement.

cut bearing surface (older system) or in the form of cast concrete extension (currently used system, which guarantees both primary and secondary protection of the entire lengths of cables including anchors).

In the U-shaped girder, cables are led through space crossways with regard to both the horizontal and the vertical planes so that the anchors would act in the vicinity of the center of gravity of the end cross section (in the cross-sectional core). The location of cross girder anchors has to be selected carefully because the prestressing forces affect the transverse semiframe; the anchors have to be placed in the center of gravity of projection of the cross girder into the main beam or slightly below it. Then the additional set of forces will be balanced with regard to the semiframe, and it will not stress it adversely in the transverse direction.

Prestressing will efficiently create conditions for the additionally cast composite slab, which, in accordance with the requirements of the investor, strengthens the original bridge deck to as high a load as the U-shaped girders and cross girders can be strengthened.

Figure 6 shows the shape and arrangement of the prestressing system for strengthening the U-shaped bridge with a span length of $l = 16.4$ m on a secondary road for load-bearing class B in accordance with ČSN 73 6203 [24]. The main girders were sufficiently prestressed with four cables; cross girders were prestressed with two cables. Therefore, conditions have been created to carry the weight of an additionally cast composite slab, which strengthened the original bridge deck. This case is also an example of
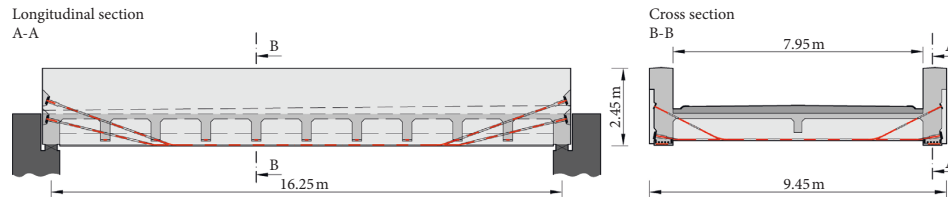
FIGURE 6: Cable arrangement in the longitudinal and transverse directions for strengthening of a U-shaped bridge with straight girders, built in Třebechovice in 1932, according to project documentation [21].
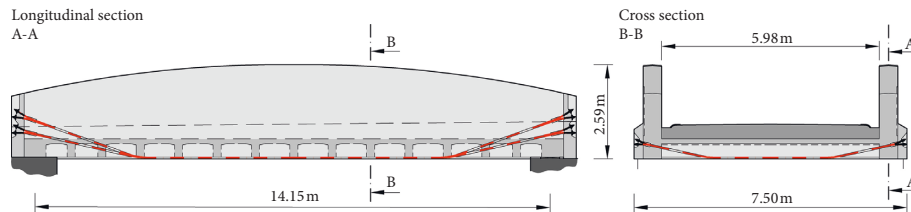
FIGURE 7: Another example of cable arrangement in the longitudinal and transverse directions for strengthening the U-shaped bridge with curved girders which was built in Vražné in 1928 according to project documentation [23].

anchoring using the single-strand wedge with bearing plates without observing the primary protection in anchors (older way). The secondary protection was guaranteed by the usual casting of anchor holes. Figures 8 and 9 show the characteristic details of this strengthening: cable saddles in U-shaped beams and the anchors at the end of these beams [21].

Figure 7 shows the shape and distribution of the prestressing system in strengthening of a U-shaped bridge with variable height of the main beam and a length span of $l = 14.1$ m on a tertiary road also to the load-bearing class B [24]. The main girders were post-tensioned with two cables of four monostrands, the cross girders were post-tensioned with one cable of monostrands. Once again, conditions to carry the weight of an additionally cast composite slab were created. However, this is an example of anchoring using the encapsulated anchor system with an observance of primary protection in anchors (newer, regularly used bridge anchoring system). The secondary protection was once again guaranteed by the usual casting of anchor areas in concrete. Figure 10 shows characteristic details of cable anchors in the main girder and the cross girder anchors at the sides of the main girder [23].

Strengthening of the U-shaped bridges with post-tensioning using the substitute cable duct system generally brings many advantages:

(1) In contrast to the glued reinforcement, which is activated only after load, and therefore does not contribute to the transfer of forces from the permanent load, transfer of prestressing into the structure balances a significant portion of internal forces created by the permanent load; this efficiently improves the condition, in which the structure is not stressed by live load and a necessary reserve is created for the transfer of effects of live load.

(2) The increase of load-bearing capacity by this method is significant, regularly 200%–300%, which

FIGURE 8: An example of the anchorage areas made directly in the existing concrete of the main girders of U-shaped bridge. The strengthening was implemented in 2002, so the old type of anchors was used [21].

is an effect, higher almost by an order than the use of glued reinforcement, for which general experience speaks on an achievable increase of approximately 30% [19].

(3) Cracks created by static or dynamic load in the tension flanges of reinforced concrete beams significantly accelerate the process of reinforced concrete corrosion significantly. The transfer of pressure forces by prestressing leads from a partial to a complete closure of cracks and a subsequent

FIGURE 9: Prestressing tendons composed of individual mono-strands (black HDPE sheaths) on the bottom side of the girder after curvature of their trajectories in saddles [21]. After the prestressing of tendons, the bottom side of the girder is provided with the anchored protective concrete cover layer (the second corrosion protection). The appearance and the concrete character of the bridge are then preserved.
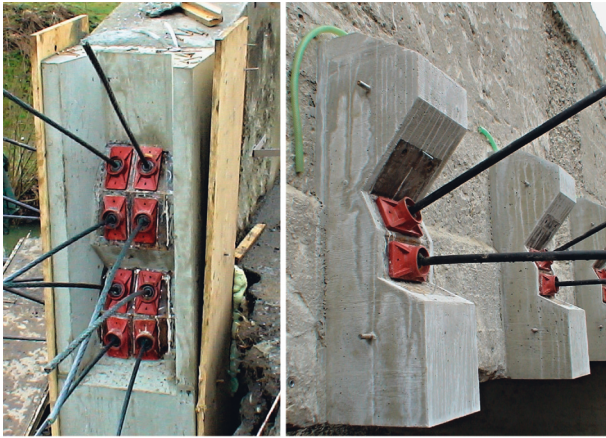

FIGURE 10: Realization of the additional anchorage areas of both main girders and cross girders. In this implementation, a new type of encapsulated single-strand anchors was used (2008). The anchors are covered and protected in concrete extensions [23].

prolongation of the concrete structure resistance against corrosion.

(4) Most construction works connected to this technology can be created without interruption of the traffic on the bridge or only with a partial limitation.

(5) When we strengthen bridges by prestressing, we use the entire prestress level interval. In the case of beam bridge strengthening, the interval usually achieves values of $\lambda = 0.15 \sim 0.25$ (in accordance with Bachmann [25]).

(6) For bridges seemingly irreparable due to their static condition, or if the requested load-bearing capacity cannot be achieved with other methods, and when the bridges are usually demolished and a new structure is built, the required parameters can be achieved using this very method of load-bearing capacity increase for a mere third or half of the price of the new structure [26].

The actual design and performance of strengthening must emphasize the fact that the static strengthening is usually a part of a total reconstruction and of retrofitting of the bridge. It must create prerequisites for reliability and durability of the selected design. That is why the below mentioned measures have to be considered and proposed:

(1) A thorough treatment of the degraded concrete of the entire bridge (surface areas including the plaster), first mechanically and then using a rotating high-pressure water jet.

(2) Careful cleaning of the exposed and corroded steel reinforcing bars in the entire bridge structure, first mechanically and then with a high-pressure water single-jet tool.

(3) Protection of the steel reinforcing bars with silicate materials.

(4) The actual post-tensioning of the bridge structure by both transfer of prestressing and by the composite slab.

(5) Application of the adhesion primer coat on the whole surface of the retrofitted concrete of the bridge.

(6) Rough and finish reprofiling of the bridge load-bearing structure.

(7) Application of a protective and unifying coating on the inner and upper areas of the U-shaped girders.

3. Static Effect of Prestressing Cables in Strengthening by Post-Tensioning

Static effect of prestressing cables, additionally built into the original reinforced concrete structures, is basically the same as the effect of a prestressing reinforcement in regular prestressed concrete [27]. This is achieved because the post-tensioned cables are built into the cross section of strengthened structures using the substitute cable ducts in a manner similar to the new, mostly fully prestressed structures. There are almost no differences in the service stage; in this case, radial effects of the additionally built-in prestressing set manifest themselves positively, while the favorable effect of the actual prestressing force manifests itself as well, but not so clearly. This is given by small, but sufficient prestressing degrees $\lambda = 0.12 \sim 0.25$ [25]. In the stage of ultimate limit state, the main difference lies in the fact that cables composed of monostrands appear to be free (without cohesion with concrete), even if built-in and injected in a cross section. However, the ultimate limit states increase as well by the very additional effect of prestressing forces, which transfer the former sections in pure bending to sections in eccentric compression [28].

3.1. Decrease of Dead Weight Effects. The basic static function of thus designed beam bridge strengthening is shown in Figure 11. It is depicted on a simple structure, and the used approach can be analogically extended to a continuous structure as well. The radial effect of additional
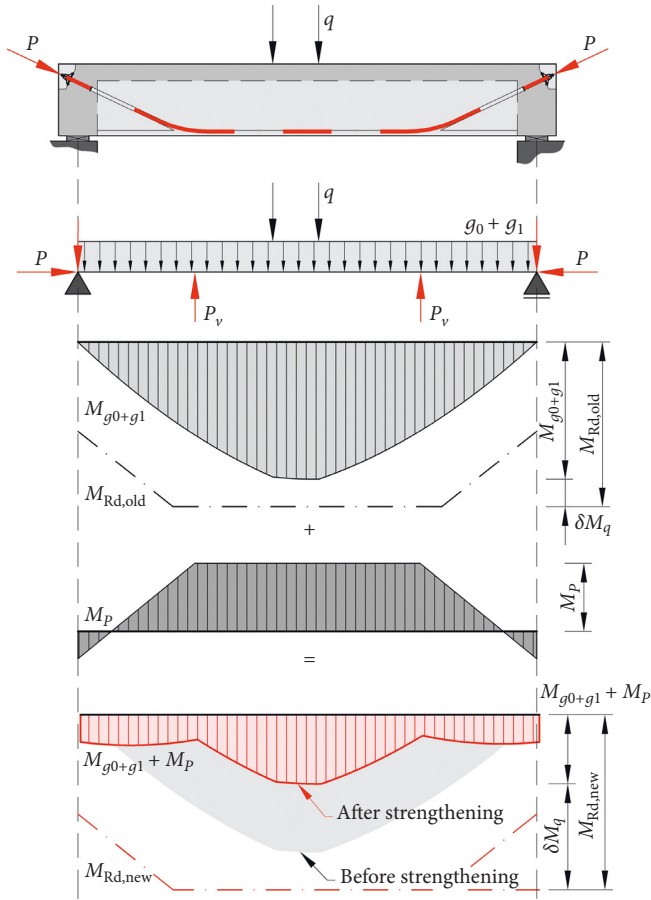
FIGURE 11: The basic scheme of prestressing static effect on the simple span bridge (reduction of dead load bending moments—application of LBM). Prestressing creates a much bigger reserve of bearing capacity which can be used for traffic load, and therefore, the load-bearing capacity is increased. The efficiency of this method is up to 300%.

cables leads to a decrease in the effect of the dead weight. Therefore, the LBM (load balancing method) is subsequently applied [27].

The beam bridge structure is loaded by its own weight g_0, other permanent load g_1 (long-term live load, the weight of all layers of the roadway with possible additional load by the raised and over-layered roadway), and live load q. The live load is usually determined as the load-bearing capacity of the bridge in accordance with the relevant technical standard before the beginning of the retrofitting preparations [29]. The load-bearing capacity of a bridge is defined here; it is determined by the following values: normal load-bearing capacity V_n, reserved load-bearing capacity V_r, and an exceptional load-bearing capacity V_e. In accordance with the respective technical standard, a bending moment of ultimate limit state can be determined for the critical sections of the structure (i.e., the limit, to which the section can be loaded in order not to exceed the maximum load on concrete and steel, set by the standard) [30].

Figure 11 shows which part of the bending moment of the ultimate limit state can be used for the moment of determining the load-bearing capacity of the bridge. The

load decisive for the load-bearing capacity of the bridge before strengthening can cause the highest bending moment M_q, and its total effect is increased by the dynamic coefficient of a moving load δ. In accordance with calculations and studies of several dozens of beam bridges built between 1915 and 1950, the load-bearing capacities of the original bridges come out to be very low. Normal load-bearing capacities V_n are between 8 and 15 t, and reserved load-bearing capacities V_r usually constitute 15 to 30 t, expressed with regard to the moment of bending moment of ultimate limit state; 1/4 to 1/3 of a bending moment of an ultimate limit state of a section can be used for the load-bearing capacity. In the case of overfilled bridges, i.e., bridges, whose roadway was simply raised with other layers of asphalt concrete in the past, this number can be even lower, often 1/10 to 1/4 of the bending moment of ultimate limit state. We can often encounter paradoxic situations, in which the entire moment of ultimate limit state can be consumed by the weight of the bridge itself, or the limit can be even lower. In terms of calculations, such a structure cannot even carry its own weight. It is clear that a collapse will not occur because of the internal reserves in the materials and sections, but the structures exploited in this way then lack the safeties guaranteed by standards and even a regular traffic overloads them and all the related negatives ensue (sagging, cracks, and vibration). This leads to a decrease of lifetime of such overloaded structures.

As shown in Figure 11, bending moment effects of suitably designed post-tensioning efficiently decrease bending moments from permanent load. The following inverse proportion applies to the bending moment stress determining the load-bearing capacity of the bridge: the decrease of bending moment effects of permanent loads (g_0, g_1) caused by bending moments since prestressing M_P is inversely proportional to the portion of the total bending moment of the ultimate limit state which can be used. Even with a small level of prestressing, the bending moment gain of thus-strengthened structures is significant and many times larger portion of the bending moment of ultimate limit state than before strengthening can be used for the determining bending moments of the ultimate limit state after structure prestressing. It can be stated that

$$M_{\text{Rd,new}} = (2\sim3)M_{\text{Rd,old}}, \qquad (1)$$

where $M_{\text{Rd,new}}$ is the largest moment determining the load-bearing capacity for structures strengthened with prestressing, $M_{\text{Rd,old}}$ is the largest moment determining load-bearing capacity on the original, nonprestressed structure.

If the usable moments $M_{\text{Rd,new}}$ after strengthening are multiple times larger than moments $M_{\text{Rd,old}}$ before strengthening, the load-bearing capacity of thus-strengthened beam bridges increases as well. The load-bearing capacity can commonly be increased by 200 to 300% in comparison with the original values before strengthening. Slab bridges were also strengthened, and in their case, 10 times higher normal load-bearing capacity values and 6 times higher reserved load-bearing capacity have been achieved.

3.2. Section Load-Bearing Capacity Increase. Axial component of prestressing force has a minor effect upon real section strengthening and therefore on the increase of the bending moment of the ultimate limit state. In accordance with Figure 12, the section originally in pure bending changes to a section in eccentric compression, which is accompanied by an expansion of the compressed area of concrete section x. This fact causes a minor increase in the bending moment of ultimate limit state in accordance with Figure 13.

Prior to strengthening, the bent bridge beam section is characterized by a pair of internal forces $N = 0$; $M = M_{Rd,old}$. In accordance with the size of the moment M in effect, its current stress can be expressed only on the horizontal axis of the failure function π. After strengthening, stressing force P is transferred into the section. In accordance with the achieved degree of prestressing λ, any horizontal line in the marked area inside the failure function π applies to the strengthened section. The intersection of this line and the failure function π is given by the pair $N = P$; $M = M_{Rd,new}$. The following statement must apply to every horizontal line in the marked area (thus for every nonzero P) on the basis of shape of the failure function π:

$$M_{Rd,new} > M_{Rd,old}, \tag{2}$$

where P is a prestressing force transferred by post-tensioning during strengthening, $M_{Rd,old}$ is the section bending moment of ultimate limit state prior to strengthening, and $M_{Rd,new}$ is the section bending moment of ultimate limit state after strengthening with prestressing force P.

Increase of height of the compressed area x of the strengthened section increased the ideal moment of inertia around the most stressed sections. Theoretically, this leads to a decrease in structure sagging (the structure becomes stiffer), which was also experimentally measured and confirmed (paragraphs 5.1 and 5.2 of this article). Attention should be paid to the fact that, for the used low levels of prestressing, the movement of the neutral axis is relatively small and the corresponding increase of the ideal moment of section inertia is only 10 to 15% in comparison with the original. We can never expect full prestressing of the sections. Their deformation behavior after strengthening is basically the same as before (crack openings occur again in the tensioned flange because of the other, nonbalanced portion of permanent loads and live loads), but their widths will decrease and sagging will slightly decrease because of the effect of the live loads.

It is clear that even in low levels of prestressing, the effects of beam bridge strengthening are significant. The load-bearing capacity values increase to multiples of the original values after strengthening. Even the mere decrease of influence of the dead weight of the structure (for example, by removing the overfilled layers of roadway), which also releases a part of the bending moment of ultimate limit state, can be surprisingly used very scarcely. The vertical alignment of the roadway is mostly the decisive factor because it is given by the connection before and after the bridge. Its decrease on the bridge causes large and therefore financially demanding modifications of long stretches of the road. Alongside the beam strengthening, the bridge deck often has to be strengthened as well so that it could withstand the wheel pressure of the cars. Additionally cast slabs, which can be efficiently designed to the very structure strengthened by prestressing, can be used for this purpose because the increase of the dead weight with an additionally cast slab can be eliminated by the very post-tensioning.

The intents to only increase the load-bearing capacity of a bridge with minimum costs because of the limited financial means are also frequent. In such cases, this is a very efficient method because all the layers of the original roadway can be kept on the structure. The fact that this strengthening can be performed under almost normal operation of the bridge with minimum demands upon traffic limitation is also worth mentioning. Substitute cable ducts as well as saddles are mostly created from the bottom part of the structure, usually with no interruption of operation of the bridge. The performance of the anchoring areas and prestressing can be performed gradually (one half of the bridge after another) because the character of post-tensioning using the subsequent cable duct method is structurally similar to the assembled structure.

3.3. Shear Forces Reduction. Similarly, the shear forces are efficiently reduced by prestressing. The reduction is depicted in Figure 14. The section above includes an example of a typical basic course of shear forces to permanent loads and a load corresponding with the V_n set. The middle section describes a course of shear forces from prestressing which has the opposite sign. The resulting reduced course of the shear forces is stated in the section below. The larger is the distance between the saddle and the support, the smaller is the angle of the cable against the axis of the beam and the smaller are the shear forces, which are able to reduce the original shear forces and which are affected by the prestressing cable. From the standpoint of the shear forces, it would be better to create saddles closer to the support; from the standpoint of bending moment, it would be better for the saddles to be as far away from the support as possible. Even though the specific design depends on many other factors of structures generally very diverse in terms of dimensions and composition, the results of as-yet designed and realized strengthenings lead to a discovery that the ideal distance for distribution of saddles in a length is in the interval from 1/5 to 1/4. This applies to both simple and continuous structures [31].

Structures with haunches require special attention. If the haunches are linear, then the beginnings of haunches mostly correspond to the abovementioned recommendation. In the substitute cable duct method, the saddles can be placed in the haunch ends. If the haunches are longer (for example, parabolic haunches often reach $l/3$), it is necessary to use separately cast blocks between beams and place those in the recommended spaces.
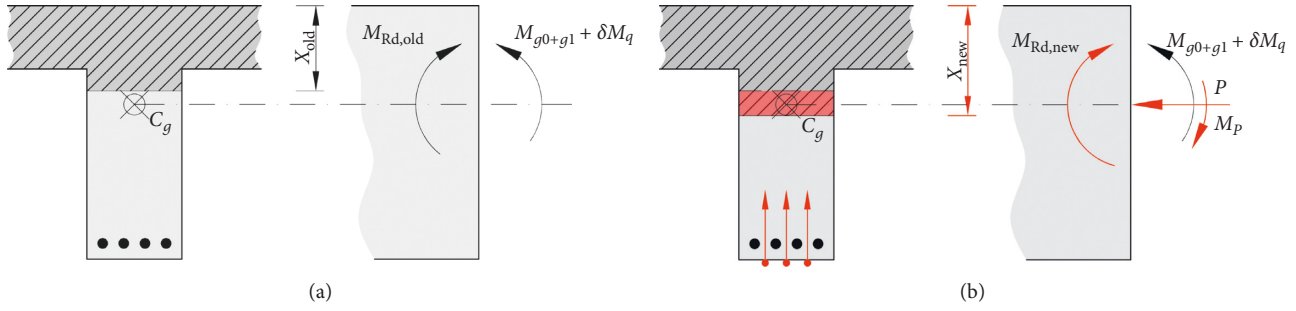
(a)

(b)

FIGURE 12: Expression of the prestressing effect on the beam structure cross section. The beam cross section and its internal forces (pure bending) (a) before and (b) after application of prestressing force. The cross section is now eccentrically in compression (a combination of bending moments and axial force), thus increasing the load-bearing capacity of the cross section.
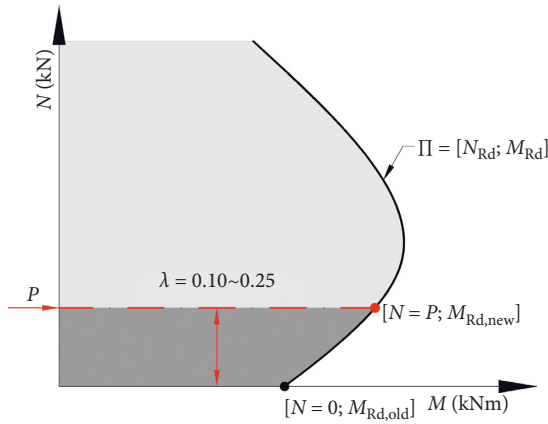
FIGURE 13: Increase of the load-bearing capacity of the cross section in the interval of partially prestressed concrete $\lambda = 0.12 \sim 0.25$ expressed by the interaction diagram (failure function π [25]).

FIGURE 14: The basic scheme of reduction of shear forces due to the radial effects of prestressing cables in polygonal trajectory in the case of strengthening the simply supported beam according to Figure 11.

4. Diagnostics, Design, and Strengthening Performance Process

4.1. Diagnostics of the Current Bridge Structure. In the diagnostics for bridge strengthening, it is necessary to determine the following:

(i) Reinforcement of the current sections of beams, cross girders, and slabs in the center of their length, or above the supports of the continuous structure. It is necessary to determine the amount, diameter, and locations of the individual reinforcement profiles including spaces between them as the source data for decision whether the substitute cable duct method can be used.

(ii) Reinforcement of the current sections of beams, cross girders, and slab in supports. It is necessary to determine the amount, diameter, and locations of the individual reinforcing profiles in order to determine the number of raised shear reinforcement. The raised shear reinforcement (bent profiles) can be swung out from the vertical plane, and they can partially intersect with the trajectory of the substitute cable duct. That is why it is better to select those spaces between reinforcements which are not

trimmed with bends. In bridge slabs, it is necessary to determine how much reinforcement is raised in the support; this usually constitutes 1/3 or 1/2 of the total amount of profiles.

(iii) Strength of the concrete of the load-bearing structure at least with nondestructive impact method (Schmidt) with specification using test core drilling. The NDT itself is not sufficient because, in older structures, it usually provides concrete strengths of one or two classes higher than the final ones after specification. The permissible stress of concrete under anchors has to be derived from the determined strengths. The concrete strength significantly codetermines the bending moment of ultimate limit state of the current section.

(iv) The concrete elastic modulus has to be determined if a verification of behavior of the bridge structure after strengthening with a stress test can be expected. In the case of historical bridge constructions, the modulus of elasticity varies depending on the possibilities of concrete production at that time and especially on the placing, processing, and compacting of the concrete mixture. In practice for

the design and calculations of strengthening, the concrete elastic modulus can be tentatively substituted with standard values or value derived from the elastic modulus, acquired from the speed of ultrasound penetration on concrete samples taken for the purpose of structural tests. It is important to keep in mind that the accurate modulus of elasticity estimation requires detailed approaches as the modulus of the elasticity value modifies as shown in [32]. However, even more important phenomenon than the variable modulus of elasticity is the uncertainty of the weakening of the cross section through cracks, but it is very difficult to determine that for historical structure [33].

(v) Using a probe drilled into the roadway, determine the thickness of roadway and all layers above the load-bearing structure. The determination of robustness of roadway layers has to be performed at least with probing drillings with suction, core drillings with core removal, performed with diamond drills, or with dug roadway probes using diamond drills. The roadway probe can be used to determine the exact thickness of the load-bearing structure (slab or bridge deck of the beam structure). In order to determine thickness, we can either use accurate leveling or (preferably) a probe drilling through the load-bearing structure. The determination of layers above the load-bearing structure is essential for determining the total dead weight $g_0 + g_1$.

(vi) The condition and functioning of bridge bearings. An important piece of information for the calculation of effects of the prestressing force and for the determination of the extent of the total repair of the bridge.

(vii) Geometrical dimensions (geometry) of the bridge structure. Determined as a part of diagnostics, or as an independent part of design preparation of bridge strengthening (retrofit).

4.2. Structural Design of Strengthening. In the structural design of strengthening, the prestressing force shall be determined as well as the location and amount of prestressing reinforcement with regard to the structural options, provided by the specific reinforcement and dimensions of the structure. The structural design can be performed roughly in accordance with the following items:

(1) Creation of a numerical model of the structure and an analysis of internal forces upon the current structure. Calculation of the load-bearing capacity of the current structure.

(2) Determination of stress of the concrete and the current reinforcement in the service stage with a determination of the ratio of dead weight upon the final material stressing, majority of reinforcement.

(3) Determination of the effect of designed prestressing (mostly by the equivalent set of forces from prestressing) [27], an analysis of internal forces on the numerical model using prestressing.

(4) Calculation and verification of the load-bearing capacity of the strengthened structure. If the first design of the prestressing set should not reach the intended values of load-bearing capacity, the procedure has to be repeated from the point 5 until it is reached.

(5) Verification of stresses during prestressing and in the service stage. If the stress assessment yields unsatisfactory results, the prestressing set has to be replaced (shapes and number of cables, prestressing design in phases in accordance with the retrofit progress) and the procedure has to be repeated again from point 4.

(6) Verification of ultimate limit states and service limit states of individual critical sections, inspection of deformations (possibly also widths of cracks).

For the construction analysis, it is sufficient to use mostly beam models, or possibly plate models and currently regular software using the FEM. From the geometric and physical standpoint, the analysis can be performed in the form of common linear calculations. This is given by the relatively small stresses, which are transferred into the original structures, and rigid, massive sections of the strengthened structures.

4.3. Structural Details of Strengthening. In beam structures with two beams in a cross section (U-shaped bridges), original reinforcements with ϕ of 50 to 60 mm are used, and correspondingly, there are larger spaces, through which the substitute cable ducts with ϕ of 52 mm for prestressing cables with three or four monostrands can be led. Figure 9 shows an example of a realized cable in accordance with [21].

Cross girders of the U-shaped bridges usually have to be prestressed with only one monostrand, or with two monostrands in the case of a span above 6 m.

On the basis of the designed prestressing reinforcement layout, the cable duct drilling scheme is processed (Figure 15) and all the necessary information are stated. These include the following:

(1) The location and distances of theoretical points (TP) for drilled ducts.

(2) The geometrical parameters (lengths, slopes in the vertical plane with regard to the horizontal plane, and in plan with regard to the axis of the beam (bridge, slab)).

(3) The design includes a definition of maximum deviations from theoretical axes prescribed for drilling. Actually, we can prescribe and achieve maximum deviations under one diameter of a cable duct on the length of the performed drilling or ± 30 mm on duct length.

Longitudinal section

Plan
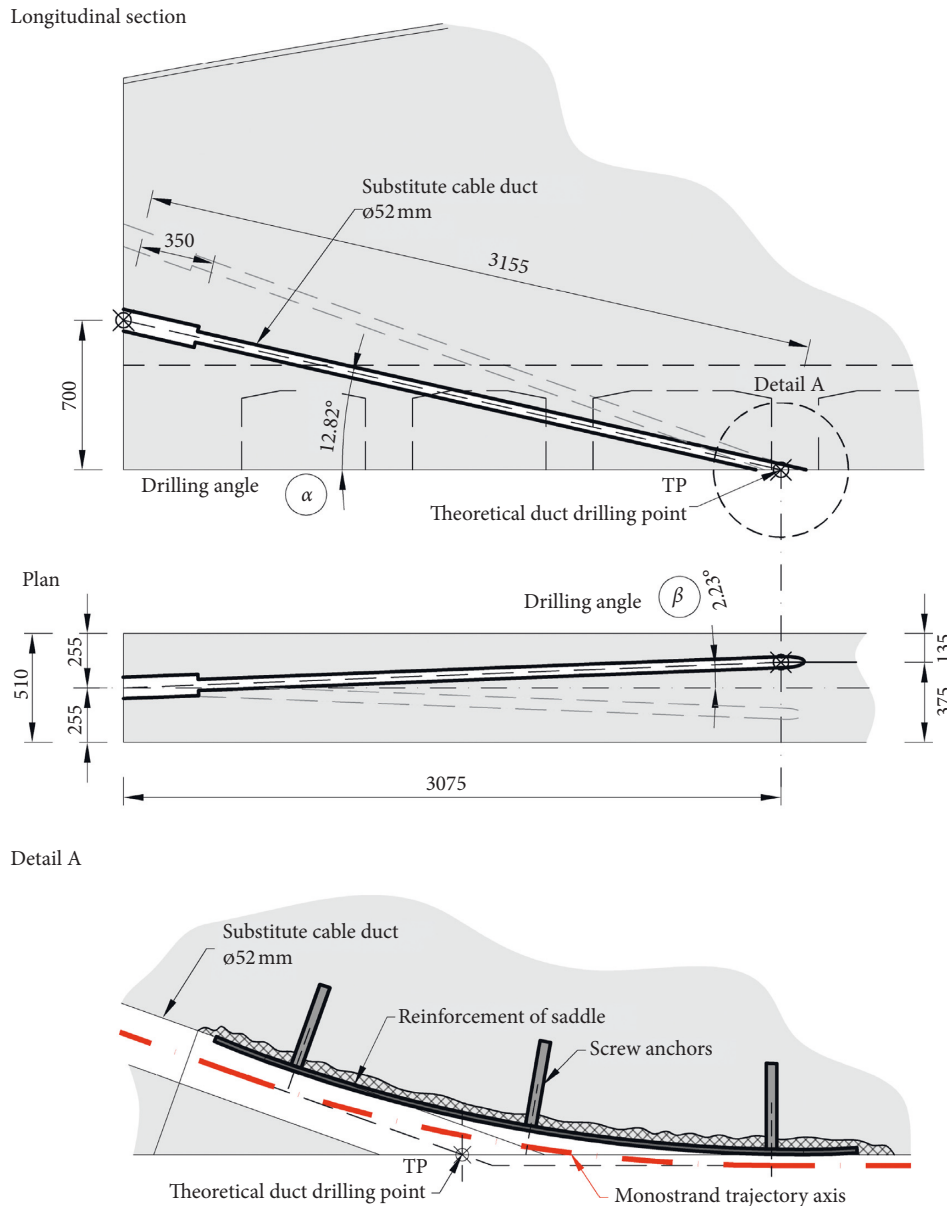
Detail A

FIGURE 15: An example drilling scheme for drilling substitute cable ducts. It describes both the vertical (α) and horizontal (β) angles for drilling ducts. The details of the saddle are also shown.

The design of bridge strengthening must include a saddle (deviator) design (Figure 15) with the statement of all parameters necessary for performance and reinforcement of the saddle and for designing the anchoring areas. It is necessary to consider the feasibility of cutting bearing surfaces for anchor-bearing plates in the original concrete from the structural and spatial reasons (whether or not it is possible to perform planar cuts). Anchoring areas in regular beam and slab bridges can be cut from bridge deck above; in the case of U-shaped bridges with anchors placed in the front side of girders, the cutting can be performed from beam side areas. Unless the anchoring areas can be created in the original concrete of the retrofitted structure, they have to be designed as additional cast (concrete extensions). Anchoring

using concrete extensions is suitable for the hiding of encapsulated anchors.

4.4. Preparatory Works for Structure Prestressing. The preparatory works stand for drilling of substitute cable ducts, construction of cable saddles, and preparation of the anchoring areas. In U-shaped bridges, preparatory works can be performed without almost any limitations to the traffic. This is a huge advantage of this technology, appreciated especially in traffic structures. In contrast, the alternative use of cast anchoring areas requires exclusion of the bridge operation (spatial reasons, vibrations caused by traffic, and their effect upon concrete hardening). The works can be

performed from revision scaffoldings built under the bridge, or from suspended work platforms, if the bridged-over obstacle is a river with high water level.

4.5. Structure Prestressing. After performing the structural details, the prestressing reinforcement can be passed through the ducts. Monostrands and the cables composed of them can be passed through the structure of regular lengths (up to 25 m) manually by pulling them into the ducts, or you can use a pulling head and pull the monostrand into the trajectory (of the duct) with a winch; if the winch is used, the pulling head has to be used as well. The head carries the plastic sheath of the monostrand with it and prevents its falling off from the steel monostrand itself. After pulling the prestressing reinforcement into the ducts, the proper cause of action is to attach the assembly to the strengthened structure. By attaching the assembly to the structure, dead lengths of the monostrand, through the duct is immediately followed by an attachment of steel-bearing plates and anchors.

Prestressing of the structure is usually performed with a hollow single-strand prestressing jacks. In accordance with the structural calculations, either we can prestress from one side (two cable bends are sufficient to cover this), or from both sides. Prestressing from both sides is usually suitable for three or more cable bends (occurs in continuous structures). In prestressing, it is necessary to measure the actual extension of the prestressing reinforcement and to compare the measured values to the theoretic (calculated) extension. The prestressing record shall form a part of the relevant project documentation. It is also recommended to measure the sagging of the structure during prestressing in order to determine a match between deformation behavior of the structure and the behavior of the structure, expected in the structural calculation.

4.6. Protection of the Prestressing Reinforcement and Its Parts. After prestressing the bridge structure, the strengthening process must be completed with a protection of the prestressing reinforcement. Its durability is only guaranteed if it is placed in a concrete section. This can be achieved with an additional covering or with a reprofiling of the original, usually unsafe cover with pieces falling off. In both cases, the covering layer of concrete (or retrofitting material) has to be reinforced and anchored to the structure. Mere cohesion based on the adhesion to the original concrete usually does not suffice because the surfaces of structures before retrofitting are usually damaged by water leaking and the related degradation of surface layers of the concrete, whose tensile strengths are too low.

Figure 16 shows a covering layer with reinforcement and anchoring to the structure. Reinforcement with a welded wire mesh with $\phi 6 \times \phi 6 \, \text{mm}/100 \times 100 \, \text{mm}$ is sufficient; the mesh limits cracking by shrinking of the thin added layer. M12 expanding screw anchors, fitted into holes with ϕ of 15 to 16 mm, are sufficient for anchoring to the structure. M12 screwed steel can be used in joining of anchors and cover reinforcement before the application of the reprofiling
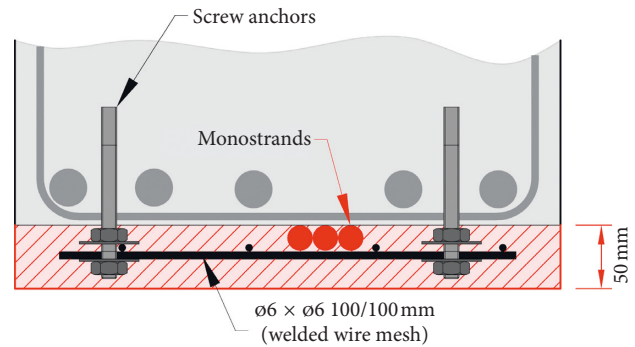

Figure 16: The arrangement of additionally anchored protective concrete covering layer (secondary corrosion protection of monostrands).

layers. Anchors glued from regular reinforcement with ϕ of 8 mm can be used into holes with ϕ of 10 mm. In this way, monostrands and their HDPE sheaths are protected from mechanical damage (random damage, for example, by floating objects, but even by an intentional vandalism) and the sheath also provides protection against heat to a certain degree (possibly even against open flame).

The protection of the anchoring areas can be designed by casting and bridge hydroisolation. As a matter of principle, it is necessary to recommend at least a structurally reinforced cover, which provides maximum protection against formation of cracks by shrinking the new concrete at the point of contact of the original and the new concrete. However, before casting and insulating, substitute cable ducts including passages through anchor wedges and jaws have to be injected. Epoxy sealant (older solution, not used any more), or, alternatively, a modified cement injection mortar, can be used for injection of ducts and anchors. The purpose of injection is to fill all additionally created spaces in the structure with injection material with passivating function against reinforcements (alkaline reaction) so that the water leaking into the structure could not enter the spaces and possibly condensate. In this case, the filling of spaces represents the function of secondary protection of the reinforcement, while the reinforcement sheath with passivating grease can be considered a primary protection of the reinforcement. The completely filled anchoring area (anchoring chambers) also have to be protected with a restored or newly created bridge hydroisolation. Even though no closer researches have been performed, under the condition of standard quality of work, this post-tensioning protective system on strengthened bridges can be considered sufficient for all intents and purposes. This statement was verified by retrofitting of bridges, e.g., [21, 23], in which no corrosion was observed.

In some cases, because of the technological possibilities of diamond cutting, the anchor cannot be embedded sufficiently deep into the original material of the structure so that it would be completely covered with concrete. In such cases, it can be protected with a reinforced concrete extension. The concrete extension reinforcement is connected to the bearing plate under the anchor with welded

joints and the concrete extension is therefore anchored by the prestressing force itself. Similarly, the concrete extension can be anchored into the original concrete with expanding screw anchors, but only if its surface quality is acceptable. It is necessary to emphasize that without concrete extension reinforcement anchoring, its durability is not guaranteed and concrete extensions cast in this manner are incorrect.

From the mid-1990s, encapsulated anchor systems were available for cables from monostrands, developed by world manufacturers of prestressing technology [34]. Anchor encapsulation is in fact its complete enclosing with exact plastic mouldings and a rubber transition piece from the monostrand to anchor body so that the technological water from the concrete could not penetrate to the anchor wedge and jaws. The anchor also consists of a plastic cover, which is attached to the anchor after prestressing (to the anchoring jaws and to monostrand ends) and which is filled with the same passivating grease which was used for the monostrand itself. In the direction towards the structure, the anchors are equipped with rubber haunches, which closely fit on the monostrands and which provide a waterproof coupling. These encapsulated anchoring systems were developed for prestressing of new monolithic structures with unbonded cables composed of two to four monostrands (base slabs, point-supported floor slabs, etc.). Its slightly profiled bearing surface area is usually cast in concrete mixture.

Encapsulated anchor systems represent another technological advancement in protection of monostrands against corrosion; currently, they are required for any bridge structure strengthening without exception. This is given by the increased corrosiveness of the environment surrounding the bridges. Encapsulated anchors with plane plates can be used the best in cast anchoring areas. Figure 17 shows finished concrete anchorage extensions of transverse cables after complete retrofit of the bridge. In the cut anchoring areas, they can be used after underlying the profile-bearing surface with a high-strength concrete (microconcrete, plastic mortar, etc.).

5. Verification of Structure Strengthening by Measuring of Deformations

The static effect of beam bridge structure strengthening with post-tensioning can be verified by measuring of deformations during prestressing and by a load test before and after bridge strengthening.

Decrease of effects of dead weight with a radial set of forces of prestressing cables decreases the bending moment effects in a structure, which manifests by a decrease of deformations caused by the dead weight, which are measurable as a hogging (negative sagging) achieved in post-tensioning. In the case of simply supported structures, the decrease of internal forces, i.e., the bending moment stress, can be calculated using simple equations in accordance with the theory of elasticity, in which we have to calculate the sections damaged by cracks using their ideal section characteristics. Generally, the FEM beam models can be used.

FIGURE 17: Protection of anchors using additionally cast concrete extensions. An aesthetic solution for anchoring the transverse cables of a U-shaped bridge [23].

The increase of deformation stiffness, created by an increase of ideal moments of inertia, post-tensioned by the structure, is relatively small. However, they can be proven by the very comparison of sagging of the nonstrengthened and strengthened structures, loaded with identical load at identical location. This can be achieved with a stress test performed with identical vehicles before and after post-tensioning of the structure.

During the verification tests (serviceability limit state), the phenomenon of variable elastic modulus is completely eliminated because the same loads are applied to the same structure in the same position. In terms of age of the historic structure and influencing of material characteristics by fatigue and seismicity, we load the structure during static tests at the same time.

Verification of post-tensioning effect can also be done by measuring the dynamic response before and after strengthening in comparison with numerical analyses. At present, the authors of the paper are using accelerometers to measure the dynamic features of bridges strengthened by the substitute cable duct method for determination of modification of the dynamic response due to post-tensioning effects as shown, e.g., [35]. This paper is primarily concerned with the static effect of post-tensioning, and the dynamic behavior of structures is investigated by the authors especially with respect to the verification of the durability of the reinforcing intervention and will be published afterwards.

5.1. U-Shaped Bridge Deformation during Prestressing (1932). A reinforced concrete bridge structure from 1932 has been selected for strengthening and total retrofit after years of operation of the tertiary road. After diagnostic investigation and static recalculation of low load-bearing capacity, the load-bearing structure manifested the following properties: for example, reserved V_r = 12 tonnes—road transport requirement (represented by the investor) was to increase the load-bearing capacity to class B (in accordance with [24]), i.e., to V_r = 40 tonnes [21].

The load-bearing structure with an effective span of 16.3 m was composed of two longitudinal (U-shaped, parapet) beams of 2.45 m high and 0.75 m wide, joined together with ten cross girders with dimensions of 0.65/0.30 m. The

cross girders were monolithically connected with reinforced concrete bearing slab with a thickness of 0.16 m. The concrete of the original load-bearing structure was of a varying quality, and in the calculation of statics, we could certainly take into consideration the C170 strength class (in compressed sections, strength class according to the current standard C12/15). The reinforcement consisted of C38 circular shapes with permissible stress values above 120 MPa for main load and with values above 140 MPa for total load. For the purpose of specification of the calculation, the slab reinforcement was uncovered even above supports, i.e., above cross girders, and the reinforcement of continuous bridge deck was stated even for negative moments. Strengthening of the bridge using prestressing cables composed of sheathed monostrands ϕLs15.7 mm was proposed on the basis of these diagnostic data. The main girders were strengthened with four three-strand cables, and cross girders were strengthened with a single three-strand cable and a single monostrand (Figure 6). The strands were placed partially in substitute cable ducts and partially leaned on the ceiling part of the girders [21].

The strengthening was structurally created by the substitute cable duct system and the prestressing cables were placed into the longitudinal supporting elements (parapets) and even into cross girders (Figure 18). The original bridge deck strengthening was designed in the form of the additionally cast composite slab from reinforced concrete. During the performance of the prestressing works, deformations (hogging) of main (parapet) girders and cross girders have been measured with induction displacement sensors with continuous computer recording during prestressing. The cables were tensioned gradually. First, the cables were tensioned alternately on both main girders. The prestressing of the main girders was followed by prestressing of cross girders in the direction from the center of the bridge span, also alternatively towards both supports. Tensioning forces for each monostrand constituted 192 kN with a period of stress of 3 minutes. The tensioning force was transferred gradually step by step, and the behavior of the structure was observed. The tensioning was performed with a single-strand electrically powered hydraulic jack for 10 hours. In case of all monostrands, the measured extensions fell into the designated tolerance of precalculated theoretical extensions [21].

Figure 19 shows hogging of the bridge (negative sagging) determined in accordance with the course of prestressing works. Between 0 and 6 hours, the cables were alternately prestressed on the main beams. It can be seen that girders have lifted alternately as well and that this phenomenon oscillated around a certain average value. After the termination of prestressing (6 hours after initiation), the negative sagging of both main girders differed only slightly (up to 10 %), and they have almost reached the values of theoretical immediate sagging from dead weight (calculated sagging of 5.0 mm on a grate numerical model; 4.2 mm negative sagging from prestressing). It is clear that the calculated static effect of strengthening (the reserved load-bearing capacity increased from 16 to 40 t) was accompanied with a positive deformational effect of prestressing. In this case, the use of the load balancing method [27] is graphically documented

FIGURE 18: Location and description of deflection sensors in the longitudinal and transverse directions on the U-shaped bridge built in 1932 [21] for the purpose of the static load test.
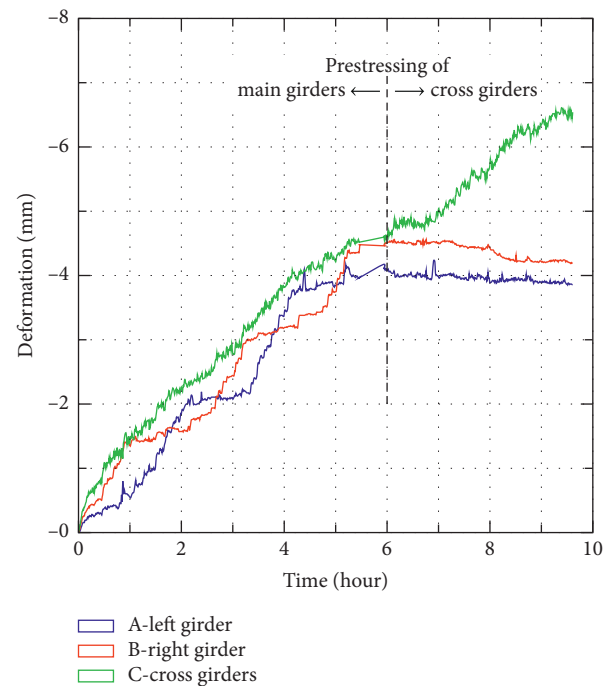
FIGURE 19: Measured deflections of the main girders and the cross girders during prestressing of the structure [21]. The graph shows the deformation effect of post-tensioning and documents an effective transfer of prestressing forces into the structure.

with a reduction of sagging from the structural dead weight of the structure by almost 85%.

During prestressing, the central cross girder as well as the girders deformed negatively. Because of the torsion of the main beams, the deformation of the central cross girder appeared even before the deformations of the main beams. The prestressing of cross girders was performed between 6 and 10 hours after initiation. Interestingly, the negative sagging of the central cross girder increased by practically the same value during prestressing of not only the central

cross girder itself but also all remaining cross girders. This was caused by the bridge deck grate rigidity and the rigidity in torsion of the main girders. The resulting negative sagging of the central cross girder in comparison with the main girders was measured at the value of 2.3 mm.

5.2. Deformation of a U-Shaped Bridge during Prestressing and a Load Test (1928).

The structure in Figure 20 is a single-span U-shaped beam bridge built in 1928 with an effective span of 14.1 m (Figure 7) [23]. Two simple U-shaped (main) girders carry the bridge deck. The bridge deck consists of the grate from cross girders, which carry the bridge deck. The load-bearing structure was built from reinforced concrete. The roadway is overlayered. 100 to 130 mm of asphalt concrete lies on the original roadway layers on average, which significantly increases the dead load of the bridge. During the construction of a nearby highway, the roadway was increased by another 80 mm within roadway modifications. This led to a reduction of bridge traffic to one traffic lane with unsatisfactory load-bearing capacity—e.g., reserved V_r = 18 tonnes.

Bridge strengthening design proposed prestressing with unbonded prestressing cables to at least a load-bearing class B (V_r = 40 tonnes) in accordance with [24]. Main girders and cross girders were strengthened with unbonded prestressing cables laid in substitute (drilled) cable ducts and at the bottom surface of the beams. The overlayered bridge deck was sufficient for the loadbearing class B. The strengthening was performed under regular operation (after reduction to one traffic lane through the center of the bridge) [23].

Four-strand cables in main beams and two-strand cables in cross girders were used for strengthening of the bridge; these cables are composed of monostrands, which are lead in the polygonal trajectory and which were tensioned from both sides. The cables pass through the concrete of the beams via substitute cable ducts in spaces between the original reinforcement. The cables were anchored in the anchoring areas with the single-strand enclosed anchoring system. The spaces above and below anchors were cast in high-strength microconcrete. On the bottom face of beams and cross girders, the cables were protected with reconstructed anchored and reinforced concrete cover layer [23].

Monostrand ϕLs15.7/20 mm1600/1800 MPa (manufactured by Austria DRAHT) prestressing sheathed tendons have been used for prestressing. The monostrands were tensioned to 196 kN with a period of stress of 5 minutes. Single-strand prestressing jacks with a maximum power of 200 kN were used for tensioning. First, the monostrands were tensioned from one side, and then from the other side, once again with a period of stress of 5 minutes. The tensioning started with the outer of the four monostrands in the deviator and ended with the central monostrand. The course of tensioning was set so that the transfer of prestressing forces into main girders and cross girders would be as balanced as possible. At first, cable No. 1 in both main girders were tensioned simultaneously (with a synchronized pair of single-strand tensioning sets), followed by cable No. 2
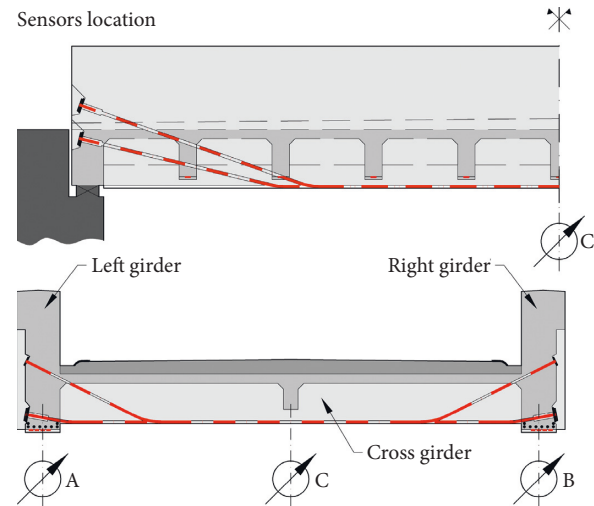

FIGURE 20: Location and description of deflection sensors in the longitudinal and transverse directions on the U-shaped bridge built in 1928 [23] for the purpose of a static load test.
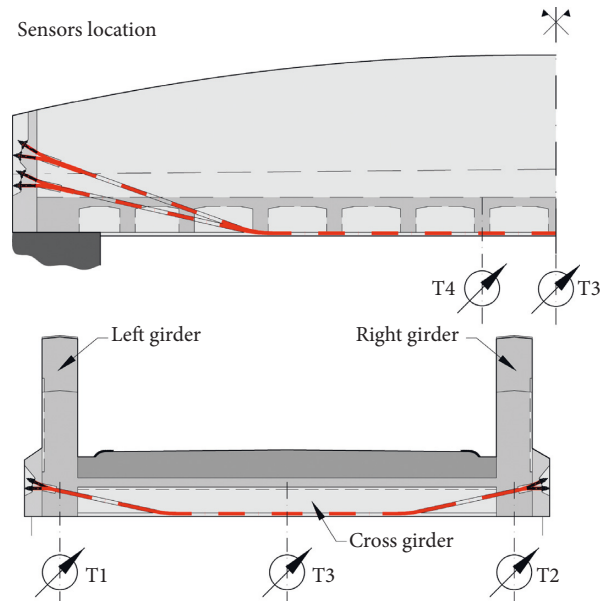
in the main girders and later by cable No. 3 in cross girders, following the course from the central cross girder symmetrically to both supports of the bridge (Figure 7).

The static effect of tensioning was monitored by the load test before strengthening, by measuring the hogging of the structure during prestressing, and by the load test after strengthening. The measurings were performed in the following manner:

(1) Test before strengthening: before strengthening, a load test was performed using two vehicles in the most efficient position so that the structure sagging before strengthening could be determined (Figure 21). The following sagging was measured using a strain gauge: sagging of the right main girder at T1, sagging of the left main girder at T2, and sagging of two central cross girders (Nos. 9 and 8) at T3 and T4.

(2) Deformations during prestressing: during the actual strengthening of the bridge during prestressing, negative sagging (structural raising), achieved by the unbonded cables in the main girders and cross girders, was measured at the aforementioned points.

(3) Test after strengthening with unbonded cables: after strengthening, a load test was once again performed using two identical vehicles in the most efficient location so that the sagging of the structure after strengthening could be determined in the same location in which the sagging was measured before strengthening (Figure 21). The measuring was once again performed by monitoring locations measured during the test before strengthening.

The monitored locations are stated in Figure 20. Figure 21 documents the positions of the test vehicles during the load test performed after strengthening. Figures 22 and 23

(a)

(b)

(c)
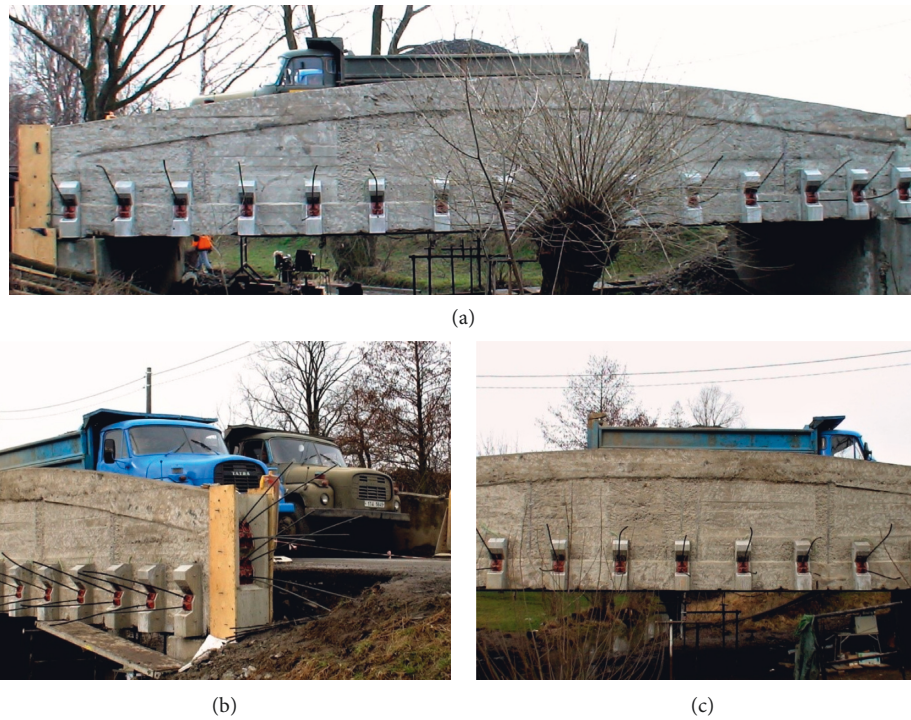
FIGURE 21: Static load test of the U-shaped bridge built in 1928 after strengthening [23]. The position of heavy vehicles (vehicles front and rear axles) in the longitudinal and transverse directions is described on the pictures.

(a)

(b)
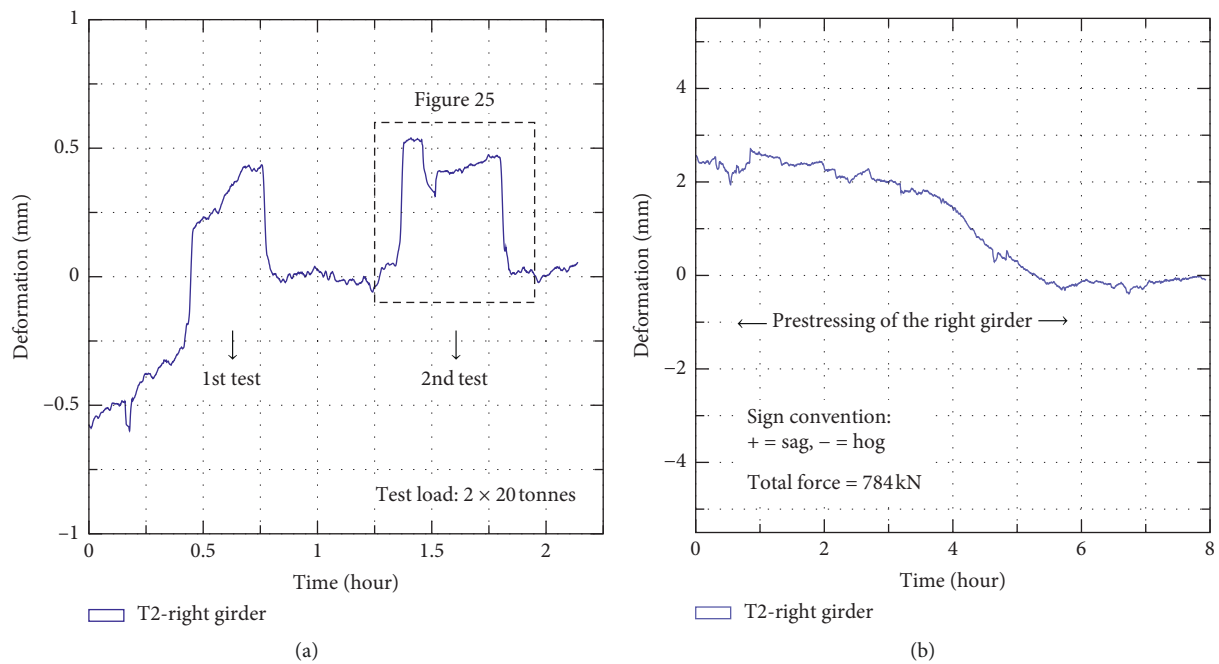
FIGURE 22: Continued.

(c)
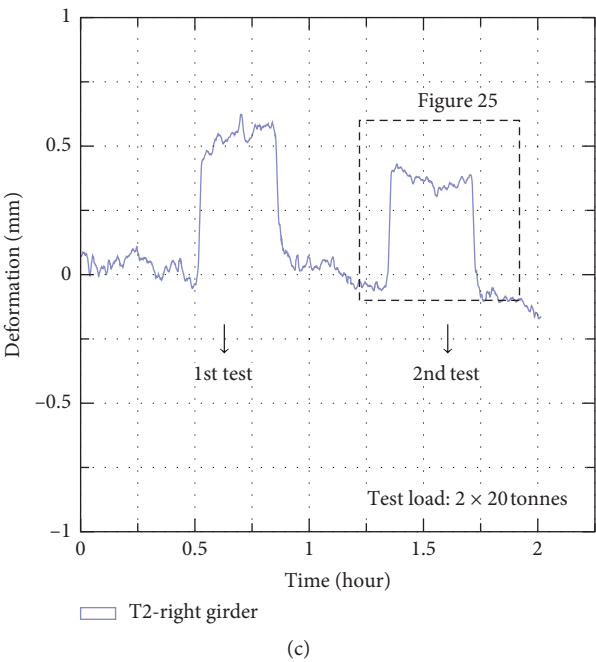
FIGURE 22: Graphs of the right girder (see sensor T2 in Figure 20) deflections (a) before strengthening (static load test with two load cases—heavy vehicles), (b) during prestressing, and (c) after strengthening (static load test with an identical load before strengthening).

(a)

(b)
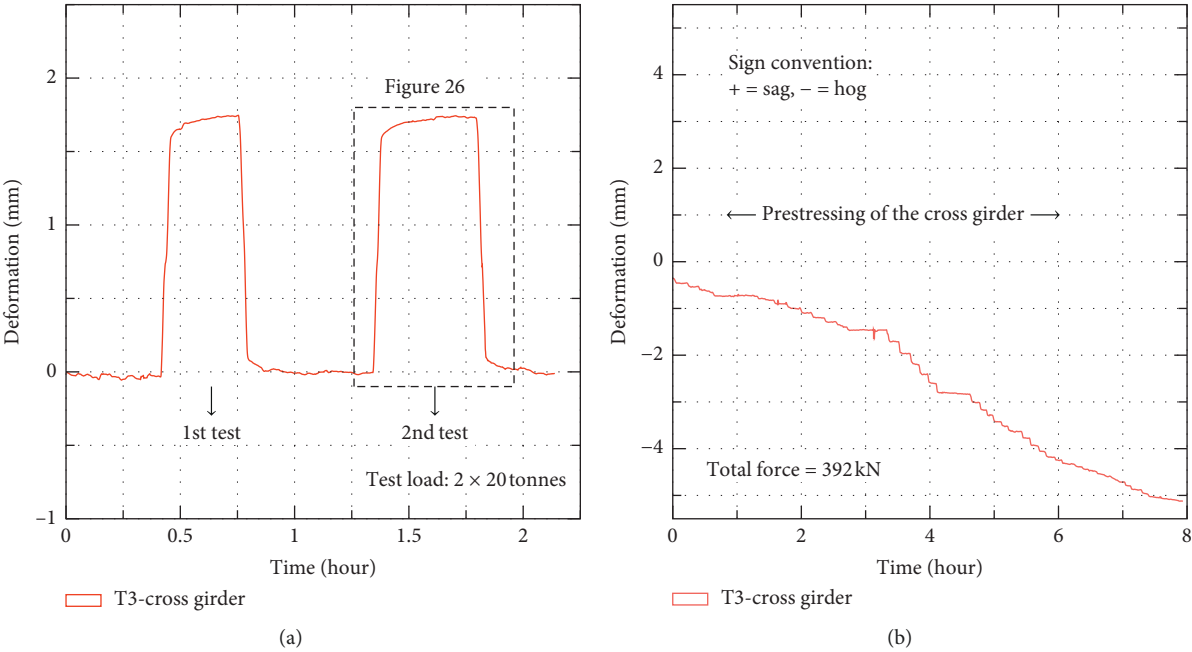
FIGURE 23: Continued.
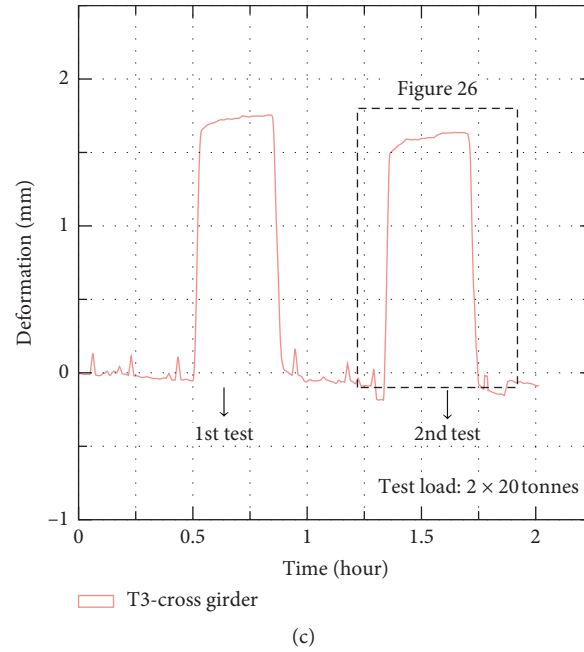
FIGURE 23: Graphs of cross girder (see sensor T3 in Figure 20) deflections (a) before strengthening (static load test with two load cases—heavy vehicles), (b) during prestressing, and (c) after strengthening (static load test with exact the same loading like before strengthening).

show examples from an extensive set of measured saggings and hoggings during prestressing and during the load test using the two test vehicles [23].

Within the evaluation of the strengthening effect, the measured values were averaged. The summary of the resulting values is stated in Figure 24. On the basis of the measured data, strengthening of the load-bearing elements of the U-shaped bridge can be evaluated as follows:

(1) Main girders strengthening: the change of internal forces, which led to an increase of load-bearing capacity of the main girders, and therefore the entire bridge, will manifest itself in the hogging of the main girders and in the ratio of the measured sagging before and after strengthening. During prestressing, the main girders have hogged (bent upward) by 2.4 mm. In the absolute value, this value is a 4.6x higher positive deformation effect than the effect caused by two Tatra vehicles weighing 2×22 t. This proves the high efficiency of the performed strengthening.

(i) After strengthening, the measured sagging of the main girders loaded by identical vehicles has decreased to 86% of sagging before strengthening (Figure 25). This proves the reinforcement of the main girders achieved by the performed strengthening. This is the proof of increase of deformation stiffness of main girders, even if at a low level of prestressing ($\lambda = 0.14$) [25].

(2) Cross girder strengthening: the change in internal forces has also manifested itself in the ratio of measured sagging before and after cross girder

Deflections of the U-shaped bridge structure (mm)				
Part of the structure	Before strengthening	During strengthening	After strengthening	Ratio of average deflections after/before strengthening
Main girder **T1**	0.50	−2.60	−0.47	0.86
Main girder **T2**	0.54	−2.20	−0.43	
Cross girder **T3**	1.75	−5.60	1.50	0.91
Cross girder **T4**	1.78	−5.20	1.70	

FIGURE 24: Assessment of deflections before and after the strengthening of the U-shaped bridge in Vražné, built in 1928 [23]. Note: downwards +; upwards −.

strengthening. The cross girders hogged (bent upwards) by 3.0 mm during the prestressing. In the absolute value, this value is a 2.4x higher positive deformation effect than the effect caused by two Tatra vehicles weighing 2×22 t. This is also an example of the high static efficiency of the performed strengthening.

After strengthening, the measured sagging of the cross girders loaded by identical vehicles has decreased to 91% of sagging before strengthening (Figure 26). This once again proves the cross girder reinforcement achieved by the performed strengthening. This is the proof of increase of deformation stiffness of cross girders, even if at a low level of prestressing ($\lambda = 0.12$) [25].
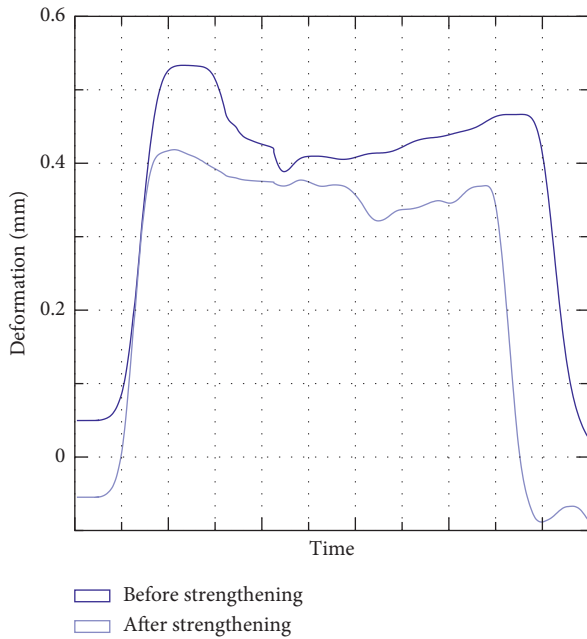
FIGURE 25: A comparison of the measured deflections of the main girder before and after the strengthening with the same test vehicles in the same position on the U-shaped bridge built in Vražné in 1928 [23].
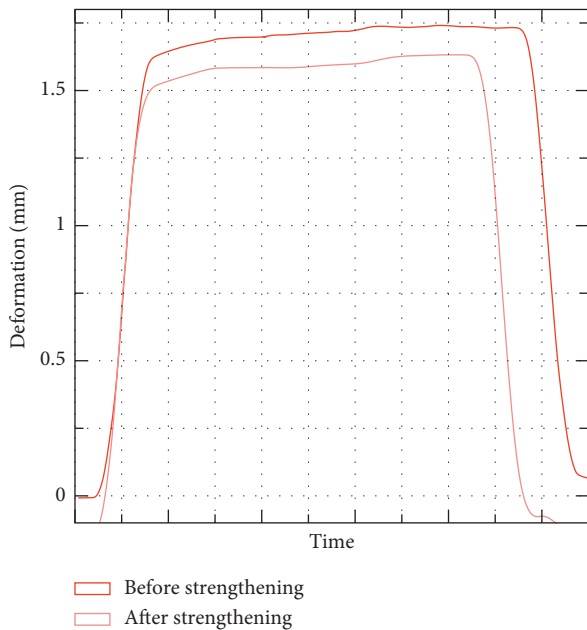

FIGURE 26: A comparison of the measured deflections of the cross girder before and after the strengthening with the same test vehicles in the same position on the U-shaped bridge built in Vražné in 1928 [23].

6. Recommendations for Design and Performance of Strengthening by Post-Tensioning

On the basis of already designed and realized structures and on the basis of measurements performed during prestressing and subsequently during structure loading, the below mentioned recommendations regarding design and the actual performance of the post-tensioning using the substitute cable duct method can be provided.

6.1. Values for Prestressing Losses. If the cables used are composed of monostrands, the coefficient of friction decreases significantly. This is caused by the lower friction of the plastic protective sheaths and the metal components of the saddle and also by the greasing effect of the anticorrosive passivating filling between the monostrand wires and the protective sheath. The passivating filling contains grease or paraffin wax, which limits friction efficiently. Even though the standard documents state the value of the coefficient of friction in a bend to be 0.06 for cables composed in this way, during practical tests performed during tensioning of the strengthened bridges, the value of 0.10 was determined. This value can be recommended for this post-tensioning system, in which the monostrands individually lean on the saddle reinforcement [31].

Single-strand encapsulated anchor systems are used regularly in bridge strengthening (e.g., [34]). The anchoring is performed using self-locking three-jaw wedges in the conical opening of the anchor. During their use, their slipping was measured at 2.60 mm to 2.90 mm while tensioning with the maximum forces of 200 kN. In consideration of slipping losses, 3.0 mm can be considered a safe value. In such a small size, the slipping reach is not significant and the slipping usually disappears already around the location of the first saddle. This allows a design of continuous cables over three or even four span lengths of continuous structures. Tensioning from both sides is used for these cables (respectively, tensioning from one side of the cable, and after anchoring, the cable is tensioned from the previously nontensioned end), and in such case, friction losses remain acceptably low at the center of the cable (usually within 15%).

The losses caused by the elastic shortening of concrete losses are negligible. This is given by the low level of prestressing (average prestressing in the section achieves 1.5 to 3.0 MPa) and therefore also by the very small elastic deformation of the concrete and the entire structure during prestressing. Because the number of tensioned cables is not large, repeated tensioning of already anchored monostrands can completely exclude this loss even in cases in which the exclusion is not advisable. Relaxation losses can be determined the same in a new structure as from prestressed concrete. In regular cases, in which low relaxation monostrands are used almost exclusively, the losses can be disregarded [27].

Losses caused by concrete shrinking can be completely disregarded because during strengthening, the prestressing is being used on concrete structures 80 to 100 years old. Only in the case of strengthening of a combination of post-tensioning and an additionally cast composite slab, the load from prevented concrete shrinking of a new slab should be included in the calculation. Losses caused by concrete creeping can be disregarded in most cases as well. This is

caused by the low level of transferred prestressing and the decrease of compressive stress in the compressed area of the original sections, which is achieved by the very balancing of a part of permanent load of the structure. Alternatively, they can be quantified more specifically using creeping models used by separately developed computer programs for time-dependent analysis of concrete structure creeping [36].

6.2. Recommendations for Structural Details. As regards the saddle radii, we recommend observation of the minimum radius of $r = 1.2$ m and a creation of haunches on the steel strap with a minimum length of 150 mm and a radius of $r = r/4$. Regular sheet steel saddles can transfer radial forces from one to four monostrands without larger structural issues. The saddle shape should be adapted width-wise for the insertion into the cable duct. Saddle length should not be smaller than 400 mm (without haunches) for practical reasons so that it could even be mounted including the required tolerances. The same radii are applied to tube saddles. Tube saddles should be equipped with haunches in the shape of a hollow cone [31].

The diameters of drilled ducts are supposed to be as small as possible, e.g., ϕ of 35 mm is sufficient for single-strand cables and ϕ of 52 mm is sufficient for multistrand cables up to four monostrands. In beam structure strengthening, it is suitable to allow for weakening by interruption of one or two profiles of the original reinforcement in the static design. Cables with even larger number of monostrands are used rarely, and in such case, they must be placed outside of the section (e.g., [6, 9]). Deviations have to be prescribed for duct drilling and for saddle mounting, and the deviations must be fulfilled.

The design of additional concrete covers always has to include anchoring into the original structure. Anchoring with mere cohesion cannot be considered sufficient because of temperature changes of the cables, elastic sagging of the structure, etc. The covering layer also has to be reinforced with welded wire mesh so that the forces would be distributed from the anchors to the entire covering layer.

7. Conclusion

The described method is suitable for rehabilitation (increase of load-bearing capacity, reconstruction, and prolongation of durability) of reinforced concrete U-shaped bridges, which were built between 1905 and 1930 and the original structure of which almost renders other strengthening methods impossible. Efficiently, the main beams and cross girders can be strengthened, and in that manner, the increase of the dead weight connected to the use of a composite slab to strengthen the bridge deck can be balanced. The static strengthening is significant, and it is accompanied with increase of deformation stiffness, which was proven by the performed load tests. In the case of U-shaped bridges, there is no other option to effectively improve their structural behavior without affecting appearances of these unique historical concrete structures.

The presented method of substitute cable ducts can also be used to strengthen other types of concrete bridges with different static schemes and cross-sectional shapes. It can be used for structural securing of the prestressed bridges and masonry vaults.

Data Availability

The data used to support the findings of this study are available from the corresponding author upon request.

Disclosure

Conflicts of Interest

The authors declare that they have no conflicts of interest.

References

[1] N. Holth, "Michigan's unique concrete camelback bridges," 2019, https://historicbridges.org.

[2] Road and Motorway Directorate of the Czech Republic, *Statistical Overviews of the Bridge Database Information System*, Prague: Road and Motorway Directorate of the Czech Republic, Prague, Czech Republic, 2018.

[3] Austrian Ministry of Railways Bridge Standard, *New Bridge Standard: Technical Standard*, Wien: Austrian Ministry of Railways Bridge Standard, Wien, Austria, 1904.

[4] Czech Office for Standards, *First Czechoslovakia Bridge Standard: Technical Standard*, Czech Office for Standards, Prague, Czech Republic, 1923.

[5] European Committee for Standardization (CEN), *Eurocode 1: Actions on Structures—Part 2: Traffic Loads on Bridges (EN 1991-2)*, European Technical Standard, European Committee for Standardization (CEN), Brussels, Belgium, 2003.

[6] A. Recupero, N. Spinella, P. Colajanni, and C. D. Scilipoti, "Increasing the capacity of existing bridges by using unbonded prestressing technology: a case study," *Advances in Civil Engineering*, vol. 2014, Article ID 840902, 10 pages, 2014.

[7] A. Recupero, N. Spinella, and C. D. Scilipoti, "Method for extending life of existing bridge: a case study," in *Proceedings of the 8th International Conference in the Low Carbon Era*, Dundee, Dundee, July 2012.

[8] J. Nilimaa, T. Blanksvärd, B. Täljsten, and L. Elfgren, "Unbonded transverse post-tensioning of a railway bridge in Haparanda, Sweden," *Journal of Bridge Engineering*, vol. 19, no. 3, Article ID 04013001, 2013.

[9] M. Petrangeli, G. Usai, and E. Zoppis, "Bridge repair by external prestress: the Gibe crossing in Ethiopia," *IABSE Symposium Report*, vol. 96, no. 8, pp. 10–19, 2009.

[10] A. Daly and W. Witarnawan, "A method for increasing the capacity of short and medium span bridges," in *Proceedings of the 10th REAAA Conference*, Tokyo, Japan, September 2000.

[11] A. Daly and W. Witarnawan, "Strengthening of bridge using external post-tensioning," in *Proceedings of the Conference of Eastern Asia Society for Transportation (EASTS 97)*, Seoul, Republic of Korea, October 1997.

[12] R. Woodward and A. Daly, *Design of Bridges with External Prestressing: Construction and Testing of a Model bridge*, TLR Report 392, TLR—Transport Research Laboratory, Berkshire, UK, 1999.

[13] L. Dai, L. Wang, M. Deng, B. Wu, R. W. Floyd, and J. Zhang, "Strengthening a 20-year-old post-tensioned concrete box beam with double-layer prestressed steel wire ropes," *Journal of Bridge Engineering*, vol. 23, no. 11, Article ID 05018009, 2018.

[14] A. Miyamoto, K. Tei, H. Nakamura, and J. W. Bull, "Behavior of prestressed beam strengthened with external tendons," *Journal of Structural Engineering*, vol. 126, no. 9, pp. 1033–1044, 2000.

[15] T. Mimoto, T. Sakaki, T. Mihara, and I. Yoshitake, "Strengthening system using post-tension tendon with an internal anchorage of concrete members," *Engineering Structures*, vol. 124, pp. 29–35, 2016.

[16] H. Lee, W. T. Jung, and W. Chung, "Post-tension near-surface mounted strengthening system for reinforced concrete beams with changes in concrete condition," *Composites Part B: Engineering*, vol. 161, pp. 514–529, 2019.

[17] W.-T. Jung, J.-S. Park, J.-Y. Kang, and H. B. Park, "Strengthening effect of prestressed near-surface-mounted CFRP tendon on reinforced concrete beam," *Advances in Materials Science and Engineering*, vol. 2018, Article ID 9210827, 18 pages, 2018.

[18] T. Aravinthan and T. Heidt, "Innovative strengthening technique using post-tensioned fibre composite wraps for bridge headstocks," *Australian Journal of Structural Engineering*, vol. 11, no. 2, pp. 117–128, 2010.

[19] J. Choi, "Comparative study of effective stresses of concrete beams strengthened using carbon-fibre-reinforced polymer and external prestressing tendons," *Structure and Infrastructure Engineering*, vol. 10, no. 6, pp. 753–766, 2014.

[20] L. Klusáček and A. Svoboda, "Strengthening of bridges by post-tensioning using monostrands in substituted cable ducts," *IOP Conference Series: Materials Science and Engineering*, vol. 236, Article ID 012057, 2017.

[21] L. Klusáček, *Rehabilitation Of U-Shaped Bridge n. 2992-2 in Třebechovice. Project Documentation*, Brno University of Technology, Brno, Czech Republic, 2002.

[22] A. Svoboda and L. Klusáček, "Possibility of increasing the load bearing capacity of parapet bridge structures," in *Proceedings of the 24th International Conference Concrete Days 2017 (Solid State Phenomena)*, vol. 272, pp. 319–324, Trans Tech Publications, Switzerland, November 2018.

[23] L. Klusáček, *Strengthening and Rehabilitation of U-Shaped Bridge n. 04732-2 in Vražné. Project Documentation*, Brno University of Technology, Brno, Czech Republic, 2008.

[24] Czech Office for Standards, ČSN 73 6203, *Traffic Loads on Bridges, Technical Standard*, Czech Office for Standards, Metrology and Testing, Prague, Czech Republic, 2010.

[25] H. Bachmann, "Design of partially prestressed concrete structures based on Swiss experiences," *PCI Journal*, vol. 29, no. 4, pp. 84–105, 1984.

[26] A. Svoboda and L. Klusáček, "Strengthening of reinforced concrete bridges by post-tensioning," in *Proceedings of the 12th International PhD Symposium in Civil Engineering*, pp. 923–930, Prague Czech Technical University in Prague, Prague, Czech Republic, August 2018.

[27] T.-Y. Lin and N. H. Burns, *Design of Prestressed Concrete Structures*, John Wiley & Sons, New York, USA, 3rd edition, 1981.

[28] O. Burdet and M. Badoux, "Comparison of internal and external prestressing for typical highway bridges," in *Proceedings of the 16th Congress of IABSE*, Lucerne, Switzerland, 2000.

[29] Czech Office for Standards, ČSN 73 6222, *Load Bearing Capacity of Road Bridges*, Technical Standard, Czech Office for Standards, Metrology and Testing, Prague, Czech Republic, 2013.

[30] European Committee for Standardization (CEN), *Eurocode 2: Design of Concrete Structures. Part 1-1: General Rules and Rules for Buildings (EN 1992-1-1)*, European Technical Standard, European Committee for Standardization (CEN), Brussels, Belgium, 2006.

[31] A. Svoboda and L. Klusáček, "Results of short-term experiments with monostrands in saddles with small radii," in *Proceedings of the 24th International Conference Concrete Days 2017 (Solid State Phenomena)*, vol. 272, pp. 147–153, Trans Tech Publications, Switzerland, November 2018.

[32] C. Chisari, C. Bedon, and C. Amadio, "Dynamic and static identification of base-isolated bridges using Genetic Algorithms," *Engineering Structures*, vol. 102, pp. 80–92, 2015.

[33] L. Wang, L. Dai, H. Bian, Y. Ma, and J. Zhang, "Concrete cracking prediction under combined prestress and strand corrosion," *Structure and Infrastructure Engineering*, vol. 15, no. 3, pp. 285–295, 2019.

[34] Freyssinet Prestressing: Technical Brochure—France: Soletanche Freyssinet Group, 2014, http://www.freyssinet.com.

[35] C. Bedon, E. Bergamo, M. Izzi, and S. Noè, "Prototyping and validation of MEMS accelerometers for structural health monitoring—the case study of the pietratagliata cable-stayed bridge," *Journal of Sensor and Actuator Networks*, vol. 7, no. 3, pp. 2224–2708, 2018.

[36] R. I. Gilbert and G. Ranzi, *Time-Dependent Behaviour of Concrete Structures*, Spon Press, Abingdon, Oxon, UK, 2011.

Research Article

Increasing the Durability and Freeze-Thaw Strength of Concrete Paving Stones Produced from Ahlat Stone Powder and Marble Powder by Special Curing Method

Abdulrezzak Bakis [ID]

Bitlis Eren University, Faculty of Engineering and Architecture, Department of Civil Engineering, Bitlis, Turkey

Correspondence should be addressed to Abdulrezzak Bakis; arezzakbakis@gmail.com

This study highlights an investigation of using construction waste materials, i.e., Ahlat stone powder and marble powder, in fabricating interlocked paving stones. In this study, the durability and freeze-thaw strength of concrete paving stones produced from Ahlat stone powder and marble powder were increased by the special curing method. Six different types of paving stones were fabricated for study and were subjected to two different curing regimes. Tests of water absorption, splitting tensile strength, surface abrasion, and freeze-thaw were carried out for the specimens. In 3 days and at $20 \pm 5°C$ of water curing, the splitting tensile strength was 3.7 MPa, the surface abrasion value was $9.8 \, cm^3/50 \, cm^2$, and the freeze-thaw value was $0.39 \, kg/m^2$ for those interlocked paving stones produced from Ahlat stone powder. After special combined curing, these improved to 3.9 MPa, $17.2 \, cm^3/50 \, cm^2$, and $0.63 \, kg/m^2$, respectively. Accordingly, for interlocked paving stones produced from marble powder, in 3 days and at $20 \pm 5°C$ water curing, the splitting tensile strength, surface abrasion, and freeze-thaw were 3.9 MPa, $7.9 \, cm^3/50 \, cm^2$, and $0.34 \, kg/m^2$, respectively. After special combined curing, these values improved to 4.1 MPa, $14.8 \, cm^3/50 \, cm^2$, and $0.57 \, kg/m^2$, respectively. The findings of this study validate increase in durability and freeze-thaw strength of concrete paving stones with special curing.

1. Introduction

Concrete paving stones, which are widely used in urban roads, pavement, and recreation areas [1], are fabricated by mixing cement, aggregate, water, and additives in certain ratios [2]. The history of parquet road applications could be traced back to as early as the age of the Roman Empire [3]. Currently, interlocked concrete paving stones have been popularized in European and American countries [4]. Concrete paving stones are produced in different grades, such as square cobblestones, tombstones, and interlocked paving stones, the third one being the most common [5].

Interlocked paving stones offer many advantages, compared with concrete and asphalt pavements. First, the need for maintenance and repair is less. Second, the material is economical as only domestic materials are consumed during production. Third, the speed of production and the material capacities are higher. Fourth, they are readily accessible for traffic immediately after being laid on the road. Fifth, a damaged surface can be repaired in a short time by provision of a new paving stone, thus preventing the occurrences of unwanted patch defects on the coating surfaces. Sixth, they can be produced in different colors and shapes, hence, the variability and design flexibility. In contrast, there are a few disadvantages in using these materials. First, although the manufacturing process is easy, the application phase to the road surface is time-consuming and necessitates high-quality workmanship [6]. Second, concrete pavements may weaken over time due to corrosion, erosion, shrinkage, fatigue cracking, or the like [7]. Third, concrete pavements are believed to increase heat waves globally [8].

The most common materials employed in the fabrication of interlocked pavement stones are crushed limestone aggregates. Relatively, this study investigates the use of alternative production materials, namely, waste materials, such as Ahlat stone powder and marble powder.

Ahlat stone is a solid waste that contributes to environmental pollution and waste landfills. Originally known as ignimbrites, Ahlat stone is widely used in Bitlis Province of the Ahlat region and is one of the pyroclastic rocks that contain abundant pumice and volcanic glass due to the explosion of Nimrod crater. Waste Ahlat stone powder is generated in a significant amount after stone cutting in the Ahlat stone quarries. Nevertheless, the presence of pores in the material body gives the extremely low compressive and bending strength, and therefore, such materials cannot be used as aggregates in concrete production. On this basis, Ahlat stone has limited applicability in the construction sector [9] and is rather used mainly as a wall stone in structures. However, the strength of Ahlat stone concrete pavement can be reinforced by mixing Ahlat stone powder with concrete using a special mixing method. Hattatoglu and Bakis stated that Ahlat stone powder was used as ignimbrite powder for producing reactive powder concrete and found out that the maximum compressive and bending strengths of the concrete were 124.99 MPa and 9.18 MPa, respectively [10]. Bostanci investigated the time-dependent weathering performance of various ignimbrites with varying color and textural properties collected from the Nevşehir region against physical and chemical influences. They also evaluated the effect of deterioration on the physical and mechanical properties of the ignimbrite specimens, as well as the capillary water absorption characteristics relative to durability performance [11]. The author of this paper realizes that no study has been carried out yet regarding the use of waste Ahlat stone powder in the production of interlocked paving stones. The Ahlat stone powder investigated herein is of the size range 0.15–0.60 mm.

Besides Ahlat stone, marble is another solid waste that contributes to environmental pollution and forms waste fields [12, 13]. A considerable amount of marble waste is formed upon removal of blocks as marble quarries are processed [14]. In this regard, there is an essential need for the conscientious evaluation of waste materials. Li et al. suggested an alternative technique called the paste replacement method, where marble dust is added as replacement to an equal volume of paste without necessarily changing the paste's mix proportions. Here, they produced a number of mortar mixes with different amounts of marble dust and added these as a replacement of either paste or cement to test the workability, compressive strength, and microstructure of the concrete material. Accordingly, they found that addition of marble dust as paste replacement has improved the strength and microstructure of the manufactured concrete [15]. Vardhan et al. investigated the strength, permeation, and microstructural properties of concrete incorporating waste marble as partial replacement of the fine aggregates and confirmed that waste marble has the potential as an alternate fine aggregate to improve the overall performance of the concrete, as well as for sustainable development [16]. Similarly, several studies investigated the use of marble waste as an additive to cementitious matrix building materials and confirmed that incorporation of marble waste significantly improved the mechanical properties and thermal insulation of concrete [17–19]. Using a special concrete mixing method for marble powder in concrete, the strength of marble

concrete pavement can be increased. Some studies discussed the production of interlocked paving stones using marble aggregate and did not use marble powder in 100% of the aggregates in the production of interlocked paving stones. In this study, marble powder, of the previously mentioned size range, is used in 100% ratio of the aggregates. Specifically, this paper investigates the usability of waste materials Ahlat stone powder and marble in the production of interlocked paving stones. Six different types of interlocked paving stones are produced, under two different types of curing applications. Two curing types, namely, standard water curing and combined curing, were applied for the interlocked paving stones. The literature did not specify any standard for the combined curing of hardened concrete. Therefore, a special combined curing type was applied for the interlocked paving stones.

Many experimental studies have been conducted on durability of concrete and mortar. Pathirage et al. investigated the effect of alkali silica reaction on the mechanical properties of aging mortar bars. Crushed limestone aggregates are used and mechanical properties of mortar at different curing temperatures are evaluated in their study [20].

Water absorption, splitting tensile strength, surface abrasion, and freeze-thaw tests of different types of interlocked paving stones were carried out, and the results were compared with reference-interlocked paving stone concrete under specification limits [21]. The results of this study indicated that waste materials, such as Ahlat stone powder and marble powder, can be potentially employed in the production of interlocked paving stones. The findings of this study validate increase in durability and freeze-thaw strength of concrete paving stones with special curing.

2. Materials and Methods

2.1. Materials

2.1.1. Binders (Cement and Silica Fume). The main material in the production of interlocked paving stones was CEM I 42.5 N Portland cement type, in accordance with TS EN 197-1 standard [22]. The cement material was supplied by Limak Cement Industry and Trade Inc.

A silica fume named MasterRoc MS 610, supplied by BASF Chemistry Industry and Trade Inc., was used in accordance with ASTM C 618 and AASHTO M 307 standards [23, 24]. The physical, chemical, and mechanical properties of the binders used in the production of the stones are shown in Table 1 [25, 26].

2.1.2. Superplasticizer. The material was supplied by BASF Chemistry Industry and Trade Inc. Its properties are listed in Table 2 [26].

A superplasticizer named MasterGlenium 128, which is based on polycarboxylic ether, was used in accordance with TS EN-934-2 + A1 standard [27].

2.1.3. Aggregates Used in Interlocked Paving Stones. Six different types of interlocked paving stones were manufactured for the purpose of this study, as depicted in Table 3.

Table 1: Chemical, physical, and mechanical properties of binders.

Properties	Cement	Silica fume
SiO_2 (%)	19.28	95.83
Fe_2O_3 (%)	2.99	0.37
Al_2O_3 (%)	5.09	0.76
Na_2O (%)	0.18	—
CaO (%)	63.14	0.53
Cl (%)	0.01	—
MgO (%)	1.96	1.29
SO_3 (%)	2.81	0.63
K_2O (%)	0.71	—
Ignition loss (%)	3.22	0.59
Compressive strength (28 days) (MPa)	52.20	—
Initial set (min)	153	—
Final set (min)	206	—
Specific gravity (g/cm^3)	3.13	2.3
Specific surface (cm^2/g)	3067	>150000

Table 2: Properties of superplasticizer.

Properties	Value
Density	1.1 kg/Liter
Form	Brown, liquid
Chloride quantity	<0.1%
Alkaline quantity	<3.0%
pH	6

Table 3: Interlocked paving stone type, code, aggregate type, and size.

Interlocked paving stone type	Interlocked paving stone code	Aggregate type	Aggregate size (mm)
RWC	6-1	Crushed limestone	0–16
RCC	6-2	Crushed limestone	0–16
ASWC	2-1	Ahlat stone powder	0.15–0.60
ASCC	2-2	Ahlat stone powder	0.15–0.60
MSWC	4-1	Marble powder	0.15–0.60
MSCC	4-2	Marble powder	0.15–0.60

In particular, RWC refers to the reference-interlocked paving stone produced from crushed limestone and obtained after 3 days at $20 \pm 5°C$ standard water curing; RCC was obtained by a curing application combined to that for RWC; ASWC was produced from only Ahlat stone powder without coarse aggregate and obtained after 3 days at $20 \pm 5°C$ standard water curing application; ASCC was obtained from a curing application combined to that for ASWC; MSWC was produced from only marble powder without coarse aggregate and obtained after 3 days at $20 \pm 5°C$ standard water curing; and MSCC was obtained from a curing application combined to that for MSWC. Table 3 defines that coarse aggregates were not used in the production of ASWC and ASCC interlocked paving stones; rather, only 0.15–0.6 mm Ahlat stone powder was used as the aggregate.

Likewise, coarse aggregates were not employed in MSWC and MSCC interlocked paving stones; rather only 0.15–0.6-mm marble powder was used as the aggregate. Drinkable city water was for the production.

(1) Limestone Aggregate for the Production of RWC (Reference) and RCC Interlocked Paving Stones. Selected limestone aggregates were employed for the production and were supplied by Adabag Building Industry Incorporated Company. The chemical, physical, and mechanical properties of the aggregates are shown in Table 4 [28], whereas the actual images are depicted in Figure 1.

Note that the aggregates used in the production of the reference-interlocked paving stone (RWC) are crushed limestone within the size range of 0–16 mm, as indicated in Table 3.

(2) Ahlat Stone Powder for the Production of ASWC and ASCC Interlocked Paving Stones. Figure 2 describes the appearance of Ahlat stone powder used in the production of ASWC and ASCC, which were retrieved from the Ahlat Ovakisla quarry.

Tables 5 and 6 provide a list of the chemical [29], physical, and mechanical properties of the Ahlat stone [29].

Table 6 describes the low unit weight of Ahlat stone, reflecting the stone's porous structure and, thereby, its low compressive and bending strengths.

(3) Marble Powder for the Production of MSWC and MSCC Interlocked Paving Stones. Figure 3 depicts the appearance of marble stone and marble powder used for the production of MSWC and MSCC. The marble powder was supplied by HMF Marble Industry.

The chemical, physical, and mechanical properties of marble are listed in Tables 7 [30, 31] and 8 [31], respectively.

In Table 8, note that marble has low porosity, indicating its low water absorption property and, thereby, the material's high compressive and bending strengths.

2.2. Method. Ahlat stone powder within the size range of 0.15–0.60 mm was the main component of the interlocked paving stones, whose production has been suggested by several studies through the use of marble aggregates. The literature did not mention the use of marble powder in 100% of the aggregates. Such is the context of this study, where marble powder of size 0.15–0.60 mm was incorporated in the production process. The usability of Ahlat stone powder and marble powder in the fabrication was validated in the fabricated six different types of interlocked paving stones, one of which was a reference concrete. Two curing applications were applied to the stones. Moreover, each stone type was subjected to water absorption, splitting tensile strength, surface abrasion, and freeze-thaw tests. Results of the tests for the new types were compared with the reference-interlocked paving stone

Table 4: Chemical, physical, and mechanical properties of the limestone aggregates.

Properties	Value
SiO_2 (%)	0.16
Fe_2O_3 (%)	0.85
Al_2O_3 (%)	0.12
CaO (%)	54.58
MgO (%)	1.75
K_2O (%)	0.09
Na_2O (%)	0.04
TiO_2 (%)	0.01
Ignition loss (%)	42.40
Specific gravity (g/cm³)	2.77
Water absorption by weight (%)	1.38
Los Angeles abrasion (%)	26.17

Figure 1: Limestone aggregates used for RWC production.

concretes and specification limits under the TS 2824 EN 1338 standard (concrete paving blocks—requirements and test methods) [21].

2.2.1. Mixture Ratio of Interlocked Paving Stones

(1) RWC and RCC Interlocked Paving Stones. As in Table 3, crushed limestone was the aggregate for RWC and RCC. A sieve analysis of the aggregates was carried out in accordance with TS EN 933-1 standard [32]. The results are shown in Table 9.

Note from Table 9 that the aggregates were designed with 30% of the crushed coarse limestone and 70% of the limestone powder. Figure 4 illustrates the gradation curves for the aggregates.

Standard TS 802 emphasizes that the gradation curve for such aggregates must lie between lines A16 and B16 or between lines B16 and C16 [33]. The concrete aggregate granulometry conforms to TS802, as depicted in Figure 4. The mixture ratio and amounts for the production of RWC and RCC interlocked paving stones are shown in Table 10.

Accordingly, note from Table 10 that the aggregates were designed with components of 70% crushed limestone sand and 30% coarse limestone. Note also that the water/binder ratio of the concrete mixture was 0.35.

(2) New Type of Interlocked Paving Stones. Different theories of mixing have been applied to achieve a tight structure of the mixture forming materials [33, 34]. Such theories were derived from Mooney's suspension viscosity model [34–36]. Table 11 shows the different mixture ratios for Mooney's model for a paving stone unit [37]. Here, the water/binder and silica fume/cement ratios were 0.12 and 0.25, respectively. All samples taken had dimensions of $165 \times 200 \times 80$ mm.

As shown in Table 11, Portland cement and silica fume were considered together as binder for calculating the water/binding ratio.

(3) ASWC and ASCC Interlocked Paving Stones. The mixing ratio and amounts established for ASWC and ASCC are listed in Table 12. The ratio between the total mixture weight and the amount of cement for one unit of the paving stone can be obtained using the following equation:

$$\text{total concrete mixture weight} = 2.806 \times \text{cement weight.}$$
(1)

Accordingly, $1\,m^3$ of the concrete mixture weight corresponds to 2200 kg. Using equation (1), the amount of cement in the mixture was calculated at 784 kg. Thus, the amount of other materials used in the production of ASWC and ASCC was based on this calculated quantity, as depicted in Table 12.

In Table 12, note that the water/binder and silica fume/cement ratios for the concrete mixture were 0.35 and 0.25, respectively.

(4) MSWC and MSCC Interlocked Paving Stones. Similarly, the water/binder and silica fume/cement ratios of the concrete mixture for MSWC and MSCC were 0.35 and 0.25, respectively. The mixing ratio and amounts are listed in Table 13.

Here, $1\,m^3$ concrete mixture corresponds to a unit weight of 2200 kg. Using equation (1), the amount of cement in the mixture was calculated at 784 kg. Thus, the amount of other materials used in mixing ratios for MSWC and MSCC was based on this quantity, as depicted in Table 13. The water/binder ratio for both MSWC and MSCC was equal to that for RWC and RCC.

2.2.2. Curing Types.

Two curing types, namely, standard water curing and combined curing, were applied for the interlocked paving stones. The literature did not specify any standard for the combined curing of hardened concrete. Hattatoglu and Bakis stated that the combined curing type with the highest compressive strength was obtained with consecutive water curing at 20°C for 7 days, hot water curing at 90°C for 2 days, and drying oven curing at 180°C for 2 days [10]. In the study, the test results of RWC, ASWC, and MSWC samples were determined after standard water curing at 20 ± 5°C for 3 days, whereas the test results of RCC, ASCC, and MSCC samples were determined after combined curing at 20 ± 5°C standard water curing for 3 days, and

FIGURE 2: Ahlat stone powder used for ASWC and ASCC production.

TABLE 5: Chemical properties of Ahlat stone.

Component	Na_2O	MgO	Al_2O_3	SiO_2	K_2O	CaO	TiO_2	Fe_2O_3
Percentage	5.51	0.24	16.01	64.11	4.78	1.64	0.44	4.91

TABLE 6: Chemical and mechanical properties of Ahlat stone.

Specific gravity (g/cm^3)	Porosity (%)	Water absorption by weight (%)	Surface abrasion loss $(cm^3/50\ cm^2)$	Unit weight (g/cm^3)	Compressive strength (MPa)	Bending strength (MPa)
2.60	27.31	20	29	1.89	10.6	1.59

FIGURE 3: Marble powder used for MSWC and MSCC production.

TABLE 7: Chemical properties of marble.

Na_2O (%)	MgO (%)	Al_2O_3 (%)	SiO_2 (%)	K_2O (%)	CaO (%)	TiO_2 (%)	Fe_2O_3 (%)	P_2O_5 (%)	Ignition loss (%)
<0.01	1.41	<0.01	0.14	<0.01	55.72	<0.01	0.11	0.01	42.6

TABLE 8: Physical and mechanical properties of marble.

Specific gravity (g/cm^3)	Porosity (%)	Water absorption by weight (%)	Surface abrasion loss $(cm^3/50\ cm^2)$	Unit weight (g/cm^3)	Compressive strength (MPa)	Bending strength (MPa)
2.73	0.2	0.1	33.3	2.71	64.8	6.5

TABLE 9: Sieve analysis for RWC and RCC.

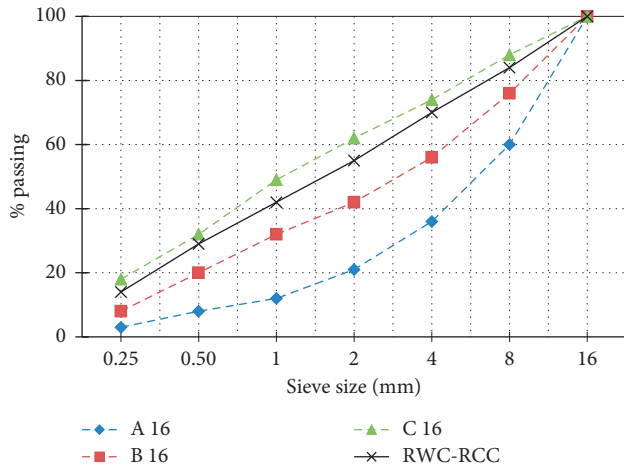| Sieve size (mm)	Weight remaining on sieve (g)	Total weight remaining on sieve (g)	Total weight remaining on sieve (%)	Passing (%)
16	—	—	—	100
8	480	480	16	84
4	420	900	30	70
2	450	1350	45	55
1	390	1740	58	42
0.5	390	2130	71	29
0.25	450	2580	86	14

FIGURE 4: Gradation curve of aggregates for RWC and RCC.

TABLE 10: The mixture ratio and amounts of RWC and RCC interlocked paving stones.

Material	Mixture ratio	Quantity (kg/m³)
Portland cement	1.00	250
Limestone aggregate (0–4 mm)	5.21	1303
Limestone aggregate (4–16 mm)	2.24	559
Water	0.35	88
Total	8.8	2200

TABLE 11: Concrete mixture ratios according to Richard and Cheyrezy [37].

Material	Mixture ratio
Portland cement	1.00
Silica fume	0.25
Quartz sand (0.15–0.60 mm)	1.10
Superplasticizer	0.016
Water	0.15
Total	2.516

$200 \pm 5^\circ$C drying oven curing for 2 days. A description for each type of curing is provided in Table 14.

Accordingly, the specimen code for the interlocked paving stones, the type of aggregate in the concrete mixtures, and the types of curing are shown in Table 15.

From Table 15, the standard curing was for 3 days at $20 \pm 5^\circ$C, whereas the combined curing involved 3 days at

TABLE 12: The mixture ratio and amounts for the production of ASWC and ASCC.

Material	Mixture ratio	Quantity (kg/m³)
Portland cement	1.00	784
Silica fume	0.25	196
Ahlat stone powder (0.15–0.60 mm)	1.10	862
Superplasticizer	0.016	13
Water	0.44	345
Total	2.806	2200

TABLE 13: The mixture and amounts for the production of MSWC and MSCC.

Material	Mixture ratio	Quantity (kg/m³)
Portland cement	1.00	784
Silica fume	0.25	196
Marble powder (0.15–0.60 mm)	1.10	862
Superplasticizer	0.016	13
Water	0.44	345
Total	2.806	2200

TABLE 14: Two curing applications for the production of interlocked paving stones.

Curing symbol	Curing description	Curing type
WC	3 days at $20 \pm 5^\circ$C water curing	Standard water curing
CC	3 days at $20 \pm 5^\circ$C water curing + 2 days at $200 \pm 5^\circ$C drying oven curing	Combined curing

$20 \pm 5^\circ$C of the standard water curing, followed by 2 days at $200 \pm 5^\circ$C of drying oven curing.

2.2.3. Test Methods. The water absorption, splitting tensile strength, surface abrasion, and freeze-thaw tests for the interlocked paving stones were performed in accordance with TS 2824 EN 1338 standard [21]. This standard covers the materials, properties, requirements, and test methods of the cement-bound concrete pavement blocks without reinforcement used for floor covering. This standard specifies the use of concrete pavement blocks such as sidewalk pavement, bicycle lane pavement, parking lots pavement, and road pavement.

TABLE 15: Code, aggregate type, and curing type for the interlocked paving stones.

Interlocked paving stone type	Specimen code	Aggregate type in concrete mixture	Curing type
RWC (reference)	6-1	Crushed limestone (0–16 mm)	Standard water curing
RCC	6-2	Crushed limestone (0–16 mm)	Combined curing
ASWC	2-1	Ahlat stone powder (0.15–0.60 mm)	Standard water curing
ASCC	2-2	Ahlat stone powder (0.15–0.60 mm)	Combined curing
MSWC	4-1	Marble powder (0.15–0.60 mm)	Standard water curing
MSCC	4-2	Marble powder (0.15–0.60 mm)	Combined curing

(1) Water Absorption Test Method. The water absorption test is performed to determine the water absorption percentage of the samples. The samples were left in the curing pool at $20 \pm 5°C$ for 3 days until constant weight was reached. The samples were then removed from the curing pool, dried, and weighed. This way, the initial weight (M_1) of the test samples was found. The samples were then placed in the drying oven and dried for 3 days at $105 \pm 5°C$ until constant dry weight (M_2) was reached. The water absorption (W_a) of each sample was calculated in terms of weight percentage using the following equation:

$$W_a = \frac{M_1 - M_2}{M_2} \times 100. \tag{2}$$

In the calculation, three samples from each type of interlocked paving stones were taken, and the average of the three values was obtained. The curing process at 200°C changes the microstructure, i.e., the pore structures. After the curing process at 200°C, the water absorption test was not made because this test for the interlocked paving stones was performed in accordance with TS 2824 EN 1338 standard. Nonstandard application was not performed.

(2) Splitting Tensile Strength Test Method. Splitting tensile strength tests for the interlocked paving stones were performed in accordance with TS 2824 EN 1338 standard [21]. The splitting tensile strength test is carried out to give information about the strength of the materials. A load was applied by increasing the tension per second (0.05 ± 0.01 MPa). The test results were calculated using the following equations [21]:

$$S = L \times t, \tag{3}$$

$$T = \frac{0.637 \times k \times P}{S}, \tag{4}$$

$$k = 1.3 - 30 \times \left(0.18 - \frac{t}{1000}\right)^2, \tag{5}$$

$$F = \frac{P}{L}, \tag{6}$$

where S is the splitting area (mm^2), L is the splitting section length (mm), t is the interlocked paving stone thickness (mm), T is the splitting tensile strength (MPa), P is the splitting load (N), k is the correction coefficient, and F is the splitting load per unit area (N/mm).

As mentioned in the earlier sections, each interlocked paving stone had dimensions of $165 \times 200 \times 80$ mm. For each specimen, the calculated values for L, t, S, and k were 200 mm, 80 mm, 16000 mm^2, and 1.00, respectively. Following the TS 2824 EN 1338 standard [21], eight samples were broken for each type of interlocked paving stones. The splitting tensile strength was calculated as the average of the values.

(3) Surface Abrasion Test Method. The abrasion test is carried out to measure the resistance of materials to surface abrasion. The Böhme abrasion test is designed to obtain abrasion loss. A total of 16 cycles, each with 22 subcycles, were applied to the samples. Abrasion loss (ΔV) at the end of the 16 cycles was calculated through the following equation [21]:

$$\Delta V = \frac{\Delta m}{\rho r}, \tag{7}$$

where ΔV is the volume loss after 16 cycles (cm^3), Δm is the mass loss after 16 cycles (g), and ρr is the density of the sample (g/cm^3).

Three samples from each type of interlocked paving stones were taken, and the abrasion loss was calculated as the average of all three values obtained.

(4) Freeze-Thaw Test Method. The freeze-thaw test is performed to measure durability of materials. Freeze-thaw tests for the interlocked paving stones were performed in accordance with TS 2824 EN 1338 standard [21]. Figure 5 displays temperature and time cycles for the freeze-thaw test according to the TS 2824 EN 1338 standard [21].

Limit values of temperature and time cycles for the freeze-thaw test are given in Table 16.

Each interlocked paving stone was cut to a dimension of $120 \times 80 \times 80$ mm. The surface area applied for the freeze-thaw test was 9600 mm^2. The mass loss (I) per unit area of the sample was calculated using the following equation [21]:

$$I = \frac{M}{A}, \tag{8}$$

where M is the total mass loss of material leaving the specimen after 28 days of cycles (kg), A is the surface area applied for freeze-thaw (m^2), and I is the mass loss per unit area (kg/m^2).

For the freeze-thaw value, three samples from each type of interlocked paving stones were taken, and the average of these three values was calculated.

3. Results and Discussion

3.1. Production of Interlocked Paving Stones. Figures 6(a)–6(d) are the illustrative photographs of the drying oven curing, and they show the appearance of the produced RWC (6-1) and
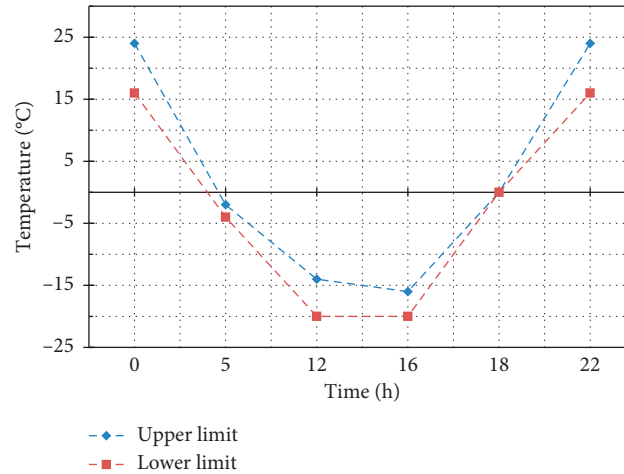
Figure 5: Temperature and time cycles for the freeze-thaw test.

Table 16: Limit values of temperature and time cycles for the freeze-thaw test [21].

Upper limit		Lower limit	
Time (h)	Temperature (°C)	Time (h)	Temperature (°C)
0	24	0	16
5	−2	3	−4
12	−14	12	−20
16	−16	16	−20
18	0	20	0
22	24	24	16

RCC (6-2), ASWC (2-1) and ASCC (2-2), and MSWC (4-1) and MSCC (4-2) interlocked paving stones, respectively.

3.2. Results of the Water Absorption Test. The results of the water absorption test for each type of the fabricated interlocked paving stones are shown in Table 17.

As indicated, the water absorption values of the new type of interlocked paving stones produced from Ahlat stone and marble powder were lower by approximately 5% and 20.34%, respectively, than that of RWC. Figure 7 provides an illustrative graph for the results.

From Table 17 and Figure 7, a specification limit was defined by the water absorption by weight (W_a) values of the interlocked paving stones. Accordingly, Figure 8 illustrates the unit volume weight for each paving stone.

TS 2824 EN 1338 [21] does not define a specification limit for the unit volume weight of the interlocked paving stones. Four of the new types of interlocked paving stones, namely, RCC, ASWC, ASCC, and MSCC, were lighter than RWC. In contrast, MSWC was heavier than RWC.

3.3. Results of the Splitting Tensile Strength Test. Figure 9 shows actual images of the broken specimens subjected to the splitting tensile strength test.

Accordingly, the results of the splitting tensile strength test are indicated in Table 18.

The splitting tensile strength of RWC increased by approximately 5%, with the application of combined curing.

Similarly, the splitting tensile strength of all other interlocked paving stones with applied combined curing was higher by 5% than those applied with standard water curing. This was due to the application of high heat to the concrete paving stone by combined curing. Hydration of the cement was accelerated by combined curing. In this way, higher strength was obtained than the concrete paving stones. Figure 10 shows the results of the splitting tensile strength test.

From Table 18 and Figure 10, the values of splitting tensile strength and splitting load per unit area (F) for the interlocked paving stones defined a specification limit. Specifically, the splitting tensile strength of all new interlocked paving stones was higher than that for RWC. Thus, ASWC, ASCC, MSWC, and MSCC proved more resistant than RWC by 2.78%, 8.33%, 8.33%, and 13.9%, respectively.

3.4. Results of the Böhme Abrasion Test. Figure 11 displays the abrasion test of RWC (6-1), RCC (6-2), ASWC (2-1), and MSWC (4-1), respectively.

Results of the Böhme abrasion test for all the interlocked paving stones are listed in Table 19.

From Table 19, the abrasion loss of RCC, ASWC, ASCC, MSWC, and MSCC was higher by approximately 9%, 7%, 87%, 14%, and 61%, respectively, than that of RWC. Figure 12 illustrates the results of the Böhme abrasion test for the interlocked paving stones.

Based on Table 19 and Figure 12, there was a defined specification limit for the values of abrasion loss for all specimens.

3.5. Results of the Freeze-Thaw Test. All abrasion values of the interlocked paving stones provide the specification limits, as shown in the results of the freeze-thaw test in Table 20.

The freeze-thaw mass loss of RCC, ASWC, ASCC, and MSCC was higher by approximately 37%, 11%, 80%, and 63%, respectively, than that of RWC. In contrast, the freeze-thaw mass loss of MSWC was lower by

(a)   (b)

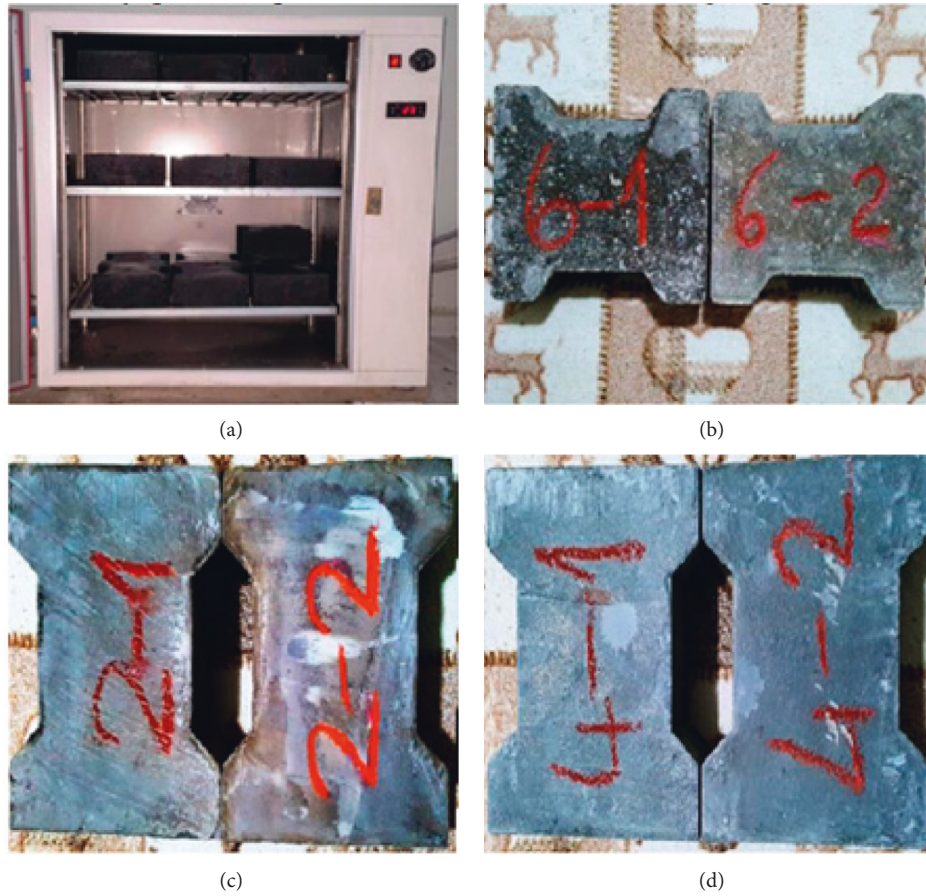(c)   (d)

FIGURE 6: The appearance of the drying oven curing and interlocked paving stones. (a) The drying oven curing. (b) RWC and RCC paving stones. (c) RWC and RCC paving stones. (d) MSWC and MSCC paving stones.

TABLE 17: Results of the absorption test for the interlocked paving stones.

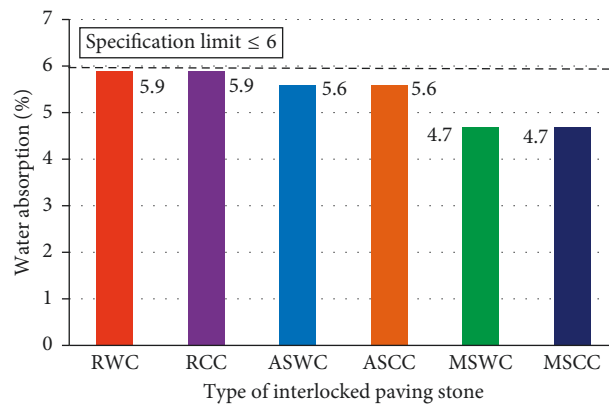| Interlocked paving stone type	Unit weight (g/cm^3)	Initial weight, M_1 (g)	Dry weight, M_2 (g)	Water absorption by weight, W_a (%)	TS 2824 EN 1338 specification limit (%)
RWC	2.149	4880	4604	5.9	
RCC	2.027	4880	4604	5.9	
ASWC	2.046	4647	4401	5.6	$W_a \leq 6$
ASCC	1.938	4647	4401	5.6	
MSWC	2.185	4963	4741	4.7	
MSCC	2.088	4963	4741	4.7	

FIGURE 7: Results of the absorption test for each type of interlocked paving stones.
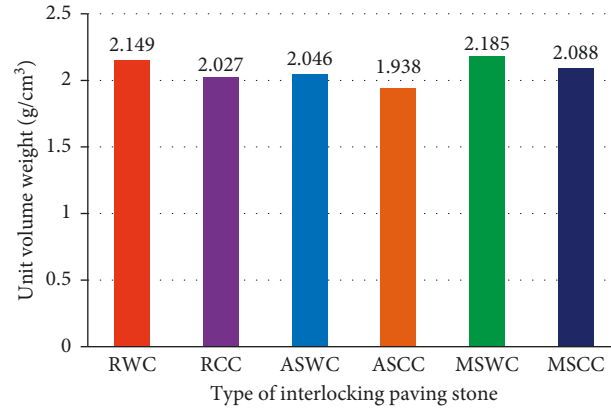
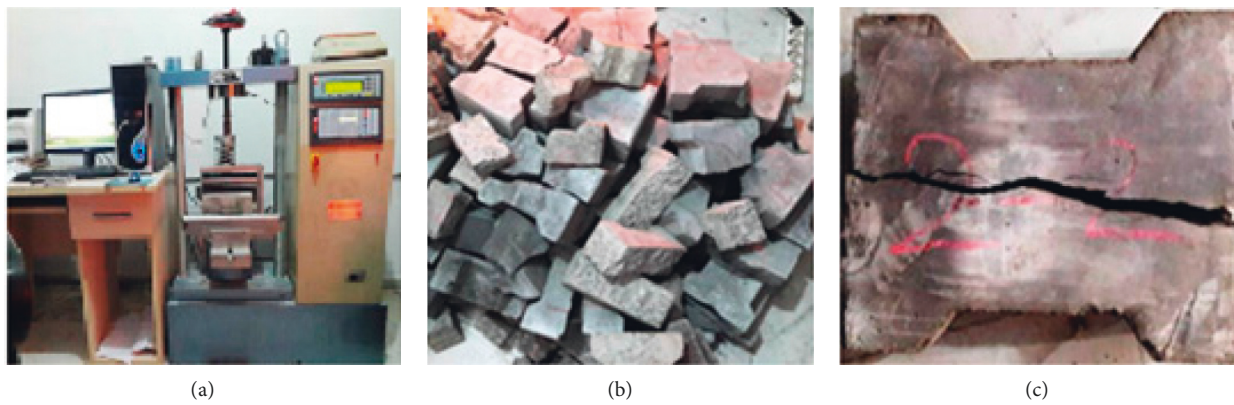FIGURE 8: Unit volume weight of the locked paving stones.

FIGURE 9: Specimen samples for the splitting tensile strength test. (a) Test device. (b) Broken samples. (c) Length of breakage.

TABLE 18: Results of the splitting tensile strength test.

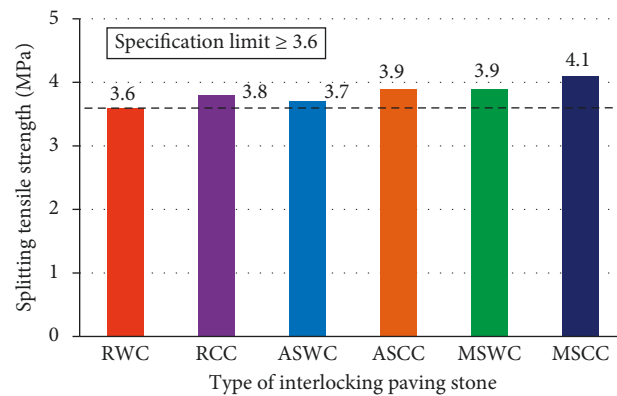| Interlocked paving stone type	Splitting tensile strength, $T_{(average)}$ (MPa)	Splitting load per unit area, $F_{(average)}$ (N/mm)	TS 2824 EN 1338 specification limits	
			$T_{(average)}$ (MPa)	$F_{(average)}$ (N/mm)
RWC (reference)	3.6	444		
RCC	3.8	466		
ASWC	3.7	460	$T_{(average)}$ ≥3.6 MPa	$F_{(average)}$ ≥250 N/mm
ASCC	3.9	479		
MSWC	3.9	488		
MSCC	4.1	510		

FIGURE 10: Results of the splitting tensile strength test for the interlocked paving stones.
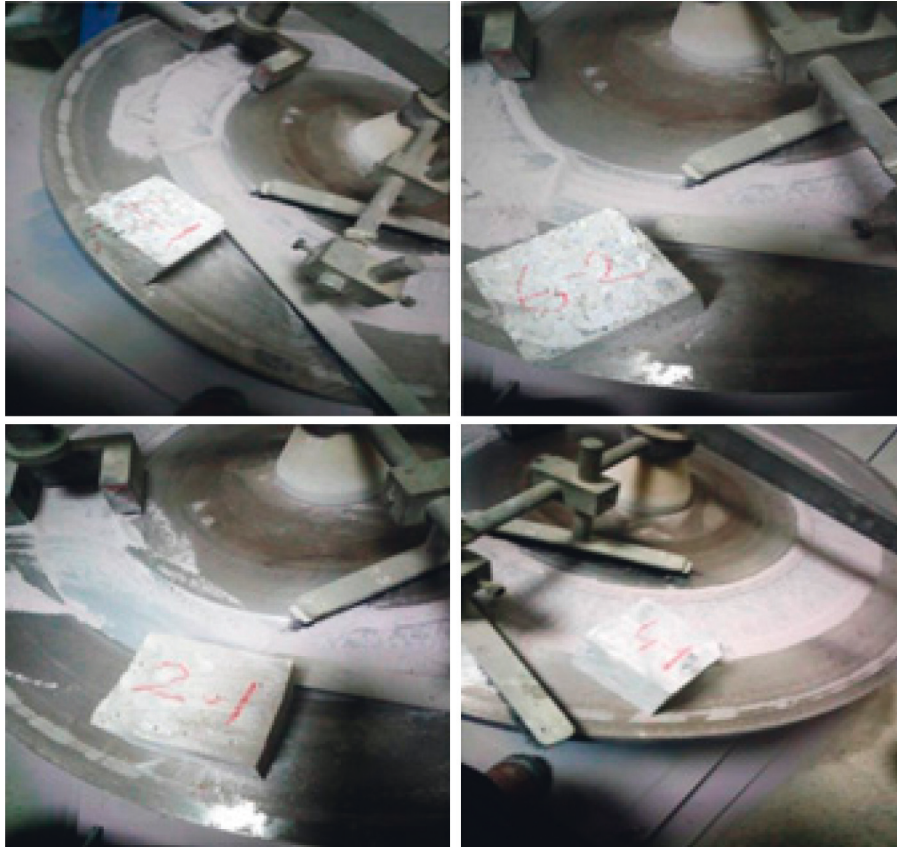
FIGURE 11: Abrasion test for RWC, RCC, ASWC, and MSWC interlocked paving stones.

TABLE 19: Results of the abrasion test for the interlocked paving stones.

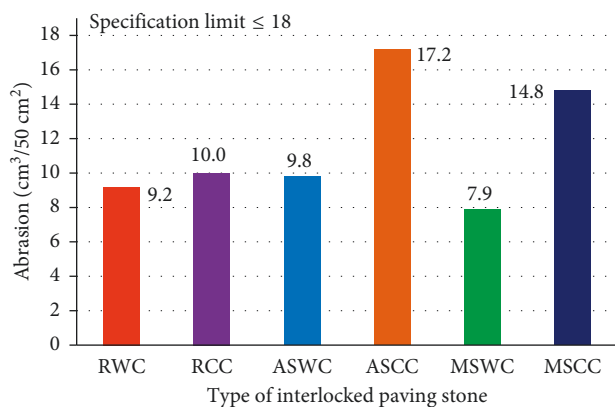| Interlocked paving stone type	Density ρr (g/cm^3)	Mass loss Δm (g)	Abrasion ΔV (cm^3/50 cm^2)	TS 2824 EN 1338 specification limit (cm^3/50 cm^2)
RWC (reference)	1.989	18.4	9.2	
RCC	1.956	19.7	10.0	
ASWC	1.986	19.5	9.8	$\Delta V \leq 18$
ASCC	1.985	34.2	17.2	
MSWC	1.993	15.8	7.9	
MSCC	1.991	29.5	14.8	

FIGURE 12: Results of the abrasion test for the interlocked paving stones.

approximately 3%. The freeze-thaw mass loss of RCC, ASCC, and MSCC was higher, respectively, than that of RWC, ASWC, and MSWC.

Figure 13 describes the results of the freeze-thaw test. Such a high temperature (200°C) induces other durability issues, such as delayed ettringite formation, since ettringite is not formed during the hydration process. Therefore, freeze-thaw values of RCC, ASCC, and MSCC were higher, respectively, than that of RWC, ASWC, and MSWC. From Table 20 and Figure 13, the values of mass loss per unit area (I) for all paving stones defined a specification limit. Results of all the tests performed for the interlocked paving stones are summarized in Table 21.

As such, all five new types of interlocked paving stones, namely, RCC, ASWC, ASCC, MSWC, and MSCC, defined the specification limits of test results.

TABLE 20: Results of the freeze-thaw test results of interlocked paving stones.

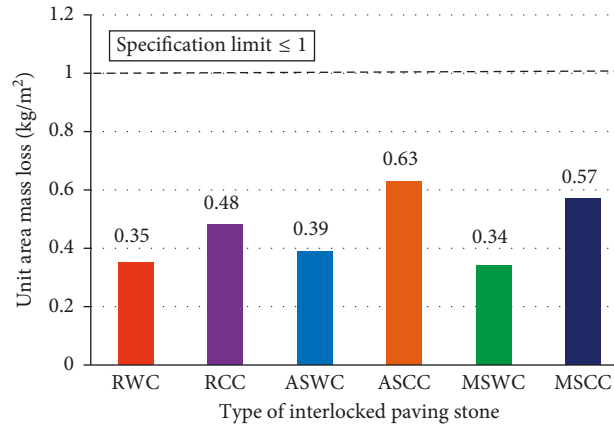| Interlocked paving stone type	Surface area, A (mm^2)	Mass loss, M (g)	Mass loss per unit area, I (kg/ m^2)	TS 2824 EN 1338 specification limit (kg/m^2)
RWC (reference)	9600	3.36	0.35	
RCC	9600	4.61	0.48	
ASWC	9600	3.74	0.39	$I \leq 1$
ASCC	9600	6.05	0.63	
MSWC	9600	3.26	0.34	
MSCC	9600	5.47	0.57	

FIGURE 13: Results of the freeze-thaw test for the interlocked paving stones.

TABLE 21: All test results of interlocked paving stones.

Tests	RWC	RCC	ASWC	ASCC	MSWC	MSCC	TS 2824 EN 1338 specification limit	Standard deviation (σ)
Unit volume weight (g/cm^3)	2.149	2.027	2.046	1.938	2.185	2.088	Unspecified	0.09
Water absorption (%)	5.9	5.9	5.6	5.6	4.7	4.7	≤ 6.0	0.56
Splitting tensile strength (MPa)	3.6	3.8	3.7	3.9	3.9	4.1	≥ 3.6	0.18
Abrasion (cm^3/50 cm^2)	9.2	10	9.8	17.2	7.9	14.8	≤ 18	3.65
Freeze-thaw (kg/m^2)	0.35	0.48	0.39	0.63	0.34	0.57	≤ 1.0	0.12

4. Conclusions

The usability of waste materials Ahlat stone powder and marble powder in fabricating interlocked paving stones was the focal subject of investigation for this study. As there was no study in the provided literature that considered the production of interlocked concrete paving stones with Ahlat stone powder, such was realized with Ahlat stone powder of size range 0.15–0.60 mm. Since the porosity of the Ahlat stone is high, it cannot be used as coarse aggregate in the concrete mixture. With the special curing method, durable concrete paving stones are produced from waste Ahlat stone powders. Likewise, a few studies considered marble aggregate in the production of interlocked paving stones, and none of these employed marble powder in 100% ratio of the aggregates, which was realized herein, with marble powder specimens of size range 0.15–0.60 mm. Six different types of interlocked paving stones were fabricated under two curing types, one of which was a reference concrete. Tests of water absorption, splitting tensile strength, surface abrasion, and freeze-thaw for each interlocked paving stone type were carried out. Test results for the five new types of concrete were compared with the reference-interlocked paving stone concrete under specification limits. The findings of this study can be generalized as follows:

(i) Waste materials, i.e., ignimbrite (Ahlat stone) powder and marble powder for this study, can be used in the production of interlocked paving stones.

(ii) Combined curing increases the splitting tensile strength of interlocked paving stones at 5%, on average.

(iii) New types of interlocked paving stones were produced from the cited waste materials. Of these, ASCC is the lightest (in particular, it was approximately 10% lighter than the reference-interlocked paving stone (RWC)); MSCC achieved the highest splitting tensile strength, and MSWC had the lowest abrasion loss.

(iv) The abrasion loss of interlocked paving stones subjected to combined curing was higher than those applied with standard water curing, which indicates the progressing damage on the surface over time under high temperatures.

(v) MSWC had the lowest freeze-thaw mass loss, which indicates its higher resistance to damage than the other types under long-time, adverse climatic conditions.

(vi) Subsequent scientific studies may extend delayed ettringite formation and fatigue and impact tests for the new types of interlocked paving stones fabricated in this study.

(vii) Delayed ettringite formation for the new types of interlocked paving stones can be investigated in subsequent scientific studies.

Data Availability

The data used to support the findings of this study are included within the article.

Conflicts of Interest

The author declares that there are no conflicts of interest regarding the publication of this paper.

Acknowledgments

References

[1] M. Semiz, "Research of the physical characteristics of concrete keystone and alternative production," Master thesis, Gazi University, Graduate School of Natural and Applied Sciences, Ankara, Turkey, 2006.

[2] Y. Acikgoz, "Research in usage of fly ashes in the production of interlocking concrete pave," Master thesis, Gazi University, Graduate School of Natural and Applied Sciences, Ankara, Turkey, 2008.

[3] T. Kaya and C. Karakurt, "Investigation of the engineering properties of implementation concrete paving stones," *Duzce University Journal of Science and Technology*, vol. 4, no. 2, pp. 469–474, 2016.

[4] T. Tekmen, "Evaluate to mechanical properties of concrete interlocking pavement blocks which was produced from limestones," Master thesis, Cukurova University, Graduate School of Natural and Applied Sciences, Adana, Turkey, 2006.

[5] MEGEP, *Covering in Sidewalk and Parks*, Construction Technology, Ankara, Turkey, 2012.

[6] B. I. Topcu and T. Uygunoglu, "Use of marble aggregate and fly ash in the production of interlocked paving stones," *Concrete Prefabrication*, vol. 98, pp. 15-16, 2011.

[7] G. Yang and M. A. Bradford, "Thermal-induced upheaval buckling of continuously-reinforced semi-infinite concrete pavements," *Engineering Structures*, vol. 168, pp. 865–876, 2018.

[8] G. Yang and M. A. Bradford, "Thermal-induced upheaval buckling of concrete pavements incorporating the effects of temperature gradient," *Engineering Structures*, vol. 164, pp. 316–324, 2018.

[9] A. Bakis, "Usability of ahlat stone in rigid pavement construction," *BEU Journal of Science*, vol. 5, no. 2, pp. 164–171, 2016.

[10] F. Hattatoglu and A. Bakis, "Usability of ignimbrite powder in reactive powder concrete road pavement," *Road Materials and Pavement Design*, vol. 18, no. 6, pp. 1448–1459, 2017.

[11] M. Bostanci, "Investigation of capillary water absorption behaviour of ignimbrites (Nevsehir Region)," Master thesis, Nevsehir Haci Bektas Veli University, Graduate School of Natural and Applied Sciences, Nevsehir, Turkey, 2016.

[12] B. I. Topcu and T. Uygunoglu, *Reduction of Environmental Pollution by Using Waste Marble Aggregates in Concrete*, International Sustainable Structures Symposium, Ankara, Turkey, 2010.

[13] M. Filiz, C. Ozel, O. Soykan, and Y. Ekiz, "Usage of waste marble dust at paving stones," *Electronic Journal of Construction Technologies*, vol. 6, no. 2, pp. 57–72, 2010.

[14] H. Ceylan and S. Manca, "Evaluation of concrete aggregate marble pieces," *SDU Journal of Technical Sciences*, vol. 3, no. 2, pp. 21–25, 2013.

[15] L. G. Li, Z. H. Huang, Y. P. Tan, A. K. H. Kwan, and H. Y. Chen, "Recycling of marble dust as paste replacement for improving strength, microstructure and eco-friendliness of mortar," *Journal of Cleaner Production*, vol. 210, pp. 55–65, 2019.

[16] K. Vardhan, R. Siddique, and S. Goyal, "Strength, permeation and micro-structural characteristics of concrete incorporating waste marble," *Construction and Building Materials*, vol. 203, pp. 45–55, 2019.

[17] R. Alyousef, O. Benjeddou, C. Soussi, M. A. Khadimallah, and M. Jedidi, "Experimental study of new insulation lightweight concrete block floor based on perlite aggregate, natural sand, and sand obtained from marble waste," *Advances in Materials Science and Engineering*, vol. 2019, Article ID 8160461, 14 pages, 2019.

[18] E. T. Tunc, "Recycling of marble waste: a review based on strength of concrete Containing marble waste," *Journal of Environmental Management*, vol. 231, pp. 86–97, 2019.

[19] D. K. Ashish, "Concrete made with waste marble powder and supplementary cementitious material for sustainable development," *Journal of Cleaner Production*, vol. 211, pp. 716–729, 2019.

[20] M. Pathirage, F. Bousikhane, M. D'Ambrosia, M. Alnaggar, and G. Cusatis, "Effect of alkali silica reaction on the mechanical properties of aging mortar bars: experiments and numerical modeling," *International Journal of Damage Mechanics*, vol. 28, no. 2, pp. 291–322, 2018.

[21] TS 2824 EN 1338, *Concrete Paving Blocks-Requirements and Test Methods*, TSE, Ankara, Turkey, 2005.

[22] TS EN 197-1, *Cement - Part 1: Composition, Specifications and Conformity Criteria for Common Cements*, TSE, Ankara, Turkey, 2012.

[23] ASTM C618-19, *Standard Specification for Coal Fly Ash and Raw or Calcined Natural Pozzolan for Use in Concrete*, ASTM International, West Conshohocken, PA, USA, 2019.

[24] AASHTO M 307, *Standard Specification for Silica Fume Used in Cementitious Mixtures*, American Association of State Highway and Transportation Officials, Washington, DC, USA, 2013.

[25] Limak Cement Industry and Trade Inc, http://www.limakcement.com.

[26] BASF Chemistry Industry and Trade Inc, http://www.master-builders-solutions.basf.com.tr.

[27] TS EN-934-2+A1, *Admixtures for Concrete, Mortar and Grout—Part 2: Concrete Admixtures-Definitions, Requirements, Conformity, Marking and Labelling*, TSE, Ankara, Turkey, 2014.

[28] Adabag Building Industry Incorporated Company, http://www.adabag.com.tr.

[29] O. Simsek and M. Erdal, "Investigation of some mechanical and physical properties of the Ahlat stone (Ignimbrite)," *Gazi University Journal of Science*, vol. 17, no. 4, pp. 71–78, 2004.

[30] HMF Marble Industry, http://www.hmfmarble.com.tr.

[31] Z. Gezen, "Grain size influences on the material properties and durability of marbles," Master thesis, Dokuz Eylul University, Graduate School of Natural and Applied Sciences, Izmir, Turkey, 2013.

[32] TS EN 933-1, *Tests for Geometrical Properties of Aggregates—Part 1: Determination of Particle Size Distribution-Sieving Method*, TSE, Ankara, Turkey, 2012.

[33] TS 802, *Design of Concrete Mixes*, TSE, Ankara, Turkey, 2016.

[34] M. Ipek, "Effects of pre-setting pressure applied during setting phase to mechanical behaviors of reactive powder concrete," Ph D. thesis, Sakarya University, Graduate School of Natural and Applied Sciences, Sakarya, Turkey, 2009.

[35] A. Bakis, "Investigation on the usability of reactive powder concrete (rpc) in rigid road superstructure construction," Ph D. thesis, Ataturk University, Graduate School of Natural and Applied Sciences, Erzurum, Turkey, 2015.

[36] F. Larrard and T. Sedran, "Optimization of ultra-high-performance concrete by the use of a packing model," *Cement and Concrete Research*, vol. 24, no. 6, pp. 997–1009, 1994.

[37] P. Richard and M. Cheyrezy, "Composition of reactive powder concretes," *Cement and Concrete Research*, vol. 25, no. 7, pp. 1501–1511, 1995.

Research Article

Highway Performance Evaluation Index in Semiarid Climate Region Based on Fuzzy Mathematics

Sanqiang Yang,[1,2] Meng Guo [ID],[3] Xinlei Liu,[1] Pidong Wang,[1] Qian Li,[1] and Haiqing Liu[3]

[1]*Baoding City Road and Bridge Engineering Assembly Technology Key Laboratory, College of Civil Engineering and Architecture, Hebei University, Baoding, Hebei 071002, China*
[2]*Hebei Institute of Transportation Planning and Design, Shi Jiazhuang, Hebei 050011, China*
[3]*The Key Laboratory of Urban Security and Disaster Engineering of Ministry of Education, Beijing University of Technology, Beijing 100124, China*

Correspondence should be addressed to Meng Guo; mguo@ustb.edu.cn

Accurate evaluation and analysis of expressway pavement performance is a prerequisite for determining the pavement design scheme and maintenance scheme. Due to the fuzziness and randomness of many factors affecting the pavement performance, this paper relies on the reconstruction and expansion project of Xinglin section of the Taihang mountain expressway, a method of highway pavement performance evaluation based on fuzzy mathematics is proposed. The results show the following: ① the study uses the factor domain, the comment level domain, the fuzzy relationship matrix, the evaluation factor full vector, and the fuzzy comprehensive evaluation result vector five-step method. The method can be effectively combined with the multi-index comprehensive detection index used in the specification. ② Based on the multi-index comprehensive test and evaluation adopted in the specification, the performance grade of the old road surface was quantitatively evaluated by the iterative calculation of fuzzy mathematics that broke through the evaluation mode which was based on the traditional detection methods. The research results provide innovative theoretical methods for the accurate evaluation and analysis of highway pavement performance in the semiarid climate region and also play a technical supporting role for the pavement design scheme and maintenance scheme decision-making in the semiarid climate region.

1. Background

By the end of 2017, the total mileage of expressways in China is close to 130,000 km, among which the service period of 5–10 years accounts for up to 45%. The performance evaluation of the old road surface and the design of the pavement maintenance scheme will determine the investment budget for the reconstruction of the old road network [1].Pavement performance evaluation is based on the collected pavement condition data to judge the degree of pavement performance to meet the requirements of use. It is helpful to understand the pavement condition and the change rule of service performance, making reasonable countermeasures, and is the basis of making corresponding maintenance and reconstruction

measures [2]. Pavement performance generally remains good for 1 to 5 years. In 6 to 15 years, pavement performance is degraded due to natural environment factors, traffic loads, and temperature changes. A series of diseases such as ruts and cracks appear on the road surface. Under the comprehensive influence of various factors [3, 4], the asphalt pavement of expressway needs a large area of maintenance for 5 to 8 years, resulting in a large capital investment. Therefore, in order to maintain the level of highway service, delaying the decline of road performance, reducing asset losses, extending the service life of the road surface are the main tasks of highway maintenance management [5].

In recent years, many experts and scholars at home and abroad have conducted a large number of theoretical studies

on pavement suitability evaluation and prediction. Developed countries engaged in this research earlier, and its research ideas and methods have been mostly in the establishment of the road management system and road maintenance system to achieve. Among them, a representative study has been developed by the U.S. Army Construction Engineering Research Institute of the PAVER system. The penalty method was first used to establish the pavement damage evaluation model by considering the road condition information, condition evaluation, and prediction. The method can accurately calculate and reduce overall damage caused by a variety of damage of pavement [6]. The Arizona management system used the evenness and cracking data to evaluate the pavement performance [7].The Milligan state road management system management proposed the road performance attenuation curve, the forecast road performance [8]. In 2001, Prozzi from the University Of California proposed a method to analyze and evaluate pavement performance by combining field test data with experimental data [9]. In the same year, Nunoo from Florida International University proposed to adopt the composite comprehensive evaluation algorithm to optimize the multiyear integrated pavement maintenance plan for the network pavement management and maintenance problems [10]. The SHRP, which began in 1987, considers pavement long-term performance (LTPP) research as a 10-year highway research project with the goal of providing the means and assistance to "improve pavement performance and service life" [11]. In 2001, Hao from Chang'an University analyzed the necessity, research plan, and research strategy of carrying out long-term pavement performance research in his doctoral thesis "pavement performance evaluation and analysis research" [12].

In terms of pavement performance evaluation, there are generally two categories of evaluation indexes: single index and comprehensive index. The evaluation model mainly includes PSI [13] of AASHO in the United States, Canada's RCI [14], Japan's MCI, and China's PQI and RQI. This paper relies on the research carried out by the Chinese project, so the Chinese PCI and RQI models are selected.

Hebei Province is a typical semiarid climate region. At present, the total length of expressways in Hebei Province is 6531 km. The performance evaluation of old highway pavement is especially difficult. The semiarid climate area has less precipitation, strong sunshine, and sharp temperature change. The shrinkage deformation of highway pavement in the semiarid climate area is particularly prominent due to high temperature rutting in summer, low temperature cracking in winter, annual temperature difference, and diurnal temperature difference.

In recent ten years, researchers began to apply fuzzy mathematics to highway performance evaluation index research. Zhou et al. proposed a prediction method of pavement performance based on grey prediction theory and clustering analysis method [15]. Chen established the evaluation model of highway asphalt pavement which is created on the basis of fuzzy evaluation, grey relationship, and ameliorated artificial neutral network (ANN) [16]. In highway pavement maintenance management decision-

making optimization, Wen discussed highway pavement maintenance project decision-making and maintenance fund allocation [17]. Li put forward a method of expressway asphalt pavement maintenance decision-making based on the matter-element model. The model can greatly reduce the calculation amount of the optimization analysis process of each maintenance section [18].

Based on the above background, this paper relies on the reconstruction and expansion project of Xinglin section of the Taihang mountain expressway, and a method of highway pavement performance evaluation based on fuzzy mathematics is proposed.

2. Climate Characteristics and Engineering Description of Semiarid Areas

The semiarid climate zone refers to the zone whose mean annual precipitation is less than the evaporation [19]; the drought index AI (the ratio of annual precipitation and the annual evaporation) is in the range of 0.2 to 0.5, the precipitation is commonly 200~400 mm, the temperature changes sharply, and the annual sunshine amount varies greatly. The difference in sunshine is more than 30 degrees Celsius, and the highest temperature can reach 75 degrees Celsius. The areas include the central and eastern Inner Mongolia, Hebei, Yanbei in Shanxi, northern region of Shanxi, Xihaigu in the south of Ningxia, Dingxi in Gansu, Yuzhong, Yushu in Qinghai, Guoluo, Lhasa in Tibet, and other regions. Rainfall is directly related to pavement water resistance, and temperature difference is directly related to pavement high and low temperature performance. Correlation analysis based on fuzzy mathematics can solve multifactor problems better.

The Xingtai–Linqing expressway based on this study is located in the south of Hebei Province, with gentle topography and topographic forms of alluvial, diluvial, and limnetic plain. For the warm temperate semiarid monsoon climate region, weather is like in spring drought windy, summer weather hot and rainy, and winter weather cold and less snowy. The annual average temperature is 13.1°C; the average temperature is 26.9°C. In July, the extreme maximum temperature is 41.8°C; the average temperature from December to January is minus 3.5 degrees Celsius, and the extreme minimum temperature is −21.6°C. The average annual precipitation is about 550 mm. Through the investigation and analysis of road conditions, it is found that the sections with high temperature rutting in summer are significantly distributed, and the transverse and longitudinal cracks of the road surface are widely distributed. The types of pavement diseases are closely related to the temperature and precipitation in this area.

3. Evaluation and Analysis of the Existing Standard Indexes

In this study, the highway from Xingtai to Linqing in the semiarid climate region of Hebei Province was selected, and the pavement performance index (PCI) [20], road driving quality index (RQI), and rutting depth evaluation (RDI)

were used to analyze the change rules of various pavement performance indexes from 2011 to 2016. Pavement structural strength [21, 22] was used to evaluate the variation rules of deflection in 2015 and 2016 (Figures 1–6).

According to Figures 1–3, from 2011 to 2016, the overall trend of the PCI index of pavement damage decreased year by year. The road surface driving quality index (RQI) is all above 90 points, indicating that the road surface is in good condition. The rutting depth index (RDI) of the road surface showed that the rutting depth index of the road surface decreased continuously with the increase of years, and the decay law of the road surface performance was obvious. It can be concluded from the analysis that the rutting depth index RDI affecting the road surface of this section is related to the quality of internal pavement material and pavement structure, as well as external climatic conditions and traffic conditions.

The bending and subsidence data of the Taihang mountain expressway from Xingtai to Linqing in the semiarid climate region of Hebei Province in 2015 and 2016 were selected for analysis, and the strength variation rules were evaluated (Figures 4–6).

According to the analysis in Figures 4–6, SSI data of the road surface from Xingtai to Linqing section of the Taihang mountain expressway in 2015 and 2016 show that, with the increase of the service period, the overall strength of the road surface structure presents a downward trend. The main factors of intensity attenuation are heavy traffic, large temperature difference, and other meteorological and environmental factors.

4. Comprehensive Evaluation of Pavement Performance Based on Fuzzy Mathematics

4.1. Analysis Steps

4.1.1. Determine the Factor Domain of the Evaluation Object. The evaluation fuzzy phenomenon first determines the evaluation factors, and the collection of these factors constitutes the evaluation factors [23]. The theory of domain of our country's current technical specification for the highway asphalt pavement maintenance JTG comprehensive evaluation index PQI H20-2007 is composed of four indexes, namely, the pavement damage index, roughness, rut, and antisliding performance. So the factors concerning domain $U = $ (PCI, RQI, RDI, SRI).

4.1.2. Domain the Evaluation Grade Theory. Domain the evaluation grade theory divides the evaluation objects into several levels, generally from 4 levels to 9 levels [24]. In this paper, the evaluation is divided into five grades, namely, the evaluation theory of field $V = $ (excellent, good, medium, secondary, bad) $= (A, B, C, D, E)$.

4.1.3. Establish the Fuzzy Relation Matrix. After the hierarchical fuzzy subset is constructed, the evaluated objects should be quantified from each factor one by one, that is, the membership degree of the evaluated objects to the
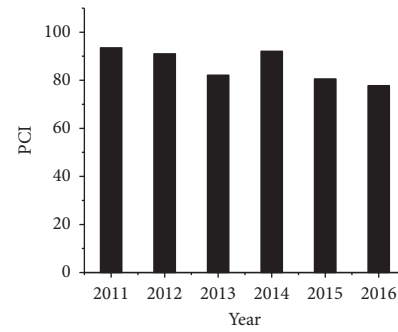

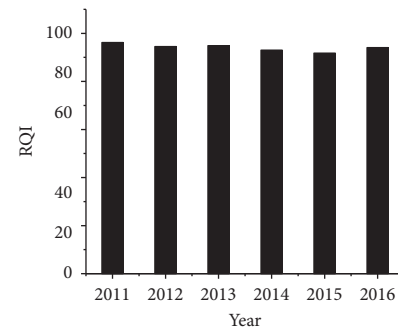FIGURE 1: Continuous chart of the road condition index.

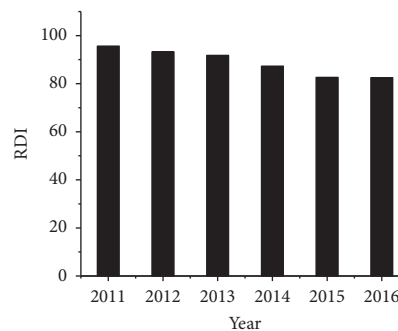FIGURE 2: Continuous statistics of the driving quality index chart.

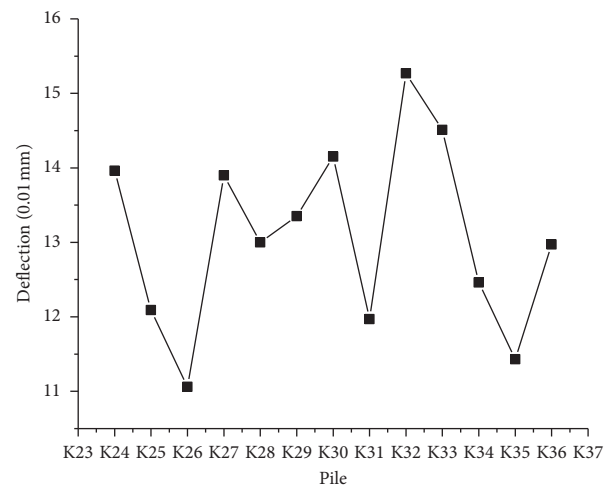FIGURE 3: Continuous chart of the rutting depth index.

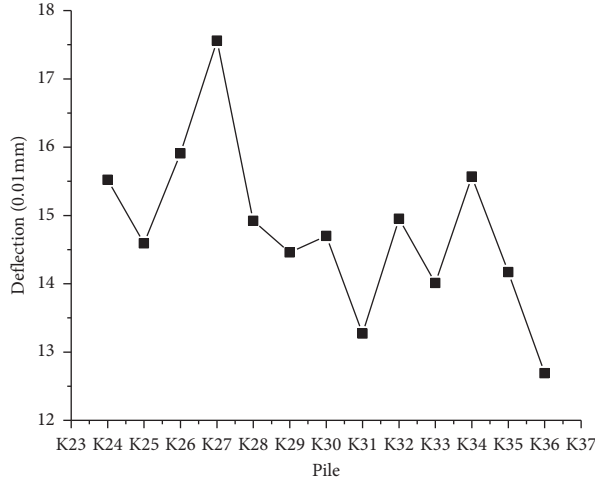FIGURE 4: Trend of pavement deflection in 2015.
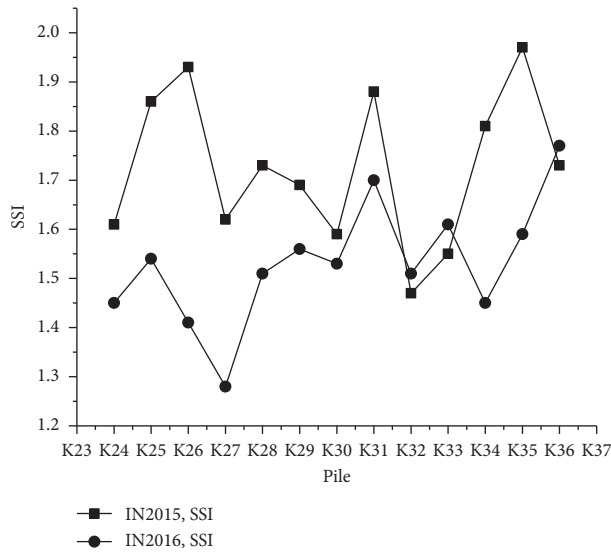
FIGURE 5: Trend of pavement deflection in 2016.

FIGURE 6: SSI comparison in 2015 and 2016.

TABLE 1: Road surface performance.

Indicators	Excellent	Good	Medium	Secondary	Bad
PCI	[85, 100)	[70, 85)	[55, 85)	[40, 55)	[0, 40)
RQI	[85, 100)	[70, 85)	[55, 85)	[40, 55)	[0, 40)
RDI	[85, 100)	[70, 85)	[55, 85)	[40, 55)	[0, 40)
SRI	[85, 100)	[70, 85)	[55, 85)	[40, 55)	[0, 40)

hierarchical fuzzy subset from the perspective of a single factor [25]. The attribute measure function of each evaluation index is shown in the following table.

As can be seen from Table 1, the attribute measurement functions of the four evaluation indicators are the same. Then, the membership functions of PCI, RQI, RDI, and SRI are as follows:

$$
r_E = \begin{cases} 1, & 85 < r \le 100, \\ \dfrac{r-70}{85-70}, & 70 < r \le 85, \\ 0, & 0 < r \le 75, \end{cases}
$$

$$
r_G = \begin{cases} \dfrac{100-r}{100-85}, & 85 < r \le 100, \\ 1, & 70 < r \le 85, \\ \dfrac{r-55}{70-55}, & 55 < r \le 70, \\ 0, & 0 < r \le 55, \end{cases}
$$

$$
r_M = \begin{cases} 0, & 85 < r \le 100, \\ \dfrac{85-r}{85-70}, & 70 < r \le 85, \\ 1, & 55 < r \le 70, \\ \dfrac{r-40}{55-40}, & 40 < r \le 55, \\ 0, & 0 < r \le 40, \end{cases} \tag{1}
$$

$$
r_S = \begin{cases} 0, & 70 < r \le 100, \\ \dfrac{70-r}{70-55}, & 55 < r \le 70, \\ 1, & 40 < r \le 55, \\ \dfrac{r-25}{40-25}, & 25 < r \le 40, \\ 0, & 0 < r \le 25, \end{cases}
$$

$$
r_B = \begin{cases} 0, & 55 < r \le 100, \\ \dfrac{55-r}{55-40}, & 40 < r \le 55, \\ 1, & 25 < r \le 40, \\ \dfrac{r-10}{25-10}, & 10 < r \le 25, \\ 0, & 0 < r \le 10. \end{cases}
$$

4.1.4. Determine the Total Vector of Evaluation Factors.

The vector coefficient W in the weight vector reflects the influence of each index on the object under evaluation [26]. In this paper, the analytic hierarchy process is adopted to determine the weight vector. When the importance of PCI of pavement damage is 1, it is considered that the importance of rut is 1/2, the importance of flatness is 2, the importance of antislip is 1, and the importance of structural strength is 3. After constructing the judgment matrix C to find its maximum eigenvalue and eigenvector and normalizing it, the weight coefficient of each index is obtained as $\omega_1, \omega_2, \omega_3$, and ω_4:

$$C = \left(c_{ij}\right) = \begin{bmatrix} c_{11} & c_{12} & \cdots & c_{1j} \\ c_{21} & c_{22} & \cdots & c_{2j} \\ \cdots & \cdots & \cdots & \cdots \\ c_{i1} & c_{i2} & \cdots & c_{ij} \end{bmatrix}. \tag{2}$$

For the consistency test on matrix C, taking the consistency index,

$$CI = \frac{\lambda_{\max} - n}{n - 1}. \tag{3}$$

The randomness index RI is shown in Table 2.

For the consistency test for matrix C using equation (3), if CR < 0.1, then judge matrix C has good consistency. Otherwise, matrix C needs to be readjusted:

$$CR = \frac{CI}{RI}. \tag{4}$$

4.1.5. Result Vector of Fuzzy Comprehensive Evaluation.

According to this formula, b_i is the i-th membership degree calculated by combining all factors of W and R. According to the principle of maximum membership, let $d_0 = \max[b_i]$, and then consider the i-th comment level in the comment domain V:

$$D[d_i] = W \cdot R = [\omega_1, \omega_2, \omega_3, \ldots, \omega_m] \cdot \begin{bmatrix} r_{11} & \cdots & r_{1n} \\ \cdots & \cdots & \cdots \\ r_{m1} & \cdots & r_{mn} \end{bmatrix}$$

$$= [b_1, b_2, \ldots, b_n]. \tag{5}$$

4.2. Example Analysis.

Taking the K23+000-K33+000 upbound line of the Xingtai–Linqing expressway in Hebei Province as an example, the performance evaluation indexes of each item were calculated. The test results are shown in Table 3.

Since PCI = 68.83, the membership function values at the optimal, good, medium, secondary, and bad levels were calculated, respectively, according to the above calculation formula and obtained after normalization.

TABLE 2: Randomness index RI.

n	1	2	3	4	5	6
RI	0	0	0.59	0.9	1.12	1.24

TABLE 3: Section K23-K33 performance evaluation indexes.

Test results	PCI	RQI	RDI	SRI
K23-K33 (uplink)	68.83	93.84	79.39	73.88

PCI = 68.83, $r_1 = [r_E, r_G, r_M, r_S, r_B] = [r_{11}, r_{12}, r_{13}, r_{14}, r_{15}] = [0, 0.922, 1, 0.078, 0]$

RQI = 93.84, $r_2 = [r_{21}, r_{22}, r_{23}, r_{24}, r_{25}] = [1, 0.411, 0, 0, 0]$

RDI = 79.39, $r_3 = [r_{31}, r_{32}, r_{33}, r_{34}, r_{35}] = [0.626, 1, 0.374, 0, 0]$

SRI = 73.88, $r_4 = [r_{41}, r_{42}, r_{43}, r_{44}, r_{45}] = [0.259, 1, 0.741, 0, 0]$

To sum up, the matrix is obtained $R_{([V_{ij}])}$:

$$R_{\left([v_{ij}]\right)} = \begin{bmatrix} 0 & 0.922 & 1 & 0.078 & 0 \\ 1 & 0.411 & 0 & 0 & 0 \\ 0.626 & 1 & 0.374 & 0 & 0 \\ 0.259 & 1 & 0.741 & 0 & 0 \end{bmatrix}. \tag{6}$$

Technical indexes of the Xinglin expressway asphalt pavement performance are C_1-PCI, C_2-RDI, C_3-RQI, and C_4-SRI. The judgment matrix is constructed by equation (2):

$$C = \left(c_{ij}\right) = \begin{bmatrix} c_{11} & c_{12} & \cdots & c_{1j} \\ c_{21} & c_{22} & \cdots & c_{2j} \\ \cdots & \cdots & \cdots & \cdots \\ c_{i1} & c_{i2} & \cdots & c_{ij} \end{bmatrix}_{i,j\,\text{take}4} = \begin{bmatrix} 1 & 2 & 1 & 3 \\ 1/2 & 1 & 1/2 & 2 \\ 1 & 2 & 1 & 3 \\ 1/3 & 1/2 & 1/3 & 1 \end{bmatrix}. \tag{7}$$

For maximum eigenvalues and eigenvectors,

$$\sum_{j=1}^{4} c_{1j} = 1 \times 2 \times 1 \times 3 = 6, \quad \overline{w_1} = \left(\sum_{j=1}^{4} c_{1j}\right)^{1/4} = 6^{1/4} = 1.565,$$

$$\sum_{j=1}^{4} c_{2j} = \frac{1}{2} \times 1 \times \frac{1}{2} \times 2 = \frac{1}{2}, \quad \overline{w_2} = \left(\sum_{j=1}^{4} c_{2j}\right)^{1/4} = \left(\frac{1}{2}\right)^{1/4} = 0.841,$$

$$\sum_{j=1}^{4} c_{3j} = 1 \times 2 \times 1 \times 3 = 6, \quad \overline{w_3} = \left(\sum_{j=1}^{4} c_{3j}\right)^{1/4} = 6^{1/4} = 1.565,$$

$$\sum_{j=1}^{4} c_{4j} = \frac{1}{3} \times \frac{1}{2} \times \frac{1}{3} \times 1 = \frac{1}{18}, \quad \overline{w_4} = \left(\sum_{j=1}^{4} c_{4j}\right)^{1/4} = \left(\frac{1}{18}\right)^{1/4} = 0.845. \tag{8}$$

Normalize the eigenvector $\overline{w} = (\overline{w_1}, \overline{w_2}, \overline{w_3}, \overline{w_4})^T = (1.565, 0.841, 1.565, 0.485)^T$:

$$w_1 = \frac{\overline{w_i}}{\sum_{j=1}^{4} \overline{w_j}}, \quad i = 1, 2, 3, 4, j = 1, 2, 3, 4, \sum_{j=1}^{4} \overline{w_j} = 4.456. \tag{9}$$

TABLE 4: Road performance evaluation results of K23~K33 section.

Stake	Excellent	Good	Medium	Secondary	Bad	Evaluation	PQI evaluation
K23-K24	0.555	0.723	0.444	0.157	0	Good	Good
K24-K25	0.466	0.803	0.534	0.073	0	Good	Good
K25-K26	0.446	0.668	0.554	0.091	0	Good	Medium
K26-K27	0.535	0.823	0.464	0.058	0	Good	Good
K27-K28	0.563	0.777	0.437	0.077	0	Good	Good
K28-K29	0.646	0.879	0.488	0	0	Good	Good
K29-K30	0.259	0.596	0.670	0.318	0	Medium	Medium
K30-K31	0.715	0.900	0.285	0	0	Good	Good
K31-K32	0.472	0.534	0.528	0.271	0	Good	Medium
K32-K33	0.624	0.879	0.376	0	0	Good	Good

So,

$$w_1 = \frac{1.565}{4.456} = 0.351,$$

$$w_2 = \frac{0.841}{4.456} = 0.189,$$

$$w_3 = \frac{1.565}{4.456} = 0.351,$$

$$w_4 = \frac{0.485}{4.456} = 0.109,$$

$$CW = \begin{bmatrix} 1 & 2 & 1 & 3 \\ 1/2 & 1 & 1/2 & 2 \\ 1 & 2 & 1 & 3 \\ 1/3 & 1/2 & 1/3 & 1 \end{bmatrix} \begin{bmatrix} 0.351 \\ 0.189 \\ 0.351 \\ 0.109 \end{bmatrix},$$

$$\lambda_{max} = \sum_{i=1}^{n} \frac{(c \cdot w)_i}{n \cdot w_i} = \frac{1.407}{4 \times 0.351} + \frac{0.758}{4 \times 0.189} + \frac{1.407}{4 \times 0.351}$$

$$+ \frac{0.437}{4 \times 0.109} = 4.01.$$

(10)

Inspection CI $= (\lambda_{max} - n)/(n - 1) = (4.01 - 4)/(4 - 1) = 0.0035$ and CR $=$ CI/RI $= 0.0035/0.90 = 0.0038 < 0.1$. It is consistent. Therefore, w_1, w_2, w_3, and w_4 are 0.351, 0.351, 0.189, and 0.109, respectively. The weight vector $w = (w_1, w_2, w_3, w_4)^T$, synthesis of the fuzzy comprehensive evaluation result vector by formula (3):

$$D = w \cdot R = [0.351, 0.351, 0.189, 0.109]$$

$$\cdot \begin{bmatrix} 0 & 0.922 & 1 & 0.078 & 0 \\ 1 & 0.411 & 0 & 0 & 0 \\ 0.626 & 1 & 0.374 & 0 & 0 \\ 0.259 & 1 & 0.741 & 0 & 0 \end{bmatrix}.$$

(11)

The resulting $D = [0.497, 0.765, 0.502, 0.027, 0]$. According to the principle of maximum membership, when $i = 2$, $D_0 = \max[d_i] = 0.765$. The corresponding rating is "good."

Similarly, performance evaluation results of uplink can be obtained based on the above model, as shown in Table 4.

It can be seen from Table 4 that, based on the multi-index comprehensive detection and evaluation adopted by the specification, the performance grade of the old road surface is quantitatively evaluated by using the iterative calculation of fuzzy mathematics, and the evaluation score of each kilometer is more quantitatively intuitive. It highlights the idea of expert evaluation based on traditional detection methods, weakens subjective judgment, highlights objective quantitative evaluation, and breaks through the evaluation mode based on traditional detection methods. The research results provide an innovative theoretical method for the accurate evaluation and analysis of highway pavement performance in semiarid climate regions.

5. Conclusions

This paper uses fuzzy mathematics to comprehensively evaluate the pavement performance of Xingtai to Linqing section of Taihang mountains expressway in the semiarid climate zone of Hebei Province. Based on the multi-index comprehensive detection and evaluation adopted by the specification, fuzzy mathematics is used to iteratively calculate and evaluate the performance grade of the old road. The research puts forward the feasibility of the fuzzy mathematics method in highway pavement performance evaluation and obtains the following research conclusions:

(1) This paper statistically analyzes the meteorological and hydrological characteristics of semiarid climate zones, combined with engineering case investigation and analysis. The results show that the types and distribution characteristics of highway pavement diseases are closely related to rainfall, extreme temperature, and temperature difference in semiarid climate areas.

(2) The study uses the factor domain, the comment level domain, the fuzzy relationship matrix, the evaluation factor full vector, and the fuzzy comprehensive evaluation result vector five-step method. The method can be effectively combined with the multi-index comprehensive detection index used in the specification.

(3) Based on the multi-index comprehensive test and evaluation adopted in the specification, the performance grade of the old road surface was quantitatively evaluated by iterative calculation with fuzzy mathematics, which broke through the evaluation mode based on the traditional detection methods. The research results provide an innovative theoretical method for the accurate evaluation and analysis of highway pavement performance in semiarid climate regions.

Data Availability

The data used to support the findings of this study are included within the article.

Conflicts of Interest

The authors declare that there are no conflicts of interest regarding the publication of this paper.

Acknowledgments

References

[1] Q. R. Li, Z. Y. Guo, Y. J. Wang, Evaluation of freeway asphalt pavement performance based on PCA—SVM," *Journal of Beijing University of Technology: Naturnal Science Eition*, vol. 44, no. 2, pp. 283–288, 2018.

[2] J. Zhao, *Performance evaluation and prediction model of asphalt pavement*, Ph.D. thesis, Dalian University of Technology, Dalian, China, 2008.

[3] (FHWA), *U.S. Department of Transportation Federal Highway Administration Office of Management Asset Management Overview*, (FHWA), Washington, DC, USA, 2007.

[4] M. Guo and Y. Q. Tan, "Interaction between asphalt and mineral fillers and its correlation to mastics' viscoelasticity," *International Journal of Pavement Engineering*, 2019.

[5] R. Hass, W. R. Huston, and J. Zaniewshi, *Modern Pavement Management*, Malabar, Florida: Krieger Publishing Company, Malabar, FL, USA, 1994.

[6] M. Y. Shahin, "Pavement management—PAVER update," in *Proceedings of the Annual Meeting of the Transportation Research Board (TRB), National Research Council*, Washington, DC, USA, 1999.

[7] K. C. P. Wang, J. Zaniewsk, and G. Way, "Probabilistic behavior of pavements," *Journal of Transportation Engineering*, vol. 120, no. 3, pp. 358–375, 1994.

[8] B. R. Kulkarni and W. R. Miller, "Pavement Management Systems: Past, Present, and Future," *Transportation Research Board*, vol. 1853, no. 1, pp. 65–71, 2003.

[9] J. L. Prozzi, *Modeling pavement performance by combining field and experimental data*, Ph.D. thesis, University of California, Oakland, CA, USA, 2001.

[10] C. Nunoo, *Optimization of Pavement Maintenance and Rehabilitation Programming Using Shuffled Complex Evolution Algorithm*, Florida International University, University Park, FL, USA, 2001.

[11] W. O. Hadley, *SHRP-LTTP Overview: Five-Year Report*, SHRP-P-416, Washington, DC, USA, 1994.

[12] D. L. Hao, *Evaluation and Analysis of Pavement Performance*, Chang'an University, Xi'an, China, 2000.

[13] R. K. Kher and M. I. Darter, *Probabilistic Concept and Their Application to AASHO Interim Guide for Design of Rigid Pavements*, HRB 466, Washington, DC, USA, 1973.

[14] Pavement Desing and Evalauation Committee, Roads and Transportation Association of Canada, "Output measurement for pavement management studies in canada," in *Proceedings of the Third International Conference on the Structural Design of Asphalt Pavements (ICSDAP)*, University of Michigan, Ann Arbor, MI, USA, 1972.

[15] H. Zhou, K. Xie, and H. M. Hu, "Evaluation and pavement model of expressway to pavement performance," *Engineering and Construction*, vol. 115, no. 1, pp. 66–69, 2018.

[16] T. Chen, *Research on Performance Evaluation Technology and Reinforcement Design Method of Expressway Asphalt Pavement*, Chang'an University, Xi'an, China, 2003.

[17] S. Q. Wen, *Research on Expressway Pavement Maintenance Decision Based on Combination Prediction and Fuzzy Optimization*, Dalian University of Technology, Dalian, China, 2009.

[18] H. M. Li, *Research on Maintenance Decision of Asphalt Pavement of Network Expressway Based on Matter-Element Model*, Southeast university, Dhaka, Bangladesh, 2017.

[19] J. P. Huang, M. X. Ji, and Y. Z. Liu, "An overview of arid and semi-arid climate change," *Progressus Inquisitiones DE Mutatione Climatis*, vol. 9, no. 1, pp. 09–14, 2013.

[20] C. Ling, L. Zhou, and F. Gu, "The application of extension theory on pavement performance evaluation," *Advanced Materials Research*, vol. 168–170, pp. 111–115, 2010.

[21] S. Q. Yang, N. Li, and S. Zhang, "Analysis of design index and structural mechanics of durable asphalt pavement in desert area," *Journal of Hebei University: Naturnal Science Edition*, vol. 36, no. 6, pp. 574–582, 2016.

[22] S. Q. Yang, W. X. Wu, and N. Li, "Ansys simulation analysis of cement concrete pavement bearing capacity under extra heavy load," *Journal of Hebei University: Naturnal Science Edition*, vol. 37, no. 6, pp. 561–566, 2017.

[23] S. W. Qi and F. Q. Wu, "Surrounding rockmass quality classification of tunnel cut by TBM with fuzzy mathematics method," *Chinese Journal of Rock Mechanics and Engineering*, vol. 30, no. 6, pp. 1225–1229, 2011.

[24] J. Bao, Y. Zhang, X. Su, and R. Zheng, "Unpaved road detection based on spatial fuzzy clustering algorithm," *EURASIP Journal on Image and Video Processing*, vol. 26, no. 12018.

[25] J. X. Tang and X. Y. Li, "On the stability evaluation of the deep subway foundation pit based on the fuzzy mathematical theory," *Journal of Safety and Environment*, vol. 18, no. 6, pp. 2135–2140, 2018.

[26] X. Li, X. W. Yang, and J. Huang, "Comprehensive evaluation system of cement pavement performance based on fuzzy mathematics," *Journal of Lanzhou University: Naturnal Science Edition*, vol. 45, no. S1, pp. 88–92, 2009.